

# e+A collisions at the EIC

A. Accardi, C. Marquet, M. Lamont (Editors)

May 31, 2011

## Contents

<b>1</b>	<b>Overview and golden measurements</b>	<b>3</b>
1.1	Golden and silver measurements . . . . .	4
1.2	QCD at high gluon density . . . . .	4
1.2.1	Integrated gluons . . . . .	6
1.2.2	Transverse momentum dependence . . . . .	7
1.2.3	Transverse position dependence . . . . .	8
1.3	Quark-gluon structure of nuclei . . . . .	9
1.4	Parton propagation and hadronization in nuclear matter . . . . .	10
<b>2</b>	<b>Small-<math>x</math> Physics and Saturation</b>	<b>12</b>
2.1	Introduction and review of linear and non-linear approaches in QCD . . . .	12
2.1.1	Collinear factorization and DGLAP evolution . . . . .	12
2.1.2	Small- $x$ re-summations . . . . .	13
2.1.3	Parton Saturation . . . . .	15
2.1.4	Universality aspects of the Color Glass Condensate . . . . .	23
2.1.5	Shadowing . . . . .	27
2.1.6	Leading-twist nuclear shadowing . . . . .	32
2.1.7	Non-perturbative approaches . . . . .	34
2.2	Inclusive DIS ( $F_2$ , $F_L$ , $F_2^c$ ) . . . . .	37
2.2.1	Estimates of higher twist in deep inelastic nucleon and nucleus scattering	37
2.2.2	Strength of nonlinear effects in nucleons and nuclei . . . . .	39
2.2.3	Nuclear PDFs and deviations from DGLAP evolution . . . . .	42
2.2.4	Constraining the nuclear gluon distribution using inclusive observables	45
2.2.5	DIS in the high-energy limit at next-to-leading order . . . . .	48
2.2.6	Running Coupling in Small- $x$ Physics . . . . .	52
2.2.7	Running-coupling and higher-order effects on the saturation scale . .	54
2.3	Diffractive DIS ( $F_2^D$ , $F_L^D$ , charm contribution) . . . . .	56
2.3.1	Diffraction in e+p and e+A collisions . . . . .	56
2.3.2	Expectations for e+A from the CGC . . . . .	59
2.3.3	Expectations for e+A from LT shadowing . . . . .	62
2.4	$k_T$ -dependent gluons: SIDIS and Jets . . . . .	65
2.4.1	Dijet and Dihadron production at EIC . . . . .	65
2.4.2	Heavy quark production in $eA$ collisions . . . . .	68
2.5	$b$ -dependent gluons: Exclusive VM, DVCS . . . . .	70
2.5.1	Gluon Density in e+A : KLN, CGC, DGLAP Glauber, or Neither? .	70

2.5.2	Coherent vs Incoherent . . . . .	77
2.5.3	Electroproduction of $J/\Psi$ . . . . .	82
2.5.4	Exclusive processes in $eA$ collisions . . . . .	88
2.5.5	Constraining the $\rho$ wavefunction . . . . .	90
<b>3</b>	<b>Nuclear Effects Across the <math>x - Q^2</math> plane</b>	<b>95</b>
3.1	Nuclear Quarks and Gluons . . . . .	95
3.1.1	Introduction . . . . .	95
3.1.2	The EMC effect at an EIC . . . . .	96
3.1.3	Nuclear gluons . . . . .	97
3.1.4	Global fits of nuclear PDFs: current status . . . . .	98
3.1.5	HKN nuclear parton distribution functions . . . . .	102
3.2	Colour Transparency . . . . .	103
3.2.1	Colour transparency phenomena . . . . .	103
3.2.2	From color transparency to color opacity . . . . .	106
3.3	Nuclear quark and gluon GPDs . . . . .	109
3.3.1	Medium $x_B > 0.05$ . . . . .	110
3.3.2	Small $x_B < 0.05$ : leading twist shadowing and exclusive diffraction . . . . .	111
3.4	Nuclear TMDs . . . . .	114
<b>4</b>	<b>Parton Propagation and Hadronization</b>	<b>117</b>
4.1	Current Fragmentation . . . . .	117
4.1.1	Introduction and the role of $e + A$ collisions . . . . .	117
4.1.2	Studying Hadronization at EIC . . . . .	121
4.1.3	Hadronization in $e + A$ collisions within GiBUU . . . . .	124
4.1.4	A global fit of nuclear fragmentation functions . . . . .	126
4.1.5	Heavy quarks and quarkonia in a nuclear environment . . . . .	130
4.2	Jets . . . . .	133
4.2.1	Jets, in-medium parton propagation and nuclear gluons . . . . .	133
4.2.2	Monte-Carlo for hard jets in $e+A$ collisions . . . . .	134
4.2.3	Jet evolution in hot and cold matter . . . . .	137
4.3	Target Fragmentation . . . . .	139
4.3.1	Fragmentation of nuclei - a critical tool for novel QCD phenomena . . . . .	139
4.3.2	In-medium hadronization and EMC effects in nuclear SIDIS . . . . .	141
4.3.3	Slow Neutrons and Final-State-Interaction Length . . . . .	144
4.4	Bose-Einstein Correlations at the Electron-Ion Collider . . . . .	144
<b>5</b>	<b><math>e+A</math> Monte Carlo Simulation Tools</b>	<b>150</b>
5.1	A Monte Carlo Generator for Diffractive Events in $e+A$ Collisions . . . . .	150
5.2	Parton propagation and hadronization simulations: overview . . . . .	156
5.3	PyQM: a pure energy loss Monte-Carlo simulation . . . . .	157
<b>6</b>	<b>Connections to Other Fields</b>	<b>159</b>
6.1	Gluon Tomography in Nuclei - The Heavy Ion Collision Initial State . . . . .	159
6.2	Constraining initial conditions in $A+A$ collisions . . . . .	163
6.3	Particle production at low- $x$ and gluon saturation: from $p + A$ to $e + A$ . . . . .	165
6.4	Small- $x$ dynamics in ultraperipheral heavy ion collisions at the LHC . . . . .	169

# 1 Overview and golden measurements

*Alberto Accardi, Matthew Lamont and Cyrille Marquet*

A basic quest of nuclear physics is the understanding of the structure of nuclei (nucleon number  $A > 1$ ) in terms of QCD Lagrangian degrees of freedom, the quarks and gluons. Deviations of the nuclear quark and gluon densities from the sum of the free nucleon densities directly attest to binding effects and elucidate the QCD origin of the internucleon interactions. Such deviations can arise through different mechanisms, such as modification of the free nucleon structure, presence of non-nucleonic degrees of freedom, and quantum-mechanical interference of the quark/gluon fields of different nucleons at small parton fractional momentum  $x$  (“shadowing”), creating a fascinating landscape. At even smaller  $x$ , the gluon density increases to the point where gluons can start interacting with each other, leading to a regime of non-linear QCD evolution called saturation. This regime is argued to be universal for any hadronic system, ranging from pions, to protons and nuclei, but its onset is enhanced in nuclear targets due to the superposition of the gluon field of many nucleons.

A peculiar pattern of nuclear modifications was observed in fixed-target experiments and caused much excitement; it shows suppression for  $0.2 < x < 0.8$  (“EMC effect”), some signs of enhancement for  $0.05 < x < 0.2$ , and significant suppression (shadowing) at smaller  $x$ . However, such experiments were unable to reach deep into the shadowing region or probe gluons. The EIC will overcome these limitations, extend measurements to very high scales of  $Q^2$ , and determine with high precision the nuclear effects on gluon distributions. Full reconstruction of the hadronic final state also opens up for the first time the possibility of measuring charged current interactions on nuclei, and to perform a full quark flavour separation based on nuclear DIS data only. Crucially, the EIC will access even lower values of  $x < 0.01$ , and study the onset of the saturation regime, which has never been directly probed experimentally, although tantalising (but not unequivocal) signatures have been found at the Relativistic Heavy-Ion Collider (RHIC).

Another possibility offered by nuclear targets is the study of the propagation of colour charges in nuclear matter and the space-time evolution of hadronization. The unique feature of the EIC compared to previous fixed target experiments is its large energy span, which allows one to experimentally boost hadronization effects completely out of the nucleus, in order to focus attention on the propagation of hard quarks and gluons, and their accompanying parton showers, through the nucleus: thus one can use the partons as coloured probes of the soft (small  $x$ ) components of the nuclear wave function, and conversely experimentally test QCD mechanisms of parton energy loss in a known nuclear medium. At smaller energy, hadronization happens partially inside the nucleus, which can then be used as a femtometer scale detector of the process. A good control of energy loss mechanisms in the partonic phase will yield unambiguous insights into the dynamics of color confinement, by which hadrons emerge from coloured quarks and gluons.

Novel observables will be available thanks to the high energy reach, namely heavy flavours, charmonium and bottomonium, and jets, greatly expanding the experimental toolbox and sensitivity to nuclear effects, and allowing a close connection to first-principle calculations in QCD. The collider mode will also make it feasible to study in detail target fragmentation and its correlation to current fragmentation, expanding considerably the study of the hadronization mechanisms.

## 1.1 Golden and silver measurements

One of the goals of the program was to identify a small number of measurements which have an undeniable new physics reach and are undoubtedly feasible at an EIC. Such measurements are referred to as “golden” measurements, they are complemented by other “silver” measurements/observables, to form a broad, robust, and compelling physics program. These measurements are summarised in Tables 1 and 2, where also their feasibility in phase-I (medium energy) and phase-II (full energy) is indicated, and further discussed below. Many more observables than can fit in this section will be available at the EIC, contributing to a very rich physics program exploring the QCD basis of nuclear physics. These will be reviewed in detail in the rest of this chapter.

Deliverables	Observables	What we learn	Phase-I	Phase-II
integrated gluon distributions	$F_{2,L}$	nuclear w.fn.; saturation, $Q_s$	gluons at $10^{-3} \lesssim x \lesssim 1$	saturation regime
$k_T$ -dep. gluons; gluon correlations	di-hadron correlations	non-linear QCD evolution/universality	onset of saturation	measure $Q_s$
transp. coefficients in cold matter	large- $x$ SIDIS; jets	parton energy loss, shower evolution; en. loss mechanisms	light flavours and charm; jets	rare probes and bottom; large- $x$ gluons

Table 1. Golden measurements in  $e + A$  collisions at an EIC

Deliverables	Observables	What we learn	Phase-I	Phase-II
integrated gluon distributions	$F_{2,L}^c, F_{2,L}^D$	nuclear w.fn.; saturation, $Q_s$	difficult measurement or interpretation	saturation regime
flavour separated nuclear PDFs	charged current & $\gamma Z$ str. fns.	EMC effect origin	full $q_i$ separation at $0.01 \lesssim x \lesssim 1$	larger $Q^2$ , smaller $x$
$k_T$ -dep. gluons	SIDIS at small- $x$	non-linear QCD evolution/universality	onset of saturation	measure $Q_s$ ; flavour sep.
$b$ -dep. gluons; gluon correlations	DVCS; diffractive $J/\Psi$ , & vector mesons	interplay between small- $x$ evolution and confinement	moderate $x$ with light, heavy nuclei	smaller $x$ , saturation

Table 2. Silver measurements in  $e + A$  collisions at an EIC

## 1.2 QCD at high gluon density

The fact that we do not know the dynamics of gluons in nuclei over basically any  $x$  range seems a compelling enough reason to build an EIC. In fact, an EIC would also allow one for the first time to experimentally probe at small  $x$  the dynamical non-Abelian aspects of a fundamental force of nature in a controlled setting by perturbative methods. This would be no small feat, since the non-Abelian nature of QCD is its distinguishing feature and controls phenomena such as colour confinement and the generation of 99% of the visible mass in the Universe. These are, however, typical non-perturbative phenomena which are difficult to attack from first principles, and where this is possible, such as in the case of the hadron spectrum from lattice QCD, only static aspects of the strong interactions are addressed.

In addition, experimentally establishing and refining an effective field theory for the saturation regime – such as the Color Glass Condensate (CGC) – as well as precisely

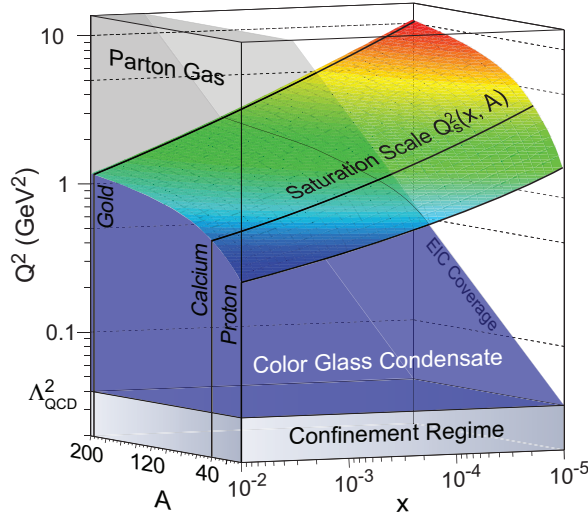


Figure 1. The saturation scale,  $Q \equiv Q_s$ , and how it scales with  $x$ , and  $A$ .

imaging the distribution and correlations of small- $x$  partons in nuclei would have wide-ranging applications. The universality of the saturation regime implies that such a theory would provide a microscopic basis for understanding and calculating total hadronic cross sections, with important applications to, *e.g.*, ultra-high energy cosmic ray physics, where extrapolations in energy of a few orders of magnitude are required to compute their spectrum and detect possible new physics effects. In high-energy relativistic heavy-ion collisions, the release of saturated low- $x$  partons represents the starting point of the subsequent space-time evolution of the Quark-Gluon Plasma (QGP). Testing and benchmarking the underlying theory opens the prospect of a controlled and precise first-principle calculation of such an initial state, reducing one of the largest sources of uncertainty in the interpretation of experimental observables, and the measurements of the QGP properties: an EIC would offer to the RHIC and LHC heavy-ion programs an important asset, as valuable as the one HERA provided to the LHC p+p program.

The onset of the saturation regime, when the gluon density becomes so large that further growth is tamed, is characterised by the so-called saturation scale  $Q_s(x)$ : it is the scale below which partons overlap in transverse space, so that parton recombination stops further growth in their number density. Given that parton distributions grow as  $x$  decreases, and dramatically so as discovered at HERA, the saturation scale is clearly expected to grow as  $x$  decreases. It is furthermore enhanced in nuclear targets because of the overlap of the gluon fields originating from different nucleons. This is illustrated in Figure 1. In the saturated, dense regime at small  $x$ , non-linear QCD dynamics becomes dominant but the scale being set by a large  $Q_s$  (of order 1 GeV), calculations can be carried out by weak coupling techniques, and suitable effective field theories, of which the CGC is a prime example, can be derived from first principles.

The dilute-dense separation is a bit subtler than just described: the larger the gluon's transverse momentum  $k_T$ , the smaller its longitudinal energy fraction  $x$  needs to be to enter the saturation regime. In a scattering process, dilute partons (with  $k_T \gg Q_s(x)$ ) behave incoherently, while when the parton density is large ( $k_T \lesssim Q_s(x)$ ), gluons scatter coherently. Therefore, transverse momentum dependent observables will be able to uncover more details than inclusive observables, which can only access averaged saturation effects.

The interplay of saturation and transverse spatial distribution of gluons is also important: as  $x$  decreases, gluon densities saturate first in the center of the nucleus; to accommodate further growth, gluons will be pushed more and more to the periphery, so that the average gluon radius is expected to increase with decreasing  $x$ .

For all these reasons, regarding the small- $x$  physics program in e+A collisions, the physics deliverables of the EIC have been classified in three main categories giving access to the integrated, transverse-momentum-dependent, and impact-parameter-dependent gluons. Here, by “gluons” we mean not only the standard single-gluon distributions but also multi-gluon distributions, *i.e.*, gluon correlations. These have in general been of secondary interest, but are now recognised as essential to a full understanding of the low- $x$  regime. Indeed, except for the most inclusive observables which are subject to cancellations, consistent QCD calculations in the non-linear regime require the knowledge of multi-gluon distributions. Integrated, transverse-momentum-dependent, and impact-parameter-dependent gluon distributions and correlations in nuclei are all unknown, and the processes we discuss below have never been measured at small  $x$ .

### 1.2.1 Integrated gluons

Being the most basic observables from both the theory and experimental sides, the inclusive ( $eA \rightarrow eX$ ) structure functions  $F_2$  and  $F_L$  stood out among other measurements, already well before the program. They were the first potential golden measurements discussed, the pros and cons of those candidates to pin down to the gluon distribution in nuclei were further reviewed during the program.

$F_2$  is the most inclusive observable in deep inelastic scattering, its measurement is no particular experimental challenge, and on the theory side it is the simplest process to calculate, along with  $F_L$ . For instance, they will be the first observables for which a full NLO calculation in QCD including non-linear effects will be available (at the moment, the existing phenomenology is still based on leading-order impact factors).

Although it is harder to extract experimentally,  $F_L$ , rather than  $F_2$ , emerged as the golden measurement regarding high-density QCD because it is more directly related to the gluon distribution, and is more sensitive to non-linear effects than  $F_2$ , which is subject to a large higher-twist cancellation which delays the onset of non-linear effects. The necessity to perform an energy scan to measure  $F_L$  implies that the accessible  $x$  range is a bit smaller than with the  $F_2$  measurement, however this increased sensitivity to non-linear effects more than overcomes this issue. It was explicitly established that an  $F_L$  measurement at the full-energy EIC (phase-II) cannot be compatible with both the presence and the absence of non-linear effects, and that DGLAP fits of EIC data should be able to quantitatively determine the onset of the saturation regime. The case of the low-energy EIC needs to be investigated more; in particular, the implementation of non-linear effects must be made more accurate, and more detailed DGLAP fits of EIC pseudo-data should be performed before establishing its sensitivity to saturation physics in the inclusive channel. One caveat that was discussed is that radiative corrections for nuclear targets can be large, and it remains to be proven that they can be controlled to the required precision – but this is likely to happen before the start of EIC operations.

The charm structure functions  $F_{2,L}^c$  were considered a silver measurement for the non-linear regime. As for  $F_L$ , these observables give a more direct access to the gluon distribution compared to  $F_2$ ; however due to the mass of the charm quark, they also probe higher values of  $x$  and are therefore less sensitive to non-linear effects. In addition, QCD calculations

with non-zero charm mass are scheme dependent, which can absorb signals of non-linear effects if not appropriately handled.. However, since they can be measured precisely with a properly-designed vertex detector, charmed structure functions will be a very important complementary measurement to pin down the gluon distribution throughout the  $(x, Q^2)$  plane.

The last silver measurement in this category is that of the diffractive structure function  $F_2^D$ , which is sensitive to the square of the gluon distribution. In fact, most hints of manifestations of non-linear effects in e+p collisions at HERA come from that measurement: the ratio of the diffractive to inclusive structure function is constant with energy, the leading-twist approximation does not explain the geometric scaling of the diffractive cross section, and the DGLAP analysis starts failing at larger and larger value of  $Q^2$  than for  $F_2$  (approximately, 8 GeV<sup>2</sup> compared to 2 GeV<sup>2</sup>). However, it is relatively difficult to measure and the additional kinematic variables involved make its analysis more involved than for  $F_2$  and  $F_L$ .

### 1.2.2 Transverse momentum dependence

The simplest process to extract the transverse momentum dependence of the gluon distribution is semi-inclusive DIS,  $e + A \rightarrow e + h + X$  (SIDIS). One reason why these processes are especially interesting is that by having two momentum scales at one's disposal, it is possible to keep  $Q^2$  large and access the saturation regime at transverse momenta  $p_T \lesssim Q_s$ . This way, non-perturbative effects and higher-twist contributions are suppressed, but one can nonetheless access the non-linear QCD dynamics. Considering that  $Q_s$  will not exceed a few GeV at the EIC, this allows one to avoid disentangling non-perturbative effects, characterized by a fixed scale ( $\Lambda_{QCD}$ ), from the weak coupling non-linear effects characterized by an energy dependent scale ( $Q_s(x)$ ), as might be necessary with inclusive observables. Furthermore, in the large  $Q^2$  and small  $x$  limits, the relation between the transverse momentum of the produced hadron  $p_T$  and that of the small- $x$  glue  $k_T$  is quite direct, enabling a rather straightforward experimental probe of the gluon's transverse momentum distribution. Thus, SIDIS has all the prerequisites to be considered a golden observable, but was nonetheless classified as silver because an even more compelling observable was found.

The golden measurement is di-hadron azimuthal correlations in  $e + A \rightarrow e + h_1 + h_2 + X$  processes. It has all the benefits mentioned above and has a broader physics reach: contrary to SIDIS, di-hadron correlations are not only sensitive to the  $k_T$  dependence of the gluon distribution but also to the  $k_T$  dependence of gluon correlations. The only drawback is that accurate theoretical calculations are presently not possible for this process because they require multi-gluon distributions, which are largely unknown; the precise measurement that the EIC can make would, in turn, constrain these very important objects and their non-linear evolution. However, even though the present theoretical uncertainties are large and the predictions are qualitative at best, saturation effects produce such a striking signal in the case of this observable that they cannot be missed.

The expected signal is a progressive disappearance as  $x$  is decreased (and  $Q_s$  increased) of the peak in the di-hadron azimuthal angle difference around  $\Delta\phi = \pi$ , which is expected in the case of hard scattering on dilute gluons on the basis of momentum conservation. A comparison of  $e + A$  and  $e + p$  collisions would clearly mark out experimentally such an effect, as has already been observed for di-hadrons produced at forward rapidity in  $d + Au$  and  $p + p$  collisions at RHIC. In that case, di-hadron production proceeds from valence quarks in the deuteron (proton) scattering on small- $x$  gluons in the target  $Au$  nucleons (proton),

$q_V + Au(p) \rightarrow h_1 + h_2 + X$ , and lacking direct experimental control over  $x$ , the onset of the saturation regime is controlled by changing the centrality of the collisions or reducing the di-hadron rapidity. Experimentally, a striking flattening of the  $\Delta\phi$  peak in  $d + Au$  collisions is observed in central collisions, but the peak reappears in peripheral collisions or for mid-rapidity di-hadrons. However, directly using the point-like electron, as opposed to a quark bound in a proton or deuteron, is extremely beneficial: it is experimentally much cleaner as there is no background to subtract and, more importantly, the access to the exact kinematics of the process allows for a much cleaner extraction of the physics than possible at RHIC or in the future with  $p + A$  collisions at the LHC. Finally, even if by the time of EIC operations, there would be LHC  $p+A$  data on di-hadron correlations, it would still be an important task to check the universality of the  $x$  and  $k_T$  dependence of the gluon distribution and correlations.

### 1.2.3 Transverse position dependence

To pin down the transverse distribution and correlations of small- $x$  gluons, exclusive measurements are needed. The prototypical observables discussed are diffractive vector meson production (DVMP) and deeply virtual Compton scattering (DVCS), with coherent diffraction (intact nuclear target) giving access to the transverse distribution of the gluon density, and incoherent diffraction (dissociated nuclear target) allowing to extract, in addition, transverse plane correlations. Both represent crucial knowledge, in particular in the quest to quantitatively understand relativistic heavy-ion collisions. The most considered final-state vector particle is the  $J/\Psi$  meson. In time, the use of other vector mesons channels ( $\rho$ ,  $\phi$ ) will be integrated into the analysis as well, but the DVCS process should be considered along with diffractive  $J/\Psi$  production in the first studies. Indeed, they have theoretical advantages (no or little theoretical uncertainties from the wave functions), and drive different aspects of detector design.

Coherent diffractive  $J/\Psi$  production has been extensively discussed as potentially the golden measurement in this category. However, while the physics goals are clearly golden, by the end of the program it was not undoubtedly established that this measurement can deliver them, and a consensus was never reached that this observable is more than a candidate. The issue is to what extent the squared momentum transfer  $t$  dependence of the cross section will teach us more than what the Woods Saxon distribution of nucleons already tells us. For instance, it has yet to be determined whether non-linear effects in the small- $x$  evolution of the gluon distribution influence sufficiently the  $t$  dependence of the cross section, considering how sensitive the observable is to the edges of the matter distribution. This is difficult to estimate since on the theory side, understanding the interplay between small- $x$  evolution and impact parameter dependence remains a challenge.

The largest differences between the various models appear in the position of the coherent diffractive peaks and valleys, which are buried under the background of incoherent diffractive events. Coherent diffraction dominates over incoherent diffraction only at rather low values of  $t$ . It was determined that a rejection of the target-dissociation background with at least 95% efficiency is required in order to measure the coherent cross section up to large enough momentum transfers, and a 20 MeV resolution on the momentum transfer is also needed in order to extract precise-enough information in impact parameter space. Both are achievable goals, meaning  $e+A \rightarrow e+J/\Psi+A$  is undeniably a silver measurement that would determine the presently unknown transverse spatial distribution of gluons from light to heavy nuclei. Whether this would only be able to image the nucleus outside the saturation region or into



it as well remains an unsettled debate at the moment.

Studies of the incoherent regime of diffractive vector meson production are slowly but surely emerging. This process is *a priori* more sensitive to small- $x$  physics than coherent diffraction, because it is much easier to measure at large  $t$ , corresponding to small values of  $b$ , nearer the center of the nucleus where the gluon density is the largest. However, the amount of information that can be extracted from the nuclear fragments is not clear, since the theoretical description of the nuclear break-up remains a challenge. The minimum requirement is to be able to identify if the nucleus breaks up into its constituent nucleons or if the nucleons themselves break-up, as the corresponding calculations require different theoretical tools. Neither experimental or theoretical works on this process are mature enough to classify it as a silver or golden measurement, but it is a promising observable and investigations should be pursued further.

### 1.3 Quark–gluon structure of nuclei

Nuclear deep–inelastic scattering with a phase-I EIC will provide an original and unique measurement of gluon and sea quark densities in the “dilute” regime at  $x \gtrsim 0.01$  in a range of nuclei. While the quark densities in the region  $0.05 \lesssim x \lesssim 0.6$  were studied in fixed target experiments and will be further explored with JLab 12 GeV, the behaviour of the gluon and sea quark densities in this region is essentially unknown. A phase-I EIC will have sufficient  $Q^2$  range to extract the nuclear gluon density through the  $Q^2$  dependence of the nuclear structure function  $F_2^A$ ; more direct access to gluons can be gained by isolating the longitudinal structure function  $F_L^A$  through measurements at different beam energies, or by additionally tagging charm production.

The reliable determination of the nuclear gluon density in the dilute regime at is essential for a quantitative assessment of the onset of the new QCD regime of high parton densities and non-linear gluon interactions, which will be more widely accessible at a full-energy EIC: nuclear shadowing may in fact slow down the approach to gluon saturation. At  $x \gtrsim 0.1$ , an EIC will also explore the gluon anti-shadowing and EMC effects – a step that might prove as revolutionary for our understanding of nuclei as the discovery of the quark EMC effect 30 years ago. For these reasons, inclusive  $F_{2,L}$  structure functions measurements at larger  $x$  complement those discussed for the small- $x$  regime, and can in fact be considered golden also if saturation in the inclusive channels turns out to be non detectable in phase-I.

As it turns out, the high luminosity envisaged for the EIC, enables measurements of nuclear electromagnetic structure functions up to  $x \approx 1$  competitively with, or even surpassing, what has been achieved to date in fixed target experiments. Furthermore, the large  $Q^2$  range and hadronic event reconstruction capabilities will also likely allow measurement of charged current structure functions, and possibly of  $\gamma - Z$  interference structure functions. See the chapter on electroweak physics for further discussion.

..... **cross-reference to be included by the editors** .....

This will enable a full quark flavour separation utilising only nuclear DIS data, and offer, for example, new handles on the origin of the EMC effect, such as its flavour dependence, and the possibility of utilising nuclear Drell-Yan data to study initial state parton energy loss (see Section 1.4). These measurements are highly interesting and important, and in some cases unique to the Electron-Ion Collider compared to previous facilities, but more work is needed to establish to what extent full flavor separation can be effectively carried out at the EIC: therefore we classify them as silver.

Much more information on the nuclear modification of the quark/gluon structure of the

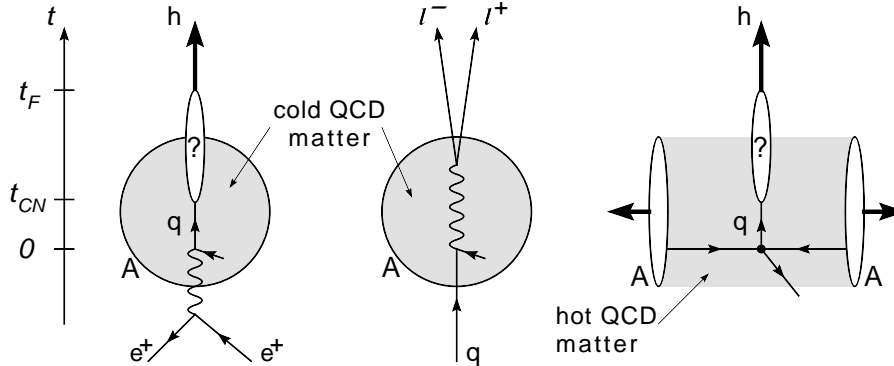


Figure 2. Parton propagation and hadronization in cold and hot nuclear matter. The color neutralization ( $t_{CN}$ ) and hadron formation ( $t_F$ ) time scales are defined on the vertical time axis.

proton and neutron can be gained from deep-inelastic measurements with detection of the spectator system of  $(A - 1)$  nucleons in the final state. In particular, measurements on deuterium with a spectator proton can measure structure functions of the bound neutron ranging from nearly on-shell to far off-shell, facilitating the extrapolation to an on-shell neutron. Measurements with a spectator neutron, which are extremely difficult with a fixed target but feasible at a collider using a zero degree calorimeter, provide completely new information on the off-shell proton structure functions, and constrain theoretical models by comparison to the well known free proton wave function. With heavier nuclear targets, one could explore the effects of nucleon embedding in a complex nuclear environment. While no technical difficulty is foreseen, detailed studies of the required detectors are needed to determine the feasibility and precision of these measurements, which for the moment we refrain from classifying.

#### 1.4 Parton propagation and hadronization in nuclear matter

The transition from colored partons (quarks and gluons) to colorless hadrons – the so-called hadronization or fragmentation process – is an exemplary process of the fundamental theory of QCD which still lacks a quantitative understanding from first principle calculations. Fragmentation functions, which encode the probability that a parton fragments into a hadron, have been obtained by fitting experimental data covering large kinematic ranges and numerous hadron species. However, knowledge about the dynamics of the process remains fragmentary and model dependent. A simple but rough general picture can be established from general considerations, see Figure 2: because of color confinement, the free color charge of the struck parton must be neutralized on a short time scale of the order of a few fm/c; the parton then originates a colorless prehadron, which will eventually form a hadron after another short time interval. Measuring these time scales will be the first step towards understanding how hadrons emerge dynamically from partons, complementing the information on the static properties of color confinement coming from hadron spectrum measurements.

Nuclear deep inelastic scattering (nDIS) provides a known and stable nuclear medium (“cold QCD matter”) and a final state with strong experimental control on the kinematics of the hard scattering. This permits one to use nuclei as femtometer-scale detectors of the hadronization process, see Figure 2. In fact, both the energy loss due to medium-induced

gluon *bremsstrahlung* off a quasi-free parton and the prehadron reinteraction with the surrounding nucleons lead to attenuation and transverse momentum broadening of hadron yields compared to proton targets, and allow experimental access to the space-time evolution of hadronization. Theoretical models of this process can be calibrated in nDIS and then applied, for example, to the study of the Quark-Gluon Plasma (“hot QCD matter”) created in high-energy nucleus-nucleus collisions.

The combination of high energy and luminosity offered by the EIC promises a truly qualitative advance in this field, compared with current and planned fixed target experiments. The large  $Q^2$  range permits measurements in the fully calculable perturbative regime with enough leverage to determine nuclear modifications in the QCD evolution of fragmentation functions; the high-luminosity permits the multidimensional binning necessary for separating the many competing effects and for detecting rare hadrons. The large  $\nu$  range ( $\approx 10 - 1000$  GeV) allows one to experimentally boost the hadronization process in and out of the nuclear medium, in order to isolate in-medium parton propagation effects (large  $\nu$ ) and cleanly extract color neutralization and hadron formation times (small  $\nu$ ); furthermore, using the quark flavor separated nuclear PDFs expected from the EIC, one could analyze nuclear Drell-Yan data, which are free from hadronization effects, and isolate initial state parton energy loss from nuclear wave function effects, enabling a complete experimental study of color charge interactions in cold nuclear matter. For the first time, one will be able to study hadronization of open charm and open bottom meson production in  $e + A$  collisions, as well as the in-medium propagation of the associated heavy quarks: these allow one to fundamentally test high-energy QCD predictions for energy loss, and confront puzzling measurements of heavy flavor suppression in the Quark-Gluon Plasma at RHIC. Within a collider environment, one would also be able to separate target from current hadronization and cross-correlate these two, adding a new dimension to hadronization studies.

The scattered quarks and gluons, from which the final-state hadrons emerge, couple to the nuclear gluons. Good control over the colour neutralization time scale will allow one to use this internally created colour radiation to explore the structure of nuclear matter in close analogy with the well-known exploration of matter with electromagnetic radiation or electrically charged particles. Furthermore, an EIC with  $\sqrt{s} \gtrsim 30$  GeV will permit for the first time the measurement of jets and their substructure in  $e + A$  collisions, furnishing a novel and extensive set of observables which directly access quark energy loss and the as yet untested parton shower mechanism, fundamentally described in QCD and pervasive in applications to particle physics simulations. Jet nuclear modifications can also be directly related to the propagation of the coloured partons shower in the nuclear medium, and used to measure the cold nuclear matter transport coefficients which encode basic information on the non-perturbative soft gluon structure of the nuclei. These measurements are complementary to direct inclusive and diffractive structure functions measurements at small  $x$  in accessing the high-density non-linear QCD regime, but are entirely feasible with a low-energy EIC.

The outlined parton propagation and hadronization program can for the most part be carried out in phase-I – in phase-II, we do not anticipate any qualitative new lesson will be learned, while the increased energy and  $Q^2$  range may prove useful, *e.g.*, for more refined studies in the jet and heavy flavor sectors, and offering an increased reach towards small  $x$  for nuclear gluon measurements via 2+1 jet production.

In conclusion, due to the physics interest, theoretical interpretability, and feasibility in phase-I, this program as a whole was classified as golden, with light quark SIDIS classified as silver.

## 2 Small- $x$ Physics and Saturation

### 2.1 Introduction and review of linear and non-linear approaches in QCD

#### 2.1.1 Collinear factorization and DGLAP evolution

*Anna M. Staśto*

The evaluation of the cross sections in QCD which involve hard scales is possible thanks to the factorization theorem. The latter ones are derived from first principles in QCD [1, 2] and allow to factorize the cross sections into the hard scattering coefficients which are computed within perturbation theory in terms of the series in the strong coupling constant and parton densities which involve information about nonperturbative physics. Parton densities, due to their non-perturbative nature, cannot yet be directly evaluated from first principles. Nevertheless, their evolution with hard scale can be calculated. This is done usually using the renormalization group equations, equivalent to DGLAP equations, as indicated by Eq. 1

$$\mu \frac{d}{d\mu} f_{j/h}(x, \mu) = \sum_k \int_x^1 \frac{dz}{z} P_{jk}(z, \alpha_s(\mu)) f_{k/h}(x/z, \mu), \quad (1)$$

with the splitting functions which have perturbative expansion in terms of the strong coupling

$$P_{jk}(z, \alpha_s(\mu)) = \sum_i (\alpha_s(\mu))^i P_{jk}^{(i)}(z). \quad (2)$$

Coefficient functions and splitting functions are known up to NNLO accuracy [3–5]. It has been found that at this order, large corrections appear which are enhanced by the logarithmic terms in  $1/x$ . The collinear approach suffers also from other limitations. The kinematical approximations, are mostly suitable for evaluation of the inclusive observables, are not sufficient for the exclusive processes and can lead to large discrepancies [6].

There are also other direct indications of the breakdown of the fixed order approach. From the global fits [7, 8], it is known that the gluon density suffers from large uncertainties at the NLO level in the region of small values of  $x$ , and the gluon density even turns negative. Even though the gluon density is not a directly observable quantity, the abovementioned uncertainties propagate into the observable longitudinal structure function  $F_L$ . The problem is concentrated at low  $Q$  and low- $x$  region, though the uncertainties remain even at larger values of  $Q$  when  $x$  is decreased. A systematic study of the compatibility of the HERA deep inelastic data with DGLAP evolution has been performed in [9]. This analysis, originally based on the NNPDF1.2 analysis [10, 11], was then extended to the global NNPDF2.0 set, which includes the very precise combined HERA-I dataset as well as all the relevant hadronic data. A ‘safe’ region was defined as the one in which the non-DGLAP effects are expected to be negligible, and it was defined by the cut on low- $x$  and  $Q$  data. A fit was then performed to the data that pass the cut and only belong to the safe region and the structure functions evaluated at different scales. It turned out that the prediction for the structure functions at low  $Q^2$  obtained from the backward-evolution of the data above the cut exhibits a systematic downward trend. Thus the precise HERA measurements indicate that the fixed order DGLAP evolution is incompatible with the data in the low  $Q^2$  and  $x$  region.

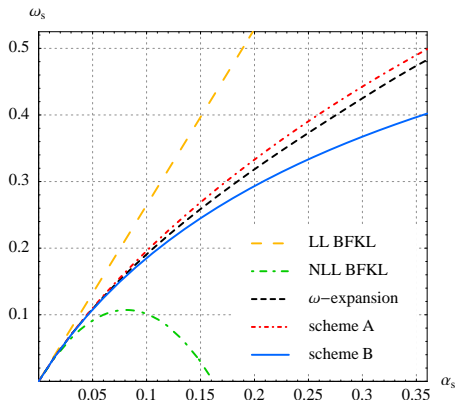


Figure 3. The intercept of the hard Pomeron extracted from the BFKL equation with fixed strong coupling in LL, NLL and re-summed cases.

### 2.1.2 Small- $x$ re-summations

*Anna M. Staśto*

Since the seminal works [12, 13], it is well known that observables at small  $x$  receive substantial corrections due to the large logarithms  $\alpha_s \ln 1/x$  which need to be re-summed in this regime. The BFKL approach [12, 13] provides a framework for this summation and it is known up to next-to-leading logarithmic accuracy. The resulting evolution of the gluon Green's function provided by this framework is with respect to the  $\ln 1/x$  or rapidity variable, with the transverse momenta of the gluons being summed over all possible configurations. The evolution has the following form

$$G(Y; \mathbf{k}, \mathbf{k}_0) = \delta^{(2)}(\mathbf{k} - \mathbf{k}_0) + \int d^2 \mathbf{k}' K(\mathbf{k}, \mathbf{k}') G(Y; \mathbf{k}', \mathbf{k}_0), \quad (3)$$

with the branching kernel having also the perturbative expansion

$$K(\mathbf{k}, \mathbf{k}') = \sum_i (\alpha_s(\mu))^i K^{(i)}(\mathbf{k}, \mathbf{k}'). \quad (4)$$

A solution for the gluon Green's function and therefore the resulting cross sections exhibit strong growth with the energy, the hard Pomeron, with the intercept being significantly larger than unity in the LO approximation,  $\omega_P = 1 + \alpha_s N_c 4 \ln 2 / \pi$ . This growth turns out to be incompatible with both the hadronic data and the data on structure functions from deep-inelastic scattering. Next-to-leading order corrections [14, 15] turned out to be rather large numerically and the pointed to the need of the re-summation of the subsequent powers of higher order corrections  $\alpha_s^k \ln 1/x$ . The size of the NLL corrections can be understood on various physical grounds. First of all, unlike in the DGLAP limit, the strong coupling constant is not naturally a small parameter. On top of that, the BFKL approach does not satisfy the momentum sum rule for the longitudinal momentum fractions (the transverse momenta are however conserved, unlike in the collinear approach). The kinematical approximations made in the BFKL limit cannot be efficiently recovered by the truncated higher orders of the perturbative expansion.

The strategy of re-summation at small  $x$  has been developed in a series of works [16–20]. It involves the construction of the appropriate re-summed kernel of the form given by Eq. 4, which includes at the same time known terms in the expansion of the splitting function, Eq. 2. Although the details of the various approaches differ, there are common fundamental

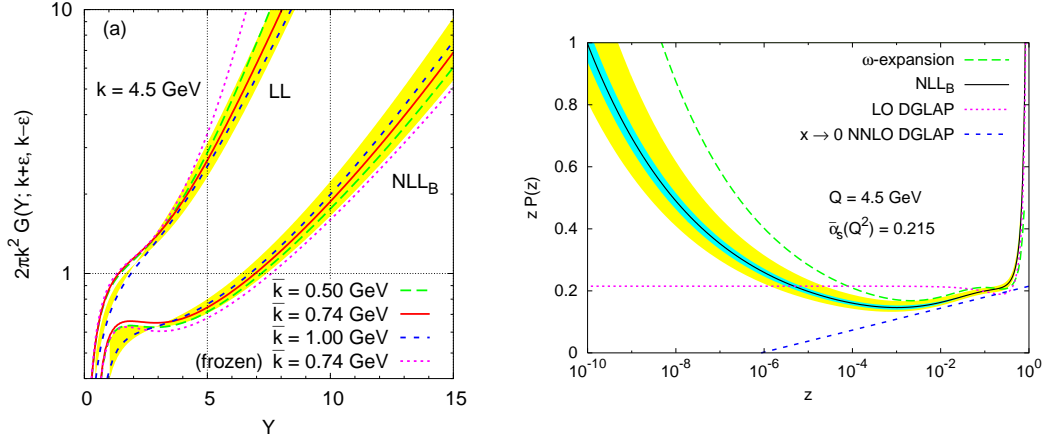


Figure 4. *Left:* The gluon Green's function extracted from the BFKL equation in LL and re-summed cases. The coupling is running in all computations, and  $\bar{k}$  denotes the scale at which the strong coupling is regularized. *Right:* The extracted effective splitting function from the re-summed approach: solid line. The scale was taken to be  $Q = 4.5\text{ GeV}$ . Dotted pink line indicates the LO DGLAP splitting function and the blue dashed indicates small  $x$  part of the NNLO DGLAP. The dashed green line corresponds to the re-summed splitting function from the  $\omega$  expansion. The band correspond to the scale variation.

ingredients. The evolution in rapidity is subjected to kinematical constraints which originate from the requirement of the consistency of the assumption about the Regge kinematics. The evolution is matched with the DGLAP evolution by including the splitting function at LO and NLO. The momentum sum rule is imposed onto the resulting re-summed splitting function. The running of the coupling is included into the evolution. Finally, matching to the NLL BFKL is performed with the suitable subtractions in order to avoid double counting. The resulting Green's function and splitting function turned out to be very stable with minimal variations across the different re-summation schemes.

**Gluon Green's function and the splitting function:** In Fig. 2.1.2, we show the results on the intercept of the gluon Green's function in the case of the fixed strong coupling constant, obtained within the re-summation framework of [16]. The linear growth is given by the LO approximation. The NLO value of the intercept is significantly below the lowest order, and turns negative even for the intermediate values of  $\alpha_s$ . The re-summed result is between the NLO and LO, it exhibits clear growth with increasing values of the coupling constant, albeit much reduced with respect to the LO value and much closer to the phenomenology.

The rapidity dependence of the gluon Green's function is shown in Fig. 4 left. The scale was chosen to be equal to  $k = 4.5\text{ GeV}$ . The reduction of the speed of growth is clear in the re-summed case. Also the scale variations are relatively small in this case.

By using the deconvolution of the integral equation, one can calculate the integrated gluon density. As a result, it is possible to solve the re-summed splitting function numerically. In this way, the perturbative and non-perturbative contributions are factorized in  $Q^2$ . In Fig. 4 right, we show the results for the splitting function as a function of the momentum fraction for the re-summed case. It is compared with the results on the LO and NNLO (only small  $x$  part) splitting functions. The results on the splitting function demonstrate that the small  $x$  growth is delayed to much smaller values of  $x$  (beyond HERA). The splitting

function also has an interesting feature, namely that of the dip. It turns out that this is a universal feature, present also in other schemes of re-summation. In general, it was found that the dip comes from the interplay between NNLO order and the re-summation.

So far, re-summation was demonstrated to give stable results for the gluon channel only. For the complete description, however, one needs to include quarks in the evolution. A matrix approach was developed which was shown to be consistent with the collinear matrix factorization of the parton densities in the singlet evolution [18]. This approach enables the calculation of the anomalous dimensions matrix, which can be directly compared with the standard DGLAP matrix. It was shown that it is possible to incorporate NLLx BFKL + NLO DGLAP in this framework [18].

**Conclusions and outlook:** The small- $x$  regime requires an extended formalism which incorporates the re-summation of the large terms  $\alpha_s \ln 1/x$ . The BFKL formalism was rebuilt to include re-summation to higher orders. This formalism includes both DGLAP NLO and BFKL NLL and the higher order terms. Stability of the results was demonstrated for scale changes and model changes. There are certain universal and characteristic features which are coming from the solutions to the evolution: the growth is delayed to smaller values of  $x$ , and the splitting function has a minimum. The matrix model was developed which gives consistent results on gluon Greens function and the splitting functions. For the complete framework, one needs to include the re-summed coefficient functions and perform the detailed fit to the data.

The EIC will bring a very important information on the parton densities at small  $x$ . Of particular importance is the high luminosity which guarantees the precision measurement of structure functions, especially in the region of low  $x$  and  $Q$ . Also, the measurements of the longitudinal and charm structure function, planned at an EIC, are essential in constraining the gluon distribution. The measurements of electron-proton and electron-ion structure functions will be crucial in distinguishing the effects coming from the re-summation of the linear evolution and/or saturation effects due to the large parton densities.

### 2.1.3 Parton Saturation

*Yuri V. Kovchegov and Cyrille Marquet*

The QCD description of hadrons in terms of quarks and gluons depends on the processes considered and on what part of the hadron wave function they are sensitive to. Consider a hadron moving at nearly the speed of light along the light cone direction  $x^+$ , with momentum  $P^+$ . Depending on their transverse momentum  $k_T$  and longitudinal momentum  $xP^+$ , the virtual partons inside the hadron behave differently, reflecting the different regimes of the hadron wave function. Soft hadronic processes are mostly sensitive to the non-perturbative part of the wave function, they involve quantum fluctuations with transverse momenta of the order of  $\Lambda_{QCD} \sim 200$  MeV. A hadron can then be thought of as a bound state of strongly-interacting partons, but a QCD description of the associated dynamics is still lacking. By contrast, hard processes in hadronic collisions are sensitive to the weakly-coupled part of the wave function and resolve the partonic structure of hadrons. They probe partons with  $k_T \gg \Lambda_{QCD}$  whose QCD dynamics is better understood.

One can distinguish two weakly-coupling regimes in the wave function: a linear one called the hard regime, involving a small density of partons, typically with  $x \lesssim 1$ , in which the hadron looks like a dilute system of independent partons, and a non-linear one called

the saturation regime, involving a large density of partons with  $x \ll 1$ , in which the hadron looks like a dense system of nevertheless weakly-interacting partons, mainly gluons (called small- $x$  gluons). The dilute-dense separation is a bit subtler than that: the larger  $k_T$  is, the smaller  $x$  needs to be to enter the saturation regime. Indeed the separation between the two regimes is characterized by a momentum scale  $Q_s(x)$ , called the saturation scale, which increases as  $x$  decreases. In a scattering process, dilute partons (with  $k_T \gg Q_s(x)$ ) behave incoherently, while when the parton density is large ( $k_T \lesssim Q_s(x)$ ), gluons scatter coherently. The dynamics of the dilute regime is well described by the leading-twist approximation of QCD, whose hallmark is collinear factorization. As explained in the previous section, when  $x$  becomes small while not yet reaching the non-linear regime, so-called small- $x$  re-summations are also needed to improve the approximation.

To describe the small- $x$  non-linear part of hadronic/nuclear wave functions in QCD, the Color Glass Condensate (CGC) effective theory has been proposed. Rather than using a standard Fock-state expansion, not efficient to deal with the numerous small- $x$  gluons, the CGC approach employs collective degrees of freedom: classical color fields. The traditional approach to saturation physics consists of two stages, corresponding to two different levels of approximation. The first approximation corresponds to the classical gluon field description of nuclear wave functions and scattering cross sections. It re-sums all multiple re-scatterings in the nucleus, but lacks energy dependence. The latter is included through quantum corrections, which are re-summed by non-linear evolution equations. This constitutes the second level of approximation. We will present both stages below.

## Classical gluon fields

**McLerran–Venugopalan model:** Imagine a single large nucleus, which was boosted to some ultrarelativistic velocity, as shown in Fig. 5 left. We are interested in the dynamics of small- $x$  gluons in the wave function of this relativistic nucleus. The small- $x$  gluons interact with the whole nucleus coherently in the longitudinal direction: therefore, only the transverse plane distribution of nucleons is important for the small- $x$  wave function. As one can see from Fig. 5, after the boost, the nucleons, as “seen” by the small- $x$  gluons, appear to overlap with each other in the transverse plane, leading to high parton density. Large occupation numbers of color charges (partons) lead to classical gluon fields dominating the small- $x$  wave function of the nucleus. This is the essence of the McLerran-Venugopalan (MV) model [21–23]. According to the MV model, the dominant gluon field is given by the solution of the classical Yang-Mills equations  $\mathcal{D}_\mu F^{\mu\nu} = J^\nu$  where the classical color current  $J^\nu$  is generated by the valence quarks in the nucleons of the nucleus from Fig. 5.

The Yang-Mills equations were solved for a single nucleus exactly [24, 25] resulting in the unintegrated gluon distribution  $\phi(x, k_T^2)$  (multiplied by the phase space factor of the gluon’s transverse momentum  $k_T$ ) shown in Fig. 5 right as a function of  $k_T$ . (Note that in the MV model,  $\phi(x, k_T^2)$  is independent of Bjorken- $x$ .) Fig. 5 demonstrates the emergence of the saturation scale  $Q_s$ : as one can see from Fig. 5, the majority of gluons in this classical distribution have transverse momentum  $k_T \approx Q_s$ . Since in this classical approximation  $Q_s^2 \sim A^{1/3}$ , for a large enough nucleus, all of its small- $x$  gluons would have large transverse momenta  $k_T \approx Q_s \gg \Lambda_{QCD}$ , justifying the applicability of the perturbative approach to the problem. Note that the gluon distribution slows down its growth with decreasing  $k_T$  for  $k_T < Q_s$  (from power-law of  $k_T$  to a logarithm): the distribution *saturates*, justifying the name of the saturation scale.



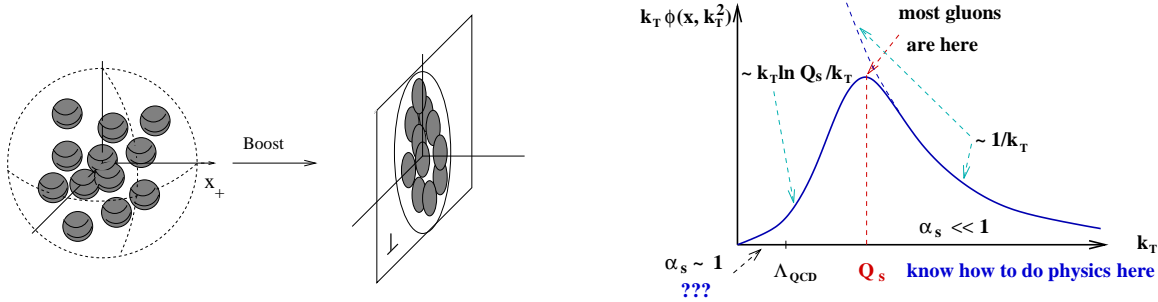


Figure 5. *Left*: Large nucleus before and after an ultrarelativistic boost. *Right*: Unintegrated gluon distribution  $\phi(x, k_T^2)$  of a large nucleus due to classical gluon fields (solid line). Dashed curve denotes the lowest-order perturbative result.

**DIS at high energy: Glauber-Mueller formula:** Let us consider deep inelastic scattering (DIS) on a large nucleus. In DIS, the incoming electron emits a virtual photon, which in turn interacts with the proton or nucleus. In the rest frame of the nucleus, the interaction can be thought of as the virtual photon splitting into a quark-antiquark pair, which then interacts with the nucleus (see Fig. 6, left panel). Since the light cone lifetime of the  $q\bar{q}$  pair is much longer than the size of the target nucleus, the total cross section for the virtual photon–nucleus scattering can be written as a convolution of the virtual photon’s light cone wave function (the probability for it to split into a  $q\bar{q}$  pair) with the forward scattering amplitude of a  $q\bar{q}$  pair interacting with the nucleus

$$\sigma_{tot}^{\gamma^*A}(Q^2, x_{Bj}) = \int \frac{d^2x dz}{2\pi} [\Phi_T(\underline{x}, z) + \Phi_L(\underline{x}, z)] d^2b N(\underline{x}, \underline{b}, Y) \quad (5)$$

with the help of the light-cone perturbation theory [26]. Here the incoming photon with virtuality  $Q$  splits into a quark–antiquark pair with the transverse separation  $\underline{x}$  and the impact parameter (transverse position of the center of mass of the  $q\bar{q}$  pair)  $\underline{b}$ .  $Y$  is the rapidity variable given by  $Y = \ln(s x_T^2) \approx \ln 1/x_{Bj}$ . The square of the light cone wave function of  $q\bar{q}$  fluctuations of a virtual photon is denoted by  $\Phi_T(\underline{x}, z)$  and  $\Phi_L(\underline{x}, z)$  for transverse and longitudinal photons correspondingly, with  $z$  being the fraction of the photon’s longitudinal momentum carried by the quark. At the lowest order in electromagnetic coupling ( $\alpha_{EM}$ )  $\Phi_T(\underline{x}, z)$  and  $\Phi_L(\underline{x}, z)$  are given by [27, 28]

$$\Phi_T(\underline{x}, z) = \frac{2N_c}{\pi} \sum_f \alpha_{EM}^f \{a_f^2 K_1^2(x_\perp a_f) [z^2 + (1-z)^2] + m_f^2 K_0^2(x_\perp a_f)\}, \quad (6)$$

$$\Phi_L(\underline{x}, z) = \frac{2N_c}{\pi} \sum_f \alpha_{EM}^f 4Q^2 z^2 (1-z)^2 K_0^2(x_\perp a_f), \quad (7)$$

with  $a_f^2 = Q^2 z(1-z) + m_f^2$ ,  $x_\perp = |\mathbf{x}|$  and  $\sum_f$  denoting the sum over all relevant quark flavors with quark masses denoted by  $m_f$ .  $\alpha_{EM}^f = e_f^2/4\pi$  with  $e_f$  the electric charge of a quark with flavor  $f$ .

Our first goal is to calculate the forward scattering amplitude of a quark–anti-quark dipole interacting with the nucleus, which is denoted by  $N(\underline{x}, \underline{b}, Y)$  in Eq. (5), including all multiple re-scatterings of the dipole on the nucleons in the nucleus. To do this we need to construct a model of the target nucleus. We assume that the nucleons are dilutely distributed in the nucleus [29]. There we can represent the dipole-nucleus interaction as a

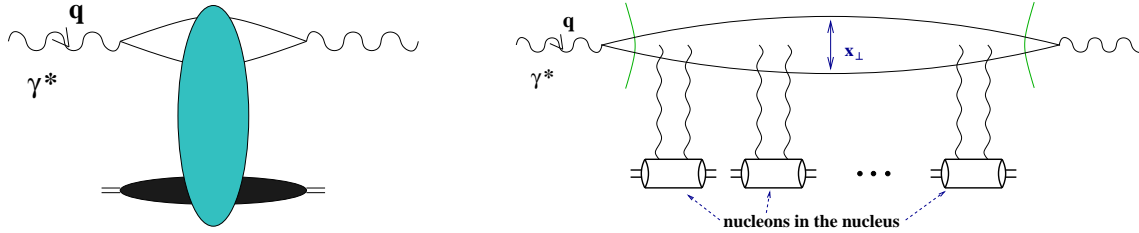


Figure 6. *Left*: Deep inelastic scattering in the rest frame of the target. *Right*: Deep inelastic scattering in the quasi-classical Glauber-Mueller approximation in  $\partial_\mu A^\mu = 0$  gauge.

sequence of successive dipole-nucleon interactions, as shown in Fig. 6, right panel. Since each nucleon is a color singlet, the lowest order dipole-nucleon interaction in the forward amplitude from Fig. 6 is a two-gluon exchange. The exchanged gluon lines in Fig. 6 are disconnected at the top: this denotes a summation over all possible connections of these gluon lines either to the quark or to the anti-quark lines in the incoming dipole.

Re-summation of the diagrams like the one in Fig. 6 yields [29]

$$N(\underline{x}, \underline{b}, Y = 0) = 1 - \exp \left\{ - \frac{x_\perp^2 Q_s^2(\underline{b}) \ln(1/x_\perp \Lambda)}{4} \right\} \quad (8)$$

with the *saturation* scale defined by

$$Q_s^2(\underline{b}) \equiv \frac{4\pi\alpha_s^2 C_F}{N_c} \rho T(\underline{b}). \quad (9)$$

Here  $\rho$  is the density of nucleons in the nucleus ( $\rho = A/[(4/3)\pi R^3]$  for a spherical nucleus of radius  $R$  with atomic number  $A$ ) and  $T(\underline{b})$  is the nuclear profile function equal to the length of the nuclear medium at a given impact parameter  $\underline{b}$ , such that  $T(\underline{b}) = 2\sqrt{R^2 - \underline{b}^2}$  for a spherical nucleus.  $\Lambda$  is an infrared cutoff. We put  $Y = 0$  in the argument of  $N$  in Eq. (8) to underline that this expression does not include any small- $x$  evolution which would bring in the rapidity dependence.

Eqs. (8) and (9) allow us to determine the parameter corresponding to the re-summation of the diagrams like the one shown in Fig. 6. Noting that for large nuclei, the profile function scales as  $T(\underline{b}) \sim A^{1/3}$  and the nucleon density scales as  $\rho \sim A^0$ , we conclude that the re-summation parameter of multiple re-scatterings is [30]:  $\alpha_s^2 A^{1/3}$ . The physical meaning of the parameter  $\alpha_s^2 A^{1/3}$  is rather straightforward: at a given impact parameter the dipole interacts with  $\sim A^{1/3}$  nucleons exchanging two gluons with each. Since the two-gluon exchange is parametrically of the order  $\alpha_s^2$  we obtain  $\alpha_s^2 A^{1/3}$  as the re-summation parameter for the quasi-classical approximation.

The dipole amplitude  $N$ , from Eq. (8), is plotted (schematically) in Fig. 2.1.3 as a function of  $x_\perp$ . One can see that, at small  $x_\perp$ ,  $x_\perp \ll 1/Q_s$ , we have  $N \sim x_\perp^2$  and the amplitude is a rising function of  $x_\perp$ . However, at large dipole sizes  $x_\perp \gtrsim 1/Q_s$ , the growth stops and the amplitude levels off (*saturates*) at  $N = 1$ . This regime corresponds to the black disk limit for the dipole-nucleus scattering where, for large dipoles, the nucleus appears as a black disk. To understand that the  $N = 1$  regime corresponds to the black disk limit, let us note that the total dipole-nucleus scattering cross section is given by:

$$\sigma_{tot}^{q\bar{q}A} = 2 \int d^2b N(\underline{x}, \underline{b}, Y) \quad (10)$$

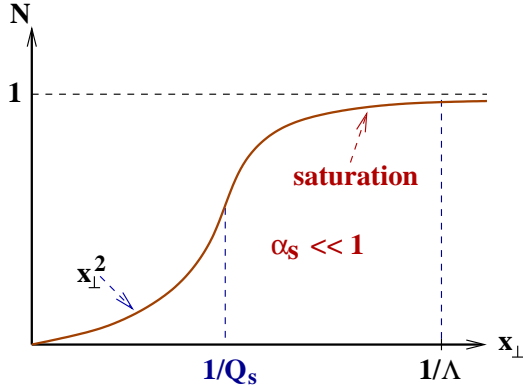


Figure 7. The forward amplitude of the dipole–nucleus scattering  $N$  plotted as a function of the transverse separation between the quark and the anti-quark in a dipole  $x_\perp$  using Eq. (8).

where the integration goes over the cross sectional area of the nucleus. If  $N = 1$  at all impact parameters  $\underline{b}$  inside the nucleus, for a spherical nucleus of radius  $R$ , Eq. (10) becomes  $\sigma_{tot}^{q\bar{q}A} = 2\pi R^2$ , which is a well-known formula for the cross section of a particle scattering on a black sphere [31].

The transition between the  $N \sim x_\perp^2$  to  $N = 1$  behavior in Fig. 2.1.3 happens at around  $x_\perp \sim 1/Q_s$ . For dipole sizes  $x_\perp \gtrsim 1/Q_s$ , the amplitude  $N$  saturates to a constant. This translates into the saturation of quark distribution functions in the nucleus, as was shown in [29] (as  $xq + x\bar{q} \sim F_2 \sim \sigma_{tot}^{\gamma^*A}$ ), and thus can be identified with parton saturation, justifying the name of the *saturation scale*.

Before we proceed, let us finally note that since  $T(\underline{b}) \sim A^{1/3}$ , the saturation scale in Eq. (9) scales as  $Q_s^2 \sim A^{1/3}$  with the nuclear atomic number [21–23, 29]. Eq. (??) implies that for a very large nucleus, the saturation scale would become very large, much larger than  $\Lambda_{QCD}$ . If  $Q_s \gg \Lambda_{QCD}$ , the transition to the black disk limit in Fig. 2.1.3 happens at momentum scales (corresponding to inverse dipole sizes) where the physics is perturbative and gluons are the correct degrees of freedom.

## Nonlinear evolution equations

**General picture:** While the classical gluon fields of the MV model exhibit many correct qualitative features of saturation physics, and give predictions about the  $A$ -dependence of observables which may be compared to the data, they do not lead to any rapidity/Bjorken- $x$  dependence of the corresponding observables, which is essential in the data on nuclear and hadronic collisions. To include rapidity dependence, one has to calculate quantum corrections to the classical fields described above.

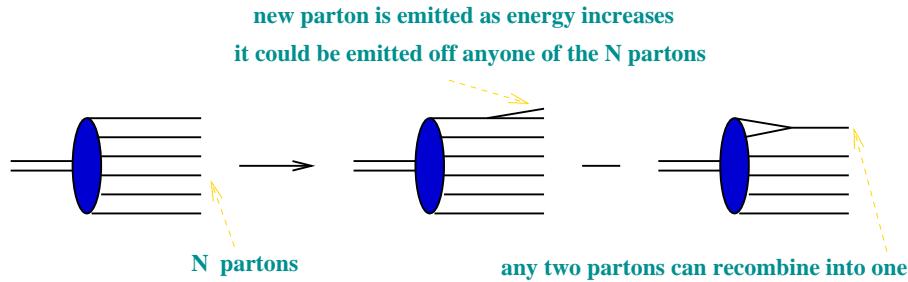


Figure 8. Nonlinear small- $x$  evolution of a hadronic or nuclear wave functions. All partons (quarks and gluons) are denoted by straight solid lines for simplicity.

The inclusion of quantum corrections is accomplished by the small- $x$  evolution equations. The first small- $x$  evolution equation was constructed before the birth of saturation physics. This is the Balitsky-Fadin-Kuraev-Lipatov (BFKL) evolution equation [12, 13]. This is a linear evolution equation, which is illustrated by the first term on the right hand side of Fig. 8. Consider a wave function of a high-energy nucleus or hadrons: it contains many partons, as shown on the left of Fig. 8. As we make one step of evolution by boosting the nucleus/hadron to higher energy, either one of the partons can split into two partons, leading to an increase in the number of partons proportional to the number of partons  $N$  at the previous step,

$$\frac{\partial N(x, k_T^2)}{\partial \ln(1/x)} = \alpha_s K_{BFKL} \otimes N(x, k_T^2), \quad (11)$$

with  $K_{BFKL}$  an integral kernel. Clearly the BFKL equation (11) introduces a Bjorken- $x$ /rapidity dependence in the observables it describes.

The main problem with the BFKL evolution is that it leads to the power-law growth of the total cross sections with energy,  $\sigma_{tot} \sim s^{\alpha_P - 1}$ , with the BFKL pomeron intercept  $\alpha_P - 1 = (4\alpha_s N_c \ln 2)/\pi > 0$ . Such power-law cross section increase violates the Froissart bound, which states that the total hadronic cross section can not grow faster than  $\ln^2 s$  at very high energies. Moreover, the power-law growth of cross sections with energy violate the black disk limit known from quantum mechanics: the high-energy total scattering cross section  $\sigma_{tot}$  of a particle on a sphere of radius  $R$  is bounded by  $2\pi R^2$  (note the factor of 2 which is due to quantum mechanics, this is not simply a hard sphere from classical mechanics!).

We see that something has to modify Eq. (11) at high energy. The modification is illustrated on the far right of Fig. 8: at very high energies, partons may start to recombine with each other on top of the splitting. The recombination of two partons into one is proportional to the number of pairs of partons, which, in turn, scales as  $N^2$ . We end up with the following non-linear evolution equation:

$$\frac{\partial N(x, k_T^2)}{\partial \ln(1/x)} = \alpha_s K_{BFKL} \otimes N(x, k_T^2) - \alpha_s [N(x, k_T^2)]^2. \quad (12)$$

This is the Balitsky-Kovchegov (BK) evolution equation [32, 33], which is valid for QCD in the limit of large number of colors  $N_c$ . An equation of this type was originally suggested by Gribov, Levin and Ryskin [34] and by Mueller and Qiu [35], though at the time it was assumed that the quadratic term is only the first non-linear correction with higher order terms possibly appearing as well: in [32, 33] the exact form of the equation was found, and it was shown that in the large- $N_c$  limit, Eq. (12) does not have any higher-order terms in  $N$ . Generalization of Eq. (12) beyond the large- $N_c$  limit is accomplished by the Jalilian-Marian–Iancu–McLerran–Weigert–Leonidov–Kovner (JIMWLK) [36, 37] evolution equation, which is a functional differential equation. Both the BK and JIMWLK evolution equations will be discussed in more details later.

The physical impact of the quadratic term on the right of Eq. (12) is clear: it slows down the small- $x$  evolution, leading to *parton saturation* and to total cross sections adhering to the black disk limit of Eq. (??). The effect of gluon mergers becomes important when the quadratic term in Eq. (12) becomes comparable to the linear term on the right-hand-side. This gives rise to the saturation scale  $Q_s$ , which now grows with energy (on top of its increase with  $A$ ).

**The Balitsky-Kovchegov equation:** Let us now include the energy dependence in the dipole amplitude  $N$  from Eq. (8). Similar to the BFKL evolution equation [12, 13], we are interested in quantum evolution in the leading longitudinal logarithmic approximation re-summing the powers of

$$\alpha_s \ln \frac{1}{x_{Bj}} \sim \alpha_s Y \quad (13)$$

with  $Y$  the rapidity variable. Again we will be working in the rest frame of the nucleus, but this time we choose to work in the light cone gauge of the projectile  $A^+ = 0$  if the dipole is moving in the light cone  $+$  direction.

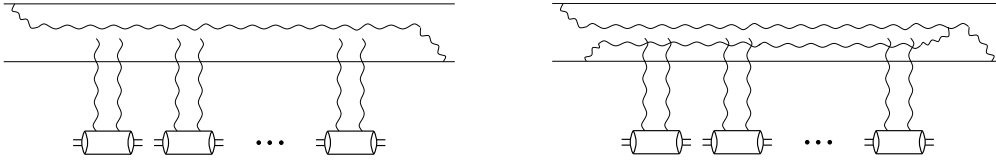


Figure 9. Quantum corrections to dipole-nucleus scattering.

The corrections of the type shown in Eq. (13) appear in the diagrams through emissions of long-lived  $s$ -channel gluons, as shown in Fig. 9. These  $s$ -channel gluons interact with the target nucleus through multiple re-scatterings. In the large- $N_c$  limit of QCD such diagrams can be re-summed by the BK evolution equation [32, 33, 38, 39]:

$$\frac{\partial N(\underline{x}_0, \underline{x}_1, Y)}{\partial Y} = \frac{\alpha_s C_F}{\pi^2} \int d^2 x_2 \frac{x_{01}^2}{x_{20}^2 x_{21}^2} \left[ N(\underline{x}_0, \underline{x}_2, Y) + N(\underline{x}_2, \underline{x}_1, Y) - N(\underline{x}_0, \underline{x}_1, Y) \right. \\ \left. - N(\underline{x}_0, \underline{x}_2, Y) N(\underline{x}_2, \underline{x}_1, Y) \right], \quad (14)$$

where we have redefined the arguments of  $N$  to depend on the transverse coordinates of the quark and antiquark (instead of dipole size and the impact parameter as was done in Eq. (8). Here  $x_{ij} = |\underline{x}_{ij}|$  and  $\underline{x}_{ij} = \underline{x}_i - \underline{x}_j$ .

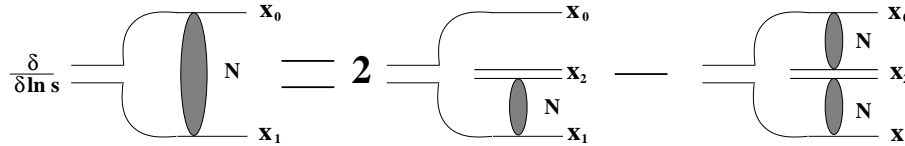


Figure 10. Diagrammatic representation of the nonlinear evolution equation (14).

In the large- $N_c$  limit, gluon cascades reduce to a cascade of color dipoles. Summation of the dipole cascade is illustrated in Fig. 10 where the dipole cascade and its interaction with the target are denoted by a shaded oval. In one step of the evolution in energy (or rapidity) a soft gluon is emitted in the dipole. If the gluon is real, then the original dipole would be split into two dipoles, as shown in Fig. 10. Either one of these dipoles can interact with the nucleus with the other one not interacting, which is shown by the first term on the right hand side of Fig. 10 with the factor of 2 accounting for the fact that there are two dipoles in the wave function now. Alternatively, both dipoles may interact simultaneously, which is shown by the second term on the right hand side of Fig. 10. This term comes in with the minus sign. The emitted gluon in one step of evolution may be a virtual correction,

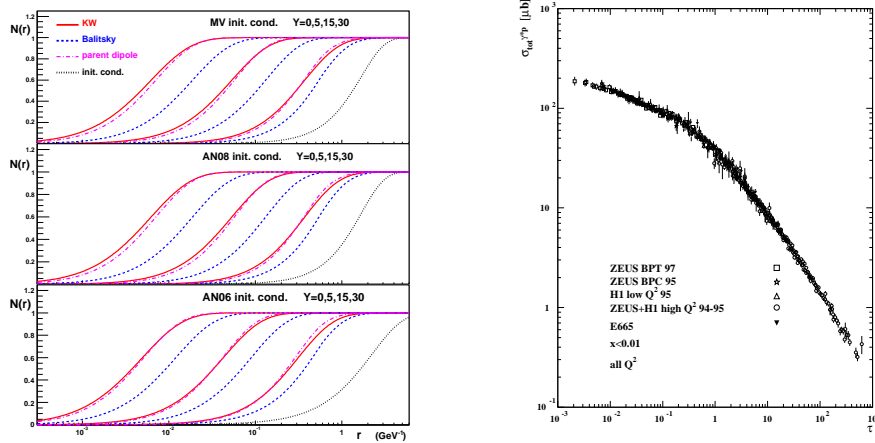


Figure 11. *Left*: Solutions of the BK equation at rapidities  $Y=0, 5, 15$  and  $30$  (curves are labeled from right to left) for the three different running coupling schemes considered in [43] *Right*: HERA data on the total DIS  $\gamma^*p$  cross section plotted in [44] as a function of the scaling variable  $\tau = Q^2/Q_s^2(x_{Bj})$ .

which is not shown in Fig. 10: in that case, the original dipole would not split into two, it would remain the same and would interact with the target. In the end, the evolved system of dipoles interacts with the nucleus. In the large- $N_c$  limit, each dipole does not interact with other dipoles during the evolution which generates all the dipoles. For a large nucleus, the dipole-nucleus interaction was given above in Eq. (8). That result re-sums powers of  $\alpha_s^2 A^{1/3}$ : hence the BK equation re-sums powers of  $\alpha_s Y$  and powers of  $\alpha_s^2 A^{1/3}$ .

## Map of high-energy QCD

Solutions of the BK and JIMWLK evolution equations have been done numerically [40–42], with asymptotic limits studied analytically. The numerical solution (for the BK equation with running coupling, which will be described later) is presented in Fig. 11 [43]. These plots are the same dipole amplitude  $N$  plotted as a function of the dipole size labeled  $r$  as was done in Fig. 2.1.3. In Fig. 11, different curves correspond to different energies/rapidities  $Y$ . One can clearly see that the curves tend to drift to the left with increasing energies, corresponding to increasing saturation scale with the energy/rapidity. Therefore we see that the saturation scale increases with rapidity, making the corresponding physics more perturbative.

We summarize our knowledge of high energy QCD in Fig. 12, in which different regimes are plotted in the  $(Q^2, Y = \ln 1/x)$  plane, by analogy with DIS. For hadronic and nuclear collisions one can think of typical transverse momentum  $p_T^2$  of the produced particles instead of  $Q^2$ . Also rapidity  $Y$  and Bjorken- $x$  variable are interchangeable. On the left of Fig. 12 we see the region with  $Q^2 \leq \Lambda_{QCD}^2$  in which the coupling is large,  $\alpha_s \sim 1$ , and small-coupling approaches do not work. In the perturbative region,  $Q^2 \gg \Lambda_{QCD}^2$ , we see the standard DGLAP evolution and the linear BFKL evolution. The BFKL equation evolves gluon distributions toward small- $x$ , where parton densities becomes large and parton saturation sets in. The transition to saturation is described by the non-linear BK and JIMWLK evolution equations. Most importantly, this transition happens at  $Q_s^2 \gg \Lambda_{QCD}^2$  where the small-coupling approach is valid.

One of the most important predictions of nonlinear small- $x$  evolution is that, at high

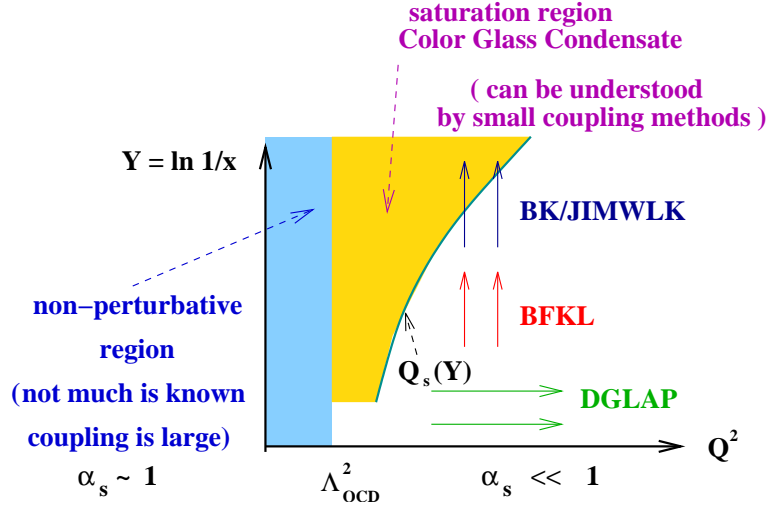


Figure 12. Map of high energy QCD in the  $(Q^2, Y = \ln 1/x)$  plane.

enough rapidity, the scattering amplitude  $N$  (and, consequently, DIS structure functions) would be a function of a single variable  $x_\perp Q_s(Y)$ , such that  $N(x_\perp, Y) = N(x_\perp Q_s(Y))$ . This prediction is spectacularly confirmed by HERA data. Geometric scaling has been demonstrated in an analysis of the HERA DIS data [44], presenting one of the strongest arguments for the observation of saturation phenomena at HERA. These results are shown here in Fig. 11 from [44], where the authors combined HERA data on the total DIS  $\gamma^*p$  cross section  $\sigma_{tot}^{\gamma^*p}$  for  $x_{Bj} < 0.01$  as a function of the scaling variable  $\tau = Q^2/Q_s^2(x_{Bj})$ . One can see that, amazingly enough, all the data falls on the same curve, indicating that  $\sigma_{tot}^{\gamma^*p}$  is a function of a single variable  $Q^2/Q_s^2(x_{Bj})$ ! This gives us the best to date experimental proof of geometric scaling. (For a similar analysis of DIS data on nuclear targets see [45].) The fact that geometric scaling is a property of the solution of the BK equation has been later demonstrated in [46, 47].

#### 2.1.4 Universality aspects of the Color Glass Condensate

*François Gelis*

The Color Glass Condensate (CGC) is an *effective field theory (EFT)* based on the separation of the degrees of freedom into fast frozen color sources and slow dynamical color fields [21–23]. A *renormalization group equation* –the JIMWLK equation [37, 48–55]– ensures the independence of physical quantities with respect to the cutoff that separates the two kinds of degrees of freedom.

The fast gluons with longitudinal momentum  $k^+ > \Lambda^+$  are frozen by Lorentz time dilation in configurations specified by a color current  $J_a^\mu \equiv \delta^{\mu+} \rho^a$ , where  $\rho^a(x^-, x_\perp)$  is the corresponding color charge density. On the other hand, slow gluons with  $k^+ < \Lambda^+$  are described by the usual gauge fields  $A^\mu$  of QCD. Because of the hierarchy in  $k^+$  between these two types of degrees of freedom, they are coupled eikonally by a term  $J_\mu A^\mu$ . The fast gluons thus act as sources for the fields that represent the slow gluons. Although it is frozen for the duration of a given collision, the color source density  $\rho^a$  varies randomly event by event. The CGC provides a gauge invariant distribution  $W_{\Lambda^+}[\rho]$ , which gives the

probability of a configuration  $\rho$ . This encodes all the correlations of the color charge density at the cutoff scale  $\Lambda^+$ , separating the fast and slow degrees of freedom. Given this statistical distribution, the expectation value of an operator at the scale  $\Lambda^+$  is given by

$$\langle \mathcal{O} \rangle_{\Lambda^+} \equiv \int [D\rho] W_{\Lambda^+}[\rho] \mathcal{O}[\rho] , \quad (15)$$

where  $\mathcal{O}[\rho]$  is the expectation value of the operator for a particular configuration  $\rho$  of the color sources.

The power counting of the CGC EFT is such that in the saturated regime, the sources  $\rho$  are of order  $g^{-1}$ . Attaching an additional source to a given Feynman graph does not alter its order in  $g$ ; the vertex where this new source attaches to the graph is compensated by the  $g^{-1}$  of the source. Thus, computing an observable at a certain order in  $g^2$  requires the re-summation of all the contributions obtained by adding extra sources to the relevant graphs. The leading order in  $g^2$  is given by a sum of tree diagrams, which can be expressed in terms of classical solutions of the Yang-Mills equations. Moreover, for inclusive observables [56, 57], these classical fields obey a simple boundary condition: they vanish when  $t \rightarrow -\infty$ .

Next-to-leading order (NLO) computations in the CGC EFT involve a sum of one-loop diagrams embedded in the above classical field. To prevent double counting, momenta in loops are required to be below the cutoff  $\Lambda^+$ . This leads to a logarithmic dependence in  $\Lambda^+$  of these loop corrections. These logarithms are large if  $\Lambda^+$  is well above the typical longitudinal momentum scale of the observable considered, and must be re-summed.

For inclusive observables, the leading logarithms are universal and can be absorbed into a redefinition of the distribution  $W_{\Lambda^+}[\rho]$  of the hard sources. The evolution of  $W_{\Lambda^+}[\rho]$  with  $\Lambda^+$  is governed by the functional JIMWLK equation

$$\frac{\partial W_{\Lambda^+}[\rho]}{\partial \ln(\Lambda^+)} = -\mathcal{H} \left[ \rho, \frac{\delta}{\delta \rho} \right] W_{\Lambda^+}[\rho] , \quad (16)$$

where  $\mathcal{H}$  is known as the JIMWLK Hamiltonian. This operator contains up to two derivatives  $\partial/\partial\rho$ , and arbitrary powers in  $\rho$ . Its explicit expression can be found in refs. [37, 48–55, 58, 59]. The derivation of the JIMWLK equation will be sketched below.

Numerical studies of JIMWLK evolution were performed in [42, 60]. An analytic, albeit formal, solution to the JIMWLK equation was constructed in [61] in the form of a path integral. Alternatively, the evolution can be expressed as an infinite hierarchy of coupled non-linear equations for  $n$ -point Wilson line correlators—often called the Balitsky hierarchy [62]. In this framework, the BK equation is a mean field approximation of the JIMWLK evolution, valid in the limit of a large number of colors  $N_c \rightarrow \infty$ . Numerical studies of the JIMWLK equation [42, 60] have found only small differences with the BK equation.

Let us finally comment on the initial condition for the JIMWLK equation which is also important in understanding its derivation. The evolution should start at some cutoff value in the longitudinal momentum scale  $\Lambda_0^+$  at which the saturation scale is already a (semi)hard scale, say  $Q_{s0} \gtrsim 1$  GeV, for perturbation theory to be applicable. The gluon distribution at the starting scale is in general non-perturbative and requires a model. A physically motivated model for the gluon distribution in a large nucleus is the McLerran-Venugopalan model [21–23]. In a large nucleus, there is a window in rapidity where evolution effects are not large but  $x$  is still sufficiently small for a probe not to resolve the longitudinal extent of the nucleus. In this case, the probe “sees” a large number of color charges, proportional



to  $A^{1/3}$ . These charges add up to form a higher dimensional representation of the gauge group, and can therefore be treated as classical color distributions [21–23, 63]. Further, the color charge distribution  $W_{\Lambda_0^+}[\rho]$  is a Gaussian distribution<sup>1</sup> in  $\rho$ . The variance of this distribution –the color charge squared per unit area– is proportional to  $A^{1/3}$  and provides a semi-hard scale that makes weak coupling computations feasible. In addition to its role in motivating the EFT and serving as the initial condition in JIMWLK evolution, the MV model allows for direct phenomenological studies in p+A and A+A collisions in regimes where the values of  $x$  are not so small as to require evolution.

**The CGC in DIS at small  $x$ :** We denote  $\sigma_{\text{dipole}}(x, \mathbf{r}_\perp)$  the QCD “dipole” cross-section for the quark-antiquark pair to scatter off the target. This process is shown in fig. 13 left, where we have assumed that the target moves in the  $-z$  direction. In the leading order (LO) CGC description of DIS, the target is described, as illustrated in fig. 13 right, as static sources with  $k^- > \Lambda_0^-$ . The field modes do not contribute at this order.

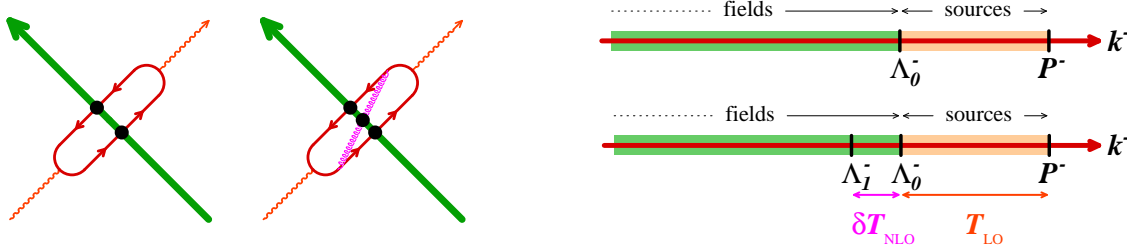


Figure 13. *Left:* LO and NLO contributions to DIS off the CGC. *Top right:* sources and fields in the CGC effective theory. *Bottom right:* NLO correction from a layer of field modes just below the cutoff.

Employing the optical theorem,  $\sigma_{\text{dipole}}(x, \mathbf{r}_\perp)$  can be expressed in terms of the forward scattering amplitude  $\mathbf{T}(\mathbf{x}_\perp, \mathbf{y}_\perp)$  of the  $q\bar{q}$  pair at LO as

$$\sigma_{\text{dipole}}^{\text{LO}}(x, \mathbf{r}_\perp) = 2 \int d^2\mathbf{b} \int [D\rho] W_{\Lambda_0^-}[\rho] \mathbf{T}_{\text{LO}}(\mathbf{b} + \frac{\mathbf{r}_\perp}{2}, \mathbf{b} - \frac{\mathbf{r}_\perp}{2}), \quad (17)$$

where, for a fixed configuration of the target color sources [67, 68]

$$\mathbf{T}_{\text{LO}}(\mathbf{x}_\perp, \mathbf{y}_\perp) = 1 - \frac{1}{N_c} \text{tr} (U(\mathbf{x}_\perp) U^\dagger(\mathbf{y}_\perp)), \quad (18)$$

with  $U(\mathbf{x}_\perp)$  a Wilson line representing the interaction between a quark and the color fields of the target, defined to be

$$U(\mathbf{x}_\perp) = \text{T exp} ig \int^{1/xP^-} dz^+ \mathcal{A}^-(z^+, \mathbf{x}_\perp). \quad (19)$$

In this formula,  $\mathcal{A}^-$  is the minus component of the gauge field generated (in Lorentz gauge) by the sources of the target; it is obtained by solving classical Yang-Mills equations with these sources. The upper bound  $xP^-$  (where  $P^-$  is the target longitudinal momentum) indicates that source modes with  $k^- < xP^-$  do not contribute to this scattering amplitude. Thus if the cutoff  $\Lambda_0^-$  of the CGC EFT is lower than  $xP^-$ ,  $\mathbf{T}_{\text{LO}}$  is independent of  $\Lambda_0^-$ .

<sup>1</sup>There is a additional term, corresponding to the cubic Casimir; which is parametrically suppressed for large nuclei [64]. This term generates Odderon excitations in the JIMWLK/BK evolution [65, 66].

However, when  $\Lambda_0^-$  is larger than  $xP^-$ , the dipole cross-section is in fact independent of  $x$  (since the CGC EFT does not have source modes near the upper bound  $xP^-$ ) and depends on the unphysical parameter  $\Lambda_0^-$ . As we shall see now, this is related to the fact that eq. (17) is incomplete and receives large corrections from higher order diagrams. Consider now the NLO contributions (one of them is shown in the right panel in figure 13 left with gauge field modes in the slice  $\Lambda_1^- \leq k^- \leq \Lambda_0^-$  (see fig. 13 right). An explicit computation of the contribution of field modes in this slice gives

$$\delta \mathbf{T}_{\text{NLO}}(\mathbf{x}_\perp, \mathbf{y}_\perp) = \ln \left( \frac{\Lambda_0^-}{\Lambda_1^-} \right) \mathcal{H} \mathbf{T}_{\text{LO}}(\mathbf{x}_\perp, \mathbf{y}_\perp), \quad (20)$$

where  $\mathcal{H}$  is the JIMWLK Hamiltonian. All dependence on the cutoff scales is in the logarithmic prefactor alone. This Hamiltonian has two derivatives with respect to the classical field  $\mathcal{A} \sim \mathcal{O}(1/g)$ ;  $\mathcal{H} \mathbf{T}_{\text{LO}}$  is of order  $\alpha_s \mathbf{T}_{\text{LO}}$  and therefore clearly an NLO contribution. However, if the new scale  $\Lambda_1^-$  is such that  $\alpha_s \ln(\Lambda_0^-/\Lambda_1^-) \sim 1$ , this NLO term becomes comparable in magnitude to the LO contribution. Averaging the sum of the LO and NLO contributions over the distribution of sources at the scale  $\Lambda_0^-$ , one obtains

$$\int [D\rho] W_{\Lambda_0^-}[\rho] (\mathbf{T}_{\text{LO}} + \delta \mathbf{T}_{\text{NLO}}) = \int [D\rho] W_{\Lambda_1^-}[\rho] \mathbf{T}_{\text{LO}}, \quad (21)$$

where  $W_{\Lambda_1^-} \equiv (1 + \ln(\Lambda_0^-/\Lambda_1^-) \mathcal{H}) W_{\Lambda_0^-}$ . We have shown here that the NLO correction from quantum modes in the slice  $\Lambda_1^- \leq k^- \leq \Lambda_0^-$  can be absorbed in the LO term, provided we now use a CGC effective theory at  $\Lambda_1^-$  with the modified distribution of sources shown in eq. (21). In differential form, the evolution equation of the source distribution,

$$\frac{\partial}{\partial \ln(\Lambda^-)} W_{\Lambda^-} = -\mathcal{H} W_{\Lambda^-}, \quad (22)$$

is the JIMWLK equation.

Repeating this elementary step, one progressively re-sums quantum fluctuations down to the scale  $k^- \sim xP^-$ . Thanks to eq. (21), the result of this re-summation for the dipole cross-section is formally identical to eq. (17), except that the source distribution is  $W_{xP^-}$  instead of  $W_{\Lambda_0^-}$ . Note that if one further lowers the cutoff below  $xP^-$ , the dipole cross-section remains unchanged.

**The CGC in A+A collisions:** Collisions between two nuclei (“dense-dense” scattering) are complicated to handle on the surface. However, in the CGC framework, because the wave functions of the two nuclei are saturated, the collision can be treated as the collision of classical fields coupled to fast partons of each nucleus respectively described by the external current  $J^\mu = \delta^{\mu+} \rho_1 + \delta^{\mu-} \rho_2$ . The source densities of fast partons  $\rho_{1,2}$  are both parametrically of order  $1/g$ , which implies that graphs involving multiple sources from both projectiles must be re-summed.

At leading order, inclusive observables<sup>2</sup> depends on the retarded classical color field  $\mathcal{A}^\mu$ , which solves the Yang-Mills equations  $[\mathcal{D}_\mu, \mathcal{F}^{\mu\nu}] = J^\nu$  with the boundary condition  $\lim_{x^0 \rightarrow -\infty} \mathcal{A}^\mu = 0$ . Among the observables to which this result applies is the expectation value of the energy-momentum tensor at early times after the collision. At leading order,

$$T_{\text{LO}}^{\mu\nu} = \frac{1}{4} g^{\mu\nu} \mathcal{F}^{\lambda\sigma} \mathcal{F}_{\lambda\sigma} - \mathcal{F}^{\mu\lambda} \mathcal{F}^\nu{}_\lambda, \quad (23)$$

---

<sup>2</sup>Exclusive observables may also be expressed in terms of solutions of the same Yang-Mills equations, but with more complicated boundary conditions than for inclusive observables.

where  $\mathcal{F}^{\mu\nu}$  is the field strength of the classical field  $\mathcal{A}^\mu$ .

Although A+A collisions are more complicated than e+A or p+A collisions, one can still factorize the leading higher order corrections into the evolved distributions  $W_{\Lambda^-}[\rho_1]$  and  $W_{\Lambda^+}[\rho_2]$ . At the heart of this factorization is a generalization of eq. (20) to the case where the two projectiles are described in the CGC framework [69–71]. When one integrates out the field modes in the slices  $\Lambda_1^\pm \leq k^\pm \leq \Lambda_0^\pm$ , the correction to the energy momentum tensor is

$$\delta T_{\text{NLO}}^{\mu\nu} = \left[ \ln \left( \frac{\Lambda_0^-}{\Lambda_1^-} \right) \mathcal{H}_1 + \ln \left( \frac{\Lambda_0^+}{\Lambda_1^+} \right) \mathcal{H}_2 \right] T_{\text{LO}}^{\mu\nu}, \quad (24)$$

where  $\mathcal{H}_{1,2}$  are the JIMWLK Hamiltonians of the two nuclei respectively. What is crucial here is the absence of mixing between the coefficients  $\mathcal{H}_{1,2}$  of the logarithms of the two projectiles; they depend only on  $\rho_{1,2}$  respectively and not on the sources of the other projectile. Although the proof of this expression is somewhat involved, the absence of mixing is deeply rooted in causality. The central point is that because the duration of the collision (which scales as the inverse of the energy) is so brief, soft radiation must occur before the two nuclei are in causal contact. Thus logarithms associated with this radiation must have coefficients that do not mix the sources of the two projectiles.

Following the same procedure for eq. (24), as for the e+A and p+A cases, one obtains for the energy-momentum tensor in an A+A collision the expression

$$\langle T^{\mu\nu} \rangle_{\text{LLog}} = \int [D\rho_1 D\rho_2] W_1[\rho_1] W_2[\rho_2] T_{\text{LO}}^{\mu\nu}. \quad (25)$$

This result can be generalized to multi-point correlations of the energy-momentum tensor,

$$\langle T^{\mu_1\nu_1}(x_1) \cdots T^{\mu_n\nu_n}(x_n) \rangle_{\text{LLog}} = \int [D\rho_1 D\rho_2] W_1[\rho_1] W_2[\rho_2] T_{\text{LO}}^{\mu_1\nu_1}(x_1) \cdots T_{\text{LO}}^{\mu_n\nu_n}(x_n). \quad (26)$$

In this expression, all the correlations between the energy-momentum tensor at different points are from the distributions  $W_{1,2}[\rho_{1,2}]$ . Thus, the leading correlations are already built into the wavefunctions of the projectiles prior to the collision.

Note that the expressions in eqs. (25) and (26) are valid for proper times  $\tau \sim 1/Q_s$  after the heavy ion collision. Complicated final state effects, possibly driven by instabilities, are expected to bring this non-equilibrium gluonic matter into a quark-gluon plasma. Although this aspect of A+A collisions is very different from what happens in DIS reactions, the Color Glass Condensate provides a universal description of the hadronic and nuclear wavefunctions prior to the collision in both cases, and a powerful framework to show that the logarithms of the collision energy are universal for inclusive enough observables. Thanks to this universality, measurements at small  $x$  in e+A collisions can provide valuable constraints on the distributions  $W[\rho]$  for a nucleus, that can then be used in order to compute the state of the system formed at early times in A+A collisions.

### 2.1.5 Shadowing

*Boris Z. Kopeliovich*

In terms of the dipole formalism, nuclear shadowing is related to the interaction of different Fock components of the projectile particle with the nuclear target. The lowest Fock states (i.e.  $\gamma^* \rightarrow \bar{q}q$ ) are responsible for higher twist shadowing, while higher Fock

components (i.e.  $\gamma^* \rightarrow \bar{q}qg$ ) give rise to leading twist gluon shadowing.

**Quark shadowing:** The magnitude of higher twist shadowing is controlled by the interplay between two fundamental quantities.

(i) The lifetime of photon fluctuations, or coherence time.

$$l_c = \frac{2\nu}{Q^2 + M^2} = \frac{P}{x_{Bj} m_N} = P l_c^{max}, \quad (27)$$

where  $x_{Bj} = Q^2/2m_N\nu$ ,  $M$  is the effective mass of the fluctuation,  $P = (1 + M^2/Q^2)^{-1}$ , and  $l_c^{max} = 1/m_N x_{Bj}$ . The usual approximation is to assume that  $M^2 \approx Q^2$  since  $Q^2$  is the only large dimensional scale available. In this case,  $P = 1/2$  and the corresponding value of  $l_c$  is called Ioffe length of time.

Shadowing is possible only if the coherence time exceeds the mean nucleon spacing in nuclei, and shadowing saturates (for a given Fock component) if the coherence time substantially exceeds the nuclear radius.

(ii) Equally important for shadowing is the transverse separation of the  $\bar{q}q$ . This controls the dipole-nucleon cross section  $\sigma_{\bar{q}q}^N(r)$ , and correspondingly the total nuclear cross section [72, 73],

$$\left(\sigma_{tot}^{\gamma^*A}\right)_{l_c \gg R_A}^{T,L} = 2 \int d\alpha \int d^2r \left| \Psi_{\bar{q}q}^{T,L}(\epsilon r) \right|^2 \int d^2b \left[ 1 - \exp\left(-\frac{1}{2} \sigma_{\bar{q}q}^N(r) T_A(b)\right) \right] \quad (28)$$

where the perturbative light-cone distribution function for the  $\bar{q}q$  has the form [74, 75],

$$\Psi_{\bar{q}q}^{T,L}(\vec{r}_T, \alpha) = \frac{\sqrt{\alpha_{em}}}{2\pi} \bar{\chi} \hat{O}^{T,L} \chi K_0(\epsilon r_T); \quad (29)$$

$\chi$  and  $\bar{\chi}$  are the spinors of the quark and antiquark respectively;  $K_0(\epsilon r_T)$  is the modified Bessel function;  $\epsilon^2 = \alpha(1 - \alpha)Q^2 + m_q^2$ ; and the operators  $\hat{O}^{T,L}$  for transversely and longitudinally polarized photons have the form,

$$\hat{O}^T = m_q \vec{\sigma} \cdot \vec{e} + i(1 - 2\alpha) (\vec{\sigma} \cdot \vec{n}) (\vec{e} \cdot \vec{\nabla}_r) + (\vec{\sigma} \times \vec{e}) \cdot \vec{\nabla}_r, \quad (30)$$

$$\hat{O}^L = 2Q\alpha(1 - \alpha) \vec{\sigma} \cdot \vec{n}. \quad (31)$$

Here  $\vec{n} = \vec{p}/p$  is a unit vector parallel to the photon momentum;  $\vec{e}$  is the polarization vector of the photon;  $m_q$  and  $\alpha$  are the mass, and fractional light-cone momentum carried by the quark.

In order to be shadowed, a  $\bar{q}q$ -fluctuation of the photon has to interact with a large cross section. As a result of color transparency [72, 76], small size dipoles with  $r^2 \sim 1/Q^2$  interact only weakly and are therefore less shadowed. The dominant contribution to shadowing comes from the aligned jet configurations ( $\alpha \rightarrow 0, 1$ ) [77] of  $\bar{q}q$  pairs, which have large transverse separation,  $\langle r^2 \rangle \sim 1/[Q^2\alpha(1 - \alpha)]$  according to (29) and (??). Although the weight of such configurations is small,  $1/Q^2$ , this is compensated by the large interaction cross section [78].

The coherence length (Eq. (27)) averaged over interacting  $|\bar{q}q\rangle$  and  $|\bar{q}qg\rangle$  fluctuations calculated in [79] is presented in Fig. 14. The mean values of the factor  $P = l_c/l_c^{max}$  in (27) are plotted for  $\bar{q}q$  fluctuations of transverse and longitudinal photons, as well as for  $\bar{q}qg$  fluctuations as a function of  $Q^2$  at fixed  $x_{Bj}$  (left panel). We see that  $\bar{q}q$  fluctuations in a longitudinal photon live about twice as long as in a transverse one. Both are different

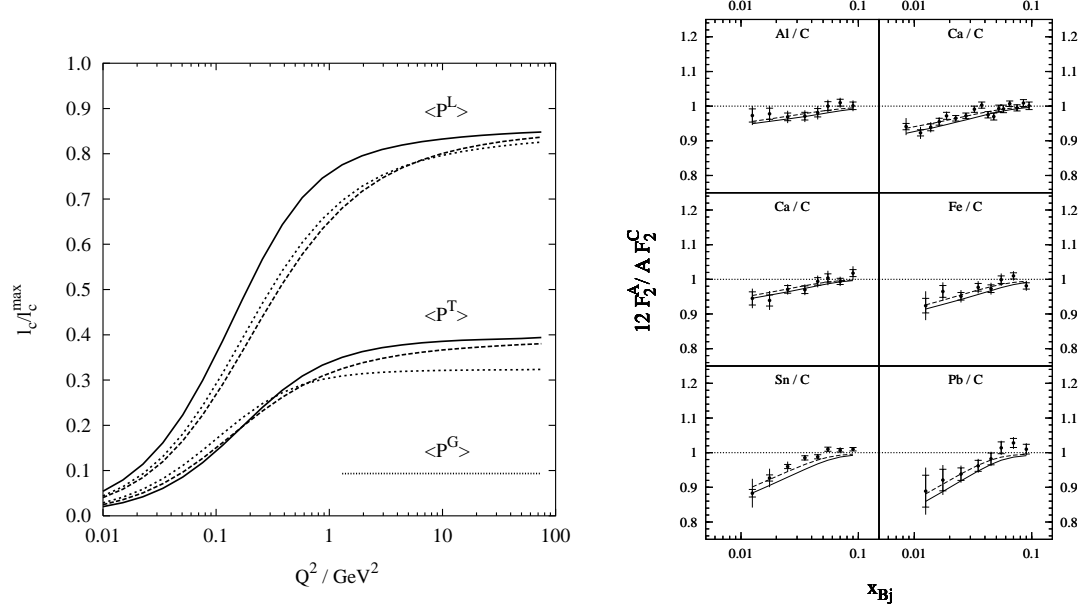


Figure 14. *Left panel:* Factor  $\langle P^{T,L} \rangle$  and  $\langle P^g \rangle$  defined in (27) for  $\bar{q}q$  fluctuations of transverse and longitudinal photons, and for  $\bar{q}qg$  fluctuations, from the top to bottom. Calculations are done as a function of  $Q^2$  at  $x_{Bj} = 0.01$ . Dotted curves correspond to perturbative wave functions and an approximate dipole cross section  $\propto r_T^2$ . Dashed curves rely on the realistic parameterization for the dipole cross section [80]. The solid curves show the most realistic case based on the nonperturbative wave functions. *Right panel:* Comparison between calculations for quark shadowing and experimental data from NMC [81, 82] for the structure functions of different nuclei relative to carbon as function of  $x_{Bj}$ . The  $Q^2$  range covered by the data is approximately  $3 \text{ GeV}^2 \leq Q^2 \leq 17 \text{ GeV}^2$  from the lowest to the highest  $x_{Bj}$  bin. Solid and dashed curves are calculated with and without the real part of the light-cone potential in (33).

from  $P = 1/2$  corresponding to the Ioffe time. The lifetime of the higher order Fock states containing gluons is about order of magnitude shorter.

**Onset of shadowing:** Eq. (28) describing quark shadowing is valid only in the limit of  $l_c \gg R_A$ , i.e. at very small  $x_{Bj}$  where the magnitude of shadowing nearly saturates. However, all available data for DIS on nuclei are in the region of shorter coherence length, and one needs theoretical tools to describe the onset of shadowing.

The Gribov theory of inelastic shadowing [83] relates nuclear shadowing to the cross section of diffractive dissociation. In the case of a deuteron target, this approach provides a full and model independent description of shadowing. The onset of shadowing can be accurately calculated, since the phase shift  $\Delta z/l_c$  between the impulse approximation term and the inelastic shadowing term is under control. However, a description of shadowing for heavy nuclei is a challenge in this approach. Indeed, only the lowest order of Gribov corrections can be calculated using data on diffraction. The higher order corrections, illustrated in Fig. 15a, need information unavailable from data, like the diffractive amplitudes between different excited states,  $X^*$ ,  $X^{**}$ , the attenuation of these states in the nuclear medium, etc.

An alternative description with the path integral technique was proposed in [79]. One should sum up over all possible trajectories of the quark and antiquark propagating through

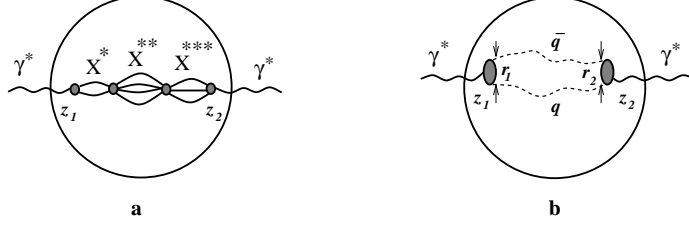


Figure 15. **a**: A high order term in Gribov inelastic shadowing corrections to  $F_2^A(x, Q^2)$ ; **b**: Dipole description based on the path integral technique, which sums up the Gribov corrections in all orders.

the nucleus, as is illustrated in Fig. 15b. This leads to the 2-dimensional Schrödinger equation for the Green function describing propagation of a dipole with initial (final) transverse separation  $\vec{r}_1$  ( $\vec{r}_2$ ) at longitudinal coordinate  $z_1$  ( $z_2$ ),

$$\left[ i \frac{\partial}{\partial z_2} + \frac{\Delta_{\perp}(r_2) - \varepsilon^2}{2\nu\alpha(1-\alpha)} + \frac{i}{2} \rho_A(b, z_2) \sigma_{q\bar{q}}^N(r_2) - \frac{a^4(\alpha) r_2^2}{2\nu\alpha(1-\alpha)} \right] G(r_2, z_2 | r_1, z_1) = 0 \quad (32)$$

The last two terms represent the imaginary and real parts of the light cone potential. The former describes the attenuation of the dipole in the nuclear medium, while the latter models the non-perturbative interactions inside the dipole. Solving this equation, one can calculate the shadowing corrections as:

$$\begin{aligned} (\sigma_{tot}^{\gamma^*A})^{T,L} &= A (\sigma_{tot}^{\gamma^*N})^{T,L} - \frac{1}{2} Re \int d^2b \int_0^1 d\alpha \int_{-\infty}^{\infty} dz_1 \int_{z_1}^{\infty} dz_2 \int d^2r_1 \int d^2r_2 \\ &\times \left[ \Psi_{q\bar{q}}^{T,L}(\varepsilon, \lambda, r_2) \right]^* \rho_A(b, z_2) \sigma_{q\bar{q}}^N(s, r_2) G(r_2, z_2 | r_1, z_1) \rho_A(b, z_1) \sigma_{q\bar{q}}^N(s, r_1) \Psi_{q\bar{q}}^{T,L}(\varepsilon, \lambda, r_1) \end{aligned} \quad (33)$$

At  $l_c \ll 1/\rho\sigma$ , the second term vanishes. For  $l_c \gg R_A$ , it saturates at the value given by Eq. (28). The numerical results are compared with data from the NMC experiment [81, 82] in the right panel of Fig. 14. The solid and dashed curves are calculated with and without the real part of the light-cone potential in (33). It worth emphasizing that this is a parameter-free calculation, no adjustment to nuclear data has been done. The dipole cross section was fitted to DIS data on a proton.

Notice that these calculations have been performed for the lowest Fock component  $|\bar{q}q\rangle$  of the photon, they miss gluon shadowing related to the higher Fock states containing gluons.

**Gluon shadowing:** Gluon shadowing is related to specific channels of diffractive gluon radiation. In terms of Regge phenomenology, these processes correspond to the triple-Pomeron contribution, and can be seen in data as the large mass tail of the invariant mass distribution,  $d\sigma_{diff}/dM_X^2 \propto 1/M_X^2$ . Such an  $M_X^2$ -dependence is the undebatable evidence of radiation of a vector particle, i.e. a gluon.

Data show that the magnitude of diffractive gluon radiation is amazingly small. The way to see that is to express the single diffraction cross section in terms of the Pomeron-proton cross section as is illustrated in the left panel of Fig. 16. The Pomeron can be treated as a gluonic dipole and its cross section is expected to be about twice as big as for a  $\bar{q}q$  dipole, i.e.  $\sigma_{tot}^{Ip} \sim 50$  mb. However, data depicted in the right panel of Fig. 16 show that  $\sigma_{tot}^{Ip} < 2$  mb. Such a dramatic disagreement gives a clue that diffractive gluon radiation is strongly suppressed compared with the expectation based on pQCD. This problem has been known in the Regge phenomenology as smallness of the triple-Pomeron coupling [85].

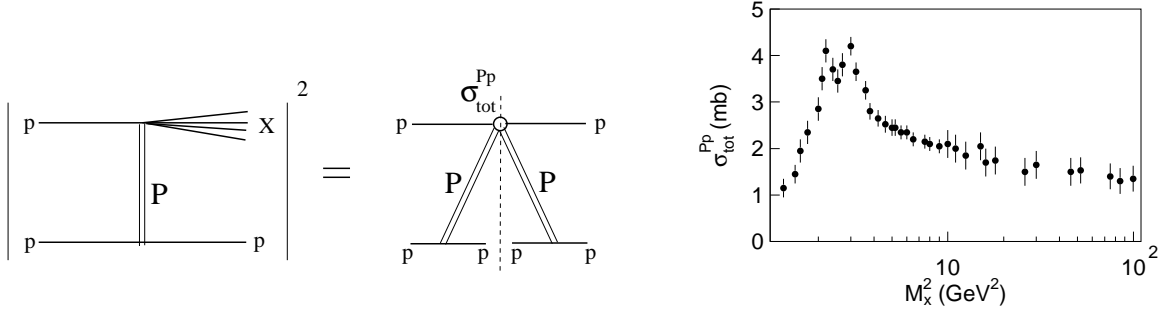


Figure 16. *Left panel:* The amplitude squared of diffractive excitation of the projectile proton, summed over all the excitations with invariant mass  $M_X$ , is related via the optical theorem with the total Pomeron-proton cross section at c.m. energy  $M_X$ . *Right panel:* The Pomeron-proton cross section extracted [84] from data on single diffraction  $pp \rightarrow pX$  as function of  $\sqrt{s}$ - $p$  c.m. squared.

Gluon radiation can be described within the dipole approach via the propagation of a  $\bar{q}qg$  dipole through the nuclear medium [86]. As the mean fractional momentum of the radiates gluon is very small,  $\langle \alpha_g \rangle \sim 1/\ln(s)$ , one can rely on equations (28) for very small  $x_{Bj}$ , or Eqs. (32)-(33) for the onset of gluon shadowing, by replacing  $\sigma_{\bar{q}q}(r) \Rightarrow \sigma_{gg}(r)$ . The only way to explain the observed suppression of gluon radiation is to reduce the mean size of the glue-gluon dipole. This can be achieved by introducing a specifically strong nonperturbative interaction within the glue-gluon dipole, which comes as the real part of the light-cone potential in Eq. (32). Adjusting the strength of this interaction to data on diffractive gluon radiation (triple-Pomeron term) one arrives at the light-cone distribution functions in (28) and (33) with the mean glue-gluon separation  $r_0 \approx 0.3$  fm [87]. This distance is smaller than the confinement radius  $\sim 1/\Lambda_{QCD} = 1$  fm and is in accord with the lattice evaluations of the  $gg$  correlation radius [88], and the instanton radius [89]. There is more experimental evidence supporting the existence of a semi-hard scale in hadrons [90].

Thus, the magnitude of gluon shadowing evaluated in [87, 91] is expected to be rather small, as is depicted in Fig. 17. The nuclear ratio  $R_g = G_A(x, Q^2)/AG_N(x, Q^2)$  is plotted as function of  $x_{Bj}$  at  $Q^2 = 4$  and  $40$  GeV<sup>2</sup> (left panel); and as function of the path length in nuclear matter at  $Q^2 = 4$  GeV<sup>2</sup> and different values of  $x_{Bj}$ .

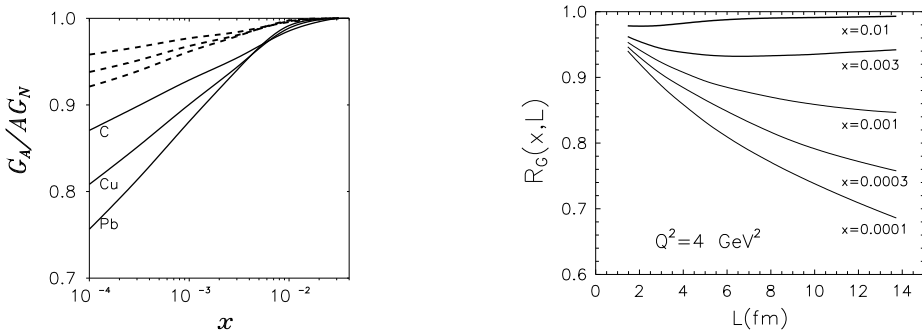


Figure 17. *Left panel:* Ratio of the gluon distribution functions in nuclei (carbon, copper and lead) and nucleons versus Bjorken  $x$  at  $Q^2 = 4$  GeV<sup>2</sup> (solid curves) and  $40$  GeV<sup>2</sup> (dashed curves) [87]. *Right panel:* Nuclear ratio  $R_g = G_A(x, Q^2)/AG_N(x, Q^2)$  for gluons as function of path length in nuclear matter, calculated in [91] at  $Q^2 = 4$  GeV<sup>2</sup> for several fixed values of  $x$ .

The path-integral approach is the most accurate method, which is valid in all regimes of gluon radiation, from incoherent to fully coherent. Nevertheless, this is still the lowest order calculation, which might be a reasonable approximation only for light nuclei, or for

the onset of shadowing. Contribution of higher Fock components is still a challenge. This problem has been solved so far only in the unrealistic limit of long coherence lengths for all radiated gluons, described by the Balitsky-Kovchegov (BK) equation [32, 33]. A numerical solution of this equation is quite complicated and includes lots of modelling [92]. A much simpler bootstrap equation, which only employs a modelled shape of the saturated gluon distribution, was derived in [93]. It includes the self-quenching effect for gluon shadowing, and leads to a gluon distribution in nuclei which satisfies the unitarity bound [94]. The results are quite similar to the numerical solutions of the BK equation [92]. The magnitude of the self-quenched gluon shadowing found in [93] is similar to the above results obtained in the leading order.

### 2.1.6 Leading-twist nuclear shadowing

*Vadim Guzey and Mark Strikman*

Nuclear shadowing in hadron (photon)-nucleus scattering is the firmly established experimental phenomenon that at high energies the scattering cross section on a nuclear target is smaller than the sum of the scattering cross sections on the individual nucleons. In the nucleus rest frame, the theory of nuclear shadowing is based on the connection between nuclear shadowing and diffraction which has been established long time ago by V.N. Gribov [83]. In the derivation, the key assumption is that nuclei can be described as dilute systems of nucleons. The accuracy of the resulting theory for hadron-nucleus cross sections is very high with the corrections at the level of a few % which reflect the small admixture of non-nucleonic degrees of freedom in nuclei and the small off-shellness of the nucleons in nuclei as compared to the soft strong interaction scale. Gribov's result can be understood [95] as a manifestation of unitarity as reflected in the Abramovsky-Gribov-Kancheli (AGK) cutting rules [96].

The connection between shadowing and diffraction is also valid in deep inelastic scattering (DIS) with nuclei; the approach based on this connection is called the leading twist theory of nuclear shadowing [95, 97–99]. In this theory, parton distribution functions (PDFs) in nuclei at small  $x$  are calculated combining the unitarity relations for different cuts of the shadowing diagrams corresponding to the diffractive and inelastic final states (AGK cutting rules) with the QCD factorization theorem for hard diffraction [100] (which provides a good description of the totality of the HERA hard diffractive data). The resulting multiple scattering series for the quark nuclear PDFs is presented in fig. 18, where graphs  $a$ ,  $b$ , and  $c$  correspond to the interaction with one, two, and three nucleons of the target, respectively. Graph  $a$  gives the impulse approximation; graphs  $b$  and  $c$  contribute to the shadowing correction. The interaction with  $N > 3$  nucleons, though not shown, is taken into account in the final expression for nuclear PDFs.

At the level of the interaction with two nucleons of a nucleus with the atomic mass number  $A$ , one can derive the *model-independent* expression for the shadowing correction to the nuclear PDF of flavor  $j$  [95] (corresponding to graph  $b$  of fig. 18):

$$\begin{aligned}
x f_{j/A}^{(b)}(x, Q^2) &= -8\pi A(A-1) \Re e \frac{(1-i\eta)^2}{1+\eta^2} \int_x^{0.1} dx_{\mathbb{P}} \beta f_j^{D(4)}(\beta, Q^2, x_{\mathbb{P}}, t_{\min}) \\
&\times \int d^2\vec{b} \int_{-\infty}^{\infty} dz_1 \int_{z_1}^{\infty} dz_2 \rho_A(\vec{b}, z_1) \rho_A(\vec{b}, z_2) e^{i(z_1-z_2)x_{\mathbb{P}}m_N}, \quad (34)
\end{aligned}$$

where  $f_j^{D(4)}$  is the diffractive parton distribution of the nucleon;  $\rho_A$  is the nuclear matter



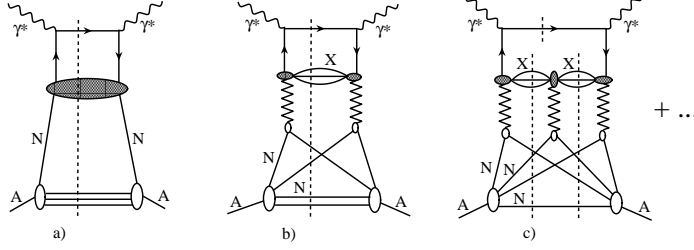


Figure 18. Multiple scattering series for nuclear quark PDFs. Graphs *a*, *b*, and *c* correspond to the interaction with one, two, and three nucleons, respectively. Graph *a* gives the impulse approximation; graphs *b* and *c* contribute to the shadowing correction.

density;  $\eta$  is the ratio of the real to imaginary parts of the elementary diffractive amplitude,  $\eta = \Re A^{\text{diff}} / \Im m A^{\text{diff}} \approx 0.17$ . The diffractive PDF  $f_j^{D(4)}$  depends on two light-cone fractions  $x_P = (M_X^2 + Q^2)/(W^2 + Q^2)$  and  $\beta = x/x_P$  and the invariant momentum transfer  $t$ , where  $W$  is the invariant virtual photon-nucleon energy,  $W^2 = (q + p)^2$ , and  $M_X^2$  is the invariant mass squared of the produced intermediate diffractive state denoted as “X” in fig. 18. The longitudinal (collinear with the direction of the photon momentum) coordinates  $z_1$  and  $z_2$  and the transverse coordinate (impact parameter)  $\vec{b}$  refer to the two interacting nucleons;  $m_N$  is the nucleon mass. The  $t$  dependence of  $f_j^{D(4)}$  can be safely neglected as compared to the strong fall-off of the nuclear form-factor for  $A > 4$  and, as a result,  $f_j^{D(4)}$  enters eq. (34) at  $t_{\min} \approx -x^2 m_N^2 (1 + M_X^2/Q^2)^2$  and all nucleons enter with the same impact parameter  $\vec{b}$ . Equation (34) satisfies the QCD evolution equations at all orders in the strong coupling constant  $\alpha_s$ .

To evaluate the contribution to nuclear shadowing of the interactions with  $N \geq 3$  nucleons in fig. 18, one needs to invoke additional *model-dependent* considerations, since the interaction of a hard probe (virtual photon) with  $N \geq 3$  nucleons is sensitive to fine details of the diffractive dynamics. In particular, the hard probe can be viewed as a coherent superposition of configurations which interact with the target nucleons with very different strengths. This effect of color (cross section) fluctuations is analogous to the inelastic shadowing in hadron-nucleus scattering with the important difference that the dispersion of the interaction strengths is much smaller in the hadron case than in DIS. However, the observation that  $\alpha_P(0) = 1.11$  found in the analysis of hard diffraction at HERA [101] is very close to  $\alpha_P^{\text{soft}}(0) = 1.08$  in soft hadronic interactions [102] indicates that hard diffraction in DIS is dominated by large-size hadron-like (aligned jet) configurations which evolve to large  $Q^2$  via the DGLAP evolution. (As to the point-like configurations, they give an important and increasing with  $Q^2$  contribution to graph *a* in fig. 18.)

This important observation reduces theoretical uncertainties in the treatment of the interactions with  $N \geq 3$  nucleons and allows one to reliably parameterize the strength of the interaction with  $N \geq 3$  nucleons by a single effective hadron-like cross section  $\sigma_{\text{soft}}^j$ . The final expression for the nuclear PDFs at a certain initial scale  $Q_0^2$  reads [98, 99]:

$$\begin{aligned}
 x f_{j/A}(x, Q_0^2) &= A x f_{j/N}(x, Q_0^2) \\
 &- 8\pi A(A-1) \Re e \frac{(1-i\eta)^2}{1+\eta^2} \int_x^{0.1} dx_P \beta f_j^{D(4)}(\beta, Q_0^2, x_P, t_{\min}) \int d^2b \int_{-\infty}^{\infty} dz_1 \\
 &\int_{z_1}^{\infty} dz_2 \rho_A(\vec{b}, z_1) \rho_A(\vec{b}, z_2) e^{i(z_1 - z_2)x_P m_N} e^{-\frac{A}{2}(1-i\eta)\sigma_{\text{soft}}^j(x, Q_0^2) \int_{z_1}^{z_2} dz' \rho_A(\vec{b}, z')} . \quad (35)
 \end{aligned}$$

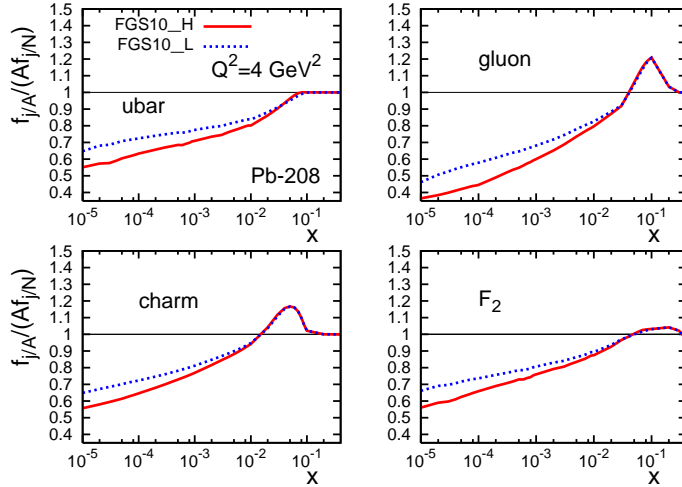


Figure 19. The leading twist theory of nuclear shadowing predictions for  $f_{j/A}/(Af_{j/N})$  ( $\bar{u}$  and  $c$  quarks and gluons) and  $F_{2A}/(AF_{2N})$  as functions of  $x$  at  $Q_0^2 = 4 \text{ GeV}^2$ . The two sets of curves correspond to the two extreme scenarios of nuclear shadowing (see the text).

Due to the QCD factorization theorem, these nuclear PDFs  $f_{j/A}(x, Q^2)$  can be applied to the calculation of any hard processes involving nuclei, including heavy-ion collisions. Removing the integration over  $d^2b$  in right-hand side of eq. (35), one obtains the impact parameter dependent nuclear PDFs (nuclear GPDs in the  $\xi = 0$  limit in the impact parameter representation) [99], see Section 3.3.

In our analysis [99], we used two models for the color fluctuations in the virtual photon which correspond to two models for  $\sigma_{\text{soft}}^j$  which cover essentially all reasonable possibilities for the resulting nuclear shadowing. An example of our predictions for the gluon,  $\bar{u}$ -quark,  $c$ -quarks, and  $F_{2A}$  structure functions is presented in fig. 19 for the two scenarios for  $\sigma_{\text{soft}}^j$  that we have mentioned above (labeled FGS10\_H and FGS10\_L). As one can see from fig. 19, we predict large nuclear shadowing for each singlet parton flavor with the characteristic feature that nuclear shadowing in the gluon channel is larger than that in the quark channel. The difference between the two extreme scenarios of color fluctuations (the solid and dotted curves in fig. 19) is less than 20% for  $A \sim 200$  and much smaller for light nuclei. The spread between the solid and dotted curves is the theoretical uncertainty of our predictions.

Accounting for the color fluctuations as done in eq. (35) tends to reduce the amount of nuclear shadowing as compared to the quasi-eikonal approximation used in the literature [95, 103]. Also, the AGK technique allows one to calculate other quantities such as nuclear diffractive PDFs and fluctuations of multiplicity in non-diffractive DIS [95, 99, 104] both of which turn out to be sensitive to the pattern of the color fluctuations, see Section 2.3.3.

Our approach to nuclear shadowing assumes the applicability of the linear (in parton densities) leading-twist DGLAP approximation. Numerical studies indicate that the dominant contribution to nuclear shadowing in eq. (35) comes from the region of relatively large  $\beta = Q^2/(M^2 + Q^2)$  corresponding to the rapidity intervals  $\leq 3$  for which the small- $x$  approximation used in the BFKL-type approaches is not applicable. These approaches predict  $\alpha_P(0) \sim 1.25$ , while the HERA experiments find  $\alpha_P(0) \sim 1.11 \approx \alpha_P^{\text{soft}}(0)$  consistent with the expectations of the QCD aligned jet approximation [105] that we effectively implemented in the derivation of eq. (35).

### 2.1.7 Non-perturbative approaches

*Hans J. Pirner*

One of the challenges in QCD is the description and understanding of high-energy scattering on protons and nuclei. Even for high energies and large  $Q^2$  in deep inelastic electron scattering a non-perturbative framework may be necessary. For the transverse structure function, the  $q\bar{q}$  dipole in the photon can be large and the saturation scale  $Q_s$  is small for the energies we discuss. In the following I will present the main features of such an approach, which of course will also include the perturbative aspects.

The most important phenomenon observed in high-energy scattering is the rise of the total cross sections with increasing c.m. energy. While the rise is slow in hadronic reactions of *large* particles such as protons, pions, kaons, or real photons, it is steep if one *small* particle is involved such as an incoming virtual photon or an outgoing charmonium. This energy behavior is best seen in the proton structure function  $F_2(x, Q^2)$ . With increasing photon virtuality  $Q^2$ , the increase of  $F_2(x, Q^2)$  towards small Bjorken  $x$  becomes significantly stronger. It is tempting to test the growth of the structure function with nuclei. In the following I will summarize my work with Shoshi, Steffen and Dosch which is published in two main papers [106, 107]. For references to other work please see these two papers.

In the two-pomeron model of Donnachie and Landshoff, the energy dependence of the cross sections at high energies results from the exchange of a soft and a hard pomeron. The first dominates in hadron-hadron and  $\gamma^*p$  reactions at low  $Q^2$  and the second in  $\gamma^*p$  reactions at high  $Q^2$ . The two pomerons may be related to a glueball trajectory, which is inherently nonperturbative, and a gluon ladder à la BFKL, which includes the perturbative aspects. The two-pomeron model, however, does not contain parton saturation nor unitarity effects. A model motivated by the concept of parton saturation is the one of Golec-Biernat and Wüsthoff which allows very successful fits to  $\gamma^*p$  data, but cannot be applied to hadron-hadron reactions. A successful description of dipole nucleon scattering which can be used for hadron-nucleon scattering and DIS with moderate  $Q^2$  has been found [87].

We have combined perturbative and non-perturbative QCD to compute high-energy reactions of hadrons and photons with special emphasis on saturation effects that manifest  $S$ -matrix unitarity [106]. We follow the *functional integral approach* to high-energy scattering of Nachtmann, in which the  $S$ -matrix element factorizes into the universal correlation of two light-like Wegner-Wilson loops  $S_{DD}$ . The light-like Wegner-Wilson loops describe color dipoles given by the quark and antiquark in the meson or photon projectile and the quark and diquark in the baryon target. This approach treats projectile and target symmetrically.  $S$ -matrix unitarity is respected as a consequence of a matrix cumulant expansion and the Gaussian approximation of the functional integrals. The resulting dipole cross sections do not show Glauber-like behavior with the dipole size as in the Golec-Biernat model. The loop-loop correlation function  $S_{DD}$  is expressed in terms of the gauge invariant bi-local gluon field strength correlator integrated over two connected minimal surfaces. Due to the symmetric treatment of the two dipoles this formalism can explicitly investigate the dependence on the impact parameter of the two scattering partners.

The gluon field strength correlator has a non-perturbative and a perturbative component. The *stochastic vacuum model* of Dosch and Simonov is used for the non-perturbative low frequency background field and *perturbative BFKL gluon exchange* for the high frequency contributions. This combination allows us to describe long and short distance correlations in agreement with Euclidean lattice calculations of the static quark-antiquark potential with color-Coulomb behavior at short distances and confining linear rise at long distances. We have tried to model both components in AdS/QCD, but the long range loop-loop correlation cannot be established on a classical level, since the connecting surface in 5 dimensions breaks off at large distances [108].

Energy dependence in the loop-loop correlation function,  $S_{DD}$ , is introduced by hand in order to describe simultaneously the energy behavior in hadron-hadron, photon-hadron, and photon-photon reactions involving real and virtual photons as well. Motivated by the two-Pomeron picture of Donnachie and Landshoff, we ascribe to the soft and hard component a weak and strong energy dependence, respectively. The parameter describing the energy dependence of the perturbative correlation function is very large because we include *multiple gluonic interactions*. In ref. [106] we have considered not only the dependence of the dipole cross section on dipole size with increasing energy and the resulting  $k_t$ -saturation, but also the scattering amplitudes in impact parameter space, where the  $S$ -matrix unitarity imposes rigid limits on the impact parameter profiles such as the *black disc limit*. We present profile functions for longitudinal photon-proton scattering that provide an intuitive geometrical picture for the energy dependence of the cross sections. The profile function first becomes greyer, turns black and then increases in transverse size. Using a leading-twist NLO DGLAP relation, we estimated the *impact parameter dependent gluon distribution* of the proton  $xG(x, Q^2, |\vec{b}_\perp|)$  from the profile function for longitudinal photon-proton scattering. We have not found saturation of the profile function at HERA energies, but at higher energies,  $xG(x, Q^2, |\vec{b}_\perp|)$  does saturate as a manifestation of the  $S$ -matrix unitarity.

In the same framework we have studied the unintegrated gluon distribution  $xG(x, k_t)$  as function of transverse momentum  $k_t$  for increasing energies [107]. To obtain the unintegrated gluon distribution, one uses the possibility to rewrite the non-perturbative scattering of an artificial external dipole as a superposition of perturbative contributions. In other words the string of the projectile dipole can be decomposed mathematically in a superposition of dipoles of smaller sizes, from which  $xG(x, k_t)$  can be extracted.

The long range confining character of the non-perturbative field strength correlators determines the low  $k_t$  behavior of the gluon structure function of the hadron as  $xG(x, k_t) \propto 1/k_t$ . In the low momentum limit  $xG(x, k_t) \cdot k_t$  converges towards a constant independent of  $x$ , related to the size of the hadron. The cross-over from the nonperturbative region to the perturbative region occurs at around  $k_t = 1 \text{ GeV}$  at  $x$ -values  $10^{-4} < x < 10^{-2}$ .

On a more fundamental level, we have analysed correlations of Wilson lines in vacuum as one approaches the light cone from space-like distances [109]. The dominant terms of the near light cone Hamiltonian for the Wilson lines define a field theory in 2+1 dimensions. In the limit of small  $x$ , the SU(3) QCD for Wilson lines reduces to a critical Z(3) theory with a diverging correlation length  $\xi(x) \propto x^{-1/(2\lambda_2)}$  where the exponent  $\lambda_2 = 2.52$  is obtained from the center group Z(3) of SU(3). We conjecture that the dipole wave function of the virtual photon behaves as the correlation function of Wilson lines in the vacuum. For transverse sizes smaller than the correlation size it scales like  $\Psi \propto 1/(x_t)^{1+n}$  with  $n = 0.04$  and for distances larger than the correlation length it decays exponentially which makes this region negligible. For  $F_2$  we integrate the square of the photon wave function weighted with a dipole proton cross section of fixed size  $R_0$  independent of  $x$ . All the energy dependence is absorbed into the photon. Because of the approximate conformality of the dipole wave function ( $n \approx 0$ ), the result depends only on  $R_0^2/\xi(x)^2 \propto R_0^2 x^{1/\lambda_2}$ , i.e. the saturation scale varies as  $Q_s^2 = Q(x_0)^2 (x_0/x)^{1/\lambda_2}$ . The critical index in this theory is a characteristic feature of Z(3) theory i.e. the center group of SU(3) in an external field given by the light quarks. This is very different from the perturbative color glass condensate where  $Q_s$  depends on the running coupling similarly to the power behaviour of BFKL.

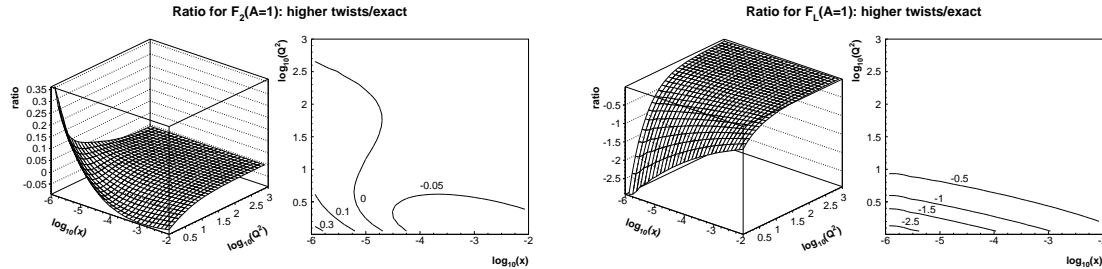


Figure 20. Higher-twist contribution estimate for  $F_2$  (left) and  $F_L$  (right) of the proton.

## 2.2 Inclusive DIS ( $F_2$ , $F_L$ , $F_2^c$ )

### 2.2.1 Estimates of higher twist in deep inelastic nucleon and nucleus scattering

*Joachim Bartels, Krzysztof Golec-Biernat and Leszek Motyka*

A deeper understanding of the transition region at low  $Q^2$  and small  $x$  in deep inelastic electron proton scattering has been one of the central tasks of HERA physics. It will be one of the key questions to be addressed by a future Electron Ion Collider. Approaching this transition region from the perturbative side one expects to see the onset of corrections to the successful DGLAP description, based upon leading twist operators in QCD. The twist expansion defines a systematic approach to the short distance limit probed in deep inelastic scattering. The study of higher-twist corrections therefore provides an attractive route for investigating the region of validity of the leading twist DGLAP evolution equations.

The validity of the leading-twist QCD evolution equations is based upon the fact that, for sufficiently large  $Q^2$  and not too small  $x$ , the gluons inside the proton are dilute. The DGLAP evolution equations, however, predict that, at small  $x$  and low  $Q^2$ , the gluon density grows. As a result, the gluons start to interact and the gluon density eventually saturates. The onset of saturation is encoded in the saturation scale,  $Q_{\text{sat}}^2(x)$ .

The investigation of saturation is of highest importance for our understanding of QCD. Saturation can be viewed as a first step of entering the strong interaction region: while the QCD coupling constant is still small, saturation phenomena probe nonlinear dynamics of the gluon sector which plays a crucial role in many areas of strong interactions. It is expected that saturation effects in deep inelastic scattering on a nucleus are enhanced in comparison with deep inelastic scattering on a proton: in the former case the incoming photon 'sees' the gluons of many nucleons, whereas in the case of a single nucleon one has to go to smaller  $x$  values (i.e. higher energies) in order to reach the same gluon density.

A brief discussion of the connection between saturation and the twist expansion has been given in [110]. Whereas in the GBW model [111, 112] there is a rather direct classification of eikonal-type exchanges of gluon ladders in terms of twist quantum numbers, in saturation models based upon the nonlinear BK-equation [113, 114] a twist decomposition is much less obvious. In the following we present some numerical estimates of higher-twist contributions, using the improved version of the GBW model [115].

**The method:** The theory of higher-twist operators and their evolution equations has been outlined in [116]: in leading order, the higher-twist evolution equations are described by the nonforward DGLAP splitting functions, and there is a particular pattern of mixing between

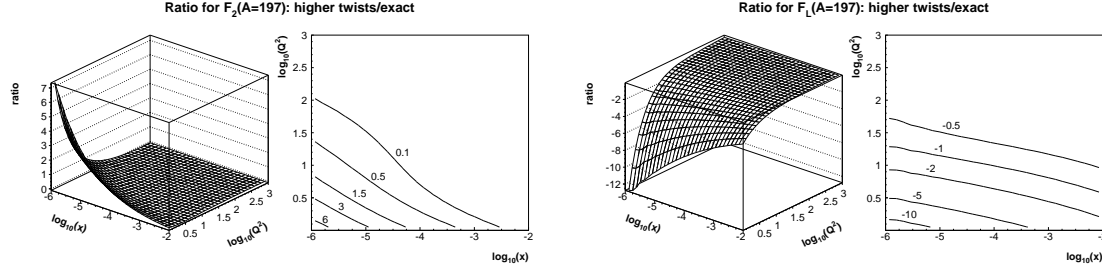


Figure 21. Higher-twist contribution estimate for  $F_2$  (left) and  $F_L$  (right) of the gold nucleus.

different operators of the same twist. In the same way as for leading twist, a numerical analysis of higher twists requires initial conditions for the set of evolution equations, which have to be adjusted to data. In [110] the magnitude of higher-twist corrections has been evaluated in a slightly different way. Starting from the observation that within the GBW saturation model the multiple exchanges of leading-twist gluon ladders can be put into a one-to-one correspondence with contributions of definite twist quantum numbers, it is possible to arrive at quantitative estimates of the leading-twist contributions and corrections due to twist  $\tau = 4, 6, \dots$ . Details have been described in [110] and will not be repeated here.

While the analysis in [110] was done for electron proton scattering, it is straightforward to extend it to electron-nucleus scattering, e.g. for scattering on gold. Assuming a cylindrical nucleus with a characteristic size  $R_A \approx A^{1/3}R_p$  (with  $R_p$  being the proton radius), we simply replace the dipole-proton cross section (eq.(42) in [110])

$$\sigma_{\text{dipole-proton}} = \sigma_0 (1 - \exp(-\Omega(x, r^2))) \quad (36)$$

by the the dipole-nucleus cross section

$$\sigma_{\text{dipole-nucleus}} = A^{2/3} \sigma_0 (1 - \exp(-A^{1/3} \Omega(x, r^2))) , \quad (37)$$

where  $\Omega(x, r^2)$  is the eikonal function given in [110]. With the parameters from [110] we simply repeat the electron proton calculations for electron gold scattering, using the modified dipole cross section formula in (2).

**Numerical results:** The numerical results for  $F_2$  and  $F_L$  are shown in Fig. 20 for the proton, and Fig. 21 for the gold nucleus. In each figure we show, on the l.h.s in a 3-dimensional view, the ratio of the higher-twist corrections and the full structure function as a function of  $x$  and  $Q^2$ ,

$$\text{ratio} = \frac{F_{2,L}^{(\text{total})} - F_{2,L}^{(\tau=2)}}{F_{2,L}^{(\text{total})}} . \quad (38)$$

The r.h.s. shows the projection onto the  $(\log x, \log Q^2)$  plane: the lines belong to fixed values of the ratio (38). One recognizes the general trend: the corrections are getting larger when  $x$  and  $Q^2$  decrease (i.e. moving towards the lower left corner). For given  $x$  and  $Q^2$ , the corrections for the longitudinal structure functions are larger than for  $F_2$ . This is a consequence of the sign structure of the corrections in  $F_L$  and  $F_T$ : the twist four corrections to  $F_L$  and  $F_T$  have opposite signs, and in the analysis [110] of  $F_2 = F_T + F_L$  a strong cancellation has been found. This explains the smallness of higher twist in  $F_2$ .

One also recognizes the general trend that for gold all corrections are larger than for the proton. Finally, the corrections to  $F_L$  are negative and those to  $F_2$  are mostly positive. In the case of the proton  $F_2$  there is a change in sign in the region of very small values of  $Q^2$ : this again is a consequence of the sign structure of the twist corrections to  $F_T$  and  $F_L$ .

**Conclusions:** Our numerical analysis confirms that, in general, the structure functions  $F_L$  are more sensitive to higher-twist corrections than  $F_2$  which, because of the sign structure in the twist 4 corrections, seems to much better "protected" against higher twist. Also, the nucleus target reveals more of the corrections than the proton. Applying this to the search for saturation, it seems clear that in a future electron ion collider the measurement of  $F_L$  is of vital importance.

### 2.2.2 Strength of nonlinear effects in nucleons and nuclei

*Tuomas Lappi*

The effects of nonlinearity and unitarity in small  $x$  DIS are most clearly visible in the dipole framework. We denote  $\mathcal{N}(x, \mathbf{b}_T, \mathbf{r}_T)$  the imaginary part of the scattering amplitude for a dipole of size  $\mathbf{r}_T$  and rapidity  $y = \ln(1/x)$  to scatter off the target at impact parameter  $\mathbf{b}_T$ . The total dipole cross section is given by twice the integral of  $\mathcal{N}(x, \mathbf{b}_T, \mathbf{r}_T)$  over the impact parameter. While the formal unitarity limit would be for  $\mathcal{N}$  to lie between 0 and 2, in practice the reasonable physical area is between 0 (no scattering) and 1 (complete absorption or the black disk limit). The typical value of the dipole scattering amplitude therefore serves as a good measure of the degree of nonlinearity of the scattering process.

As the total cross section depends on the integral of the scattering amplitude over the impact parameter, statements about the magnitude of the scattering amplitude depend on the profile of the target in  $\mathbf{b}_T$ . The  $\mathbf{b}_T$ -dependence for the scattering amplitude on a nucleon is, however, very much constrained by the  $t$ -dependence of exclusive vector meson production. Using this information, in addition to the total cross section, results in the two commonly used  $\mathbf{b}_T$ -dependent dipole amplitude parametrizations that we will use here, the IPsat and bCGC models [117–119]. They have successfully been used to describe HERA data on the inclusive cross section, exclusive vector meson production and diffractive structure functions [120].

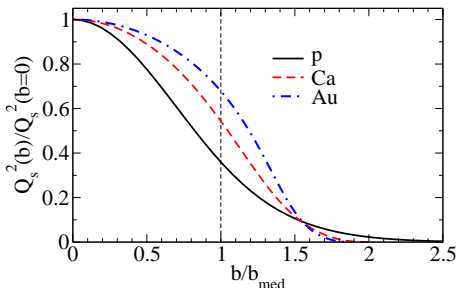


Figure 22. The saturation scale in a proton and Ca and Au nuclei as a function of  $b/b_{\text{med}}$ , where  $b_{\text{med}}$  is the median impact parameter probed in inclusive DIS at  $x = 0.001$  and  $Q^2 = 1 \text{ GeV}^2$ .

**The saturation scale:** To a first approximation the impact parameter dependence of the nuclear scattering amplitude can then be obtained by combining the nucleon one with basic knowledge of nuclear geometry in a Glauber-like treatment (see e.g. Refs. [121, 122] for details). This yields a characteristic pattern of nuclear suppression (shadowing) of the

inclusive cross section, a nuclear enhancement of diffraction to small mass states and a suppression in diffraction to large masses (small  $\beta$ ) [120].

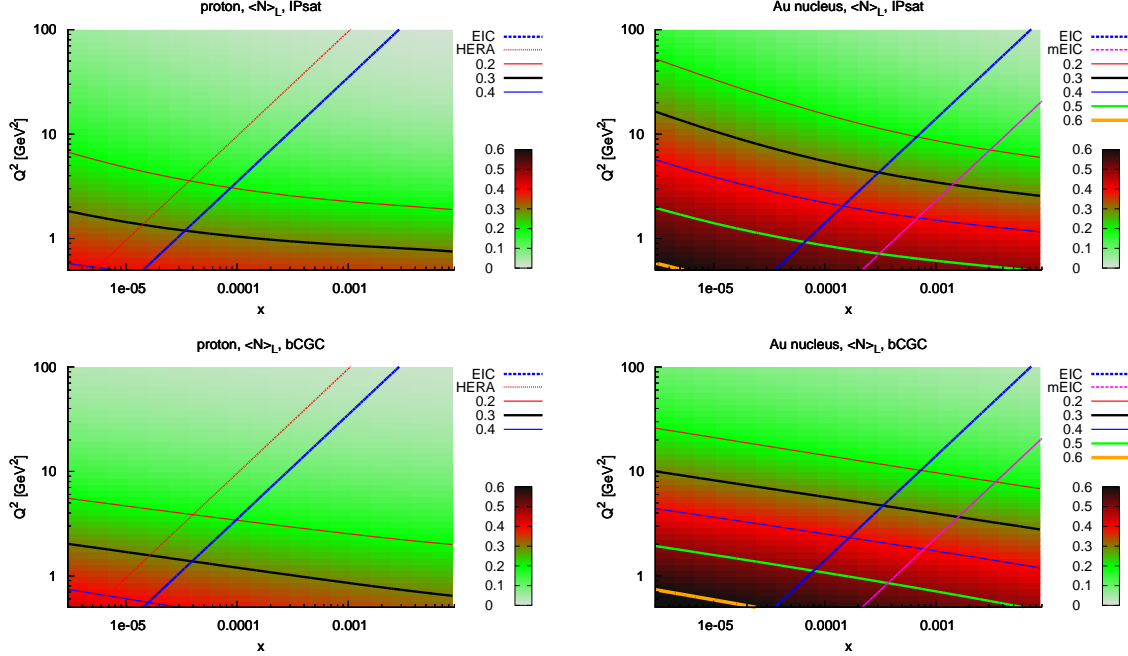


Figure 23. Longitudinal mean scattering amplitude  $\langle N \rangle_L$  for a proton (left) and a gold nucleus (right) with the IPsat parametrization (first row) and bCGC parametrization (second row).

One way of quantifying the importance of nonlinear effects is to compare the value of the ( $\mathbf{b}_T$  and  $x$ -dependent) *saturation scale*  $Q_s^2$  to the virtuality  $Q^2$  of the process. The saturation scale is defined as the inverse of the dipole size at which the scattering amplitude  $\mathcal{N}$  reaches some specific value defined by convention. For  $Q^2 \gg Q_s^2$  one is in the dilute limit and for  $Q^2 \sim Q_s^2$  nonlinear effects become important. A naive argument of the  $A$ -dependence of the saturation scale for nuclei would give  $Q_{sA}^2 \sim A^{1/3}$ . The importance of a realistic impact parameter dependence for nuclei was discussed in more detail in Ref. [121], where it was found that this dependence is indeed true to a very good approximation, but the picture is more intricate than that. For the center of a nucleus vs. the center of a proton the saturation scale is suppressed by a geometrical factor  $\sim 0.3 \approx R_p^2 A^{2/3} / R_A^2$ . Both a nucleon and a nucleus have a dilute edge at large impact parameters. The thickness of this edge is determined by confinement scale physics and is thus of the same order for both. The proton is, however, a much smaller object and therefore the dilute edge region is responsible for a much larger fraction of the total cross section than in a nucleus. One way to see this is to look at the saturation scale at the *median impact parameter* contributing to the inclusive cross DIS cross section. The value of  $Q_s^2(b_{\text{med}})$  is  $\sim 35\%$  of the value at  $b = 0$  for a proton, but  $\sim 70\%$  for a gold nucleus (see Fig. 22, [121]).

**The mean scattering amplitude:** An alternative way of assessing the typical values of the scattering amplitude is to calculate its expectation value weighted by the cross section



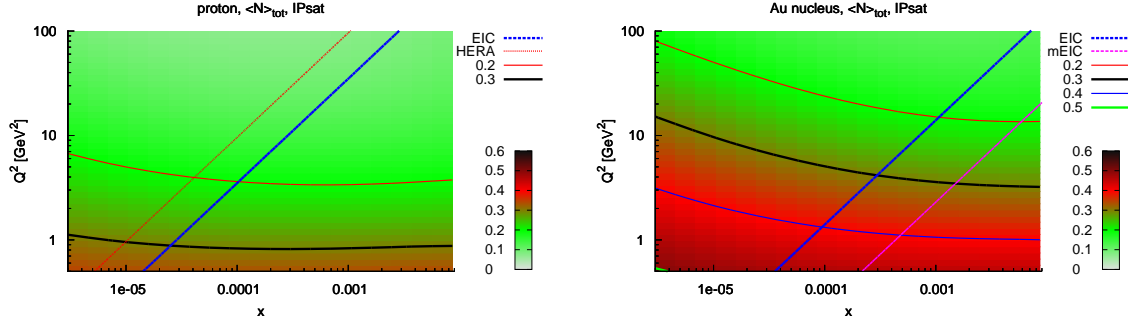


Figure 24. The mean scattering amplitude  $\langle \mathcal{N} \rangle_{\text{tot}}$  for the total cross section for a proton (left) and a gold nucleus (right) with the bCGC parametrization.

of a particular process. We thus define the mean scattering amplitude as

$$\langle \mathcal{N} \rangle_{T,L} = \frac{\int d^2 \mathbf{r}_T \int_0^1 dz \left| \Psi_{L,T}^{\gamma*} \right|^2 \int d^2 \mathbf{b}_T \mathcal{N}^2(x, \mathbf{b}_T, \mathbf{r}_T)}{\int d^2 \mathbf{r}_T \int_0^1 dz \left| \Psi_{L,T}^{\gamma*} \right|^2 \int d^2 \mathbf{b}_T \mathcal{N}(x, \mathbf{b}_T, \mathbf{r}_T)}. \quad (39)$$

This will yield a value between 0 and 1 for all points in the  $Q^2, x$ -plane. Note that although in principle  $\langle \mathcal{N} \rangle$  varies between 0 and 1, the maximal value for a Gaussian  $\mathbf{b}_T$ -distribution, which describes the proton very well, is only 1/2. The longitudinal and transverse structure functions probe a slightly different distribution of dipole sizes  $r$ , with the longitudinal structure function showing a stronger  $Q^2$ -dependence. The same quantities can easily be computed also for charm quarks only.

Figure 23 shows the mean scattering amplitude probed in the longitudinal total cross section in a proton and a gold nucleus in the IPsat model. The characteristic feature of the eikonalized DGLAP-evolved gluon distribution in this parametrization is the fact that the  $x$ -dependence becomes faster at higher energies. The same quantity for the bCGC cross section is plotted in Figure 23. Here one sees the characteristic constant energy dependence  $Q_s^2 \sim x^{-\lambda}$  in the bCGC parametrization leading to straight lines of constant  $\mathcal{N}$  in a log-log plot. The amplitude weighted by the total cross section is shown in Fig. 24 for the IPsat parametrization. It shows a slower  $Q^2$ -dependence than the longitudinal one, connected with the well-known fact that the longitudinal structure function is more sensitive to higher-twist effects than the total one.

In all plots for protons we have shown the kinematical limits for HERA and the EIC (325 GeV proton on 30 GeV electron with  $y < 0.9$ ) and in the nucleus plots for the EIC (130A GeV nucleus on 30 GeV electron with  $y < 0.9$ ) and lower energy mEIC option (130A GeV nucleus on 5 GeV electron with  $y < 0.9$ ). The comparison between nuclei and protons is striking. In the IPsat parametrization, as is typical of DGLAP evolution, the energy dependence at the initial small  $Q^2$ -scale is very slow. Thus the lower energy of the EIC compared to HERA would be insignificant in face of the effect of using nuclei. A value of  $\langle \mathcal{N} \rangle_{\text{tot}}$  of 0.3 could, for example, be reached at  $Q^2 = 4 \text{ GeV}^2$  at the EIC vs.  $Q^2 = 1 \text{ GeV}^2$  at HERA; much more safely in the weak coupling regime. With nuclei the EIC could, at  $Q^2 = 1 \text{ GeV}^2$ , reach values of  $\langle \mathcal{N} \rangle_L \approx 0.5$  that are simply inaccessible in an ep collider at practically any energy for an approximately Gaussian proton profile.

*Acknowledgments:* M. Diehl came up with the idea of visualizing the strength of the non-linear effects in the way presented here.

### 2.2.3 Nuclear PDFs and deviations from DGLAP evolution

*Alberto Accardi, Vadim Guzey and Juan Rojo*

Two of the main physics goals of the future EIC will be to accurately measure nuclear modifications of gluons and quarks as well as the possible onset of non-linear QCD dynamics in heavy nuclei. In this contribution we present a preliminary analysis which aims at determining the potential of the EIC to measure gluon shadowing and anti-shadowing and its sensitivity to saturation dynamics.

The input for this analysis is the EIC pseudo data for the inclusive DIS cross section in two scenarios, a medium energy EIC ( $\sqrt{s} = 12, 17, 24, 32, 44$  GeV, denoted by stage I) and a full energy EIC ( $\sqrt{s} = 63, 88, 124$  GeV, stage II), with  $0.004 < y < 0.8$  in either case. The kinematic coverage is summarized in Fig. 25. The pseudo-data was generated starting from  $e + p$  and  $e + n$  cross sections computed using the central values of the NNPDF2.0 parton distributions [123]. An integrated luminosity of  $4 \text{ fb}^{-1}$  was assumed for all energies, and the pseudo-data has been corrected for the expected statistical fluctuations. For most of the  $x$  range the resulting statistical errors are negligible compared to the assumed 2% systematic error. Nuclear effects have been included in a  $K$ -factor approximation, so that the longitudinal and transverse cross sections in Lead ( $^{208}\text{Pb}$ ) can be expressed in terms of the proton cross sections as

$$\sigma_{T,L}^{\text{Pb}}(x, Q^2, y) = K_{T,L}^{\lambda}(x, Q^2, y) \sigma_{T,L}^{\text{p}}(x, Q^2, y) , \quad (40)$$

where the label  $\lambda$  sets the intensity of the assumed saturation effects, and  $\lambda = 1$  corresponds to the nominal saturation in the IP Non-sat model [117]. In particular, the  $K$ -factor in Eq. (40) is given by the following piece-wise expression. For small  $x$ ,  $x \leq 0.01$ ,

$$K_{T,L}^{\lambda} = \frac{2}{\langle \sigma_{q\bar{q}} \rangle_{T,L}} \int d^2b \left\langle \left( 1 - e^{-\lambda \frac{1}{2} A \sigma_{q\bar{q}} T_A(b)} \right) \right\rangle_{T,L} , \quad (41)$$

where  $\sigma_{q\bar{q}}$  is the dipole cross section in the IP Non-sat model (we assume for simplicity that in the EIC kinematic range there is no saturation at the proton level, and search for the nuclear medium-induced saturation);  $T_A(b) = \int dz \rho_A(b, z)$ , where  $\rho_A(b, z)$  is the nuclear density normalized to unity; the brackets  $\langle \dots \rangle_{T,L}$  stand for the integration with the wave function squared of a virtual photon with transverse or longitudinal polarization, respectively. In the  $0.01 \leq x \leq 0.1$  interval, we assume that  $K_{T,L}^{\lambda}$  increases linearly from the value given by Eq. (41) at  $x = 0.01$  up to  $K_{T,L}^{\lambda} = 1$  at  $x = 0.1$ . For  $x > 0.1$ , we assumed that  $K_{T,L}^{\lambda}$  is equal to the ratio of the nuclear to free nucleon structure functions,  $F_{2A}(x, Q^2)/[AF_{2N}(x, Q^2)]$ , which is given by the leading-order parameterization of Ref. [124]

Nuclear parton distributions are then determined by a Next-to-Leading Order QCD fit of the pseudo-data within the NNPDF framework [10, 123]. The kinematic cuts used to ensure the validity of DGLAP evolution are  $Q^2 \geq 2 \text{ GeV}^2$  and  $W^2 \geq 12.5 \text{ GeV}^2$ . In this preliminary study, we consider pseudo-data for Pb targets only, and postpone discussion of the dependence of the nuclear PDFs on  $A$  to a future investigation. In the collinear factorization approximation, Lead structure functions are related to Lead parton distributions

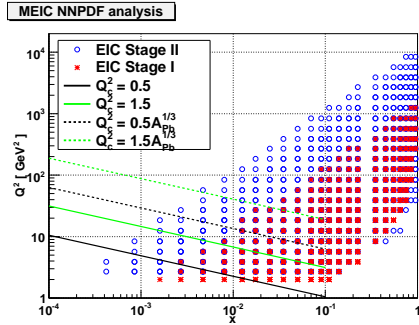


Figure 25. Kinematical coverage of the pseudo-data included in the NNPDF analysis of the EIC Pb cross sections, both for stage I and for stage II. Possible kinematical cuts relevant to study the onset of non-linear phenomena are also shown.

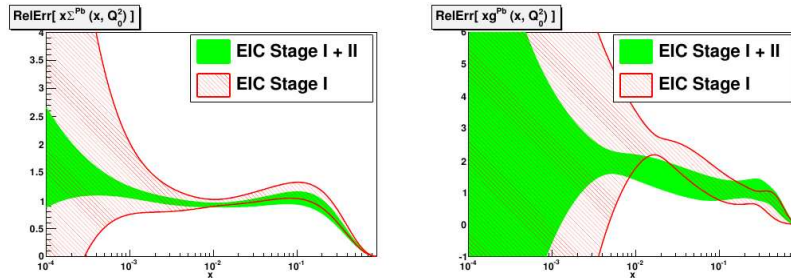


Figure 26. The quark singlet (left plot) and the gluon PDFs in Lead (right plot) at the initial evolution scale  $Q_0^2 = 2 \text{ GeV}^2$ , for stage I and stage I+II.

in the same way as in the proton case (see Section 3.1.4 and Ref. [125]). We also assumed for simplicity the Lead nucleus to be isoscalar, so that the structure functions depend only on three independent nuclear PDFs: the singlet quark PDF,  $\Sigma^{\text{Pb}}(x, Q^2)$ , the gluon PDF  $g^{\text{Pb}}(x, Q^2)$ , and the strange PDF; the latter was furthermore set to be a fixed fraction of the singlet PDF.

Now we discuss some preliminary results of the nuclear PDF fits. We show in Fig. 26 the singlet and the gluon Lead PDFs at the initial scale  $Q^2 = 2 \text{ GeV}^2$  obtained using only stage I data, and then adding the stage II data. To illustrate the accuracy that the EIC can reach in the determination of nuclear PDFs we show in Fig. 27 their relative uncertainties alongside those of the proton's NNPDF2.0 [123] combined with those of the EPS09 nuclear modifications [126] for  $^{208}\text{Pb}$ , which allows a comparison of the relative error bands. Since the restrictive EPS09 parametrization may underestimate the nuclear uncertainties outside the region where data is presently available, notably at  $x \lesssim 0.01$ , we added the relative NNPDF2.0 and EPS09 relative uncertainties linearly for a conservative estimate of the total uncertainty.

The measurement of the nuclear modifications of the gluon are one of the most important measurements at the EIC, since this quantity is essentially unknown from present data. Inclusive cross sections are sensitive to the gluon both via scaling violations and to a lesser extent thorough the longitudinal structure function, accessed through the proposed  $\sqrt{s} = 12 - 124 \text{ GeV}$  energy scan. From Fig. 26 we see that one can determine with a reasonable accuracy the gluon shadowing down to  $x \sim 10^{-3}$  in stage II and down to  $x \sim 10^{-2}$  in stage I. The better capabilities of stage II stem both from its greater lever arm in  $Q^2$  and its coverage of smaller values of  $x$ , see Fig. 25. In particular, the precision of the lead gluon in Stage II at small  $x$  is comparable to estimates from global proton fits. On top of this, at the EIC it will be possible to study gluon anti-shadowing, EMC and Fermi motion effects with much better accuracy than afforded by current global nuclear fits (see Sections 3.1.4

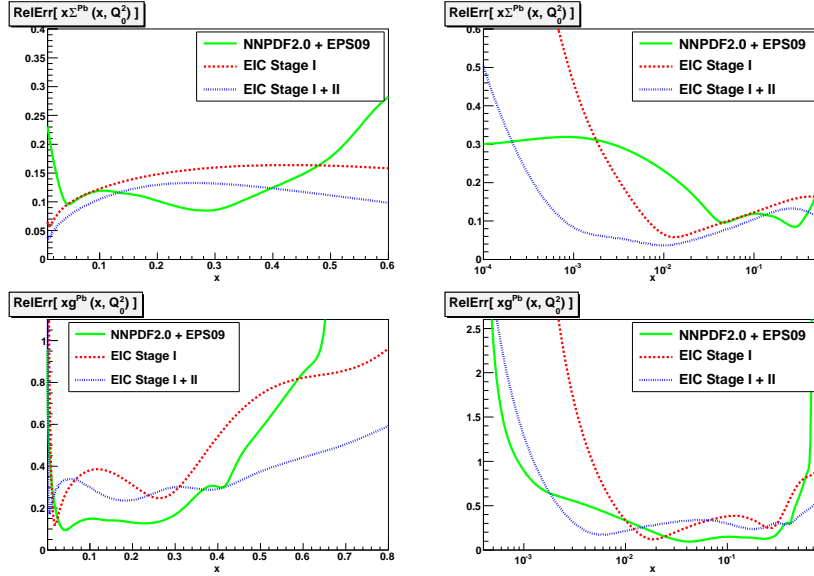


Figure 27. The relative uncertainty in the quark singlet (two upper panels) and the gluon PDFs in Lead (two lower panels) at the initial evolution scale  $Q_0^2 = 2 \text{ GeV}^2$ , with stage I and stage I+II data. Results are shown on linear (left plot) and logarithmic (right plot) scales. For reference, the analogous results for the Lead PDFs using NNPDF2.0+EPS09 parametrizations are also shown.

and 3.1.5. We can also see that EIC will measure accurately the sea quark shadowing, and that nuclear modifications of light quarks at large  $x$  could be measured a precision similar or even better than for the proton case.

The presented analysis was based on the validity of collinear factorization for nuclei, and the validity of linear DGLAP evolution in  $Q^2$ . However, at small enough  $x$  and  $Q^2$ , deviations from linear fixed order DGLAP evolution are expected to appear, e.g., due to small- $x$  re-summation effects [127] or gluon saturation, see Section 2.1.3. In heavy nuclei, the effects due to gluon saturation are boosted to higher  $Q^2$  and  $x$  by the atomic number; one then has the possibility of experimentally separating small- $x$  and saturation effects, which is not possible with HERA  $e + p$  data.

In Refs. [9, 128] a general strategy was presented to quantify potential deviations from NLO DGLAP evolution, which was then applied to proton HERA data. In a global PDF fit, deviations from DGLAP in the data can be hidden in a distortion of parton distributions; however, these can be singled out by determining undistorted PDF from data in regions where such effects are expected to be small. More in detail, one can fit PDFs using data at large  $x$  and  $Q^2$ , where DGLAP is likely to hold with high accuracy, and then evolving them down in the  $Q^2$  region where deviations are expected to arise. DGLAP deviations can then be quantitatively determined by comparing calculations to data in this region, which were not used in the PDF determination.

This approach can be applied as well to the nuclear case. From simple theoretical arguments about the energy and  $A$  dependence of the saturation scale (see Section 2.1.3), we expect deviations from linear evolution to appear when  $Q^2 \lesssim \bar{Q}^2 (A\bar{x}/x)^{\frac{1}{3}}$ , where  $\bar{x}$  is a reference value, say  $\bar{x} = 10^{-3}$ , and  $\bar{Q}^2$  is the scale where DGLAP evolution at  $\bar{x}$  would be broken in the proton. Note however that the  $A$ -dependence of the saturation scale may in fact be tamed by the leading twist nuclear shadowing, see Section 2.1.6. While saturation

models may give an indication of the value of  $\bar{Q}^2$ , we wish to determine this scale in a model independent way as the scale at which deviations from DGLAP evolution can be detected from EIC nuclear target (pseudo-)data. The unsafe region for DGLAP evolution can also be written as  $Q^2 \lesssim Q_c^2 x^{-\frac{1}{3}}$  with  $Q_c^2$  some constant setting the strength of the deviations from DGLAP. In Refs.[9, 128] the range  $Q_c^2 \in [0.5, 1.5]$  GeV<sup>2</sup> was considered for the proton case; in the nuclear case this range should be rescaled by a factor  $A_{\text{Pb}}^{1/3} \approx 6$ . Typical values of these kinematical cuts for the Lead nucleus are shown in Fig. 25.

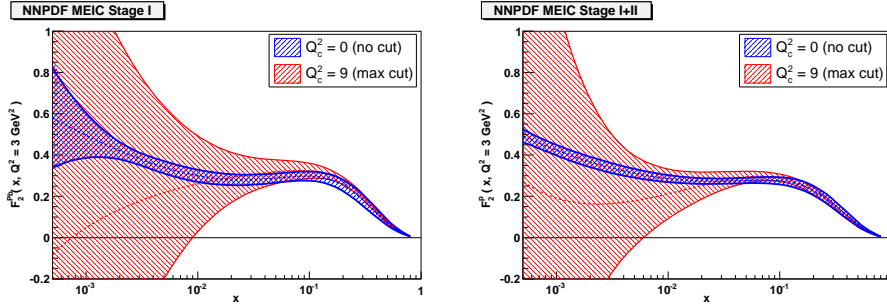


Figure 28. The Lead structure function  $F_2^{\text{Pb}}(x, Q^2)$  at  $Q^2 = 3$  GeV<sup>2</sup> from the analysis of the EIC stage I (left plot) and stage I+II (right plot) simulated data with  $\lambda = 1$ , without kinematical cuts and with cuts using  $Q_c^2 = 1.5A_{\text{Pb}}^{1/3} \sim 9$ .

We show in Fig. 28 a representative result of the fits to the EIC pseudo-data after applying the cut with  $\bar{Q}^2 = 1.5A_{\text{Pb}}^{1/3} \sim 9$ , compared to the reference uncut fits to stages I and I+II pseudo-data with  $\lambda = 1$ . As expected when data is removed the uncertainties in the physical observables become much larger, but one can still see a systematic downwards shift in the central value, which is the signature of the departure from linear evolution [9, 128]. Note that this signal is already apparent with stage I data only, although its statistical significance might be marginal.

We plan to systematically explore the sensitivity of the EIC to non-linear dynamics using this technique, by optimizing the kinematical cuts for different values of the saturation scale used to generate the pseudo-data, exploit the interplay between the  $F_2^{\text{Pb}}$  and  $F_L^{\text{Pb}}$  structure functions, and quantitatively measuring the statistical significance of the signal. This will determine in a fairly model-independent way the smallest saturation scale that can be detected at the EIC in either stage I or stage II.

*Acknowledgments:* We thank F. Caola, R. Ent, S. Forte and L. Zhu for discussions and collaboration.

## 2.2.4 Constraining the nuclear gluon distribution using inclusive observables

*Victor P. Gonçalves*

Since the early days of the parton model and of the first deep inelastic scattering (DIS) experiments, determining the precise form of the gluon distribution of the nucleon has been a major goal of high energy hadron physics. Over the last 30 years enormous progress has been achieved. In particular, data from HERA allowed for a good determination of the gluon density of the proton. A much harder task has been to determine the gluon distribution of nucleons bound in a nucleus, i.e., the nuclear gluon distribution ( $xg^A(x, Q^2)$ ). In

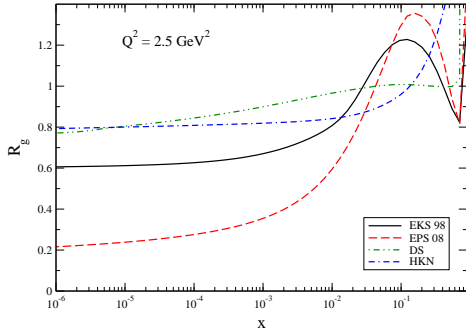


Figure 29. Ratio  $R_g = xg^A/A.xg^N$  predicted by the EKS, DS, HKN and EPS parametrizations for  $A = 208$  and  $Q^2 = 2.5 \text{ GeV}^2$ .

past years several experiments have been dedicated to high precision measurements of deep inelastic lepton scattering (DIS) off nuclei. The data, taken over a wide kinematic range  $10^{-5} \leq x \leq 0.1$  and  $0.05 \text{ GeV}^2 \leq Q^2 \leq 100 \text{ GeV}^2$ , show a systematic reduction of the nuclear structure function  $F_2^A(x, Q^2)/A$  with respect to the free nucleon structure function  $F_2^N(x, Q^2)$ . This phenomenon is known as *nuclear shadowing effect* and is associated to the modification of the target parton distributions so that  $xq^A(x, Q^2) < Axq^N(x, Q^2)$ , as expected from a superposition of  $ep$  interactions. The modifications depend on the parton momentum fraction: for momentum fractions  $x < 0.1$  (shadowing region) and  $0.3 < x < 0.7$  (EMC region), a depletion is observed in the nuclear structure functions. These two regions are bridged by an enhancement known as antishadowing for  $0.1 < x < 0.3$ . The experimental data for the nuclear structure function determine the behaviour of the nuclear quark distributions, while the behaviour of the nuclear gluon distribution is indirectly determined using the momentum sum rule as a constraint and/or studying the  $\log Q^2$  slope of the ratio  $F_2^{Sn}/F_2^C$ . Currently, the behaviour of  $xg^A(x, Q^2)$  at small  $x$  (high energy) is completely uncertain as shown in Fig. 29, where we present the ratio  $R_g = xg^A/(A.xg^N)$ , for  $A = 208$ , predicted by four different groups which realize a global analysis of the nuclear experimental data using the DGLAP evolution equations in order to determine the parton densities in nuclei. In particular, the magnitude of shadowing and the presence or not of the antishadowing effect is completely undefined. It is expected that measurements over the extended  $x$  and  $Q^2$  ranges, which would become possible in a future  $eA$  collider, will give more information in order to discriminate between the distinct models of shadowing and the understanding of the QCD dynamics at small  $x$ . This collider is expected to have statistics high enough to allow for the determination of several inclusive and exclusive observables which are directly dependent on the behaviour of the nuclear gluon distribution, as for example, the longitudinal and charm structure functions, the logarithmic slopes with respect to  $x$  and  $Q^2$ , as well as the diffractive lepton production of vector mesons. In particular, the longitudinal structure function is expected to be measured for the first time in the kinematical regime of small  $x$ , since the electron - ion collider will be able to vary the energies of both the electron and ion beams.

In this contribution we study the behaviour of the nuclear longitudinal structure function  $F_L^A$  and the charm structure function  $F_2^{c,A}$  and analyse the possibility to constrain the nuclear effects present in  $xg^A$  using these inclusive observables (For more details and references see Ref. [129]).

**$F_L^A$  and  $F_2^{c,A}$  in the collinear formalism:** The longitudinal structure function in deep inelastic scattering is one of the observables from which the gluon distribution can be unfolded. In the collinear formalism,  $F_L$  is described in terms of the Altarelli-Martinelli

equation

$$F_L(x, Q^2) = \frac{\alpha_s(Q^2)}{2\pi} x^2 \int_x^1 \frac{dy}{y^3} \left[ \frac{8}{3} F_2(y, Q^2) + 4 \sum_q e_q^2 \left(1 - \frac{x}{y}\right) y g(y, Q^2) \right]. \quad (42)$$

At small  $x$  the second term with the gluon distribution is the dominant one. This expression can be reasonably approximated by  $F_L(x, Q^2) \approx 0.3 \frac{4\alpha_s}{3\pi} x g(2.5x, Q^2)$ , which demonstrates the close relation between the longitudinal structure function and the gluon distribution. Therefore, we expect the longitudinal structure function to be sensitive to nuclear effects.

In order to estimate the charm contribution to the structure function we treat the charm quark as a heavy quark and estimate its contribution by fixed-order perturbation theory. This involves the computation of the boson-gluon fusion process. A  $c\bar{c}$  pair can be created by boson-gluon fusion when the squared invariant mass of the hadronic final state is  $W^2 \geq 4m_c^2$ . Since  $W^2 = \frac{Q^2(1-x)}{x} + M_N^2$ , where  $M_N$  is the nucleon mass, the charm production can occur well below the  $Q^2$  threshold,  $Q^2 \approx 4m_c^2$ , at small  $x$ . The charm contribution to the proton/nucleus structure function, in leading order (LO), is given by

$$\frac{1}{x} F_2^c(x, Q^2, m_c^2) = 2e_c^2 \frac{\alpha_s(\mu'^2)}{2\pi} \int_{ax}^1 \frac{dy}{y} C_{g,2}^c\left(\frac{x}{y}, \frac{m_c^2}{Q^2}\right) g(y, \mu'^2), \quad (43)$$

where  $a = 1 + \frac{4m_c^2}{Q^2}$  and the factorization scale  $\mu'$  is assumed  $\mu'^2 = 4m_c^2$ .  $C_{g,2}^c$  is the coefficient function given by

$$\begin{aligned} C_{g,2}^c\left(z, \frac{m_c^2}{Q^2}\right) &= \frac{1}{2} \left\{ [z^2 + (1-z)^2 + z(1-3z) \frac{4m_c^2}{Q^2} - z^2 \frac{8m_c^4}{Q^4}] \ln \frac{1+\beta}{1-\beta} \right. \\ &\quad \left. + \beta [-1 + 8z(1-z) - z(1-z) \frac{4m_c^2}{Q^2}] \right\}, \end{aligned} \quad (44)$$

where  $\beta = 1 - \frac{4m_c^2 z}{Q^2(1-z)}$  is the velocity of one of the charm quarks in the boson-gluon center-of-mass frame. Therefore, in leading order,  $\mathcal{O}(\alpha_s)$ ,  $F_2^c$  is directly sensitive only to the gluon density via the well-known Bethe-Heitler process  $\gamma^* g \rightarrow c\bar{c}$ . The dominant uncertainty in the QCD calculations arises from the uncertainty in the charm quark mass. In this contribution we assume  $m_c = 1.5 \text{ GeV}$ .

**The nuclear ratios:** Lets now study the behaviour of the nuclear longitudinal structure function  $F_L^A$  and the charm structure function  $F_2^{c,A}$  and analyze the possibility to constrain the nuclear effects present in  $xg^A$  using these inclusive observables. We estimate the normalized ratios

$$R_L(x, Q^2) = \frac{F_L^A(x, Q^2)}{A F_L^p(x, Q^2)} \quad \text{and} \quad R_C(x, Q^2) = \frac{F_2^{c,A}(x, Q^2)}{A F_2^{c,p}(x, Q^2)} \quad (45)$$

considering four distinct parametrizations for the nuclear gluon distributions and compare their behaviour with those predicted for the ratio  $R_g = xg^A/A.xg^N$ .

In Fig. 30 we present our results. Firstly, let us discuss the small- $x$  region,  $x \leq 10^{-3}$ , determined by shadowing effects. We observe that  $R_L$  practically coincides with  $R_g$  for all parametrizations and for the two values of  $Q^2$  considered. This suggests that shadowing effects can be easily constrained in an  $eA$  collider by measuring  $F_L$ . This conclusion is, to a good extent, model independent. On the other hand, the ratio  $R_C$  gives us an upper bound

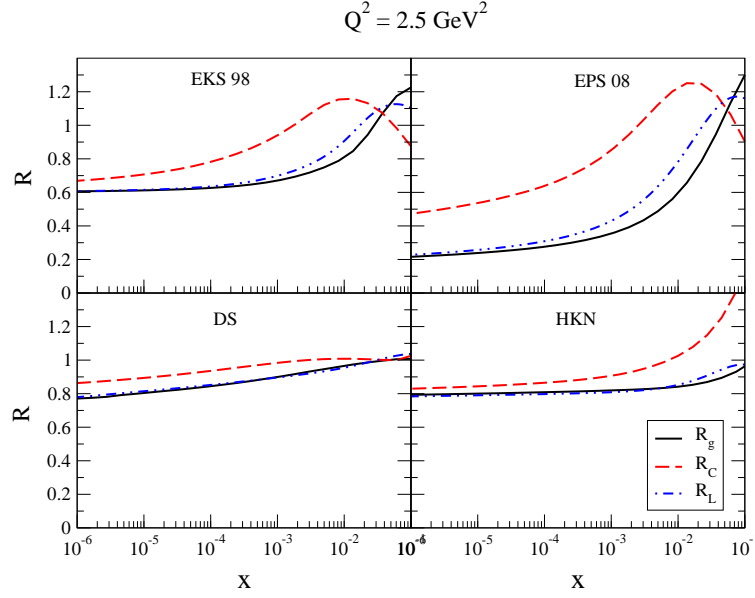


Figure 30. Ratios  $R_g$ ,  $R_C$  and  $R_L$  for the four considered nuclear parametrizations,  $Q^2 = 2.5 \text{ GeV}^2$  and  $A = 208$ .

for the magnitude of the shadowing effects. For example, if it is found that  $R_C$  is equal to  $\approx 0.6$  at  $x = 10^{-4}$  and  $Q^2 = 2.5 \text{ GeV}^2$  the nuclear gluon distributions from DS and HKN parametrizations are very large and should be modified. Considering now the kinematical range of  $x > 10^{-3}$  we can analyse the correlation between the behaviour of  $R_L$  and  $R_C$  and the antishadowing present or not in the nuclear gluon distribution. Similarly to observed at small values of  $x$ , the behaviour of  $R_L$  is very close to the  $R_g$  one in the large- $x$  range. In particular, the presence of antishadowing in  $xg^A$  directly implies an enhancement in  $F_L^A$ . It is almost 10% smaller in magnitude that the enhancement predicted for  $xg^A$  by the EKS and EPS parametrizations. Inversely, if we assume the non-existence of the antishadowing in the nuclear gluon distribution at  $x < 10^{-1}$ , as in the DS and HKN parametrizations, no enhancement will be present in  $F_L^A$  in this kinematical region. Therefore, it suggests that also the antishadowing effects can be easily constrained in an  $eA$  collider measuring  $F_L$ . On the other hand, in this kinematical range the behavior of  $R_C$  is distinct of  $R_g$  at a same  $x$ . However, we observe that the behavior of  $R_C$  at  $x = 10^{-2}$  is directly associated to  $R_g$  at  $x = 10^{-1}$ . In other words, the antishadowing is shifted in  $R_C$  by approximately one order of magnitude in  $x$ . For example, the large growth of  $R_g$  predicted by the HKN parametrization at  $x \geq 10^{-1}$  shown in Fig. 29 implies the steep behavior of  $R_C$  at  $x \geq 10^{-2}$  observed in Fig. 30. Consequently, by measuring  $F_2^c$  it is also possible to constrain the existence and magnitude of the antishadowing effects.

*Acknowledgments:* The author thank E.R. Cazaroto, F. Carvalho, and F.S. Navarra for collaboration.

### 2.2.5 DIS in the high-energy limit at next-to-leading order

Giovanni A. Chirilli

Nowadays it is widely accepted, that non-linear dynamics effects dominate deep inelastic



lepton hadrons scattering processes (DIS) at very high-energy (Regge limit), and non-linear equations have been derived in order to describe the evolution of the structure of hadronic matter at this regime. One of these equations is the Balitsky-Kovchegov equation (BK) derived by Balitsky [62] in the Wilson lines formalism, and by Kovchegov [33, 39] in the dipole frame. The Wilson line formalism is an operator language based on the concept of factorization of the scattering amplitude in rapidity space and on the extension of the application of the Operator Product Expansion (OPE) formalism to high-energy (Regge limit). So far the OPE formalism was known only in the Bjorken limit as an expansion in terms of local operators or in terms of light ray operators.

The relevance of the BK equation for future experiments like Electron Ion Collider (EIC) or Large electron Hadron Collider (LeHC) can be determined by the running of the coupling constant and the evolution kernel at the next-leading-order (NLO) approximation (NLO corrections in power of the strong coupling constant  $\alpha_s$ ). The argument of the coupling constant has been obtained by the authors of ref. [130, 131] where only the quark contribution has been calculated explicitly, while the gluonic part was obtained conjecturing that its contribution would follow the same pattern of the quark contribution. However, this result did not fully solve the problem of the argument of the running coupling constant due to an ambiguity of one term which is not proportional to  $b = \frac{11}{3}N_c - \frac{2}{3}n_f$ . The complete results of the NLO-BK kernel including the gluon contribution to the argument of the coupling constant has been obtained in [132] where it was shown that the result agrees with the NLO Balitsky-Fadin-Kuraev-Lipatov (BFKL) kernel. The BFKL equation [13, 133] can be obtained from the BK equation by dropping out the non linear terms. Indeed, a caveat of such linear evolution equation is the violation at very high energy of the unitarity condition which is instead preserved by the BK equation.

Conformal symmetry is a symmetry violated in QCD by the running of the coupling constant. What one would then expect from the calculation of the NLO BK-kernel is that the only source of violation of such symmetry come from the running of coupling while the rest of the kernel preserve conformal (Möbius) symmetry. However, although Wilson lines are formally conformal invariant, at one loop correction they are rapidity-divergent, and since it is not known how to regulate them in a conformal invariant way, the NLO-BK kernel contains non-conformal terms (besides to the running coupling constant) as remnant of the prescription used to cure such divergences. In order to study the source of the loss of conformal invariance it is convenient to consider a conformal invariant theory like the  $\mathcal{N}=4$  super-symmetric Yang-Mills (SYM) theory. The NLO evolution kernel obtained in this framework is also not conformal invariant[134] contrary to what one would expect from a conformal field theory. It was then shown in [134], that suitable operators for the description of processes at high-energy (Regge) theory are composite conformal (Wilson line) operators constructed order by order in perturbation theory. These operators absorb the undesired non conformal terms in the same way as counterterms are added to renormalize local composite operators in order to restore the symmetry that the bare operator lost at the level of NLO (and higher) corrections. Indeed, the NLO evolution of such composite conformal operator in QCD resolve in a running coupling part and in a conformal invariant part. In ref. [134, 135] the conformal expression for the NLO BFKL has been obtained for the first time.

In order to obtain the full NLO amplitude for DIS at High energy, one needs to calculate the coefficient function (photon impact factor) at NLO and convolute it with the NLO evolution kernel of the relative operator (the NLO BK kernel). The NLO impact factor has been calculated in ref. [136] where an analytic expression (in coordinate space) has been

obtained for the first time.

**High-energy operator product expansion:** In the usual OPE, due to the presence of two different scales of the transverse momentum  $k_\perp$ , one introduces a factorization scale, usually denoted by  $\mu$ , which factorizes the amplitude of DIS processes in perturbatively calculable contributions (hard part) and in non-perturbatively calculable ones (soft part) represented by matrix elements made of light-ray operators. The evolution of such matrix elements with respect to the renormalization point  $\mu$  is the DGLAP evolution equation.

At high-energy (Regge limit) all the transverse momenta are of the same order of magnitude therefore, a suitable factorization scale would be the rapidity scale: one introduces the rapidity  $\eta$  which separates "fast" fields from "slow" fields. Thus, the amplitude of the process can be represented as a convolution of contributions coming from fields with rapidity  $\eta < Y$  (fast fields) and contributions coming from fields with rapidity  $\eta > Y$  (slow fields). As in the case of the usual OPE, the integration over the fields with rapidity  $\eta < Y$  gives us the coefficient functions while the integrations over fields with rapidity  $\eta > Y$  are the matrix elements of the operators. A general feature of high-energy scattering is that a fast particle moves along its straight-line classical trajectory and the only quantum effect is the eikonal phase factor acquired along this propagation path. In QCD, for the fast quark or gluon scattering off some target, this eikonal phase factor is a Wilson line - an infinite gauge link ordered along the straight line collinear to the particle's velocity  $n^\mu$ :

$$U^\eta(x_\perp) = \text{Pexp} \left\{ ig \int_{-\infty}^{\infty} du \, n_\mu A^\mu(un + x_\perp) \right\}, \quad (46)$$

Here,  $A_\mu$  is the gluon field of the target,  $x_\perp$  is the transverse position of the particle which remains unchanged throughout the collision, and the index  $\eta$  labels the rapidity of the particle. Repeating the above argument for the target (moving fast in the spectator's frame) we see that particles with very different rapidity perceive each other as Wilson lines and therefore Wilson-line operators are the convenient effective degrees of freedom in high-energy QCD (for a review, see Ref. [137]). The expansion of the T product of two electromagnetic currents at high-energy (Regge limit) is then in terms of Wilson lines

$$\begin{aligned} T\{\hat{j}_\mu(x)\hat{j}_\nu(y)\} &= \int d^2z_1 d^2z_2 I_{\mu\nu}^{\text{LO}}(x, y; z_1, z_2) \hat{\mathcal{U}}(z_1, z_2) \\ &+ \int d^2z_1 d^2z_2 d^2z_3 I_{\mu\nu}^{\text{NLO}}(x, y; z_1, z_2, z_3) [\hat{\mathcal{U}}(z_1, z_3) + \hat{\mathcal{U}}(z_2, z_3) - \hat{\mathcal{U}}(z_1, z_2) - \hat{\mathcal{U}}(z_1, z_3)\hat{\mathcal{U}}(z_3, z_2)] \end{aligned}$$

where

$$\hat{\mathcal{U}}^\eta(x_\perp, y_\perp) = 1 - \frac{1}{N_c} \text{Tr} \{ \hat{U}^\eta(x_\perp) \hat{U}^{\dagger\eta}(y_\perp) \} \quad (47)$$

The evolution of the Wilson line operator in eq. (47) is given by the BK equation [33, 39, 62]

$$\begin{aligned} \frac{d}{d\eta} \hat{\mathcal{U}}(x, y) &= \frac{\alpha_s N_c}{2\pi^2} \int d^2z \frac{(x-y)^2}{(x-z)^2(z-y)^2} [\hat{\mathcal{U}}(x, z) + \hat{\mathcal{U}}(y, z) \\ &\quad - \hat{\mathcal{U}}(x, y) - \hat{\mathcal{U}}(x, z)\hat{\mathcal{U}}(z, y)] \end{aligned} \quad (48)$$

The first three terms correspond to the linear BFKL evolution equation [13, 133] and describe the partons emission while the last term is responsible for the partons annihilation. For sufficiently low  $x_B$  the partons emission balances the partons annihilation so the partons reach the state of saturation [34, 138, 139] with the characteristic transverse momentum  $Q_s$

growing with energy  $1/x_B$ . The NLO evolution equation for composite Wilson line operator (preserving conformal invariance as explained in the introduction) has been calculated in [132], where one can find the full analytic expression

In order to obtain the DIS amplitude at high-energy at the NLO we now need the coefficient function ("impact factor") at next to leading order. Here, we present the NLO impact factor (IF) for the study of DIS in the linearized case (two gluon approximation) where the NLO BK equation reduces to the NLO BFKL equation. In this case the OPE at high energy for DIS reduces to

$$\begin{aligned} & \frac{1}{N_c}(x-y)^4 T\{\bar{\psi}(x)\gamma^\mu\hat{\psi}(x)\bar{\psi}(y)\gamma^\nu\hat{\psi}(y)\} \\ &= \frac{\partial\kappa^\alpha}{\partial x^\mu}\frac{\partial\kappa^\beta}{\partial y^\nu}\int\frac{dz_1dz_2}{z_{12}^4}\hat{\mathcal{U}}_{a_0}(z_1,z_2)[\mathcal{I}_{\alpha\beta}^{\text{LO}}(1+\frac{\alpha_s}{\pi})+\mathcal{I}_{\alpha\beta}^{\text{NLO}}] \end{aligned} \quad (49)$$

where

$$\mathcal{I}_{\text{LO}}^{\alpha\beta}(x,y;z_1,z_2) = \mathcal{R}^2 \frac{g^{\alpha\beta}(\zeta_1\cdot\zeta_2) - \zeta_1^\alpha\zeta_2^\beta - \zeta_2^\alpha\zeta_1^\beta}{\pi^6(\kappa\cdot\zeta_1)(\kappa\cdot\zeta_2)} \quad (50)$$

is the LO impact factor and where we used the notation  $\mathcal{R} \equiv \frac{\kappa^2(\zeta_1\cdot\zeta_2)}{2(\kappa\cdot\zeta_1)(\kappa\cdot\zeta_2)}$ , and the conformal vectors  $\kappa = \frac{\sqrt{s}}{2x_*}(\frac{p_1}{s} - x^2p_2 + x_\perp) - \frac{\sqrt{s}}{2y_*}(\frac{p_1}{s} - y^2p_2 + y_\perp)$ ,  $\zeta_i = (\frac{p_1}{s} + z_{i\perp}^2p_2 + z_{i\perp})$  with  $x_* = p_2^\mu x_\mu = \frac{\sqrt{2}}{s}x^+$  (s Mandelstam variable). The analytic expression of the NLO impact factor for DIS at high energies can be found in Ref. [136]. Note that the NLO IF is conformal (Möbius) invariant and is given by a linear combination of five conformal tensor structures as predicted in [140]. The next natural step would be the Fourier transformation of Eq. (??) which gives the momentum-space impact factor convenient for phenomenological applications (and available at present only as a combination of numerical and analytical expressions[141–143]).

**Conclusions:** We have briefly summarized the status of the NLO calculation of the structure function for DIS at high energy. The main ingredients for the full amplitude, namely the NLO BK kernel and the NLO IF, have been calculated. The main result of this analysis is that the OPE for high energy (Regge limit) is at the same status as the usual OPE in the Bjorken limit. This means that the factorization in rapidity did not break down at NLO accuracy. As an application of the factorization in rapidity, the full NLO analytic amplitude in  $\mathcal{N} = 4$  SYM was calculated, the NLO result for the Pomeron intercept at small  $\alpha_s$  was confirmed, and for the first time the NLO Pomeron residue was obtained [144].

The Wilson line formalism proved to be very successful not only in obtaining in more efficient way many results that in the usual perturbative QCD (pQCD) were obtained after many years of calculations by several groups, but also to obtain some results that have not been obtained (not for lack of efforts) in the usual pQCD, like the NLO IF, the NLO conformal BFKL kernel and the NLO pomeron residue, and in addition to generalize these results to include the non linear effects dominant at high energies. Another example which proves the efficiency of this formalism is the calculation, in a very easy way, of the triple pomeron vertex for diffractive and non-diffractive ("fan diagrams") processes, including the subleading  $N_c$  contributions [145].

*Acknowledgments:* The author is grateful to the organizer of the workshop, in particular to Markus Diehl and Raju Venugopalan, and to the INT institute for the warm hospitality.

### 2.2.6 Running Coupling in Small- $x$ Physics

*Yuri V. Kovchegov*

Running coupling corrections have been included into BFKL/BK/JIMWLK evolution following the Brodsky-Lepage-Mackenzie (BLM) scale-setting procedure [146] in [43, 130, 131, 147, 148]. The BLM prescription requires one to first re-sum the contribution of all quark bubble corrections giving powers of  $\alpha_\mu N_f$ , with  $N_f$  the number of quark flavors and  $\alpha_\mu$  the physical coupling at some arbitrary renormalization scale  $\mu$ . One then has to complete  $N_f$  to the full beta-function by replacing  $N_f \rightarrow -6\pi\beta_2$  in the obtained expression. Here  $\beta_2 = (11N_c - 2N_f)/(12\pi)$  is the one-loop QCD beta-function. After this, the powers of  $\alpha_\mu\beta_2$  should combine into physical running couplings  $\alpha_s(Q^2) = \alpha_\mu/(1 + \alpha_\mu\beta_2 \ln(Q^2/\mu^2))$  at various momentum scales  $Q$  which would follow from this calculation. The running coupling below will be written in the  $\overline{\text{MS}}$  renormalization scheme.

Below we will concentrate on the case of running coupling corrections to the BFKL and BK evolution equations. Running-coupling corrections to the JIMWLK equation can be found in [43, 131]. At the moment the running coupling corrections to BK have been better explored numerically than those for JIMWLK.

**Analytic result:** Let us briefly summarize the results of [43, 130, 131]. The Balitsky-Kovchegov evolution equation with the running coupling corrections included (rcBK) reads

$$\frac{\partial S(\underline{x}_0, \underline{x}_1; Y)}{\partial Y} = \mathcal{R}[S] - \mathcal{S}[S]. \quad (51)$$

Here we use the  $S$ -matrix notation, related to the forward dipole amplitude by  $S(\underline{x}_0, \underline{x}_1; Y) = 1 - N(\underline{x}_0, \underline{x}_1; Y)$ . The first term on the right hand side of Eq. (51) is referred to as the running coupling contribution, while the second term on the right hand side of Eq. (51) is referred to as the subtraction contribution. Separation into the two parts is arbitrary, and was done differently in [130] and [131], with the net sum being the same [43].

The running coupling part was calculated independently in [130] and in [131]: the results of those calculations are

$$\mathcal{R}^{\text{Bal}}[S] = \int d^2z \tilde{K}^{\text{Bal}}(\underline{x}_0, \underline{x}_1, \underline{z}) [S(\underline{x}_0, \underline{z}; Y) S(\underline{z}, \underline{x}_1; Y) - S(\underline{x}_0, \underline{x}_1; Y)] \quad (52)$$

$$\mathcal{R}^{\text{KW}}[S] = \int d^2z \tilde{K}^{\text{KW}}(\underline{x}_0, \underline{x}_1, \underline{z}) [S(\underline{x}_0, \underline{z}; Y) S(\underline{z}, \underline{x}_1; Y) - S(\underline{x}_0, \underline{x}_1; Y)]. \quad (53)$$

The integral kernels in the two cases are given by

$$\tilde{K}^{\text{Bal}}(\underline{r}, \underline{r}_1, \underline{r}_2) = \frac{N_c \alpha_s(r^2)}{2\pi^2} \left[ \frac{r^2}{r_1^2 r_2^2} + \frac{1}{r_1^2} \left( \frac{\alpha_s(r_1^2)}{\alpha_s(r_2^2)} - 1 \right) + \frac{1}{r_2^2} \left( \frac{\alpha_s(r_2^2)}{\alpha_s(r_1^2)} - 1 \right) \right] \quad (54)$$

as found in [130] and by

$$\tilde{K}^{\text{KW}}(\underline{r}, \underline{r}_1, \underline{r}_2) = \frac{N_c}{2\pi^2} \left[ \alpha_s(r_1^2) \frac{1}{r_1^2} - 2 \frac{\alpha_s(r_1^2) \alpha_s(r_2^2)}{\alpha_s(R^2)} \frac{\underline{r}_1 \cdot \underline{r}_2}{r_1^2 r_2^2} + \alpha_s(r_2^2) \frac{1}{r_2^2} \right], \quad (55)$$

as found in [131], where

$$R^2(\underline{r}, \underline{r}_1, \underline{r}_2) = r_1 r_2 \left( \frac{r_2}{r_1} \right)^{\frac{r_1^2 + r_2^2}{r_1^2 - r_2^2} - 2} \frac{r_1^2 r_2^2}{\underline{r}_1 \cdot \underline{r}_2} \frac{1}{r_1^2 - r_2^2}. \quad (56)$$

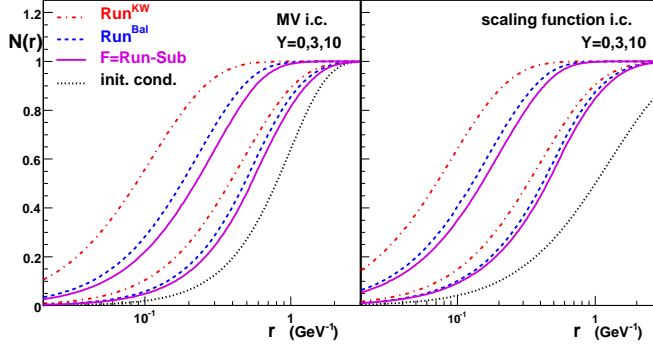


Figure 31. Solutions of the complete (all orders in  $\alpha_s \beta_2$ ) evolution equation given in Eq. (51) (solid lines), and of the equation with Balitsky's (dashed lines) and KW's (dashed-dotted) running coupling schemes at rapidities  $Y = 0, 5$  and  $10$ . Left plot uses quasi-classical McLerran-Venugopalan (MV) initial condition. The right plot employs the initial condition given by the dipole amplitude at rapidity  $Y = 35$  evolved using Balitsky's running coupling scheme and with  $r$ -dependence rescaled down such that  $Q_s = Q'_s = 1$  GeV.

One notices immediately that  $\mathcal{R}^{\text{Bal}}[S]$  calculated in [130] is different from  $\mathcal{R}^{\text{KW}}[S]$  calculated in [131] due to the difference in the kernels  $\tilde{K}^{\text{Bal}}$  and  $\tilde{K}^{\text{KW}}$  in Eqs. (54) and (55). However that does not imply disagreement between the calculations of [130] and [131]: after all, it is the full kernel on the right of Eq. (51),  $\mathcal{R}[S] - \mathcal{S}[S]$ , that needs to be compared. To do that one has to calculate the second term on the right hand side of Eq. (51) (the subtraction contribution). This was done in [43], yielding

$$\begin{aligned} \mathcal{S}[S] = & \alpha_\mu^2 \int d^2 z_1 d^2 z_2 K_{\textcircled{1}}(\underline{x}_0, \underline{x}_1; \underline{z}_1, \underline{z}_2) \\ & \times [S(\underline{x}_0, \underline{w}, Y) S(\underline{w}, \underline{x}_1, Y) - S(\underline{x}_0, \underline{z}_1, Y) S(\underline{z}_2, \underline{x}_1, Y)] \end{aligned} \quad (57)$$

and the re-summed BK kernel  $K_{\textcircled{1}}$  can be found in the original reference. Substituting  $\underline{w} = \underline{z}_1$  (or, equivalently,  $\underline{w} = \underline{z}_2$ ) in Eq. (57) yields the subtraction term  $\mathcal{S}^{\text{Bal}}[S]$ , which has to be subtracted from  $\mathcal{R}^{\text{Bal}}[S]$  calculated in [130] and given by Eq. (52) to obtain the complete evolution equation re-summing all orders of  $\alpha_s N_f$  in the kernel. Substituting  $\underline{w} = \underline{z} = \alpha \underline{z}_1 + (1 - \alpha) \underline{z}_2$  in Eq. (57) yields the term  $\mathcal{S}^{\text{KW}}[S]$ , which has to be subtracted from  $\mathcal{R}^{\text{KW}}[S]$  calculated in [131] and given in Eq. (53) again to obtain the complete evolution equation re-summing all orders of  $\alpha_s N_f$  in the kernel.

**Numerical Solution:** The numerical solution of the running-coupling BK (rcBK) evolution just presented was performed in [43] and plotted in Fig. 31. One plots the running-coupling parts from Eqs. (52) and (53) [130, 131] (dashed and dash-dotted lines correspondingly), along with the full solution (solid line). As one can see the full solution is best approximated by the Balitsky's running coupling scheme from Eq. (52) [130]. Hence in most phenomenological applications one simply solves rcBK with Balitsky's prescription [113, 149]. Note that the rcBK solution also exhibits the property of geometric scaling [44], as was shown in [43].

**Running-coupling BFKL evolution:** Running-coupling BFKL equation (rcBFKL) was

constructed in [148] and reads

$$\frac{\partial \phi(k, Y)}{\partial Y} = \frac{N_c}{2\pi^2} \int d^2 q \left\{ \frac{2}{(\mathbf{k} - \mathbf{q})^2} \alpha_s \left( (\mathbf{k} - \mathbf{q})^2 e^{-5/3} \right) \phi(q, Y) - \frac{\mathbf{k}^2}{q^2 (\mathbf{k} - \mathbf{q})^2} \frac{\alpha_s(q^2 e^{-5/3}) \alpha_s((\mathbf{k} - \mathbf{q})^2 e^{-5/3})}{\alpha_s(\mathbf{k}^2 e^{-5/3})} \phi(k, Y) \right\}, \quad (58)$$

where the unintegrated gluon distribution  $\phi(k, Y)$  is defined by

$$N(x_{01}, Y) = \int \frac{d^2 k}{(2\pi)^2} \left( 1 - e^{i\mathbf{k} \cdot \mathbf{x}_{01}} \right) \tilde{N}(k, Y) \quad (59)$$

with

$$\alpha_s(k^2) \phi(k, Y) = \frac{N_c S_\perp}{(2\pi)^3} k^2 \tilde{N}(k, Y). \quad (60)$$

Here  $S_\perp$  is the transverse area of the target. The running-coupling BFKL equation (58) was originally conjectured in [150, 151] by postulating the validity of the bootstrap equation for running-coupling corrections.

## 2.2.7 Running-coupling and higher-order effects on the saturation scale

*Guillaume Beuf*

The DGLAP [152–154] and BFKL [12, 13, 155] equations give the evolution with kinematics of the partonic content of hadrons and nuclei in the regime where these are dilute. Since those equations are linear, they can be solved analytically by using Mellin transform. By contrast, when the phenomenon of gluon saturation [34] is taken into account, the relevant evolution equations - B-JIMWLK [37, 48, 49, 51–55, 62] or BK [33, 39, 62] - are nonlinear, and thus cannot be solved analytically.

Nevertheless, the solutions of these nonlinear equations in the leading order (LO) approximation (where the coupling  $\alpha_s$  is kept fixed) are well understood, by combining results from numerical simulations [42, 156, 157] and analytical asymptotic expansions [47, 158–161]. Indeed, the BK equation belongs to a well-studied class of nonlinear equations, whose solutions develop asymptotically a universal traveling wave-front structure [162, 163], which is independent of the initial condition<sup>3</sup>. In QCD context, that traveling wave-front structure of the solution implies the *geometric scaling* [44] property found in the DIS data at HERA: the total virtual photon - target cross sections  $\sigma_{T,L}^{\gamma^*}(Y, Q^2)$  depend on  $Y$  and  $Q^2$  essentially only through the combination  $Q^2/Q_s^2(Y)$ , because the dipole-target amplitude solution of the BK equation depends only on  $r^2 Q_s^2(Y)$  at large  $Y$ ,  $r$  being the dipole size. The evolution of the saturation scale  $Q_s^2(Y)$  is obtained from the propagation of the wave-front. For the LO BK equation, one gets a large  $Y$  expansion of the form

$$\log Q_s^2(Y) = a_1 Y + a_0 \log Y + \text{Const.} + a_{-1/2} Y^{-1/2} + \mathcal{O}(Y^{-1}), \quad (61)$$

where  $a_1$ ,  $a_0$  and  $a_{-1/2}$  are three known universal coefficients [161], whereas the constant term and all the ones of order  $Y^{-1}$  or less do depend on the initial conditions, *i.e.* on the

---

<sup>3</sup>More precisely, in the QCD case, that asymptotic behavior in rapidity is reached from any initial condition compatible with perturbative QCD in the UV.

nature of the target used for the DIS. From geometric considerations, the initial  $Q_s^2$  of a nucleus  $A$  is enhanced by a factor  $A^{1/3}$  with respect to the one of a proton. That nuclear enhancement of  $Q_s^2(Y)$  is preserved by the LO high-energy evolution, in the constant term of the expansion (61). Both from numerical simulations and from the expansion (61), one learns that the evolution of  $Q_s^2(Y)$  implied by the LO BK equation is too fast to be compatible with the data for DIS and other observables, which favor  $\log Q_s^2(Y) \sim \lambda Y$ , with  $\lambda \simeq 0.2$  or  $0.3$ . We are thus forced to consider higher order corrections to the BK equation.

**Running vs. fixed coupling:** As discussed in the previous contribution, the BK equation is now known at next-to-leading order (NLO) [132, 134]. However, its solutions are much less understood than the ones of the LO equation. Indeed no numerical simulations of the full NLO BK equation have been performed yet, for technical reasons, but only simulations [42, 43, 156, 157, 164] of the BK equation with LO kernel and running coupling  $\alpha_s$ , with various prescriptions used to set the scale in the coupling. By contrast, it is non-trivial to go from fixed coupling to running coupling in the analytical studies, since it leads to a different class of wave-front solutions, for which universality of the asymptotics is not fully established. The inclusion of other NLO corrections gives however no additional difficulty. Let us first discuss the effects of running coupling only.

A priori, the running of the coupling brings the additional scale  $\Lambda_{QCD}$  in the problem, which may spoil the geometric scaling property. Indeed, there is no interval where the solutions of the running coupling BK equation show exact geometric scaling, by contrast to fixed coupling solutions, but they satisfy an approximate geometric scaling in some range. Equivalently, the wave-front in the solutions is being slowly distorted during its propagation, instead of being uniformly translated as in the fixed coupling case.

Running coupling effects turn the asymptotic behavior of the saturation scale into  $\log Q_s^2(Y) \propto \sqrt{Y}$ , as found in early analytical studies [34, 47, 158, 160]. More precisely its large  $Y$  asymptotics writes

$$\log (Q_s^2(Y)/\Lambda_{QCD}^2) = b_{1/2} \sqrt{Y} + b_{1/6} Y^{1/6} + b_0 + b_{-1/6} Y^{-1/6} + b_{-1/3} Y^{-1/3} + \mathcal{O}(Y^{-1/2}), \quad (62)$$

where the first five terms are universal and known<sup>4</sup>, whereas the following ones of order  $Y^{-1/2}$  or less are sensitive to the initial conditions. The universality of the constant term  $b_0$  in (62) implies that initial conditions effects such as the nuclear  $A^{1/3}$  enhancement of  $Q_s^2$  are washed-out at high rapidity when the coupling is running, as first predicted in [166]. Numerically, it has been found [42, 157, 167] that this effect happens at very high rapidity. Hence, the nuclear enhancement of  $Q_s^2$ , which is one of the motivations for doing nuclear DIS at the EIC, should still be present in the kinematical range accessible at the EIC. Remarkably, the evolution of the saturation scale in the running coupling case is such that very good fits of DIS data can be performed with solutions of the running coupling BK equation [113, 114], by contrast to the fixed coupling case, without the inclusion of other NLO effects.

**Other NLO effects:** Apart from the contributions re-summed into the running of the coupling, there are large NLO corrections to the BK kernel, related to the large NLO corrections to the BFKL kernel [14, 15].

In a conformal gauge field theory, terms of arbitrary  $N^n$ LO order from the kernel would

---

<sup>4</sup>The calculation of  $b_0$ ,  $b_{-1/6}$  and  $b_{-1/3}$  has been performed recently in [165].

contribute at each order of the expansion (61). By contrast, the running of the coupling is dynamically quenching the effect on the solutions of higher order terms in the kernel. NLO contributions start to appear at order  $Y^0$  in (62), NNLO contributions at order  $Y^{-1/2}$  and so on. Moreover, the coefficient  $b_{-1/6}$  has been found NLO-independent [165]. Apart from the running of the coupling, NLO contributions thus affect mostly the normalization of  $Q_s^2(Y)$  at large  $Y$ , via  $b_0$ , and only mildly the asymptotic  $Y$ -evolution of  $Q_s^2(Y)$ , via  $b_{-1/3} Y^{-1/3}$  and further subleading terms. That property is indeed seen in numerical simulations with running coupling and a subset of other NLO contributions included [164]. That result shed some light on the spectacular success of the running coupling LO BK equation to describe DIS data. There is a degeneracy in (62) between the contribution of  $\Lambda_{QCD}$  and  $b_0$  to  $Q_s^2(Y)$ . Hence, treating  $\Lambda_{QCD}$  as a free fit parameter as in Refs. [113, 114] allows to fit the bulk of NLO effects, without actually simulating the BK evolution with NLO kernel.

Several prescriptions [130, 131] have been proposed to split NLO corrections into contributions to the running coupling or to the kernel. Hence, BK equations with running coupling and LO kernel obtained following different prescriptions differ formally by terms of order NLO and beyond in the kernel. In numerical simulations [43] of such running coupling LO BK equations, solutions with different prescriptions differ at large  $Y$  mostly by a constant rescaling of  $Q_s^2(Y)$ , in agreement with our previous discussion.

**The problems brought by the impact-parameter dependence:** Implicitly, we have discussed so far only results from studies of impact parameter independent solutions of the BK equation. The BK equation preserves unitarity at fixed impact parameter. However its impact parameter dependent solutions violate unitarity since they violate the Froissart bound [168] on the cross-section [164, 169], due to the unphysical possibility of gluon emission at arbitrarily long range in the transverse plane. The running of the coupling reveals another problem: there is a reappearance of the diffusion into the infrared [164], which was thought to be cured by gluon saturation, from studies of impact parameter independent solutions of the BK equation. Hence, the impact parameter dependent solutions of the BK solutions are very sensitive to strongly coupled infrared physics, which is not yet implemented in the formalism. This is certainly the most challenging open theoretical problem about gluon saturation. Therefore, it is not yet clear to what extent the results about impact parameter independent solutions presented in the previous sections are reliable for realistic proton or nuclear targets.

## 2.3 Diffractive DIS ( $F_2^D$ , $F_L^D$ , charm contribution)

### 2.3.1 Diffraction in e+p and e+A collisions

*Cyrille Marquet*

A non-negligible fraction of the events in DIS are diffractive, meaning that the hadronic target, of mass  $M$ , escapes the collision intact. As a colorless object has been exchanged in the t-channel, there is rapidity gap void of particles in the final state, between the outgoing target and the so-called diffractive final state  $X$ , made of all the other particles in the event. On top of  $x$  and  $Q^2$ , two additional kinematic invariants are needed to characterize diffraction in DIS: the momentum transfer  $t < 0$  at the hadronic vertex, and the mass  $M_X$



of the diffractive final state. In practice, the variable  $M_X$  is sometimes traded for

$$\beta = \frac{Q^2}{Q^2 + M_X^2 - t} . \quad (63)$$

Small values of  $\beta$  refer to events with diffractive masses much bigger than the photon virtuality, while values of  $\beta$  close to unity refer to the opposite situation. In addition, the variable  $x$  is also often substituted by

$$x_{\mathbb{P}} = \frac{x}{\beta} = \frac{Q^2 + M_X^2 - t}{Q^2 + W^2 - M^2} , \quad (64)$$

as  $x_{\mathbb{P}}$  characterizes the size of the rapidity gap  $\Delta\eta \simeq \ln(1/x_{\mathbb{P}})$ .

There are events in which the hadronic target, instead of staying intact, may dissociate into a low-mass excited state  $Y$ , while still leaving a rapidity gap in the final state. These events are also classified as diffractive, they occur only if the mass  $M_Y$  of the excited state is close enough to the initial mass  $M$ . Coherent diffraction is employed when the target scatters elastically ( $\text{ep} \rightarrow \text{eXp}$ ), while incoherent diffraction refers to the more general case  $\text{ep} \rightarrow \text{eXY}$  which is a sum of coherent diffraction ( $Y=p$ ) and target-dissociative diffraction ( $Y \neq p$ ). The former dominates at low  $|t|$  and the latter at large  $|t|$ .

While in the leading-twist approximation of QCD, there is a collinear factorization theorem to compute diffractive structure functions in DIS at large  $Q^2$ , the description of hard diffraction in this framework is not as natural as for inclusive events. This is reflected in the fact that standard parton distribution functions (pdfs) are of no help to compute  $F_2^D$ , and one has to introduce a different set of parton distributions called diffractive pdfs (dpdfs). Therefore in the collinear factorization framework, the description of the parton content of the proton depends on whether or not the final state is diffractive. While this is successful - and should be since collinear factorization is a good approximation of QCD at large  $Q^2$  - conceptually it is not so satisfactory as one would like to be able to describe any process with a single proton wave function.

No further conceptual advances are expected within the leading-twist approximation of QCD. There are some technical improvements that can be made, for instance it is nowadays practically impossible to extract dpdfs without assuming what is called Regge factorization:  $\text{dpdf}(x_{\mathbb{P}}, t, \beta, Q^2) = f(x_{\mathbb{P}}, t) g(\beta, Q^2)$ . This is not satisfactory, since such a factorization is not a property of QCD. However, there is little doubt that if one could bypass this practical problem - perhaps with a larger data sample in all four directions:  $Q^2$ ,  $\beta$ ,  $x_{\mathbb{P}}$  and  $t$  - this approach would succeed at large  $Q^2$ .

But in fact, the purpose of an electron-ion collider is not to check whether DGLAP evolution will work at large  $Q^2$ , the goal is rather to explore what we don't know as well: the non-linear regime of QCD where collinear factorization breaks down. To be more specific, we are interested in the regime  $Q^2 < 5 \text{ GeV}^2$  and  $x$  as small as possible. Interestingly enough, studying the non-linear *saturation* regime will be easier with diffractive than with inclusive measurements. This is so because at small  $x$ , diffractive processes are mostly sensitive to quantum fluctuations in the proton wave function that have a virtuality of order  $Q_s^2$ , instead of  $Q^2$ . As a result, power corrections (not the generic  $\Lambda_{QCD}^2/Q^2$  corrections, but rather the sub-class of them of order  $Q_s^2/Q^2$  important at small  $x$ ) are expected to come into play starting from a higher value of  $Q^2$  in diffractive DIS, compared to inclusive DIS. In fact, there is already a hint that this is happening at HERA: collinear factorization starts to fail below about  $2 \text{ GeV}^2$  in the case of  $F_2$ , while already below about  $8 \text{ GeV}^2$  in the case of  $F_2^D$ .

The QCD description of diffractive DIS in the small- $x$  limit turns out to be much more insightful than that of the large- $Q^2$  limit. It is so because at small  $x$ , DDIS can be expressed as in the Good-Walker picture (which was originally imagined for soft diffraction in hadron-hadron collisions), with the benefit that, thanks to the point-like nature of the photon, the modeling part of the Good-Walker approach can be replaced by actual QCD computations. This remarkable realization of the Good-Walker picture in small- $x$  DIS is more commonly referred to as the dipole picture: dipoles are eigenstates of high-energy scattering in QCD, and it is known how to expand the photon wave function onto the dipole basis. At the end in this approach, the parton content of the proton - both in the linear and non-linear regimes - is parametrized through the dipole cross section. As a result diffractive structure functions also feature geometric scaling [170]. Another important fact is that at small  $x$ , diffraction can be entirely predicted, once the dipole cross section has been constrained with inclusive data.

In spite of the fact that this approach has been able to successfully predict  $F_2^D$  at small  $x$ , there are still important conceptual progresses to be made. For instance, the transverse impact parameter dependence of the dipole scattering amplitude is very poorly constrained. Indeed, one has been able to describe  $F_2$  and correctly predict  $F_2^D$  with two kinds of impact parameter dependences, neither of which is fully satisfactory. In a first class of dipole models, the impact parameter profile of the proton is independent of energy, yielding a dipole cross section bounded from above. In the other class of models, the black-disk regime of maximal scattering strength spreads too quickly in the transverse plane with increasing dipole size  $r$ , leading to a dipole cross section which diverges for large  $r$ . It is quite clear that the LHeC is needed to help us understand better this issue.

Finally, let us say a few important words on  $ep \rightarrow eXY$  diffractive events. In past experiments, events with  $Y \neq p$  have mostly been regarded as background, and model-dependent substrations have been applied to data, yielding large normalization uncertainties. Within the kinematic reach of HERA, it has been observed that the ratio  $d\sigma^{ep \rightarrow eXY}/d\sigma^{ep \rightarrow eXp}$  is a constant independent of all kinematic variables other than  $M_Y$  and  $t$  (that ratio increases with  $M_Y$  and  $|t|$ ). Here we would like to emphasise that proton-dissociative events are also intrinsically interesting. For instance, at small  $x$  the cross section difference  $d\sigma^{ep \rightarrow eXY} - d\sigma^{ep \rightarrow eXp}$  is  $1/N_c^2$  suppressed, meaning that if it were measured accurately, it would give access to details of the QCD dynamics which are untestable otherwise. The EIC provides such an opportunity.

After many fixed target experiments, it took a collider to discover diffractive events in  $e+p$ . Since no  $e+A$  collider has ever been built, diffraction in  $e+A$  has simply never been measured. That such a deficiency exists in our knowledge of nuclear structure is compelling enough to build the EIC. Everything we would learn about DDIS off nuclei at the EIC will be new, in any kinematical domain, implying a huge discovery potential. Nevertheless, we have expectations of what diffraction off nuclei should look like, based on our current understanding of QCD. For instance, the theory of nuclear shadowing allows to construct nuclear dpdfs for the large  $Q^2$  physics, while within the Color Glass Condensate framework, nuclear diffractive structure functions can be predicted at small  $x$ . Depending on these kinematics, different patterns of nuclear shadowing or antishadowing as a function of  $\beta$  and  $x_{\mathbb{P}}$  are expected. This is just one example out of many that should be checked with an  $e+A$  collider. Since the current predictions rely on rather simple models for impact parameter dependence, they need to be confronted to data, in order to, in return, improve our understanding.

Finally, there is one aspect of diffraction which is specific to nuclei that one should

mention. The structure of incoherent diffraction  $eA \rightarrow eXY$  is more complex than with a proton target, and also can teach us a lot more. In the case of a target nucleus, we expect the following qualitative changes in the  $t$  dependence. First, the low- $|t|$  regime in which the nucleus scatters elastically will be dominant up to a smaller value of  $|t|$  (to about  $|t| = 0.05 \text{ GeV}^2$ ) compared to the proton case, reflecting the bigger size of the nucleus. Then, the nucleus-dissociative regime will be made of two parts: an intermediate regime in momentum transfer up to about  $0.7 \text{ GeV}^2$  where the nucleus will predominantly break up into its constituents nucleons, and a large- $|t|$  regime where the nucleons inside the nucleus will also break up, implying pion production in the  $Y$  system for instance. These are only qualitative expectations, it is crucial to study this aspect of diffraction quantitatively in order to complete our understanding of the structure of nuclei.

### 2.3.2 Expectations for $e+A$ from the CGC

*Cyrille Marquet*

In this work, hard diffraction in electron-nucleus ( $e+A$ ) collisions is considered within the IPsat model,[117] corresponding to the classical limit of the Color Glass Condensate approach. This effective theory of QCD at high partonic density is the most natural framework to describe the saturation phenomenon, and therefore to study  $e-A$  scattering at high energies, in particular diffractive observables. Here we shall focus on the nuclear diffractive structure function  $F_{2,A}^D$ .

Let us recall the kinematics of diffractive DIS:  $\gamma^* A \rightarrow X A$ . With a momentum transfer  $t \leq 0$ , the proton/nucleus gets out of the  $\gamma^*-A$  collision intact, and is separated by a rapidity gap from the other final-state particles whose invariant mass we denote  $M_X$ . The photon virtuality is denoted  $Q^2$ , and the  $\gamma^*-A$  total energy  $W$ . It is convenient to introduce the following variables:  $x = Q^2/(Q^2 + W^2)$ ,  $\beta = Q^2/(Q^2 + M_X^2)$  and  $x_{\mathbb{P}} = x/\beta$ . The size of the rapidity gap is  $\ln(1/x_{\mathbb{P}})$ .

The diffractive structure function is expressed as a function of  $\beta$ ,  $x_{\mathbb{P}}$ ,  $Q^2$ , and  $t$ , and we will only consider the  $t$ -integrated structure function  $F_2^{D,3}$ . While at large values of  $x_{\mathbb{P}}$  and  $Q^2$ , the leading-twist collinear factorization is appropriate to describe hard diffraction off protons, this is not the case at small  $x_{\mathbb{P}}$  or off nuclei, as higher twists are enhanced by  $\sim (A/x_{\mathbb{P}})^{0.3}$ . In this situation, the dipole picture is better suited to address the problem. It naturally incorporates the description of both inclusive and diffractive events into a common theoretical framework:[73, 171, 172] the same dipole-nucleus scattering amplitudes, which can be computed treating the nucleus as a CGC, enter in the formulation of the inclusive and diffractive cross-sections.

**Diffractive structure functions in the dipole picture:** In our approach,  $F_2^D = F_T^{q\bar{q}} + F_L^{q\bar{q}} + F_T^{q\bar{q}g}$  where the different pieces correspond to transversely (T) or longitudinally (L) polarized photons dissociating into a  $q\bar{q}$  or  $q\bar{q}g$  final state. For instance, the  $q\bar{q}$  contributions are

$$\begin{aligned} x_{\mathbb{P}} F_T^{q\bar{q}}(\beta, x_{\mathbb{P}}, Q^2) &= \frac{N_c Q^4}{8\pi^3 \beta} \sum_f e_f^2 \int_0^1 dz \Theta(\kappa_f^2) z(1-z) [f_T(z) \varepsilon_f^2(z) I_1(\kappa_f, \epsilon_f) + m_f^2 I_0(\kappa_f, \epsilon_f)] \\ x_{\mathbb{P}} F_L^{q\bar{q}}(\beta, x_{\mathbb{P}}, Q^2) &= \frac{N_c Q^6}{8\pi^3 \beta} \sum_f e_f^2 \int_0^1 dz \Theta(\kappa_f^2) z(1-z) f_L(z) I_0(\kappa_f, \epsilon_f) , \end{aligned} \quad (66)$$

with

$$\varepsilon_f^2(z) = z(1-z)Q^2 + m_f^2, \quad \kappa_f^2(z) = z(1-z)M_X^2 - m_f^2, \quad f_T(z) = z^2 + (1-z)^2, \quad f_L(z) = 4z^2(1-z)^2. \quad (67)$$

The  $x_{\mathbb{P}}$  dependence comes in the functions  $I_\lambda$  from  $N_A(r, b, x_{\mathbb{P}})$ , the  $q\bar{q}$  dipole-nucleus scattering amplitude:

$$I_\lambda(\kappa, \epsilon) = \int d^2b \left[ \int_0^\infty r dr J_\lambda(\kappa r) K_\lambda(\epsilon r) N_A(r, b, x_{\mathbb{P}}) \right]^2 \quad (68)$$

where  $J_\lambda$  and  $K_\lambda$  are Bessel functions. In formula (68), the integration variables  $r$  and  $b$  are the  $q\bar{q}$ -dipole transverse size and its impact parameter.

In principle, it is justified to neglect final states containing gluons, because these are suppressed by extra powers of  $\alpha_s$ . However, for small values of  $\beta$  or large values of  $Q^2$ , the  $q\bar{q}$  pair will emit soft or collinear gluons whose emissions are accompanied by large logarithms  $\ln(1/\beta)$  or  $\ln(Q^2)$  which compensate the factors of  $\alpha_s$ . In those situations, multiple gluons emissions should be re-summed; in practice, including the  $q\bar{q}g$  final state is enough to describe the HERA data. In both the small- $\beta$  and large- $Q^2$  limits, this can be done within the dipole picture. An implementation of the  $q\bar{q}g$  contribution  $F_T^{q\bar{q}g}$  that correctly reproduces both limits was recently proposed,[173] while at large  $\beta$  and small  $Q^2$ , the  $q\bar{q}$  contributions (66) dominate. The formulae that we shall use can be found in this work [173].

**The dipole-nucleus scattering amplitude:** We shall use the IPSat parametrization to describe the dipole-nucleus scattering amplitude:

$$N_A(r, b, x) = 1 - e^{-r^2 F(r, x) \sum_{i=1}^A T_p(b-b_i)}, \quad F(x, r^2) = \frac{\pi^2}{2N_c} \alpha_s \left( \mu_0^2 + \frac{C}{r^2} \right) x g \left( x, \mu_0^2 + \frac{C}{r^2} \right). \quad (69)$$

This is a model of a nucleus whose nucleons interact independently. Indeed,  $N_A$  is obtained from  $A$  dipole-nucleon amplitudes  $N_p = 1 - \exp[-r^2 F(r, x) T_p(b)]$  assuming that the probability  $1 - N_A$  for the dipole not to interact with the nucleus is the product of the probabilities  $1 - N_p$  for the dipole not to interact with the nucleons. This assumption is not consistent with the CGC quantum evolution, which sums up nonlinear interactions between the nucleons. However, the classical limit (69) of the dipole-CGC scattering amplitude can be thought of an initial condition. Note that in the small  $r$  limit, one has  $N_A = \sum_i N_p$ , and there is no leading twist shadowing.

In (69),  $T_p(b) \propto \exp[-b^2/(2B_G)]$  is the impact parameter profile function in the proton with  $\int d^2b T_p(b) = 1$ , and  $F$  is proportional to the DGLAP evolved gluon distribution. The parameters  $\mu_0$ ,  $C$ , and  $B_G$  (as well as two other parameters characterising the initial condition for the DGLAP evolution) are fit to reproduce the HERA data on the inclusive proton structure function  $F_2$ . The diffractive proton structure function  $F_2^D$  is well reproduced [120] after adjusting  $\alpha_s = 0.14$  in the  $q\bar{q}g$  component. Vector-meson production at HERA is also well described.[118]

We introduced in (69) the coordinates of the individual nucleons  $\{b_i\}$ , they are distributed according to the Woods-Saxon distribution  $T_A(b_i)$ , which means that to compute an observable, one has to perform the following average

$$\langle \mathcal{O} \rangle_N \equiv \int \left( \prod_{i=1}^A d^2b_i T_A(b_i) \right) \mathcal{O}(\{b_i\}). \quad (70)$$

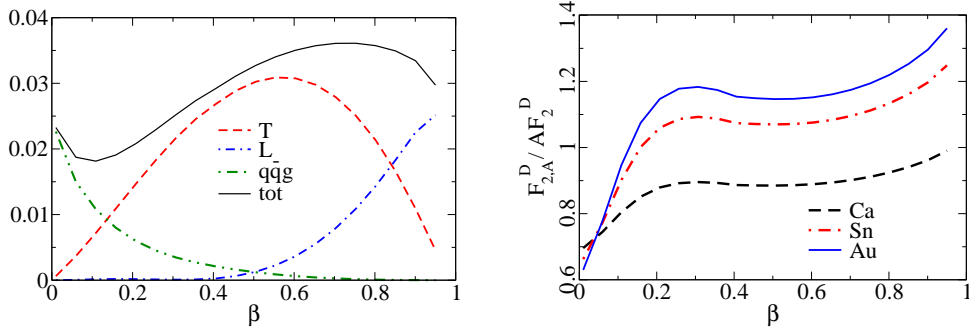


Figure 32. Left plot:  $\beta$ -dependence of the different contributions to the proton diffractive structure function  $F_{2,p}^D$ . Right plot: the ratio  $F_{2,A}^D / (A F_{2,p}^D)$  as a function of  $\beta$  for Ca, Sn and Au nuclei. In both cases, results are for the “non breakup” case, and at  $Q^2 = 5 \text{ GeV}^2$  and  $x_{\mathbb{P}} = 0.001$ .

The Woods-Saxon parameters are measured from the electrical charge distribution, no additional parameters are introduced. The resulting dipole cross sections give a good agreement [121] with the small- $x$  NMC data on the nuclear structure function  $F_{2,A}$ . We will use this parametrization of  $N_A$  to predict the nuclear diffractive structure function  $F_{2,A}^D$ .

Note that performing the average (70) at the level of the amplitude, meaning calculating  $\langle N_A \rangle_N^2$  in (66), imposes that the nucleus is intact in the final state, it hasn’t broken up. By contrast, when performing the average at the level of the cross-section, meaning calculating  $\langle N_A^2 \rangle_N$  in (66), one allows the nucleus to break up into individual nucleons, which will typically happen when the momentum transfer is bigger than the inverse nuclear radius. In what follows, we shall refer to those possibilities as “non breakup” and “breakup” cases.

**Nuclear enhancement and suppression of  $F_2^D$ :** In Figure 1, the  $\beta$  dependence of the diffractive structure function is displayed for  $Q^2 = 5 \text{ GeV}^2$  and  $x_{\mathbb{P}} = 0.001$ . On the left plot, the hierarchy of the different contributions is analysed in the case of  $F_{2,p}^D$ . The dominant contribution is: the  $q\bar{q}g$  component for values of  $\beta < 0.1$ , the longitudinally polarized  $q\bar{q}$  component for values of  $\beta > 0.9$ , and the transversely polarized  $q\bar{q}$  component for intermediate values. In the case of  $F_{2,A}^D$ , this separation is still true but the  $q\bar{q}$  and  $q\bar{q}g$  components behave differently as a function of  $A$ . The  $q\bar{q}$  components are enhanced compared to  $A$  times the proton diffractive structure functions while the  $q\bar{q}g$  component, on the contrary, is suppressed for nuclei compared to the proton (the  $Q^2$  and  $x_{\mathbb{P}}$  dependence of these effects will be discussed shortly).

This leads to a nuclear suppression of the diffractive structure function in the small  $\beta$  region, and to an enhancement at large  $\beta$ . This is illustrated by the right plot of Figure 1, where the ratio  $F_{2,A}^D / (A F_{2,p}^D)$  is shown as a function of  $\beta$  for different nuclei (for the “non breakup” case). The net result of the different contributions is that  $F_{2,A}^D / A$ , for a large  $\beta$  range down to 0.1, is close to  $F_{2,p}^D$ , and is increasing with  $A$ .

In Figure 2, for the Au nucleus case, the ratios  $F_{2,A}^D / (A F_{2,p}^D)$  of individual contributions are analyzed (for values of  $\beta$  at which they are dominant). Comparisons between the “breakup” and “non breakup” cases are made, as functions of  $Q^2$  (left plot) and  $x_{\mathbb{P}}$  (right plot). For the  $q\bar{q}g$  component, the nuclear suppression is almost constant (the suppression slightly decreases with  $Q^2$ ). For the  $q\bar{q}$  components, the enhancement becomes bigger with increasing  $Q^2$  and  $x_{\mathbb{P}}$ . The result for the total diffractive cross-section in e-A scattering is that it decreases more slowly with increasing  $Q^2$  or  $x_{\mathbb{P}}$  compared to the e-p case. Finally,

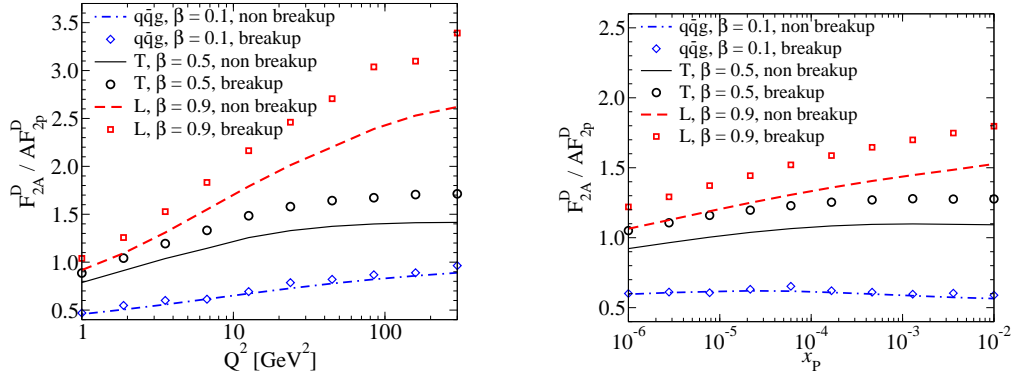


Figure 33. The ratios  $F_{2,A}^{D,x}/(AF_{2,p}^{D,x})$  of the different components ( $x = q\bar{q}g, q\bar{q}T, q\bar{q}L$ ) of the diffractive structure function for both “breakup” and “non breakup” cases. Left plot: as a function of  $Q^2$  for  $x_P = 0.001$ . Right plot: as a function of  $x_P$  for  $Q^2 = 5$  GeV<sup>2</sup>. In both cases, results are for Au nuclei and the different components are evaluated where they are dominant: at  $\beta = 0.1$  for  $q\bar{q}g$ ,  $\beta = 0.5$  for  $q\bar{q}T$  and  $\beta = 0.9$  for  $q\bar{q}L$ .

cross sections in the “non breakup” case are about 15% lower than in the “breakup” case.

Comparing with other approaches, we obtain similar features. We notice one interesting difference with the results obtained using diffractive parton distributions modified by leading twist shadowing [104]: even at large  $\beta$ , it is found that  $F_{2,A}^D/A$  is suppressed compared to  $F_{2,p}^D$  as a function of  $Q^2$ . This could be tested with measurements at a future EIC where diffraction will be an important part of a rich program. A typical nuclear enhancement of diffraction, for a Au nucleus, is a factor of  $\sim 1.2$ . Combining this with the typical nuclear suppression in the inclusive case ( $\sim 0.8$ , see [121]), we expect the fraction of diffractive events to be increased by a factor of  $\sim 1.5$  compared to the proton, meaning 25 to 35 % at the EIC.

### 2.3.3 Expectations for e+A from LT shadowing

*Vadim Guzey and Mark Strikman*

The leading twist theory of nuclear shadowing (see section 2.1.6) that uses the connection between nuclear shadowing and diffraction [83] and allows one to predict nuclear parton distributions (PDFs) at small  $x$  [95, 97–99] can also be used to predict nuclear *diffractive* PDFs and *diffractive* structure functions [104]. At small  $x$  and in the nuclear target rest frame, the virtual photon interacts coherently with all nucleons of the nuclear target and the  $\gamma^*A \rightarrow XA$  scattering amplitude is given by the sum of the multiple scattering contributions presented in fig. 34. Graphs *a*, *b*, and *c* correspond to the coherent interaction with one, two, and three nucleons of the nuclear target, respectively: graph *a* is the impulse approximation; graphs *b* and *c* contribute to the shadowing correction. Note that the interactions with four and more nucleons (at the amplitude level) are not shown, but they are implied. The application of the Abramovsky-Gribov-Kancheli (AGK) cutting rules [96] allows one to relate these diagrams to the corresponding diagrams for the total cross section in  $\gamma^*A$  scattering.

Combining the Glauber-Gribov multiple scattering formalism for the  $\gamma^*A \rightarrow XA$  scattering amplitude with the QCD factorization theorem [100], one can derive the nuclear

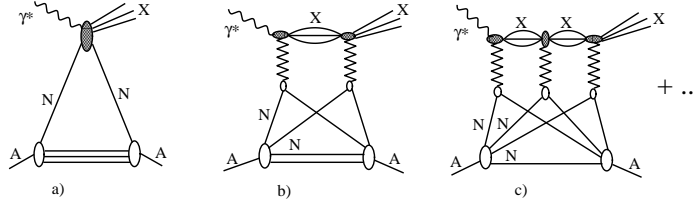


Figure 34. The multiple scattering series for the  $\gamma^* A \rightarrow X A$  diffractive scattering amplitude. Graph *a* is the impulse approximation; graphs *b* and *c* correspond to the interaction with two and three nucleons of the nuclear target, and contribute to the shadowing correction.

diffractive parton distribution of flavor  $j$  [99, 104]:

$$\begin{aligned} \beta f_{j/A}^{D(3)}(\beta, Q_0^2, x_P) &= 4\pi A^2 \beta f_{j/N}^{D(4)}(\beta, Q_0^2, x_P, t_{\min}) \int d^2b \\ &\times \left| \int_{-\infty}^{\infty} dz e^{ix_P m_N z} e^{-\frac{A}{2}(1-i\eta)\sigma_{\text{soft}}^j(x, Q_0^2)} \int_z^{\infty} dz' \rho_A(b, z') \rho_A(b, z) \right|^2, \quad (71) \end{aligned}$$

where the notation is the same as in eqs. (34) and (35).

While at the level of the interaction with two nucleons (the square of graph *a* in fig. 34) our predictions are model-independent, the contribution of the interaction with  $N \geq 2$  nucleons requires additional model-dependent considerations since these interactions probe the details of the diffractive dynamics beyond of what is encoded in the elementary diffractive distribution  $f_j^{D(4)}$ , as discussed in Section 2.1.6. Viewing the hard probe (virtual photon) as a coherent superposition of the configurations that interact with the target nucleons with very different strengths (from align-jet configurations to point-like configurations) and which are present in the virtual photon with the probability  $P(\sigma)$ , one immediately sees from fig. 34 that diffractive scattering probes all moments of the cross section (color) fluctuations of the virtual photon,  $\langle \sigma^n \rangle \equiv \int d\sigma P(\sigma) \sigma^n$ , up to the order  $n = 2A$ . One should note that coherent diffraction probes these fluctuations differently from inclusive scattering. For instance, while the shadowing correction to the deuteron usual parton distributions is proportional to  $\langle \sigma^2 \rangle$  (i.e., it is unambiguously expressed in terms of the corresponding diffractive PDFs, see eq. 34 in section 2.1.6), the shadowing correction to the deuteron diffractive PDFs is proportional to  $\langle \sigma^3 \rangle$  (interference of graphs *a* and *b* in fig. 34). (Note that the square of graph *b* in fig. 34 proportional to  $\langle \sigma^4 \rangle$  also contributes, but its contribution is numerically very small.) Since the cross section fluctuations of the virtual photon ( $\langle \sigma^n \rangle$  moments) are rather weakly constrained by the present data, predictions of the leading twist theory of nuclear shadowing contain unavoidable theoretical uncertainty associated with modeling of  $\langle \sigma^n \rangle$  with  $n \geq 3$ . Precise measurements of the  $t$  dependence of nuclear shadowing in  $eD$  diffraction at an EIC will dramatically reduce this uncertainty by determining exactly these moments.

Equation (71) determines nuclear diffractive PDFs at a certain initial scale  $Q_0^2$  ( $Q_0^2 = 4 \text{ GeV}^2$  in our case). As a consequence of the QCD factorization [100], the subsequent  $Q^2$  evolution is given by the DGLAP evolution equations (at fixed  $x_P$  and  $t$ ). As another consequence of the QCD factorization, the same nuclear diffractive PDFs  $f_{j/A}^{D(3)}$  enter the perturbative QCD description of many processes and observables: the diffractive structure function  $F_{2A}^{D(3)}$ , the longitudinal diffractive structure function  $F_{LA}^{D(3)}$ , the charm structure functions  $F_{2A}^{D(3)(c)}$  and  $F_{LA}^{D(3)(c)}$ , and diffractive electroproduction of jets and heavy flavors.

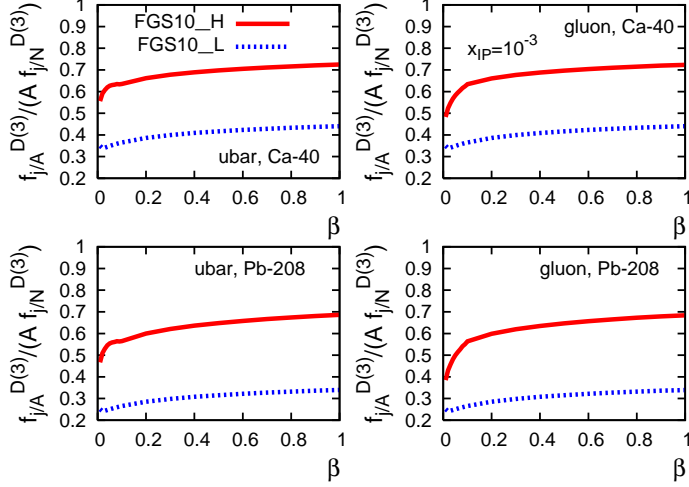


Figure 35. The leading twist theory of nuclear shadowing predictions for the ratio of nuclear to nucleon gluon and  $\bar{u}$ -quark diffractive PDFs,  $f_{j/A}^{D(3)}/(A f_{j/N}^{D(3)})$ , as a function of  $\beta$  at  $x_P = 10^{-3}$  and  $Q_0^2 = 4$  GeV<sup>2</sup>. The two sets of curves (labeled FGS10\_H and FGS10\_L) correspond to the two extreme scenarios of nuclear shadowing.

As an example of our predictions for nuclear diffractive PDFs, in fig. 2.3.3 we present the ratio of the nuclear ( $^{40}\text{Ca}$  and  $^{208}\text{Pb}$ ) to nucleon diffractive PDFs,  $f_{j/A}^{D(3)}/(A f_{j/N}^{D(3)})$ , as a function of  $\beta$  at fixed  $x_P = 10^{-3}$  and  $Q_0^2 = 4$  GeV<sup>2</sup>. The left column of panels corresponds to the  $\bar{u}$ -quark distribution; the right column corresponds to the gluon distribution. The two sets of curves (labeled FGS10\_H and FGS10\_L) correspond to the two scenarios for the effective cross section  $\sigma_{\text{soft}}^j$ , which also determines shadowing effects as discussed in Section 2.1.6. As one can see from the comparison of fig. 2.3.3 to our predictions for the usual nuclear PDFs presented in fig. 19, nuclear diffractive PDFs are much more sensitive to the effect of the color fluctuations (the spread between the solid and dotted curves is much larger for  $f_{j/A}^{D(3)}/(A f_{j/N}^{D(3)})$  than for  $f_{j/A}(x, Q_0^2)/[A f_{j/N}(x, Q_0^2)]$ ).

$A/\text{model}$	$F_{2A,\text{incoh}}^{D(3)}/F_{2A}^{D(3)}, x_P = 10^{-3}$	$F_{2A,\text{incoh}}^{D(3)}/F_{2A}^{D(3)}, x_P = 10^{-2}$
$^{40}\text{Ca}$ , FGS10_H	0.35	0.33
$^{40}\text{Ca}$ , FGS10_L	0.43	0.38
$^{208}\text{Pb}$ , FGS10_H	0.12	0.11
$^{208}\text{Pb}$ , FGS10_L	0.20	0.16

Table 3. The leading twist theory of nuclear shadowing predictions for the ratio of the nuclear structure functions measured in incoherent and coherent diffraction in  $eA$  DIS,  $F_{2A,\text{incoh}}^{D(3)}/F_{2A}^{D(3)}$ , at  $x_P = 10^{-3}$  and  $10^{-2}$  and  $Q_0^2 = 4$  GeV<sup>2</sup>. The ratio is approximately  $\beta$ -independent.

The simplest observable to measure at an EIC is the diffractive structure function  $F_{2A}^{D(3)}$ . Our predictions for  $F_{2A}^{D(3)}/(A F_{2N}^{D(3)})$  for  $Q^2 \sim \text{few GeV}^2$  are similar in shape and close in the absolute value for  $^{40}\text{Ca}$  and model FGS10\_H to the corresponding predictions made in the framework of the color dipole model, where the main contribution originates from the aligned-jet configurations [120]. (Note that at the level of the interaction with two nucleons, the expressions for the shadowing correction in our leading twist approach and in the dipole formalism are essentially the same and are unambiguously expressed in terms of  $\gamma^*$ -nucleon diffraction.) Hence, it appears that the  $x_P$  and  $\beta$  dependence of coherent inclusive diffraction in  $eA$  DIS at  $Q^2 \sim Q_0^2$  may not give unambiguous information on the onset of the non-linear regime of parton dynamics; to distinguish between the non-saturation and saturation regimes one will need to study the  $Q^2$  dependence of various



diffractive observables.

In addition to inclusive coherent diffraction that we have discussed above, the leading twist theory of nuclear shadowing makes predictions for incoherent diffraction (with nuclear break-up into its constituents) in  $eA$  DIS, see [99] for details. Experimentally, coherent and incoherent diffraction can be separated (triggered on) using a Zero-Degree-Calorimeter. An example of our predictions for the ratio of the nuclear structure functions measured in incoherent and coherent diffraction in  $eA$  DIS at  $x_P = 10^{-3}$  and  $x_P = 10^{-2}$  and  $Q_0^2 = 4$  GeV<sup>2</sup> is presented in table 3. To a good accuracy, the ratio is approximately  $\beta$ -independent.

## 2.4 $k_T$ -dependent gluons: SIDIS and Jets

### 2.4.1 Dijet and Dihadron production at EIC

*Fabio Dominguez, Cyrille Marquet, Bowen Xiao and Feng Yuan*

**Dijet production at an EIC:** The operator definition of the Weizsäcker-Williams (WW) gluon distribution can be written as follows [174, 175]:

$$xG^{(1)}(x, k_\perp) = 2 \int \frac{d\xi^- d\xi_\perp}{(2\pi)^3 P^+} e^{ixP^+ \xi^- - ik_\perp \cdot \xi_\perp} \langle P | \text{Tr} \left[ F^{+i}(\xi^-, \xi_\perp) \mathcal{U}^{[+]\dagger} F^{+i}(0) \mathcal{U}^{[+]} \right] | P \rangle, \quad (72)$$

where the gauge link  $\mathcal{U}_\xi^{[+]} = U^n[0, +\infty; 0] U^n[+\infty, \xi^-; \xi_\perp]$  represents final state interactions with  $U^n$  being the light-like Wilson line in covariant gauge. By choosing the light-cone gauge with certain boundary condition for the gauge potential ( $A_\perp(\zeta^- = \infty) = 0$  for the specific case above), we can drop out the gauge link contribution in equation (72) and find that this gluon distribution has the number density interpretation. Then, it can be calculated from the wave functions or the WW field of the nucleus target [21, 23, 176]. At small- $x$  for a large nucleus, it was found

$$xG^{(1)}(x, k_\perp) = \frac{S_\perp}{\pi^2 \alpha_s} \frac{N_c^2 - 1}{N_c} \int \frac{d^2 r_\perp}{(2\pi)^2} \frac{e^{-ik_\perp \cdot r_\perp}}{r_\perp^2} \left( 1 - e^{-\frac{r_\perp^2 Q_s^2}{4}} \right), \quad (73)$$

where  $N_c = 3$  is the number of colors,  $S_\perp$  is the transverse area of the target nucleus, and  $Q_s^2 = \frac{g^2 N_c}{4\pi} \ln \frac{1}{r_\perp^2 \lambda^2} \int dx^- \mu^2(x^-)$  is the gluon saturation scale with  $\mu^2$  the color charge density in a large nuclei.

The second gluon distribution, the Fourier transform of the dipole cross section, is defined in the fundamental representation

$$xG^{(2)}(x, k_\perp) = 2 \int \frac{d\xi^- d\xi_\perp}{(2\pi)^3 P^+} e^{ixP^+ \xi^- - ik_\perp \cdot \xi_\perp} \langle P | \text{Tr} \left[ F^{+i}(\xi^-, \xi_\perp) \mathcal{U}^{[-]\dagger} F^{+i}(0) \mathcal{U}^{[-]} \right] | P \rangle, \quad (74)$$

where the gauge link  $\mathcal{U}_\xi^{[-]} = U^n[0, -\infty; 0] U^n[-\infty, \xi^-; \xi_\perp]$  stands for initial state interactions. It has been shown in ref. [175] that the Weizsäcker-Williams gluon distribution can be directly probed in the dijet production processes in DIS while the second gluon distribution enters in the total and semi-inclusive DIS cross section. The quark-antiquark dijet cross section in DIS can be calculated in both the CGC formalism and the TMD approach. In the CGC formalism, the photon splits into a quark-antiquark pair which subsequently undergoes multiple interactions with the nucleus (see figure 36 left).

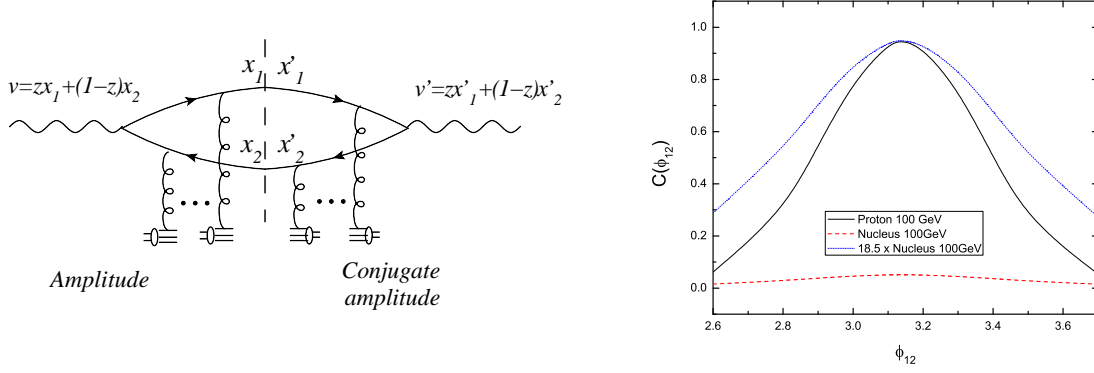


Figure 36. *Left:* Typical diagrams contributing to the cross section in the DIS at small- $x$  limit. *Right:* EIC dihadron correlation function

After averaging over the photon's polarization and summing over the quark and anti-quark colors and helicities in the splitting functions  $\psi_{\alpha\beta}^{T,L\lambda}(p^+, z, r)$ , we obtain,

$$\begin{aligned} \frac{d\sigma_{T,L}^{*A \rightarrow q\bar{q}X}}{d^3k_1 d^3k_2} &= N_c \alpha_{em} e_q^2 \delta(p^+ - k_1^+ - k_2^+) \int \frac{d^2x_1}{(2\pi)^2} \frac{d^2x'_1}{(2\pi)^2} \frac{d^2x_2}{(2\pi)^2} \frac{d^2x'_2}{(2\pi)^2} \\ &\times e^{-ik_{1\perp} \cdot (x_1 - x'_1)} e^{-ik_{2\perp} \cdot (x_2 - x'_2)} \sum_{\lambda\alpha\beta} \psi_{\alpha\beta}^{T,L\lambda}(x_1 - x_2) \psi_{\alpha\beta}^{T,L\lambda*}(x'_1 - x'_2) \\ &\times \left[ 1 + S_{x_g}^{(4)}(x_1, x_2; x'_2, x'_1) - S_{x_g}^{(2)}(x_1, x_2) - S_{x_g}^{(2)}(x'_2, x'_1) \right], \end{aligned} \quad (75)$$

where  $k_1$  and  $k_2$  are momenta for the final state quark and antiquark, respectively. We further define  $\vec{P}_\perp = \vec{k}_{1\perp} - \vec{k}_{2\perp}$  and  $\vec{q}_\perp = \vec{k}_{1\perp} + \vec{k}_{2\perp}$ . All transverse momenta are defined in the center of mass frame of the virtual photon and the nucleus target. The two- and four-point functions are defined as

$$S_{x_g}^{(2)}(x_1, x_2) = \frac{1}{N_c} \left\langle \text{Tr} U(x_1) U^\dagger(x_2) \right\rangle_{x_g}, \quad (76)$$

$$S_{x_g}^{(4)}(x_1, x_2; x'_2, x'_1) = \frac{1}{N_c} \left\langle \text{Tr} U(x_1) U^\dagger(x'_1) U(x'_2) U^\dagger(x_2) \right\rangle_{x_g}. \quad (77)$$

The notation  $\langle \dots \rangle_{x_g}$  is used for the CGC average of the color charges over the nuclear wave function where  $x_g$  is the smallest fraction of longitudinal momentum probed, and is determined by the kinematics.

In order to simplify the above result and obtain a factorized expression, we take the correlation limit of equation (75). For convenience, we introduce the transverse coordinate variables:  $u = x_1 - x_2$  and  $v = zx_1 + (1-z)x_2$ , and similarly for the primed coordinates. The respective conjugate momenta are  $\vec{P}_\perp = (1-z)k_{1\perp} - zk_{2\perp} \approx P_\perp$  and  $q_\perp$ , and therefore the correlation limit ( $\vec{P}_\perp \gg q_\perp$ ) can be taken by assuming  $u$  and  $u'$  are small and then expanding the integrand with respect to these two variables before performing the Fourier transform. Therefore, we can obtain the following expression which agrees perfectly with the TMD approach:

$$\frac{d\sigma_{\text{TMD}}^{\gamma_{T,L}^* A \rightarrow q\bar{q}+X}}{d\mathcal{P} \cdot \mathcal{S}} = \delta(x_{\gamma^*} - 1) x_g G^{(1)}(x_g, q_\perp) H_{\gamma_{T,L}^* g \rightarrow q\bar{q}}, \quad (78)$$

where  $x_g$  is the momentum fraction carried by the gluon and is determined by the kinematics,  $x_{\gamma^*} = z_q + z_{\bar{q}}$  with  $z_q = z$  and  $z_{\bar{q}} = 1 - z$  being the momentum fractions of the virtual photon carried by the quark and antiquark, respectively. The phase space factor is defined as  $d\mathcal{P}.S. = dy_1 dy_2 d^2 P_{\perp} d^2 q_{\perp}$ , and  $y_1$  and  $y_2$  are rapidities of the two outgoing particles in the lab frame. The leading order hard partonic cross section reads

$$H_{\gamma_T^* g \rightarrow q\bar{q}} = \alpha_s \alpha_{em} e_q^2 \frac{\hat{s}^2 + Q^4}{(\hat{s} + Q^2)^4} \left( \frac{\hat{u}}{\hat{t}} + \frac{\hat{t}}{\hat{u}} \right), \quad H_{\gamma_L^* g \rightarrow q\bar{q}} = \alpha_s \alpha_{em} e_q^2 \frac{8\hat{s}Q^2}{(\hat{s} + Q^2)^4}, \quad (79)$$

with the usually defined partonic Mandelstam variables  $\hat{s} = P_{\perp}^2/(z(1-z))$ ,  $\hat{t} = -(P_{\perp}^2 + \epsilon_f^2)/(1-z)$ , and  $\hat{u} = -(P_{\perp}^2 + \epsilon_f^2)/z$  with  $\epsilon_f^2 = z(1-z)Q^2$ .

**Dihadron correlations in DIS:** By including the  $k_t$  dependent fragmentation functions as proposed in ref. [177], one can compute the dihadron production cross section and the correlation function  $C(\phi_{12})$  which is defined as follows

$$C(\phi_{12}) = \frac{1}{\frac{d\sigma_{\text{tot}}^{\gamma^* A \rightarrow h_1 X}}{dz_{h1}}} \frac{d\sigma_{\text{tot}}^{\gamma^* A \rightarrow h_1 h_2 + X}}{dz_{h1} dz_{h2} d\phi_{12}}, \quad (80)$$

where  $z_{h1}$  and  $z_{h2}$  are the longitudinal momentum fractions of two produced hadrons w.r.t. the photon momentum.  $p_{1\perp}$  and  $p_{2\perp}$  are the transverse momenta of these two back-to-back hadrons and  $\phi_{12}$  is the azimuthal angle between them. Thus, it is straightforward to numerically evaluate the correlation function and plot it in figure 36 right, where we fix  $z_{h1} = z_{h2} = 0.3$ ,  $Q^2 = 4.0 \text{ GeV}^2$ ,  $\sqrt{s} = 100 \text{ GeV}$  (upper curve),  $200 \text{ GeV}$  (lower curve).  $p_{1\perp}$  and  $p_{2\perp}$  are integrated in the range  $[2, 3] \text{ GeV}$  and  $[1, 2] \text{ GeV}$ , respectively. For the gluon distribution in gold nuclei, we have used a parametrization inspired by *GBW* model. From figure 36, one sees the suppression of the away-side peak at higher energy due to gluon saturation.

**Conclusion:** First of all, we would like to compare the dijet production process in DIS to the inclusive and semi-inclusive DIS. As shown above, we derive that the dijet production cross section in DIS is proportional to the WW gluon distribution in the correlation limit. On the other hand, it is well-known that inclusive and semi-inclusive DIS involves the dipole cross section instead [178], which can be related to the second gluon distribution. This might look confusing at first sight, so let us take a closer look at equation (75). If one integrates over one of the outgoing momenta, say  $k_1$ , one can easily see that the corresponding coordinates in the amplitude and conjugate amplitude are identified ( $x_1 = x'_1$ ) and, therefore, the four-point function  $S_{x_g}^{(4)}(x_1, x_2; x'_2, x'_1)$  collapses to a two-point function  $S_{x_g}^{(2)}(x_2, x'_2)$ . As a result, the SIDIS and inclusive DIS cross section only depend on two-point functions, thus they only involve the dipole gluon distribution.

Now we can see the unique feature of the dijet production process in DIS. By keeping the momenta of the quark and antiquark unintegrated, we can keep the full color structure of the four-point function which eventually leads to the WW gluon distribution in the correlation limit. Therefore, measuring the dijet production cross sections or dihadron correlations in DIS at future experimental facilities like EIC would give us a first direct and unique opportunity to probe and understand the Weizsäcker-Williams gluon distribution. Last but not least, by measuring the SIDIS and inclusive DIS cross section at EIC, one can also probe and constrain the dipole gluon distribution.

*Acknowledgments:* We thank A. Accardi, M. Diehl, L. McLerran, A. Mueller, J.-W. Qiu, A. Stasto and R. Venugopalan for stimulating discussion.

## 2.4.2 Heavy quark production in $eA$ collisions

*Victor P. Gonçalves*

In this contribution we calculate the cross section of heavy quark production using the dipole approach and a nuclear saturation model based on the physics of the Color Glass Condensate (CGC) (For more details and references see Ref. [179]). The main input of our calculation is the dipole-nucleus cross section,  $\sigma_{dA}(x, r)$ , which is determined by the QCD dynamics at small  $x$ . In the eikonal approximation it is given by twice the impact-parameter  $b$  integral of  $\mathcal{N}^A(x, r, b)$ , the forward dipole-target scattering amplitude for a dipole with size  $r$  which encodes all the information about the hadronic scattering, and thus about the nonlinear and quantum effects in the hadron wave function. In our calculations we will assume as before that the forward dipole-nucleus amplitude is given by Eq. (129). It is important to emphasize that this model describes the current experimental data on the nuclear structure function as well as includes the impact parameter dependence in the dipole nucleus cross section. For the dipole-proton cross section we will use the b-CGC model.

To estimate the magnitude of the saturation effects in heavy quark production, let us compare the CGC predictions with those associated to linear QCD dynamics. As a model for the linear regime we consider the leading logarithmic approximation for the dipole-target cross section, where  $\sigma_{dA}$  is directly related to the nuclear gluon distribution  $xg_A$  as follows

$$\sigma_{dA}(x, r^2) = \frac{\pi^2}{3} r^2 \alpha_s x g_A(x, 10/r^2) . \quad (81)$$

The use of this cross section in the formulas given below will produce results which we denote CT, from color transparency. In this limit we are disregarding multiple scatterings of the dipole with the nuclei and are assuming that the dipole interacts incoherently with the target. In what follows we consider two different models for the nuclear gluon distribution. In the first one we disregard the nuclear effects and assume that  $xg_A(x, Q^2) = A.xg_N(x, Q^2)$ , with  $xg_N$  being the gluon distribution in the proton and given by the GRV98 parameterization. We will refer to this model as CT. In the second model we take into account the nuclear effects in the nuclear gluon distribution as described by the EKS98 parameterization. We will call this model CT + Shad. In our calculations the charm quark mass is  $m_c = 1.5$  GeV and the bottom quark mass is  $m_b = 4.5$  GeV.

**Heavy quark production in the color dipole approach:** Heavy quark production is usually estimated using the collinear factorization approach, where all partons involved are assumed to be on mass shell, carrying only longitudinal momenta, and their transverse momenta are neglected in the QCD matrix elements. On the other hand, in the large energy (small- $x$ ) limit, we have that the characteristic scale  $\mu$  of the hard subprocess of parton scattering is much less than  $\sqrt{s}$ , but greater than the  $\Lambda_{QCD}$  parameter. In this limit, the effects of the finite transverse momenta of the incoming partons become important, and the factorization must be generalized, implying that the cross sections are now  $k_\perp$ -factorized into an off-shell partonic cross section and a  $k_\perp$ -unintegrated parton density function  $\mathcal{F}(x, k_\perp)$ , characterizing the  $k_\perp$ -factorization approach. In the last years, an alternative approach to

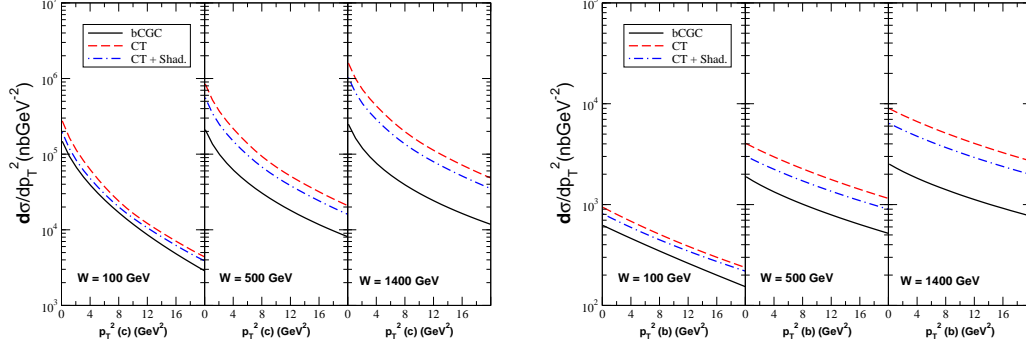


Figure 37. Transverse momentum charm spectrum (left) and bottom spectrum (right) for  $Q^2 = 2 \text{ GeV}^2$  and different energies.

calculated the heavy quark production at high energies was proposed considering the quasi-multi-Regge-kinematics (QMRK) framework. It is based on an effective theory implemented with the non-Abelian gauge-invariant action. The heavy quark production can also be calculated using the color dipole approach. This formalism can be obtained from the  $k_\perp$ -factorization approach after the Fourier transformation from the space of quark transverse momenta into the space of transverse coordinates. It is important to emphasize that this equivalence is only valid in the leading logarithmic approximation, being violated if the exact gluon kinematics is considered. A detailed discussion of the equivalence or not between the dipole and the QMRK approaches still is an open question. The main advantage to use the color dipole formalism, is that it gives a simple unified picture of inclusive and diffractive processes and the saturation effects can be easily implemented in this approach.

In the color dipole approach, the heavy quark production cross section is given by

$$\begin{aligned} \frac{d\sigma(\gamma^* A \rightarrow Q X)}{d^2 p_Q^\perp} &= \frac{6e_Q^2 \alpha_{em}}{(2\pi)^2} \int d\alpha \left\{ \left[ m_Q^2 + 4Q^2 \alpha^2 (1 - \alpha)^2 \right] \left[ \frac{I_1}{p_Q^{\perp 2} + \epsilon^2} - \frac{I_2}{4\epsilon} \right] \right. \\ &\quad \left. + \left[ \alpha^2 + (1 - \alpha)^2 \right] \left[ \frac{p_Q^\perp \epsilon I_3}{p_Q^{\perp 2} + \epsilon^2} - \frac{I_1}{2} + \frac{\epsilon I_2}{4} \right] \right\} \end{aligned} \quad (82)$$

with

$$\begin{aligned} I_1 &= \int dr r J_0(p_Q^\perp r) K_0(\epsilon r) \sigma_{dA}(r) \\ I_2 &= \int dr r^2 J_0(p_Q^\perp r) K_1(\epsilon r) \sigma_{dA}(r) \\ I_3 &= \int dr r J_1(p_Q^\perp r) K_1(\epsilon r) \sigma_{dA}(r) . \end{aligned} \quad (83)$$

where  $J_{0,1}$  and  $K_{0,1}$  are Bessel functions, and  $\epsilon^2 = \alpha(1 - \alpha)Q^2 + m^2$ .

**Results:** In Fig. 37 we show the transverse momentum spectrum of charm quarks. The main purpose of this figure is to show that the predictions of the linear physics (CT + Shad) differ from the total (i.e. bCGC) by a factor which increases with the energy  $W$  and goes from 1.5 ( $W = 100 \text{ GeV}$ ) to 4 ( $W = 1400 \text{ GeV}$ ). Moreover, this difference persists for a wide momentum window. At very large  $p_T$  we enter the deep linear regime and expect that the two curves coincide.

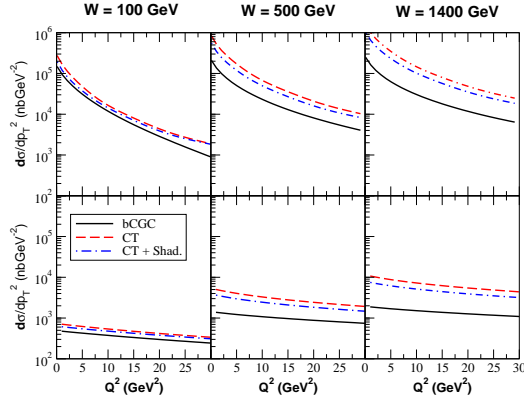


Figure 38. Dependence on the photon virtuality at  $p_T^2 = 4 \text{ GeV}^2$ .

In Fig. 37 we show the transverse momentum spectrum of bottom quarks. As expected, we observe the same features of the charm distribution, except that now the non-linear effects are weaker. Nevertheless they are still noticeable. In Fig. 38 we show the  $Q^2$  dependence of the  $p_T$  distribution at a fixed value  $p_T = 4 \text{ GeV}^2$  for different energies. The upper and lower panels show the charm and bottom distributions respectively. Here again, we observe a remarkable strenght and persistence up to large virtualities of the differences between CT + Shad and bCGC.

*Acknowledgments:* The author thanks M. S. Kugeratski and F.S. Navarra for collaboration.

## 2.5 $b$ -dependent gluons: Exclusive VM, DVCS

### 2.5.1 Gluon Density in e+A : KLN, CGC, DGLAP Glauber, or Neither?

*William A. Horowitz*

Perturbative quantum chromodynamics (pQCD) predicts a nontrivial expansion in the size of the nuclear wavefunction at small  $x$  as the perturbative power law tails of the gluon distribution near the edge of the nucleus become important compared to the exponential dropoff due to confinement effects [34, 58, 168]. Similarly, in order to not violate unitarity, the enormous growth in the gluon parton distribution function as  $x$  becomes small found via naïve application of DGLAP evolution (see [180] and references therein) must be tamed by perturbatively-calculable saturation effects [34, 58]. However it is not yet clear from a theoretical standpoint at what values of  $x$  these nontrivial changes in the dominant dynamics occur [58]. Additionally a quantitative theoretical understanding of experimental heavy ion data requires a quantitative understanding of the initial geometry of a heavy ion collision. Certainly observables such as the azimuthal anisotropy of particles [181–183] is correlated with the anisotropy of the initial geometry; surprisingly the event-by-event fluctuations in the initial geometry also strongly affect these observables [184, 185]. In particular the viscosity to entropy ratio ( $\eta/s$ ) of the quark-gluon plasma (QGP) found by comparing hydrodynamics simulations to heavy ion collision data is directly related to the eccentricity of the initial thermal quark-gluon plasma distribution that is evolved hydrodynamically. Currently the uncertainty in the initial thermal distribution due to the uncertainty in the importance of saturation effects in the initial nuclear profiles is large enough that it is not

clear whether the physics of the QGP is better described by leading order weakly-coupled perturbative quantum chromodynamics (LO pQCD) or by LO strongly-coupled anti-de-Sitter/conformal field theory (AdS/CFT) methods [182]. An experimental measurement of the spatial gluon distribution in a highly boosted nucleus, and hence the relevant physics in this kinematic range, would thus be a very interesting and important contribution to our understanding of QCD.

Exclusive vector meson production (EVMP) in  $e + A$  collisions has been proposed as a channel for just such a measurement [186, 187]. In this Letter we will focus on the production of heavy vector mesons, in particular  $J/\Psi$  mesons. To leading order, EVMP of a  $J/\Psi$  meson occurs in an  $e + A$  collision when a photon emitted by the electron splits into a  $c\bar{c}$  pair which communicates with the gluon density in the highly boosted nucleus via a two gluon exchange and subsequently forms a  $J/\Psi$  meson and nothing else (we will be interested here in coherent EVMP, in which case the nucleus remains intact); see figure 39 for a visualization of the process. It is precisely this two gluon exchange which yields a diffractive measurement of the gluon density in a nucleus.

Previous work [187] explored how modest changes in the Woods-Saxon distribution [188] of a nucleus might manifest themselves as changes in the diffractive peaks in EVMP if one assumes that the spatial distribution of gluons in a nucleus is proportional to the Glauber thickness function found from the Woods-Saxon distribution. That these modest changes do result in a visually obvious modification of the diffraction pattern motivated our further study, in which we consider whether two very different physical pictures of the gluon distribution in a highly boosted nucleus can be experimentally distinguished via EVMP: in particular we wish to compare the diffraction patterns that emerge when the gluon distribution 1) has normalization dictated by DGLAP evolution and spatial distribution given by the Glauber thickness function and 2) is given by the KLN parameterization (see [189, 190] and references therein) of the Color Glass Condensate (CGC) (see, e.g., [58, 191] for a review). We choose to investigate these two ansätze of the gluon distribution in nuclei as they have been the dominant models used in heavy ion physics calculations to estimate the uncertainty in the viscosity to entropy ratio of the QGP produced at RHIC due to the uncertainty of the currently poorly constrained initial conditions in heavy ion collisions [181, 182].

It is worth taking a moment to comment on some common—yet confusing—terminology in the EVMP field. As mentioned above, to leading order the coherent production of a vector meson in an  $e + A$  collision involves a two-gluon exchange between the  $q\bar{q}$  pair and the nucleus. If one assumes that all two-gluon exchanges occur independently, then one may exponentiate the single two-gluon exchange result. Making this independence assumption is often referred to in the EVMP field as using “saturation” physics because the cross section is unitarized via the exponentiation process. However this “saturation” *does not refer to unitarizing the gluon distribution functions themselves*. For instance in the “IP-Sat” [117] and “b-Sat” [118] models, where “Sat” is short for saturation, the  $x$  evolution of the gluon PDF is effected through the use of the DGLAP equations. On the other hand, the “b-CGC” model [118] incorporates both the exponentiation of the two-gluon exchange *and* the CGC physics of the saturation of the gluon PDF. We note that, in principle, small- $x$  evolution effects and exponentiation effects in the dipole cross section should become appreciable simultaneously [29]. In order to (hopefully) make the presentation more clear, and to simplify some of the numerics, we will not exponentiate the two-gluon exchange; we will present results using only the leading order two-gluon exchange in which the gluon PDF is given either via DGLAP evolution or from the CGC. Any subsequent reference to “saturation”

in this paper will refer to the saturation of the gluon distribution function alone.

**Formalism:** Following [117, 187], the diffractive production of a vector meson from a photon scattering off a target is

$$\frac{d\sigma}{dt} = \frac{1}{16\pi} \left| \int d^2\mathbf{r} \int \frac{dz}{4\pi} \int d^2\mathbf{b} \langle V|\gamma \rangle_T e^{i\mathbf{b}\cdot\mathbf{\Delta}} \frac{d\sigma_{q\bar{q}}}{d^2\mathbf{b}} \right|^2, \quad (84)$$

where  $\langle V|\gamma \rangle_T$  is the overlap of the vector meson wavefunction and the transversely polarized virtual photon wavefunction—the contribution from the longitudinally polarized photon is zero as we are interested in  $Q^2 = 0$  photoproduction—and we used the photon-meson overlap and Gauss-LC model for the  $J/\Psi$  wavefunction from [117]<sup>5</sup>, and  $\mathbf{\Delta}^2 = -t$ .  $d\sigma_{q\bar{q}}/d^2\mathbf{b}$  is the differential cross section for the interaction of the dipole with the target; its form depends on the physics assumptions we make for the nuclear gluon distribution, as we discuss in detail below.

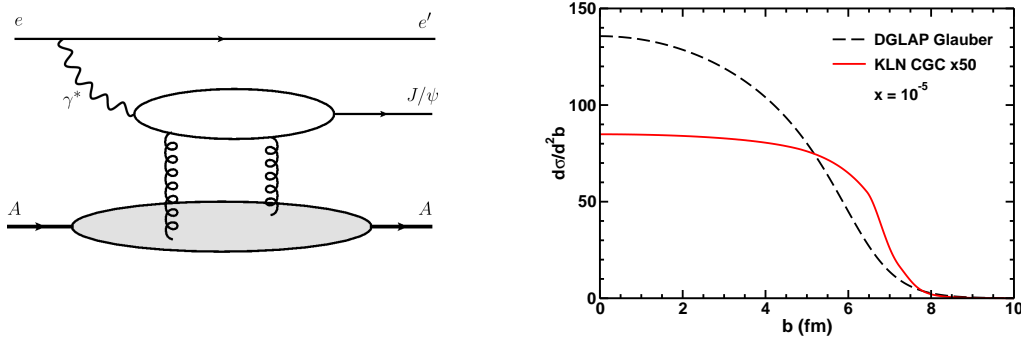


Figure 39. *Left:* Leading order Feynman diagram for the exclusive vector meson production of a  $J/\Psi$  meson. *Right:* The two gluon dipole cross section,  $d\sigma_{q\bar{q}}/d^2\mathbf{b}$  from Eq. 85 for the DGLAP Glauber calculation and Eq. 89 for the KLN version of the CGC (multiplied by 50), which is proportional to the gluon density distribution in a nucleus probed by a  $q\text{-}\bar{q}$  dipole of size  $r = 1 \text{ GeV}^{-1}$  at  $x = 10^{-5}$ .

**DGLAP Evolution in  $x$ , Glauber Distribution of Gluons in  $b$ :** If we assume that the two gluon exchange from the dipole to the nucleus occurs within an individual nucleon then

$$\frac{d\sigma_{q\bar{q}}}{d^2\mathbf{b}} = \frac{\pi^2}{N_c} r^2 \alpha_s(\mu^2) xg(x, \mu^2) T(b), \quad (85)$$

where  $r$  is the size of the dipole,  $\mu = \sqrt{(\mu_0 + C/r^2)}$  is the relevant momentum scale for the dipole,  $xg$  is the gluon distribution function, and

$$T(b) = \frac{1}{2\pi B_G} e^{-b^2/2B_G} \quad (86)$$

is the assumed spatial distribution of gluons in a nucleon. We use the MSTW parameterization of the gluon PDF [7]. As described in [115],  $\mu_0$  and  $C$  are free parameters; as in

<sup>5</sup>Note that the normalization of the  $J/\Psi$  wavefunction in [117] is erroneously reported as a factor of 100 smaller than the correct value; one can readily see this by comparing with the normalization condition defined in [117] and with the results reported in [118]. It is surprising that this error was not noted in [118], in which the results found in [118] are explicitly compared to those in [117].



[115, 117, 122], we take  $\mu_0 = 1 \text{ GeV}^2$  and  $C = 4$ . From HERA data [192] the measured slope of  $d\sigma/dt$  yields  $B_G \approx 4.25 \text{ GeV}^{-2}$  [117]. Then

$$\frac{d\sigma^{DGLAP}}{dt} = 4\pi \sigma_p^2 e^{-B_G t} \left| \int db J_0(b\sqrt{t}) T_A(b) \right|^2, \quad (87)$$

where  $J_0$  is the usual Bessel function,  $T_A(b) \equiv \int dz \rho_A(\sqrt{b^2 + z^2})$ , with  $\int d^2\mathbf{b} T_A(b) = A$ , is the usual thickness function, and  $\rho_A$  is the density of the nucleus (here taken as the Woods-Saxon distribution of  $^{197}\text{Au}$  with the usual  $R = 6.38 \text{ fm}$  and  $a = 0.535 \text{ fm}$  [193]) and

$$\sigma_p \equiv \frac{1}{4\pi} \int d^2\mathbf{r} \int dz \langle V|\gamma \rangle_T \frac{\pi^2}{N_c} r^2 \alpha_s(\mu^2) xg(x, \mu^2). \quad (88)$$

**CGC Distribution of Gluons in  $x$  and  $b$ :** Alternatively we may view the nucleus as a whole and that the gluon distribution is found from the CGC. In this case

$$\frac{d\sigma_{q\bar{q}}}{d^2\mathbf{b}} = \frac{\pi^2}{N_c} r^2 \alpha_s(\mu^2) xg_A(\mu^2, Q_s^2), \quad (89)$$

where  $xg_A$  is the integrated gluon distribution function related to the unintegrated gluon distribution (UGD)  $\phi_A$  by

$$xg_A(\mu^2, Q_s^2) = \int d^2\mathbf{k} \phi_A(k^2, Q_s^2) = \pi \int_0^{k_{max}^2 = \mu^2} dk^2 \phi_A(k^2, Q_s^2) \quad (90)$$

The  $x$  and  $b$  dependence of the two-gluon exchange dipole scattering formula, Eq. 89, comes in implicitly through the  $x$  and  $b$  dependence of  $Q_s^2$  [190],

$$Q_s^2 \equiv \frac{2\pi^2}{C_F} \alpha_s(Q_s^2) xg(x, Q_s^2) T_A(b), \quad (91)$$

where  $C_F \equiv (N_c^2 - 1)/2N_c$ .

In principle one determines the UGD via the JIMWLK evolution equations or, in the large- $N_c$  limit, the BK evolution equations (see [58, 191] and references therein). However, instead of solving the full evolution equations many heavy ion physics calculations use instead the KLN prescription of the CGC (see, e.g., [189, 190]), which attempts to capture the main feature of CGC physics; in particular, the KLN UGD becomes saturated at momenta on the scale of the saturation scale  $Q_s$ . Because of its widespread use in heavy ion physics calculations and in order to simplify our own calculations we, too, will use the KLN UGD,

$$\phi_A^{KLN}(k, Q_s^2) = \frac{\kappa C_F Q_s^2}{2\pi^3 \alpha_s(Q_s^2)} \begin{cases} (Q_s^2 + \Lambda^2)^{-1}, & k^2 \leq Q_s^2 \\ (k^2 + \Lambda^2)^{-1}, & k^2 > Q_s^2, \end{cases} \quad (92)$$

where  $\kappa$  is an  $O(1)$  parameter meant to represent higher order corrections to the UGD, and  $\Lambda = 0.2 \text{ GeV}$  [190].

In principle  $\kappa$  is set by comparing to known experimental observables such as the measured multiplicity at midrapidity at RHIC [194–196] or LHC [197, 198] or to the diffractive cross sections for protons measured at HERA [192]. However we found that the results from the leading order multiplicity formula [189] are linearly dependent on the cutoff taken for  $\alpha_s$ ,

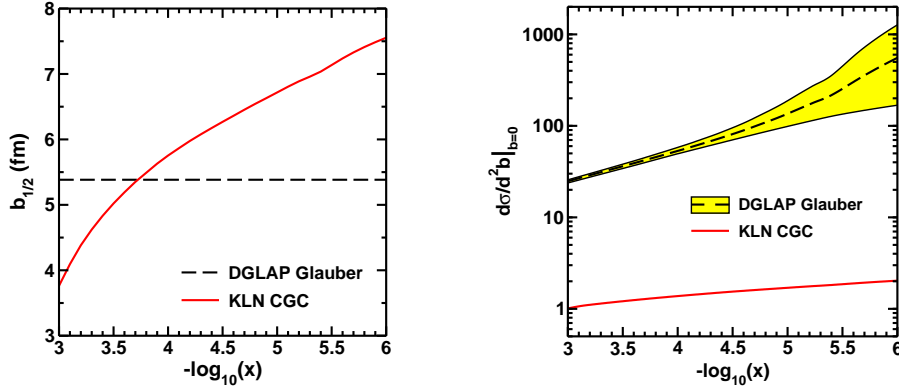


Figure 40. (a)  $b_{1/2}$ , the distance out from the center of the nucleus at which the dipole cross section is half its value at the center of the nucleus as a function of  $x$ . (b)  $d\sigma_{q\bar{q}}/d^2b|_{b=0}$ , the value of the dipole cross section evaluated at the center of the nucleus, as a function of  $x$ . The yellow band represents the 1- $\sigma$  uncertainty (and the dashed black curve the central value) in the DGLAP Glauber results due to the uncertainty in the extracted LO MSTW gluon PDF [7]. Both (a) and (b) are evaluated at dipole size  $r = 1 \text{ GeV}^{-1}$ .

$\alpha_s^{max}$ . The KLN UGD itself, though, is not nearly as sensitive to  $\alpha_s^{max}$ , so the multiplicity prescription does not provide a robust way of setting  $\kappa$ . We note in passing that the centrality dependence of the particles produced via the leading order CGC multiplicity formula using the KLN UGD's also depends on  $\alpha_s^{max}$ . Perhaps the use of the next-to-leading order results in the UGD [199] and/or the production formula [200] will mitigate this dependence enough to make reasonable comparisons of CGC multiplicity to current data. Currently, though, there does not appear to be any quantitative estimate of the size of the dependence of the predicted CGC multiplicity as a function of centrality on  $\alpha_s^{max}$ .  $\kappa$  also cannot be set by comparing to the proton diffractive cross section as the currently available data does not probe regions of  $x$  small enough such that  $Q_s^2$  is a perturbative scale (at least when using the LO MSTW PDFs). In our calculations we will set  $\kappa = 1$ .

It is important to contrast the interaction of the dipole in the KLN CGC approach taken here, in which the  $q\bar{q}$  pair interacts with the entire nucleus, and the Glauber approach, in which the pair interacts with individual nucleons. By interacting with individual nucleons the diffractive cross section for the DGLAP Glauber model picks up an extra exponential suppression in  $t$  proportional to the square of the width of the nucleon,  $B_G$ .

**Results:** In figure 39 we plot  $d\sigma_{q\bar{q}}/d^2b$ , which is directly proportional to the gluon density probed by the heavy quark dipole, for Eq. 85 and Eq. 89, the DGLAP and KLN CGC distributions, respectively. The saturation physics of the CGC has resulted in a wider and flatter gluon distribution than that from the Glauber treatment; the DGLAP growth of the small- $x$  gluon distribution—tamed by the saturation physics of the KLN CGC—leads to a significant, nearly two orders of magnitude, enhancement in the cross section at  $x = 10^{-5}$  compared to that found using the KLN CGC gluon distribution. It is worth noting that figure 39 shows that the KLN prescription for the CGC satisfies the black disk limit even at the level of two gluon exchange whereas application of LO DGLAP evolution leads to a violation of the black disk limit by an order of magnitude at  $x = 10^{-5}$ .

We attempt to quantify the changes in both the nuclear gluonic width and density as a function of  $x$  in figure 40. In figure 40 (a) we show the quantity  $b_{1/2}$ , which we define as

the radius at which the dipole cross section reaches half its value at the origin:

$$\frac{1}{2} \left. \frac{d\sigma_{q\bar{q}}}{d^2\mathbf{b}} \right|_{b=0} \equiv \left. \frac{d\sigma_{q\bar{q}}}{d^2\mathbf{b}} \right|_{b=b_{1/2}}, \quad (93)$$

for the DGLAP and KLN CGC dipole cross sections. We note that even out to extremely small values of  $x \sim 10^{-13}$ ,  $b_{1/2}$  from the KLN CGC continues to rise sublinearly with  $\log(s)$ ; thus the implementation of the KLN CGC used here, with the MSTW gluon PDF, satisfies the Froissart bound [168]. Intriguingly this sublinear (as opposed to linear) growth in radius as a function of  $\log s$  is a surprise compared to other CGC parameterizations [169]. In figure 40 (b) we show the dependence of the dipole cross section at  $b = 0$  on  $x$  for the DGLAP Glauber and KLN CGC models. Note the enormous growth of the dipole cross section as  $x$  decreases for the LO DGLAP-evolved gluonic density. This unitarity-violating enhancement is clearly reduced tremendously with the saturation physics of the KLN CGC. The yellow band in the figure represents the  $1\text{-}\sigma$  uncertainty in the LO MSTW gluon PDF; the dashed black curve represents the result using the central value of the LO gluon PDF [7].

In figure 41 we show the LO diffractive cross section for the EVMP of a  $J/\Psi$  in  $e + A$  collisions, Eq. 84, at  $x = 10^{-3}$ ,  $10^{-4}$ ,  $10^{-5}$ , and  $10^{-6}$  when the gluon density grows in  $x$  and  $b$  according to DGLAP and Glauber overlap or KLN CGC. As before, the yellow band describes the  $1\text{-}\sigma$  uncertainty in the LO MSTW gluon PDF, with the dashed black curve representing the central value. Several KLN CGC curves are plotted; they correspond to the results when the maximum cutoff for  $\alpha_s$ ,  $\alpha_s^{max}$ , is varied from  $\infty$  down to 0.5. Note that all previous figures in this paper used  $\alpha_s^{max} = \infty$ . For the various  $\alpha_s^{max}$  curves in figure 41, the maximum value of the running coupling was set to  $\alpha_s^{max}$  in: the dipole cross section, Eq. 89; the determination of the saturation scale, Eq. 91; and also in the KLN UGD, Eq. 92. While an interesting question, the influence of the uncertainty in the gluon PDF on the saturation scale is beyond the scope of this work. Clearly the KLN CGC diffractive cross section is not particularly sensitive to the specific  $\alpha_s^{max}$  chosen, which implies that higher order running coupling corrections to the result are small. The increase in the radial size of the gluon distribution as a function of  $x$  shown in figure 40 (a) for the KLN CGC model manifests itself as a decrease in the spacings of the diffractive minima,  $\Delta t_{\text{minima}} \sim 1/b_{1/2}$ , as one expects from a Fourier transform; on the other hand the positions in  $t$  of the maxima and minima of the diffractive cross section for the DGLAP Glauber dipole do not change as a function of  $x$ .

The drastically faster increase in the gluon density from the DGLAP evolved PDF seen in figure 40 (b) results in a cross section that increases much faster as a function of  $x$  than for the KLN CGC case. As was shown in [122]<sup>6</sup> the incoherent cross section, in which the nucleus breaks up, begins to dominate the total diffractive cross section by  $t \sim 0.02 \text{ GeV}^{-2}$ . It is likely that the  $t$  dependence of the incoherent EVMP of the two models will be different, although we do not provide a quantitative estimate here: the decrease in cross section as a function of  $t$  for the DGLAP Glauber model will be enhanced by  $\exp(-B_G t)$  due to the assumption that the heavy quark dipole interacts with individual nucleons. And in the case of coherent scattering shown in figure 40, one can discern a stronger  $t$  dependence in the DGLAP Glauber results due precisely to the extra  $\exp(-B_G t)$  factor that

<sup>6</sup>Figure 8 in [187] also shows that the incoherent process quickly dominates the coherent one as a function of  $t$ , although we note that there was an error in the calculation of the figure and that the curves plotted do not correspond to the equations in the text of the paper.

results from treating the nucleus as a collection of individual nucleons. More importantly, the much larger gluon density yields a particularly noticeable difference at  $t = 0$ , where possible nuclear breakup effects are negligible: the DGLAP Glauber case is an order of magnitude larger than the KLN CGC case at  $x = 10^{-3}$  and is a full two orders of magnitude larger at  $x = 10^{-6}$ . Even with the very large PDF uncertainties as  $x$  decreases, there is a clear increase in the coherent diffractive cross section for the DGLAP Glauber dipole compared to the KLN CGC dipole. Note that the enormous normalization differences seen in figure 40 (b) between the DGLAP Glauber and KLN CGC dipoles for the most likely dipole size of  $r = 1 \text{ GeV}^{-1}$  for the photon-vector meson overlap do not directly translate into as large normalization differences in  $d\sigma/dt$  due to the integration over all dipole sizes,  $r$ .

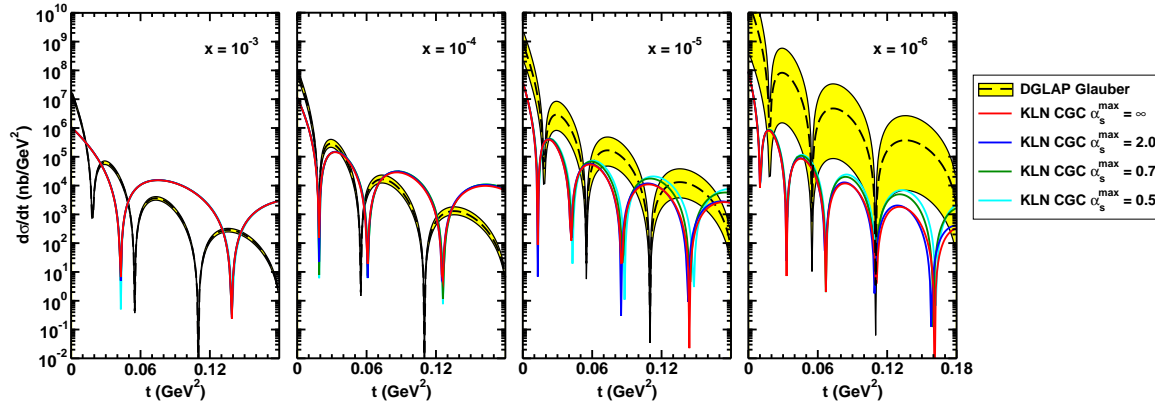


Figure 41. The diffractive cross section  $d\sigma/dt$  from Eq. 84 for 1) the DGLAP evolved dipole cross section, Eq. 85, with gluons spatially distributed according to the Glauber thickness function of the Woods-Saxon distribution and 2) for the dipole cross section from the KLN model of the CGC, Eq. 89, for  $x = 10^{-3}, 10^{-4}, 10^{-5}$ , and  $10^{-6}$ . The various  $\alpha_s^{max}$  values shown explore some of the systematic theoretical uncertainty for the KLN CGC calculation, which is clearly much smaller than the difference between the results from DGLAP evolution and those from saturation physics. The yellow band represents the  $1\text{-}\sigma$  uncertainty (and the dashed black curve the central value) in the DGLAP Glauber results due to the uncertainty in the extracted LO MSTW gluon PDF [7].

**Conclusions and Discussion:** An enormous wealth of information on the gluonic structure of highly relativistic nuclei can be found using exclusive vector meson production. In particular we investigated the experimental signatures of the coherent scattering of a  $c\bar{c}$  dipole onto a nucleus that results in an intact nucleus and a  $J/\Psi$  meson in  $e + A$  collisions at eRHIC energies. We found that the diffractive cross section will readily experimentally differentiate between the two common initial highly boosted nucleus prescriptions used in heavy ion physics phenomenology: 1) the gluon density is found using DGLAP evolution and its spatial distribution is assumed to be proportional to the at-rest Glauber nuclear thickness function and 2) the gluon density and distribution is given by the KLN parameterization of the CGC. In particular there is the exciting possibility of literally watching a nucleus grow with center of mass energy as the positions in  $t$  of the minima and maxima in the diffractive cross section for the saturation physics calculation depend quite strongly on  $\log(x)$ . On the other hand the DGLAP Glauber model yields a nucleus of constant size as a function of  $x$ ; the positions in  $t$  of the diffractive minima and maxima do not change as a function of  $x$ . At the same time one is determining the width of a nucleus in  $e + A$  collisions, one will also measure the  $x$  dependence of the normalization of  $d\sigma/dt$ . Due to

the explosion of small- $x$  gluons the DGLAP Glauber approach yields a normalization that rapidly increases as a function of  $x$ ; additionally the  $t$  dependence of the DGLAP Glauber  $d\sigma/dt$  is also quite strong as it is proportional to  $\exp(-B_G t)$  due to the assumption that the  $q\bar{q}$  dipole interacts with individual nucleons. Conversely the KLN CGC dipole description does not have a strong  $x$  dependence in its normalization due to its inclusion of saturation effects; similarly, the interaction of the dipole with the whole nuclear gluonic wavefunction yields a weaker  $t$  dependence than is displayed by the DGLAP Glauber results.

It is clear that, at the very least, the striking difference between the  $x$  dependence of the peaks and minima from the DGLAP Glauber model and the KLN CGC model are robust: these differences will persist should we use even more sophisticated models of these two physical pictures; the  $x$  dependence of the peaks and minima will persist should we attempt to approximate multiple scattering within the nucleus by exponentiating the dipole cross section, should we use a less approximate CGC calculation such as is found in [199], or should we examine the results from other vector mesons such as the  $\phi$  or  $\rho$ . We regrettably leave the quantification of the diffractive cross section for these more sophisticated physical models and additional vector mesons for future work. Exponentiating the two-gluon exchange cross section will reduce the enormous growth in the diffractive cross section in the DGLAP Glauber picture compared to the CGC case; we suspect this reduction will not be too large, although we also leave the quantification of this reduction to future work.

*Acknowledgments:* The author wishes to thank E. Aschenauer, M. Diehl, Y. Kovchegov, H. Kowalski, T. Lappi, C. Marquet, and T. Ullrich for invaluable discussions and the INT for its hospitality and support. The author wishes to especially thank Y. Kovchegov for reading and commenting on the manuscript.

## 2.5.2 Coherent vs Incoherent

*Tuomas Lappi and Cyrille Marquet*

The purpose of this section is to investigate incoherent diffraction in a simpler context than with inclusive diffraction  $\gamma^* A \rightarrow XY$ , mainly using diffractive vector meson production  $\gamma^* A \rightarrow VY$ , where the diffractive final state  $X$  consists of a vector meson and nothing else,  $A$  stands for the target nucleus and  $Y$  for the final state it may dissociate into. At high energies, the  $q\bar{q}$  dipole that the virtual photon has fluctuated into scatters off the gluonic field of the nucleus before recombining into the vector meson. While this scattering involves a color-singlet exchange, leaving a rapidity gap in the final state, the nucleus can still interact elastically ( $Y = A$ , this is called coherent diffraction) or inelastically (*i.e.* break up, called incoherent diffraction). In this process, the momentum transfer  $t$  can be determined from the meson regardless of the fate of the target, and elastic and inelastic interactions of the target can be experimentally distinguished.

Kinematically, a low invariant mass of the system  $Y$  corresponds to a large rapidity gap in the final state between that system and the vector meson, and implies that the longitudinal momentum of the meson is close to that of the incoming photon. In this case, the eikonal approximation can be assumed to compute the dipole-nucleus scattering. At small values of  $x = (Q^2 + M_V^2)/(Q^2 + W^2)$  where  $Q^2$  is the photon virtuality,  $M_V$  the vector meson mass, and  $W$  the energy of the  $\gamma^* - A$  collision, a target proton can also be considered. Indeed in that case, since partons with an energy fraction as small as  $x$  are probed in the target wave function, the dipole will scatter off large gluon densities generated

by the QCD evolution.

In e+p collisions, the cross-section is maximal at minimum momentum transfer with exclusive production (or coherent diffraction) dominating. As the transfer of momentum gets larger, the role of incoherent diffraction increases and eventually it becomes dominant, typically for momenta bigger than the inverse target size; the elastic contribution decreases exponentially while the inelastic contribution decreases only as a power law. It is known that saturation models describe well the exclusive cross section [117, 118, 201, 202], while the BFKL Pomeron exchange approach works well for the target-dissociation cross-section [203, 204]. In the section on proton breakup, we show that, within the Color Glass Condensate (CGC) picture of the small- $x$  part of the hadronic wave function, both coherent and incoherent diffraction can be described in the same framework. We also explicitly calculate both contributions to the diffractive vector meson production cross-section using the McLerran-Venugopalan (MV) model for the CGC wave function, and discuss phenomenological consequences in the context of a future electron-ion collider [205].

Diffractive dissociation is an aspect of diffraction that changes qualitatively with nuclear targets. Indeed, the structure of incoherent diffraction  $eA \rightarrow eXY$  is more complex than with a proton target, and also can teach us a lot more. In the case of a target nucleus, we expect the following qualitative changes in the  $t$  dependence. First, the low- $|t|$  regime in which the nucleus scatters elastically will be dominant up to a smaller value of  $|t|$  (to about  $|t| = 0.05 \text{ GeV}^2$ ) compared to the proton case, reflecting the bigger size of the nucleus. Then, the nucleus-dissociative regime will be made of two parts: an intermediate regime in momentum transfer up to about  $0.7 \text{ GeV}^2$  where the nucleus will predominantly break up into its constituents nucleons, and a large- $|t|$  regime where the nucleons inside the nucleus will also break up, implying pion production in the  $Y$  system for instance. These are only qualitative expectations, it is crucial to study this aspect of diffraction quantitatively in order to complete our understanding of the structure of nuclei. The transition from the coherent to the intermediate regime is studied in the nuclear breakup section, following Ref. [122].

**Proton breakup:** In diffractive vector meson production, the relevant quantity is (the photon is a right mover, the CGC a left mover, and the gauge is  $\mathcal{A}^+ = 0$ ):

$$T_{\mathbf{xy}}[\mathcal{A}^-] = 1 - \frac{1}{N_c} \text{Tr} \left( U_{\mathbf{y}}^\dagger U_{\mathbf{x}} \right) , \quad \text{with } U_{\mathbf{x}}[\mathcal{A}^-] = \mathcal{P} \exp \left( ig_S \int dz^+ T^c \mathcal{A}_c^-(z^+, \mathbf{x}) \right) . \quad (94)$$

In terms of this object, the differential cross sections for a transversely (T) or longitudinally (L) polarized photon are given by (with  $t = -q_\perp^2$  the momentum transfer squared)

$$\frac{d\sigma_{T,L}}{dt} = \frac{1}{4\pi} \left\langle \left| \int dz d^2x d^2y e^{iq_\perp \cdot (z\mathbf{x} + (1-z)\mathbf{y})} \Psi_{T,L}(z, \mathbf{x} - \mathbf{y}) T_{\mathbf{xy}} \right|^2 \right\rangle_x , \quad (95)$$

where  $2\Psi_T = \Psi_{V|\gamma}^{++} + \Psi_{V|\gamma}^{--}$  and  $\Psi_L = \Psi_{V|\gamma}^{00}$  with

$$\Psi_{V|\gamma}^{\lambda'\lambda}(z, \mathbf{r}) = \sum_{h\bar{h}} [\phi_{\lambda'}^{h\bar{h}}(z, \mathbf{r})]^* \phi_{\lambda}^{h\bar{h}}(z, \mathbf{r}) , \quad (96)$$

the overlap between the photon and meson wave functions.  $\lambda$  and  $h$  denote polarizations and helicities while  $z$  is the longitudinal momentum fraction of the photon carried by the quark and  $\mathbf{x}$  and  $\mathbf{y}$  are the quark and antiquark positions in the transverse plane.

The target average  $\langle . \rangle_x$  is done with the CGC wave function squared  $|\Phi_x[\mathcal{A}^-]|^2$  :

$$\langle f \rangle_x = \int DA^- |\Phi_x[A^-]|^2 f[A^-] . \quad (97)$$

If one had imposed elastic scattering on the target side to describe the exclusive process  $\gamma^* A \rightarrow VA$ , the CGC average would be at the level of the amplitude, and the two-point function  $\langle T_{\mathbf{xy}} \rangle_x$  inside the  $|\cdot|^2$  in (95), recovering the formula often used with dipole models.

Instead, when also including the target-dissociative part, the diffractive cross section involves the 4-point correlator  $\langle T_{\mathbf{xy}} T_{\mathbf{uv}} \rangle_x$ . In order to compute it, we must specify more about the CGC wave function. We shall use the McLerran-Venugopalan (MV) model [21, 22, 206], which is a Gaussian distribution for the color charges which generate the field  $\mathcal{A}$  :

$$|\Phi_x[A^-]|^2 = \exp \left( - \int d^2x d^2y dz^+ \frac{\rho_c(z^+, \mathbf{x}) \rho_c(z^+, \mathbf{y})}{2\mu^2(z^+)} \right) , \quad (98)$$

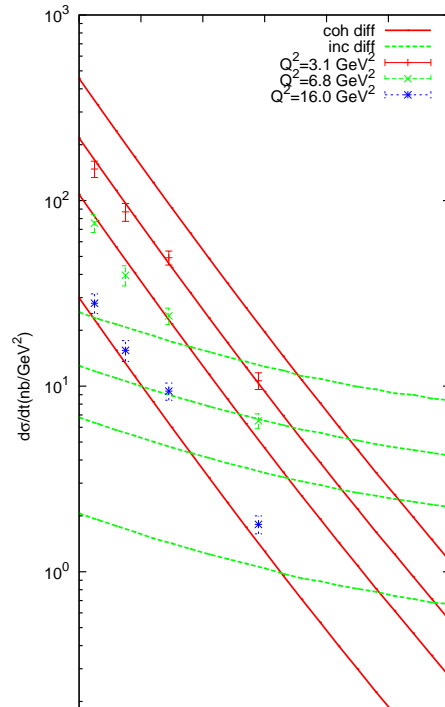
where the color charge  $\rho_c$  and the field  $\mathcal{A}_c^-$  obey the Yang-Mills equation  $-\nabla^2 \mathcal{A}_c^-(z^+, \mathbf{x}) = g_S \rho_c(z^+, \mathbf{x})$ . The variance of the distribution is the transverse color charge density squared along the projectile's path  $\mu^2(z^+)$ , with

$$\langle \rho_c(z^+, \mathbf{x}) \rho_d(z'^+, \mathbf{y}) \rangle = \delta_{cd} \delta(z^+ - z'^+) \delta^{(2)}(\mathbf{x} - \mathbf{y}) \mu^2(z^+) . \quad (99)$$

The only parameter is the saturation momentum  $Q_s$ , with  $Q_s^2$  proportional to the integrated color density squared. Note that there is no  $x$  dependence in the MV model, it should be considered as an initial condition to the small- $x$  evolution.

The MV distribution is a Gaussian distribution, therefore one can compute any target average by expanding the Wilson lines in powers of  $g_S \mathcal{A}_c^-$  (see (94)), and then use Wick's theorem [207, 208]. The results for the 4-point function  $\langle T_{\mathbf{xy}} T_{\mathbf{uv}} \rangle$  are given in [209]. We note that, in the large- $N_c$  limit, one has  $\langle T_{\mathbf{xy}} T_{\mathbf{uv}} \rangle = \langle T_{\mathbf{xy}} \rangle \langle T_{\mathbf{uv}} \rangle$ , which means that at small- $x$ , the target-dissociative part of the diffractive cross-section is suppressed at large  $N_c$ , compared to the exclusive part.

The numerical results presented below are obtained with the  $x$  evolution of the saturation scale modeled as in [111]:  $Q_s(x) = (x_0/x)^{\lambda/2}$  GeV, with  $\lambda = 0.277$  and  $x_0 = 4.1 \cdot 10^{-5}$  for the case of a target proton. The collinear logarithm of  $Q_s$  is neglected, which corresponds to exact geometric scaling [44, 170, 210]:  $F(x, \mathbf{r}) = F[\mathbf{r}^2 Q_s^2(x)]$ . As an illustration, the resulting cross-section for diffractive  $J/\Psi$  production is displayed in Fig.1, and separated into its coherent and incoherent contributions. The light-cone Gaussian  $J/\Psi$  wave function [211, 212] has been used in (96). At small values of  $|t|$  where coherent diffraction dominates, our results are in agreement with HERA data [213] (one can get a better agreement with more realistic saturation models [117, 118, 201, 202], but this is not our point). Our model indicates that



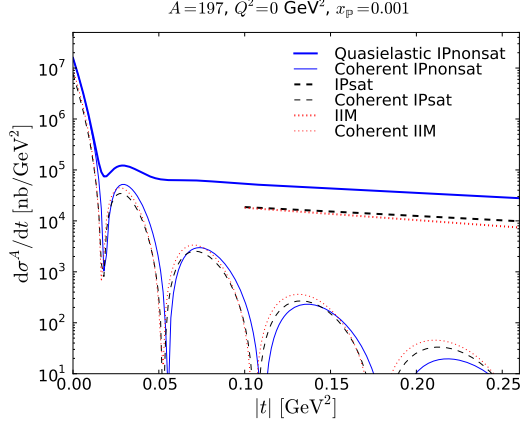


Figure 43. The quasielastic and coherent diffractive  $J/\Psi$  cross sections in gold nuclei at  $Q^2 = 0$  and  $x_p = 0.001$ . Shown are the IPsat and IIM parametrizations. We also show the result for the linearized “IPnonsat” version (used e.g. in Ref. [214]) where the incoherent cross section is explicitly  $A$  times that of the proton. Our approximation (104) is not valid for small  $|t|$ ; the corresponding part of the distribution has been left out.

for  $|t| > 0.7 \text{ GeV}^2$  or so (this value slightly decreases when  $Q^2$  increases), incoherent diffraction starts to dominate. This may be the reason why the data on exclusive production stop: there is too much proton-dissociative ‘background’. We observe that this part of the cross-section decreases as a power law with  $|t|$ , rather than exponentially as the exclusive part does.

In the case of a target nucleus, we expect the following qualitative changes in the  $t$  dependence. First, the low- $|t|$  regime with elastic scattering of the nucleus will be dominant up to a smaller value of  $|t|$  compared to the proton case, reflecting the bigger size of the nucleus. Then, the nucleus-dissociative part will be split into two: an intermediate regime in momentum transfer up to about  $0.7 \text{ GeV}^2$  where the nucleus will predominantly break up into its constituents nucleons, and a large- $|t|$  regime where the nucleons inside the nucleus will also break up, implying pion production in the  $Y$  system for instance.

The model discussed in this work is well adapted to describe the low- and large- $|t|$  regimes, but not the intermediate regime since the constituent nucleons are absent from the description (??). This problem has been addressed in a complementary setup in the case of inclusive diffraction off nuclei [120, 121], and the coherent diffraction regime was found to be dominant up to about  $|t| = 0.05 \text{ GeV}^2$ . The vector meson production case will be addressed next. While in the proton case, both exclusive and diffractive processes can be measured, it is likely that at a future electron-ion collider, the exclusive cross section cannot be extracted: when the momentum transfer is small enough for the nucleus to stay intact, then it will escape too close to the beam to be detectable. Therefore the diffractive physics program will rely on our understanding of incoherent diffraction.

**Nuclear breakup into its constituent nucleons:** To simplify our calculation we will here use a factorized impact parameter profile for the dipole cross section in a proton

$$\frac{d\sigma_{\text{dip}}^p}{d^2\mathbf{b}_T}(\mathbf{b}_T, \mathbf{r}_T, x) = 2(1 - S_p(\mathbf{r}_T, \mathbf{b}_T, x)) = 2T_p(\mathbf{b}_T)\mathcal{N}(r, x), \quad (100)$$

where  $T_p$  is a Gaussian profile  $T_p(\mathbf{b}_T) = \exp(-b^2/2B_p)$ . In the following we shall consider



two dipole cross section parametrizations, the IIM model [173, 215, 216], for which we take  $B_p = 5.59 \text{ GeV}^{-2}$ , and a factorized approximation of the IPSat parametrization [117, 118], for which  $B_p = 4.0 \text{ GeV}^2$ . See [122] for a discussion of the origin of these values in different fits.

To extend the dipole cross section from protons to nuclei we will take the independent scattering approximation that is usually used in Glauber theory and write the  $S$ -matrix as

$$S_A(\mathbf{r}_T, \mathbf{b}_T, x) = \prod_{i=1}^A S_p(\mathbf{r}_T, \mathbf{b}_T - \mathbf{b}_{T_i}, x). \quad (101)$$

Here  $\mathbf{b}_{T_i}$  are the nucleon coordinates. This independent scattering assumption natural in IPSat-like parametrizations or the MV-model, where, denoting  $r = |\mathbf{r}_T|$ ,  $S(\mathbf{r}_T) \sim e^{-r^2 Q_s^2/4}$  with a saturation scale  $Q_s^2$  proportional to the nuclear thickness  $T_A(b)$ . High energy evolution, however, introduces an anomalous dimension that leads, in the nuclear case, to what could be called leading twist shadowing. With an anomalous dimension  $S \sim e^{-(Q_s r)^{2\gamma}}$  with  $\gamma \neq 1$ , a proportionality  $Q_s^2 \sim T_A(b)$  is not equivalent to Eq. (101). A solution to this problem (see also the more detailed discussion in [120]) would require a realistic impact parameter dependent solution to the BK [33, 39, 62] equation which, we feel fair to say, is not yet available. We point the reader e.g. to Ref. [169] for a discussion of the difficulties. These are related to the long distance Coulomb tails that, physically, are regulated at the confinement length scale that is not enforced in a first principles weak coupling calculation.

The average over the positions of the nucleon in the nucleus is denoted here by

$$\langle \mathcal{O}(\{\mathbf{b}_{T_i}\}) \rangle_N \equiv \int \prod_{i=1}^A [d^2 \mathbf{b}_{T_i} T_A(\mathbf{b}_{T_i})] \mathcal{O}(\{\mathbf{b}_{T_i}\}). \quad (102)$$

Here  $T_A$  is the Woods-Saxon distribution with nuclear radius  $R_A = (1.12A^{1/3} - 0.86A^{-1/3}) \text{ fm}$  and surface thickness  $d = 0.54 \text{ fm}$ . This expectation value is equivalent to the average over nucleon configurations in a Monte Carlo Glauber calculation. We are assuming that the positions  $\mathbf{b}_{T_i}$  are independent, i.e. neglecting nuclear correlations that would be a subject of interest in their own right (see e.g. [217]). The coherent cross section is obtained by averaging the amplitude before squaring it,  $|\langle \mathcal{A} \rangle_N|^2$ , and the incoherent one is the variance  $\langle |\mathcal{A}|^2 \rangle_N - |\langle \mathcal{A} \rangle_N|^2$  that measures the fluctuations of the gluon density inside the nucleus. Because  $\langle \mathcal{A} \rangle_N$  is a very smooth function of  $\mathbf{b}_T$ , its Fourier transform vanishes rapidly for  $\Delta \gtrsim 1/R_A$ . Therefore at large  $\Delta$  the quasielastic cross section is almost purely incoherent.

The cross section for quasielastic vector meson production is now expressed in terms of the dipole scattering amplitude as

$$\begin{aligned} \frac{d\sigma^{\gamma^* A \rightarrow V A^*}}{dt} &= \frac{R_g^2(1 + \beta^2)}{16\pi} \int \frac{dz}{4\pi} \frac{dz'}{4\pi} d^2 \mathbf{r}_T d^2 \mathbf{r}_{T'} \\ &\times [\Psi_V^* \Psi](r, z, Q) [\Psi_V^* \Psi](r', z', Q) \left\langle |\mathcal{A}_{q\bar{q}}|^2(x_{\mathbb{P}}, r, r', \Delta_T) \right\rangle_N, \end{aligned} \quad (103)$$

where we have applied corrections for the skewedness  $R_g$  and real part of the scattering amplitude (see e.g. [119]) We now average the square of the dipole scattering amplitude over the nucleon coordinates, using the assumptions of Eqs. (101) and (100) and taking the large  $A$  limit. We are additionally assuming that  $T_A$  is a smooth function on the distance scale defined by  $B_p$ . Averaging the square of the amplitude gives the total quasielastic contribution.

Note that Eqs. (101) and (100) have enabled us to write the leading contributions as proportional to the (Gaussian) proton impact parameter profile, which can then be Fourier-transformed analytically. Giving up either of these approximations would force us to numerically Fourier-transform the “lumpy”  $b$ -dependence corresponding to a fixed configuration of the nucleon positions. Keeping only the terms that contribute at large  $|t| \gg 1/R_A^2$  leaves us with the expression

$$|A_{q\bar{q}}|^2(x_{\mathbb{P}}, r, r', \Delta_T) = 16\pi^2 B_p^2 A \int d^2\mathbf{b}_T \times e^{-B_p \Delta_T^2} e^{-2\pi B_p (A-1) T_A(b) [\mathcal{N}(r) + \mathcal{N}(r')]} \mathcal{N}(r) \mathcal{N}(r') T_A(b). \quad (104)$$

Equation (104) has a very clear interpretation. The squared amplitude is proportional to  $A$  times the squared amplitude for scattering off a proton, corresponding to the dipole scattering independently off the nucleons in a nucleus. This sum of independent scatterings is then multiplied by a nuclear attenuation factor which accounts for the requirement that the dipole must *not* scatter inelastically off the other  $A-1$  nucleons in the target (otherwise the interaction would not be diffractive). Note that factor  $4\pi B_p \mathcal{N}(r, x_{\mathbb{P}}) = \sigma_p(r, x_{\mathbb{P}})$  is the proton-dipole cross section for a dipole of size  $r$ . Thus this attenuation corresponds to the probability of a dipole with a cross section which is the average of dipoles with  $r$  and  $r'$  to pass through the nucleus. A similar expression can be found e.g. in Ref. [218].

The coherent cross section in our approximation is given by

$$\frac{d\sigma^{\gamma^* A \rightarrow V A}}{dt} = \frac{R_g^2(1 + \beta^2)}{16\pi} |\langle \mathcal{A}(x_{\mathbb{P}}, Q^2, \Delta_T) \rangle_N|^2, \quad (105)$$

where in the large  $A$  and smooth nucleus limit the amplitude is

$$\langle \mathcal{A}(x_{\mathbb{P}}, Q^2, \Delta_T) \rangle_N = \int \frac{dz}{4\pi} d^2\mathbf{r}_T d^2\mathbf{b}_T e^{-i\mathbf{b}_T \cdot \Delta_T} [\Psi_V^* \Psi](r, Q^2) 2 \left[ 1 - e^{-2\pi B_p A T_A(b) \mathcal{N}(r, x_{\mathbb{P}})} \right]. \quad (106)$$

Figure 2.5.2 summarizes the  $t$ -dependence of the quasielastic and coherent cross sections. Also shown is the approximation used in [214] where nonlinear effects are left out. The most striking result is the large suppression by a factor of  $\sim 3$  of the incoherent cross section due to nonlinear effects. The incoherent and coherent curves cross around  $|t| \approx 0.05 \text{ GeV}^2$ , as anticipated. With a very good detection of the nuclear breakup events the first, even the second, diffractive dips in the coherent cross section could be measurable at the EIC, providing detailed information about the average spatial distribution of gluons inside the nucleus. For understanding the initial conditions of ultrarelativistic heavy ion collisions what has turned out to be equally important are the fluctuations in the gluon density, which are directly measured by the incoherent part of the spectrum.

### 2.5.3 Electroproduction of $J/\Psi$

*Boris Z. Kopeliovich*

**Proton target:** The diffractive electro-production of charmonia and the charmonium-nucleon elastic scattering are closely related. The amplitudes of diffractive electro-production

of a charmonium and elastic charmonium-proton scattering in the dipole approach have the form,

$$\mathcal{M}_{\gamma^* p}(s, Q^2) = \sum_{\mu, \bar{\mu}} \int_0^1 d\alpha \int d^2 r_T \Phi_{\Psi}^{*(\mu, \bar{\mu})}(\alpha, \vec{r}_T) \sigma_{q\bar{q}}(r_T, s) \Phi_{\gamma^*}^{(\mu, \bar{\mu})}(\alpha, \vec{r}_T, Q^2); \quad (107)$$

$$\mathcal{M}_{\Psi p}(s) = \sum_{\mu, \bar{\mu}} \int_0^1 d\alpha \int d^2 r_T \Phi_{\Psi}^{*(\mu, \bar{\mu})}(\alpha, \vec{r}_T) \sigma_{q\bar{q}}(r_T, s) \Phi_{\Psi}^{(\mu, \bar{\mu})}(\alpha, \vec{r}_T). \quad (108)$$

Here  $\mu$  and  $\bar{\mu}$  are the spin indexes of the  $c$  and  $\bar{c}$  quarks,  $Q^2$  is the photon virtuality,  $\Phi_{\gamma^*}(\alpha, r_T, Q^2)$  is the light-cone distribution function of the photon for a  $c\bar{c}$  fluctuation of separation  $r_T$  and relative fraction  $\alpha$  of the photon light-cone momentum carried by  $c$  or  $\bar{c}$ . Correspondingly,  $\Phi_{\Psi}(\alpha, \vec{r}_T)$  is the light-cone wave function of  $J/\Psi$ , or  $\Psi'$ , or  $\chi$ .

The wave functions of charmonia are calculated in [219] solving the Schrödinger equation with four realistic potentials, which are labelled as COR [220], BT [221], LOG [222], and POW [223]. Then one should make a Lorentz boost from the charmonium rest frame to the infinite momentum frame, and to switch from 3-dimensional coordinates to the light-cone variables,  $p_T$  and  $\alpha$ , which are the  $c$ -quark transverse and fractional longitudinal momenta respectively. This was done in [219] using the popular prescription [224].

The important ingredient of the calculations done in [219] (compare with [225]) is the Melosh spin rotation [226] which relates the 2-dimensional spinors  $\chi_c$  and  $\chi_{\bar{c}}$ , describing  $c$  and  $\bar{c}$  in the infinite momentum frame, to the spinors  $\bar{\chi}_c$  and  $\bar{\chi}_{\bar{c}}$  in the rest frame:

$$\bar{\chi}_c = \hat{\mathbf{R}}(\alpha, \vec{p}_T) \chi_c, \quad \bar{\chi}_{\bar{c}} = \hat{\mathbf{R}}(\mathbf{1} - \alpha, -\vec{p}_T) \chi_{\bar{c}}, \quad (109)$$

where the matrix  $R(\alpha, \vec{p}_T)$  has the form:

$$\hat{R}(\alpha, \vec{p}_T) = \frac{m_c + \alpha M - i [\vec{\sigma} \times \vec{n}] \vec{p}_T}{\sqrt{(m_c + \alpha M)^2 + p_T^2}}. \quad (110)$$

Since the  $c\bar{c}$  pair is in  $S$ -wave, the spatial and spin dependences in the wave function factorize, and one arrives at the following light cone wave function of the  $c\bar{c}$  in the infinite momentum frame

$$\Phi_{\psi}^{(\mu, \bar{\mu})}(\alpha, \vec{p}_T) = U^{(\mu, \bar{\mu})}(\alpha, \vec{p}_T) \cdot \Phi_{\psi}(\alpha, \vec{p}_T), \quad (111)$$

where

$$U^{(\mu, \bar{\mu})}(\alpha, \vec{p}_T) = \chi_c^{\mu\dagger} \hat{R}^\dagger(\alpha, \vec{p}_T) \vec{\sigma} \cdot \vec{e}_{\psi} \sigma_y \hat{R}^*(1 - \alpha, -\vec{p}_T) \sigma_y^{-1} \tilde{\chi}_{\bar{c}}^{\bar{\mu}}. \quad (112)$$

Now we can determine the light-cone wave function in the mixed longitudinal momentum - transverse coordinate representation:

$$\Phi_{\psi}^{(\mu, \bar{\mu})}(\alpha, \vec{r}_T) = \frac{1}{2\pi} \int d^2 p_T e^{-i\vec{p}_T \vec{r}_T} \Phi_{\psi}^{(\mu, \bar{\mu})}(\alpha, \vec{p}_T). \quad (113)$$

With this wave function and with the standard distribution functions of the photon one can calculate the amplitudes Eqs. (107)-(108) and predict the cross section of  $J/\Psi$  photoproduction on a proton. The results for the energy dependence are compared with HERA data (see references in [219]) in Fig. 44. The calculation was done in [219] with two parametrizations of the dipole cross section labelled as GBW [80] and KST [87]. We see

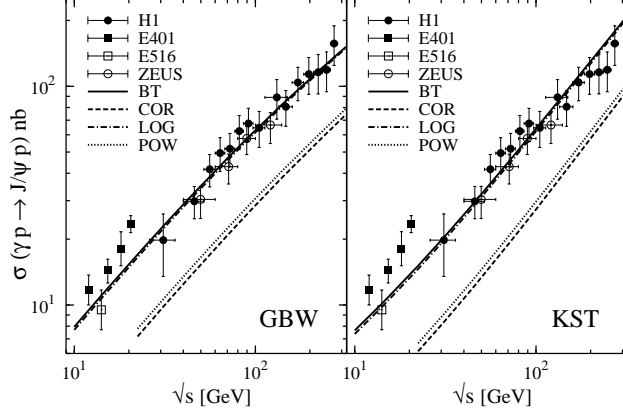


Figure 44. Integrated cross section for elastic photoproduction  $\gamma p \rightarrow J/\Psi p$  with real photons ( $Q^2 = 0$ ) as a function of the energy calculated with GBW and KST dipole cross sections and for four potentials to generate  $J/\Psi$  wave functions. Experimental data points from the H1 and ZEUS experiments.

that only BP and LOG potentials well describe the data, which, however, are not sensitive to the choice of the phenomenological dipole cross section.

The  $Q^2$  dependence of the cross section is compared to HERA data (see references in [219]) in Fig. 45 (left) for the LOG and BT potentials.

It turns out that the effects of Melosh spin rotation have a gross impact on the cross section of elastic photoproduction  $\gamma p \rightarrow J/\Psi(\psi)p$ . It increases the photoproduction cross section by about 50%. These effects have even more dramatic impact on  $\psi'$  increasing the photoproduction cross section by a factor 2-3 eliminating the large discrepancy with data observed previously [225].

Eventually we are in a position to predict the charmonium-proton total cross section, which is impossible to extract directly from photoproduction data, either on proton, or nuclear target. Indeed, neither vector dominance [227], nor Glauber model [228] can be used for data analysis. We believe that the only way is to predict the charmonium cross section within a model, which successfully describe data on photoproduction in a parameter free way. Our predictions for the energy dependent charmonium-proton total cross section is depicted in Fig. 45 (right) for  $J/\Psi$  and  $\Psi'$ .

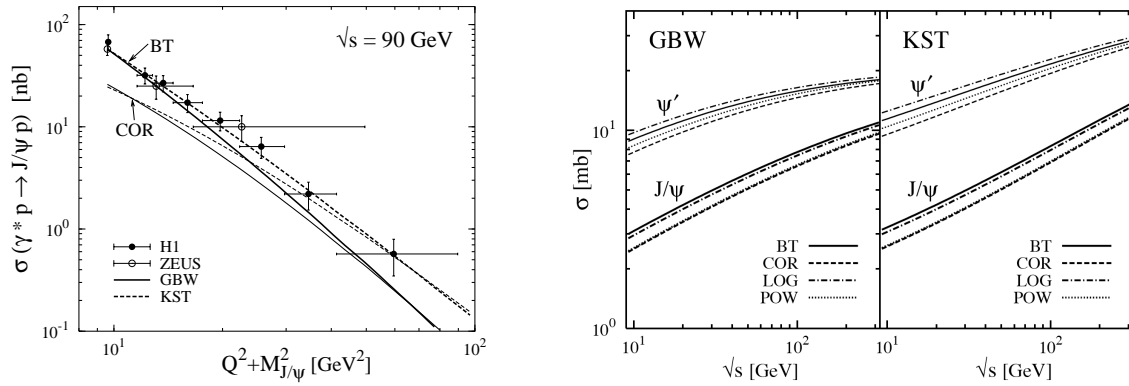


Figure 45. *Left*: Integrated cross section for elastic photo production as a function of the photon virtuality  $Q^2 + M_{J/\Psi}$  at energy  $\sqrt{s} = 90$  GeV. *Right*: Total  $J/\Psi$ - $p$  (thick curves) and  $\Psi'$ - $p$  (thin curves) cross sections with the GBW and KST parameterizations for the dipole cross section.

**Nuclear targets:** Charmonium photoproduction on nuclei is controlled by two length

scales. The first one is called coherence length,

$$l_c = \frac{2\nu}{M_{c\bar{c}}^2 + Q^2} \approx \frac{2\nu}{M_{J/\Psi}^2 + Q^2}. \quad (114)$$

This length or time scale can be interpreted as the lifetime of a  $\bar{c}c$  fluctuation in the projectile photon in the nuclear rest frame. When  $l_c$  is short compared to the mean nucleon spacing, one can treat  $\bar{c}c$  production as instantaneous, with following propagation of the  $\bar{c}c$  dipole through the nucleus. In the opposite limit of  $l_c \gg R_A$  the  $\bar{c}c$  dipole propagates and attenuates through the whole nucleus.

The next scale is the formation length,

$$l_f = \frac{2\nu}{M_{\Psi'}^2 - M_{J/\Psi}^2}, \quad (115)$$

which characterizes the formation of the charmonium wave function. Indeed, the produce  $\bar{c}c$  dipole has a certain size and interaction cross section, but does not have any certain mass. It might be the  $J/\Psi$ , or its radial excitation. To disentangle between them, takes time Eq. 115) according to the uncertainty principle.

The cross section of charmonium photoproduction on nuclei is easiest to write in the limit of long  $l_c \gg R_A$ . In this case the size of the  $\bar{c}c$  dipoles "frozen" by Lorentz time dilation for propagation of the dipole through the nucleus. The cross sections of incoherent (the nucleus break up to fragments) and coherent (the nucleus remains intact) production have the form [228, 229],

$$\sigma_{inc}^{\gamma^* A}(s, Q^2) = \int d^2b T_A(b) \left| \left\langle \Psi \left| \sigma_{\bar{c}c}(r_T, s) \exp \left[ -\frac{1}{2} \sigma_{\bar{c}c}(r_T, s) T_A(b) \right] \right| \Psi_{c\bar{c}}^{T,L} \right\rangle \right|^2 \quad (116)$$

$$\sigma_{coh}^{\gamma^* A}(s, Q^2) = \int d^2b \left| \left\langle \Psi \left| 1 - \exp \left[ -\frac{1}{2} \sigma_{\bar{c}c}(r_T, s) T_A(b) \right] \right| \Psi_{c\bar{c}}^{T,L} \right\rangle \right|^2, \quad (117)$$

where  $\Psi_{c\bar{c}}^{T,L}$  are the photon wave functions given by Eq. (29);  $\Psi(\vec{r}_T, \alpha)$  is the charmonium light-cone wave function calculated in the previous section. These expressions are significantly different from the Glauber model [230] and effectively include the Gribov corrections in all orders.

We define the nuclear ratios for coherent and incoherent reactions as,

$$R_{\Psi}^{coh}(s, Q^2) = \frac{\sigma_{coh}^{\gamma^* A}(s, Q^2)}{A \sigma^{\gamma^* N}(s, Q^2)}, \quad R_{\Psi}^{inc}(s, Q^2) = \frac{\sigma_{inc}^{\gamma^* A}(s, Q^2)}{A \sigma^{\gamma^* N}(s, Q^2)}. \quad (118)$$

These ratios calculated with Eqs. (116)-(117) for real photoproduction of  $J/\Psi$  and  $\Psi'$  are depicted as function of energy in Fig. 46. For coherent production the cross section rises with  $A$  nearly as  $A^{4/3}$ , so the ratio may reach a large magnitude.

One can also predict the dependence on the momentum transfer  $\vec{k}_T$  for the charmonium electroproduction on nuclei. In the case of incoherent production this dependence is the same as for production on free nucleons. However, in coherent production the nuclear formfactor comes into play and one has

$$\frac{d\sigma_{coh}^{\gamma^* A}(s, Q^2)}{d^2k_T} = \left| \int d^2b e^{i\vec{k}_T \cdot \vec{b}} \left\langle \Psi \left| 1 - \exp \left[ -\frac{1}{2} \sigma_{\bar{q}q}(r_T, s) T_A(b) \right] \right| \Psi_{c\bar{c}}^{T,L} \right\rangle \right|^2. \quad (119)$$

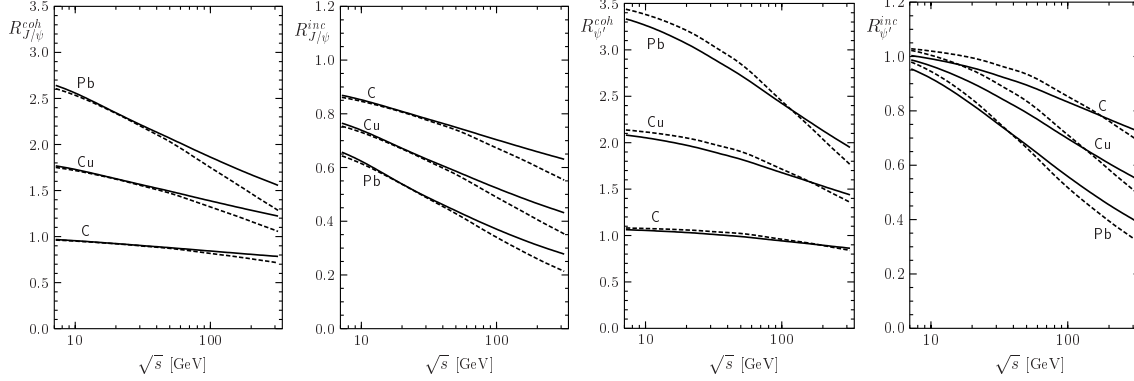


Figure 46. Ratios  $R_{J/\psi}^{coh}$ ,  $R_{J/\psi}^{inc}$ ,  $R_{\psi'}^{coh}$  and  $R_{\psi'}^{inc}$  for coherent and incoherent production on carbon, copper and lead as function of  $\sqrt{s}$  and at  $Q^2 = 0$ . The solid and dashed curves refer to the GBW and KST parameterizations respectively.

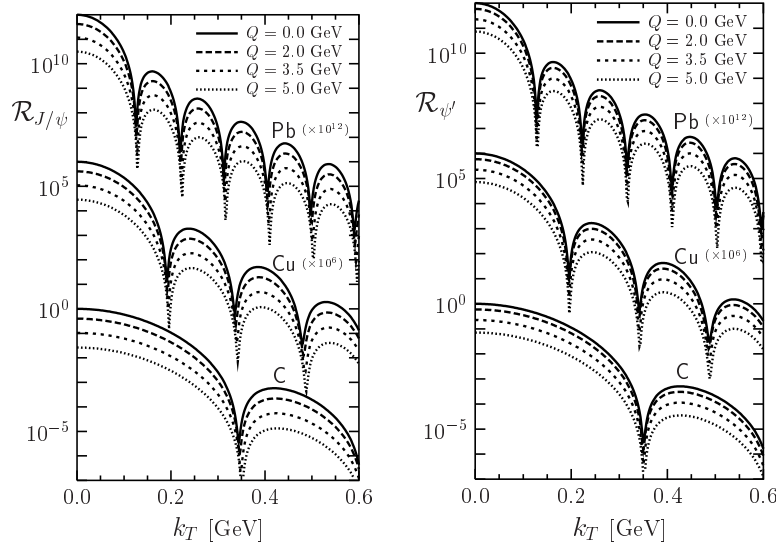


Figure 47. Ratios  $\mathcal{R}_{J/\psi}$  and  $\mathcal{R}_{\psi'}$  as functions of  $k_T$  at  $s = 4000 \text{ GeV}^2$  for different values of  $Q$ . All curves are calculated with the GBW parameterization of the dipole cross section.

We introduce the ratios the sum of  $T$  and  $L$  components of Eq. (119) to the cross section at  $Q^2 = 0$  and  $k_T = 0$ ,

$$\mathcal{R}(s, Q^2, k_T) = \frac{d\sigma_{coh}^{*\gamma A}(s, Q^2)}{d^2k_T} \bigg/ \frac{d\sigma_{coh}^{*\gamma A}(s, Q^2 = 0)}{d^2k_T} \bigg|_{k_T=0} \quad (120)$$

This ratio is plotted in Fig. 47 as functions of  $k_T$  at  $s = 4000 \text{ GeV}^2$  for different virtualities  $Q$  of the photon. We see that the  $k_T$  dependences are rather similar for  $J/\psi$  and  $\Psi'$ . The shape of the distribution is determined mainly by the nuclear geometry (and not by the size of the (small) charmonium). The calculated curves show the familiar diffraction pattern known from elastic scattering on nuclei.

Interesting that the effects of gluon shadowing, calculated in [229] do not affect much the shape and position of the minima in  $k_T$  dependence of the coherent cross section. However the cross section integrated over  $k_T$  may be significantly affected by gluon shadowing. To see the magnitude of gluon shadowing we introduce the ratio of the cross sections calculated

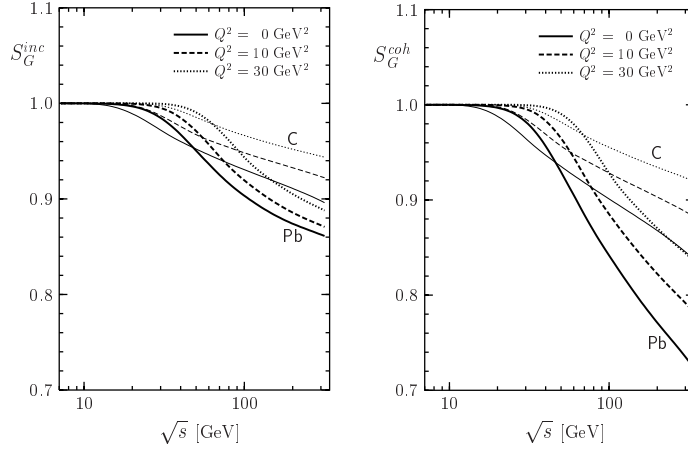


Figure 48. Ratios  $S_g(s, Q^2)$ , defined in (121), of cross sections calculated with and without gluon shadowing for incoherent and coherent  $J/\Psi$  production.

with and without gluon shadowing,

$$S_g(s, Q^2) = \frac{\sigma_g^{\gamma^* A}(s, Q^2)}{\sigma^{\gamma^* A}(s, Q^2)}. \quad (121)$$

for incoherent and coherent exclusive charmonium electroproduction. The predicted effects of gluon shadowing are depicted in Fig. 17. We only plot ratios for  $J/\Psi$  production, because ratios for  $\Psi'$  are practically the same. All curves are calculated with the GBW parameterization of the dipole cross section. We see that the onset of gluon shadowing happens at a c.m. energy of few tens GeV. This is controlled by the longitudinal nuclear form factor

$$F_A(q_c^g, b) = \frac{1}{T_A(b)} \int_{-\infty}^{\infty} dz \rho_A(b, z) e^{iq_c z} \quad (122)$$

where the longitudinal momentum transfer  $q_c^g = 1/l_c^g$ . For the onset of gluon shadowing  $q_c^g R_A \gg 1$  one can keep only the double scattering shadowing correction,

$$S_g \approx 1 - \frac{1}{4} \sigma_{eff} \int d^2b T_A^2(b) F_A^2(q_c^g, b), \quad (123)$$

where  $\sigma_{eff}$  is the effective cross section which depends on the dynamics of interaction of the  $\bar{q}qg$  fluctuation with a nucleon.

It was found in [79] that the coherence length for gluon shadowing is rather short,  $l_c^g \approx (10 x m_N)^{-1}$ , where Bjorken  $x$  in our case should be an effective one,  $x = (Q^2 + M_\Psi^2)/2m_N\nu$ . The onset of shadowing according to (122) and (123) should be expected at  $q_c^2 \sim 3/(R_A^{ch})^2$  corresponding to  $s_g \sim 10m_N R_A^{ch}(Q^2 + M_\Psi^2)/\sqrt{3}$ , where  $(R_A^{ch})^2$  is the mean square of the nuclear charge radius. This estimate is in a good agreement with Fig. 17. Remarkably, the onset of shadowing is delayed with rising nuclear radius and  $Q^2$ . This follows directly from Eq. (123) and the fact that the formfactor is a steeper falling function of  $R_A$  for heavy than for light nuclei, provided that  $q_c^g R_A \gg 1$ .

At medium energies the effects of finite coherence length,  $l_c \sim R_A$ , skipped here, become important. They increase the incoherent and suppress coherent cross sections of charmonium electroproduction. One can find the details of the corresponding calculations in [229].

#### 2.5.4 Exclusive processes in $eA$ collisions

*Victor P. Gonçalves*

Exclusive processes in deep inelastic scattering (DIS) have appeared as key reactions to trigger the generic mechanism of diffractive scattering. In particular, diffractive vector meson production and deeply virtual Compton scattering (DVCS) have been extensively studied at HERA and provide a valuable probe of the QCD dynamics at high energies. The cross sections for exclusive processes in DIS are proportional to the square of the scattering amplitude, which makes them strongly sensitive to the underlying QCD dynamics.

In this contribution we present our estimate for the coherent and incoherent cross sections for exclusive  $\rho$ ,  $J/\Psi$ , and  $\phi$  production as well as for the nuclear DVCS making use of the numerical solution of the Balitsky-Kovchegov equation including running coupling corrections in order to estimate the contribution of the saturation physics to exclusive processes (For more details and references see Refs. [231, 232]).

**Exclusive production:** In the color dipole approach, the exclusive production  $\gamma^* A \rightarrow EY$  ( $E = \rho, \phi, J/\Psi$  or  $\gamma$ ) in electron-nucleus interactions at high energies (large coherence length:  $l_c \gg R_A$ ) is given by

$$\sigma^{coh}(\gamma^* A \rightarrow EA) = \int d^2b \langle \mathcal{N}^A(x, r, b) \rangle^2 \quad (124)$$

where

$$\langle \mathcal{N} \rangle = \int d^2r \int dz \Psi_E^*(r, z) \mathcal{N}^A(x, r, b) \Psi_{\gamma^*}(r, z, Q^2) \quad (125)$$

and  $\mathcal{N}(x, r, b)$  is the forward dipole-target scattering amplitude for a dipole with size  $r$  and impact parameter  $b$  which encodes all the information about the hadronic scattering, and thus about the non-linear and quantum effects in the hadron wave function. On the other hand, if the nucleus scatters inelastically, i.e. breaks up ( $Y = X$ ), the process is denoted incoherent production. In this case one sums over all final states of the target nucleus, except those that contain particle production. The  $t$  slope is the same as in the case of a nucleon target. Therefore we have:

$$\sigma^{inc}(\gamma^* A \rightarrow EX) = \frac{|\text{Im } \mathcal{A}(s, t=0)|^2}{16\pi B_E} \quad (126)$$

where at high energies ( $l_c \gg R_A$ ) :

$$|\text{Im } \mathcal{A}|^2 = \int d^2b T_A(b) \left\langle \sigma_{dp} \exp\left[-\frac{1}{2} \sigma_{dp} T_A(b)\right] \right\rangle^2 \quad (127)$$

and  $\sigma_{dp}$  is the dipole-proton cross section. In the incoherent case, the  $q\bar{q}$  pair attenuates with a constant absorption cross section, as in the Glauber model, except that the whole exponential is averaged rather than just the cross section in the exponent. The coherent and incoherent cross sections depend differently on  $t$ . At small- $t$  ( $-t R_A^2/3 \ll 1$ ) coherent production dominates, with the signature being a sharp forward diffraction peak. On the other hand, incoherent production will dominate at large- $t$  ( $-t R_A^2/3 \gg 1$ ), with the  $t$ -dependence being to a good accuracy the same as in the production off free nucleons.



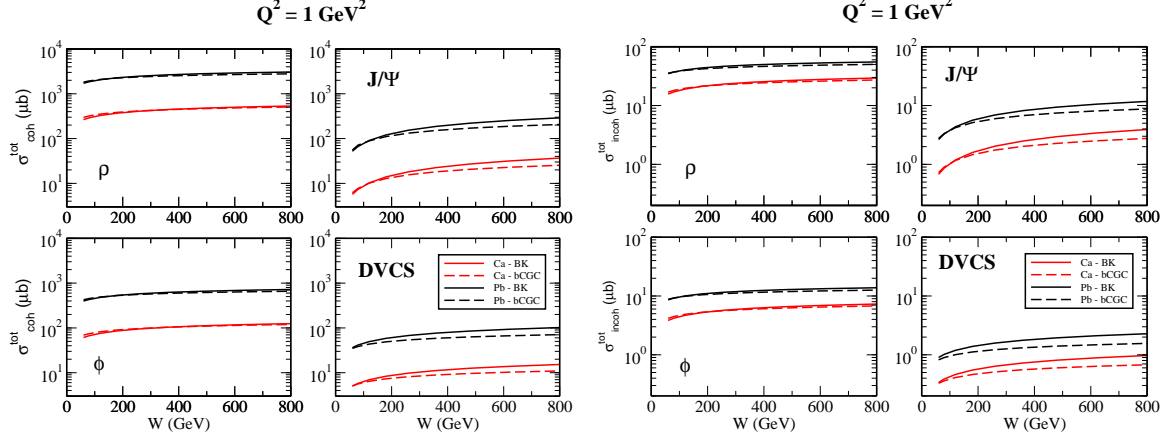


Figure 49. Energy dependence of the coherent (left) and incoherent (right) cross sections for different final states and  $Q^2 = 1 \text{ GeV}^2$ .

In the Eqs. (125) and (127) the functions  $\Psi^\gamma(z, r)$  and  $\Psi^E(z, r)$  are the light-cone wavefunctions of the photon and the exclusive final state, respectively. The variable  $r$  defines the relative transverse separation of the pair (dipole) and  $z(1-z)$  is the longitudinal momentum fraction of the quark (antiquark). In the dipole formalism, the light-cone wavefunctions  $\Psi(z, r)$  in the mixed representation  $(r, z)$  are obtained through a two dimensional Fourier transform of the momentum space light-cone wavefunctions  $\Psi(z, k)$ . The photon wavefunctions are well known in literature. For the meson wavefunction, we have considered the Gauss-LC model. In the DVCS case, as one has a real photon at the final state, only the transversely polarized overlap function contributes to the cross section. Summed over the quark helicities, for a given quark flavour  $f$  it is given by,

$$(\Psi_\gamma^* \Psi)_T^f = \frac{N_c \alpha_{\text{em}} e_f^2}{2\pi^2} \{ [z^2 + \bar{z}^2] \varepsilon_1 K_1(\varepsilon_1 r) \varepsilon_2 K_1(\varepsilon_2 r) + m_f^2 K_0(\varepsilon_1 r) K_0(\varepsilon_2 r) \}, \quad (128)$$

where we have defined the quantities  $\varepsilon_{1,2}^2 = z\bar{z}Q_{1,2}^2 + m_f^2$  and  $\bar{z} = (1-z)$ . Accordingly, the photon virtualities are  $Q_1^2 = Q^2$  (incoming virtual photon) and  $Q_2^2 = 0$  (outgoing real photon).

In order to estimate the coherent production in  $eA$  collisions we need to specify the forward dipole - nucleus scattering amplitude,  $\mathcal{N}^A(x, r, b)$ . In our calculations we assume that the forward dipole-nucleus amplitude is given by

$$\mathcal{N}^A(x, r, b) = 1 - \exp \left[ -\frac{1}{2} \sigma_{dp}(x, r^2) T_A(b) \right], \quad (129)$$

where  $\sigma_{dp}$  is the dipole-proton cross section and  $T_A(b)$  is the nuclear profile function, which is obtained from a 3-parameter Fermi distribution for the nuclear density normalized to  $A$ . The above equation sums up all the multiple elastic re-scattering diagrams of the  $q\bar{q}$  pair and is justified for large coherence length, where the transverse separation  $r$  of partons in the multiparton Fock state of the photon becomes a conserved quantity, *i.e.* the size of the pair  $r$  becomes eigenvalue of the scattering matrix. In what follows we assume that  $\sigma_{dp}$  is given by the bCGC model or by the solution of the BK equation with running coupling corrections.

**Results:** In Fig.49 left we show the coherent production cross section as a function of the photon-target c.m.s energy,  $W$ , for a fixed photon virtuality  $Q^2 = 1 \text{ GeV}^2$ . Fig.49

right is the exact analogue for the corresponding incoherent cross sections. Each one of the panels shows the results obtained for one specific final state. In each single figure the two upper (lower) curves show the results for a Pb (Ca) target. In all figures the dashed (solid) lines are obtained with the bCGC (rcBK) dipole-proton cross section. At low  $W$  the bCGC and rcBK production cross sections are indistinguishable one from the other because the dipole cross sections tend to coincide. These latter have been tuned to fit DIS data, which are taken in this kinematical region. Another expected feature is the observed decrease of the cross sections with increasing vector meson masses, which comes from the wave functions. Differences are expected to appear at higher energies, where we enter the lower  $x$  (extrapolation) region. In all cases we see that the results obtained with the rcBK cross section are larger than those obtained with the bCGC one. This is related to the fact that the numerical solutions of the BK equation tend to reach later the unitarity limit. Due to this fact, the results obtained with the rcBK dipole cross section grow faster with energy than those obtained with the bCGC one. Another feature is that the differences between bCGC and rcBK are larger for heavier vector mesons. Comparing the results shown in Fig. 49 we verify the dominance of the coherent production with a small contribution coming from incoherent processes.

*Acknowledgments:* The author thank E.R. Cazaroto, F. Carvalho, M. S. Kugeratski, M.V.T. Machado, and F.S. Navarra by collaboration.

### 2.5.5 Constraining the $\rho$ wavefunction

*Jeffrey R. Forshaw and Ruben Sandapen*

In the dipole model [27, 233], the imaginary part of the amplitude for diffractive  $\rho$  production is written as [202]

$$\Im \mathcal{A}_\lambda(s, t; Q^2) = \sum_{h, \bar{h}} \int d^2 \mathbf{r} dz \Psi_{h, \bar{h}}^{\gamma^*, \lambda}(r, z; Q^2) \Psi_{h, \bar{h}}^{\rho, \lambda}(r, z)^* e^{-i \mathbf{z} \mathbf{r} \cdot \mathbf{\Delta}} \mathcal{N}(x, \mathbf{r}, \mathbf{\Delta}) \quad (130)$$

where  $t = -|\mathbf{\Delta}|^2$ . In a standard notation [201, 202, 234],  $\Psi_{h, \bar{h}}^{\gamma^*, \lambda}$  and  $\Psi_{h, \bar{h}}^{\rho, \lambda}$  are the light-cone wavefunctions of the photon and the  $\rho$  meson respectively while  $\mathcal{N}(x, \mathbf{r}, \mathbf{\Delta})$  is the imaginary part of the dipole-proton elastic scattering amplitude. The energy dependence of the latter is via the dimensionless variable  $x$  taken here to be  $x = (Q^2 + 4m_f^2)/(Q^2 + s)$  where  $m_f$  is a phenomenological light quark mass.<sup>7</sup> Setting  $t = 0$  in equation (130), we obtain the forward amplitude used in reference [234], i.e

$$\Im \mathcal{A}_\lambda(s, t; Q^2)|_{t=0} = s \sum_{h, \bar{h}} \int d^2 \mathbf{r} dz \Psi_{h, \bar{h}}^{\gamma, \lambda}(r, z; Q^2) \hat{\sigma}(x, r) \Psi_{h, \bar{h}}^{\rho, \lambda}(r, z)^* \quad (131)$$

where we have used the optical theorem to introduce the dipole cross-section  $\hat{\sigma}(x, r) = \mathcal{N}(x, r, \mathbf{0})/s$ . Note that since the momentum transfer  $\mathbf{\Delta}$  is Fourier conjugate to the impact parameter  $\mathbf{b}$ , the dipole cross-section at a given energy is simply the  $b$ -integrated dipole-proton scattering amplitude, i.e

$$\hat{\sigma}(x, r) = \frac{1}{s} \int d^2 \mathbf{b} \mathcal{N}(x, r, \mathbf{b}) . \quad (132)$$

---

<sup>7</sup>We shall take  $m_f = 0.14$  GeV, the value used when extracting the dipole cross section from  $F_2$  data.

This dipole cross-section can be extracted from the  $F_2$  data since

$$F_2(x, Q^2) \propto \int d^2\mathbf{r} \, dz \, |\Psi_{\gamma^*}(r, z; Q^2)|^2 \hat{\sigma}(x, r) \quad (133)$$

and the photon's light-cone wavefunctions are known in QED, at least for large  $Q^2$ . The  $F_2$ -constrained dipole cross-section can then be used to predict the imaginary part of the forward amplitude for diffractive  $\rho$  production and thus the forward differential cross-section,

$$\left. \frac{d\sigma_\lambda}{dt} \right|_{t=0} = \frac{1}{16\pi} (\Im \mathcal{A}_\lambda(s, 0))^2 (1 + \beta_\lambda^2), \quad (134)$$

where  $\beta_\lambda$  is the ratio of real to imaginary parts of the amplitude and is computed as in reference [234]. The  $t$ -dependence can be assumed to be the exponential dependence as suggested by experiment [235]:

$$\frac{d\sigma_\lambda}{dt} = \left. \frac{d\sigma_\lambda}{dt} \right|_{t=0} \times \exp(-B|t|), \quad B = N \left( 14.0 \left( \frac{1 \text{ GeV}^2}{Q^2 + M_\rho^2} \right)^{0.2} + 1 \right) \quad (135)$$

with  $N = 0.55 \text{ GeV}^{-2}$ . After integrating over  $t$ , we can compute the total cross-section  $\sigma = \sigma_L + \epsilon \sigma_T$  which is measured at HERA.<sup>8</sup>

Presently several dipole models [115, 118, 119, 216, 236] are able to fit the current HERA  $F_2$  data and there is evidence that the data prefer those incorporating some form of saturation [237]. We can use the  $F_2$ -constrained dipole cross-section in order to extract the  $\rho$  light-cone wavefunction using the current precise HERA data [235, 238]. This has recently been done in reference [234] using the Regge-inspired FSSat dipole model [236] and we shall report the results of this work here. In addition, we repeat the analysis using two alternative models [118, 119, 216] both based on the original Colour Glass Condensate (CGC) model [215]. They differ from the original CGC model by including the contribution of charm quarks when fitting to the  $F_2$  data. Furthermore in one of them [119, 216], the anomalous dimension  $\gamma_s$  is treated as an additional free parameter instead of being fixed to its LO BFKL value of 0.63. We shall refer to these models as CGC[0.74] and CGC[0.63] models where the number in the square brackets stands for the fitted and fixed value of the anomalous dimension respectively. For both models, we use the set of fitted parameters given in reference [119]. All three models, i.e FSSat, CGC[0.63] and CGC[0.74] account for saturation although in a  $b$ - (or equivalently  $t$ -) independent way. Indeed, at a given energy, the dipole cross-section is equal to the forward dipole-proton amplitude or to the  $b$ -integrated dipole proton amplitude given by equation (132). Finally, all three dipole models we consider here give a good description of the diffractive structure function data [173, 239].

**Fitting the HERA data:** Previous work [119, 201, 202] has shown that a reasonable assumption for the scalar part of the light-cone wavefunction for the  $\rho$  is of the form

$$\begin{aligned} \phi_\lambda^{\text{BG}}(r, z) &= \mathcal{N}_\lambda 4[z(1-z)]^{b_\lambda} \sqrt{2\pi R_\lambda^2} \exp\left(\frac{m_f^2 R_\lambda^2}{2}\right) \exp\left(-\frac{m_f^2 R_\lambda^2}{8[z(1-z)]^{b_\lambda}}\right) \\ &\times \exp\left(-\frac{2[z(1-z)]^{b_\lambda} r^2}{R_\lambda^2}\right) \end{aligned} \quad (136)$$

---

<sup>8</sup>To compare with the HERA data, we take  $\epsilon = 0.98$ .

### Boosted Gaussian predictions

Dipole model	$\chi^2/\text{data point}$
FSSat	310/75
CGC[0.74]	262/75
CGC[0.63]	401/75

### BG fits

Model	$\chi^2/\text{d.o.f}$
FSSat [234]	82/72
CGC[0.74]	64/72
CGC[0.63]	83/72

### Improved fits

Model	$\chi^2/\text{d.o.f}$
FSSat [234]	68/70
CGC[0.63]	67/70

Table 4. *Left:* Predictions of the  $\chi^2/\text{data point}$  using the BG wavefunction. *Center:*  $\chi^2/\text{d.o.f}$  obtained when fitting  $R_\lambda$  and  $b_\lambda$  to the leptonic decay width and HERA data. *Right:*  $\chi^2/\text{d.o.f}$  obtained when fitting  $b_\lambda$ ,  $R_\lambda$ ,  $c_T$ ,  $d_T$  the leptonic decay width and HERA data.

### Best fit parameters

	$R_L^2$	$R_T^2$	$b_L$	$b_T$	$c_T$	$d_T$
FSSat [234]	26.76	27.52	0.5665	0.7468	0.3317	1.310
CGC[0.63]	27.31	31.92	0.5522	0.7289	1.6927	2.1457
CGC[0.74]	26.67	21.30	0.5697	0.7929	0	0

Table 5. Best fit parameters for each dipole model.

and is referred to as the 'Boosted Gaussian' (BG). This wavefunction is a simplified version of that proposed originally by Nemchik, Nikolaev, Predazzi and Zakharov [240]. In the original BG wavefunction,  $b_\lambda = 1$  while the parameters  $R_\lambda$  and  $\mathcal{N}_\lambda$  are fixed by the leptonic decay width constraint and the wavefunction normalization conditions [234]. However, when the BG wavefunction is used in conjunction with either the FSSat model or any of the CGC models, none of them is able to give a good quantitative agreement with the current HERA  $\rho$ -production data. This is illustrated by the large  $\chi^2$  values in table 4, the situation is considerably improved by fitting  $R_\lambda$  and  $b_\lambda$  to the leptonic decay width and HERA data (we fit to the same data set and with the same cuts as in reference [234]).

For the FSSat and CGC[0.63] models, we can further improve the quality of fit by allowing for additional end-point enhancement in the transverse wavefunction, i.e. using a scalar wavefunction of the form

$$\phi_T(r, z) = \phi_T^{\text{BG}}(r, z) \times [1 + c_T \xi^2 + d_T \xi^4] \quad (137)$$

where  $\xi = 2z - 1$ . The results are shown in table 4.

The best fits obtained with each dipole model are compared to the HERA data in figure 50, 50 and 51. The corresponding fitted parameters are given in table 5. Note that we achieve a lower  $\chi^2/\text{d.o.f} = 0.89$  with CGC[0.74] than with CGC[0.63] and FSSat for which we obtain  $\chi^2/\text{d.o.f} = 0.96$  and  $\chi^2/\text{d.o.f} = 0.97$  respectively. Compared to the FSSat and CGC[0.63] fits, note that no additional enhancement in the transverse wavefunction is required in the CGC[0.74] fit. Nevertheless the extracted wavefunction still exhibits enhancement compared to the old BG wavefunction. The extracted light-cone wavefunctions are shown in figure 52 left.

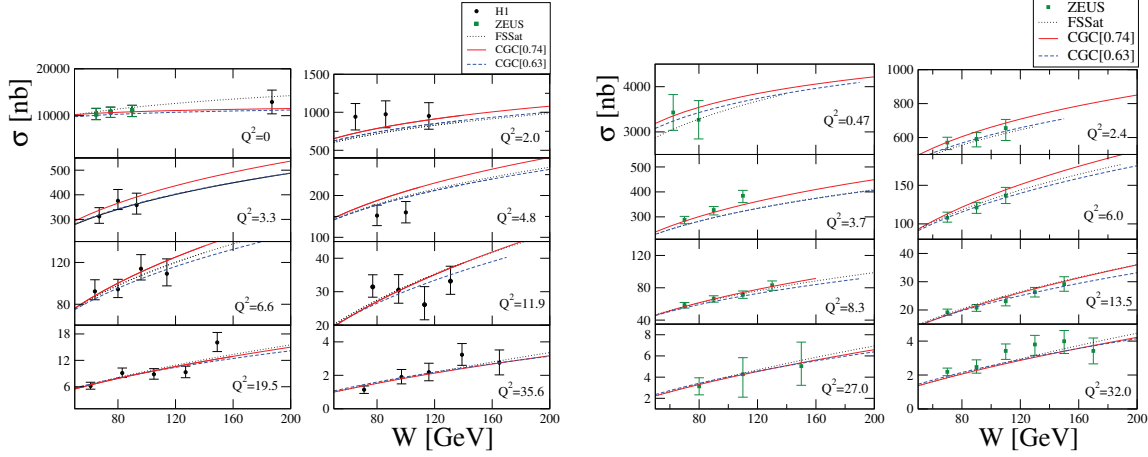


Figure 50. Best fits to the HERA (left) and ZEUS (right) total cross-section data. CGC[0.74]: solid; FSSat: dotted; CGC[0.63]: dashed.

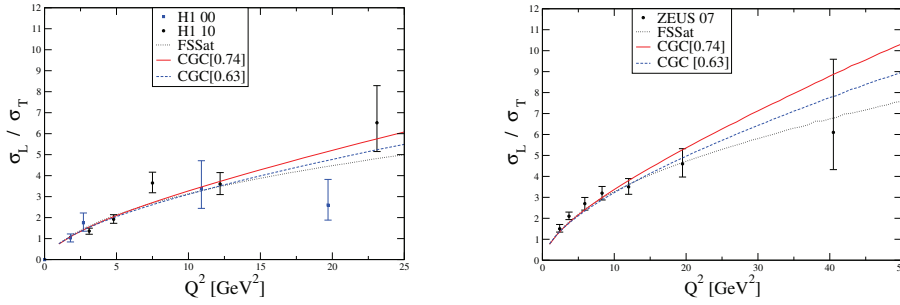


Figure 51. Best fits to the  $\sigma_L/\sigma_T$  data. The H1 data are at  $W = 75$  GeV while the ZEUS data are at  $W = 90$  GeV. CGC[0.74]: solid; FSSat: dotted; CGC[0.63]: dashed.

**Distribution Amplitudes:** The leading twist-2 Distribution Amplitude (DA) reads [234]

$$\varphi(z, \mu) \sim \left(1 - e^{-\mu^2/\Delta(z)^2}\right) e^{-m_f^2/\Delta(z)^2} [z(1-z)]^{b_L}, \quad (138)$$

where  $\Delta(z)^2 = 8[z(1-z)]^{b_L}/R_L^2$ . This leading twist DA is only sensitive to the longitudinal wavefunction and, as illustrated in figure 52 right, we expect little variation in the predictions using the different dipole models. To compare with existing theoretical predictions for the DA, we compute moments, i.e.

$$\langle \xi^n \rangle_\mu = \int_0^1 dz \xi^n \varphi(z, \mu). \quad (139)$$

where by convention [234]  $\int_0^1 dz \varphi(z, \mu) = 1$ . In reference [234], we noted that our DA is very slowly varying with  $\mu$  for  $\mu > 1$  GeV, i.e our parameterization neglects the perturbatively known  $\mu$ -dependence of the DA. This statement remains true if we use the CGC[0.63] or CGC[0.74] instead of the FSSat model.

Our results are compared with the existing predictions in table 6. The moments obtained with our best fit, i.e with the CGC[0.74] model, are very similar to those obtained with FSSat model or the CGC[0.63]. In all cases, the results are in very good agreement with expectations based on QCD sum rules and the lattice. Finally, in figure 52 right we

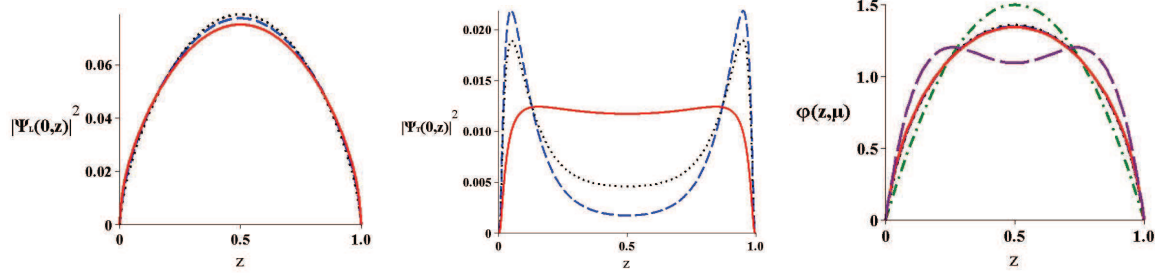


Figure 52. *Left and center:* The longitudinal and transverse light-cone wavefunctions squared at  $r = 0$ . (CGC[0.74]: solid; FSSat: dotted; CGC[0.63]: dashed.) *Right:* The extracted leading twist-2 DAs at  $\mu = 1$  GeV compared to the DA of reference [241] also at 1 GeV (long-dashed) and the asymptotic DA (dot-dashed).

**Moments of the leading twist DA at the scale  $\mu$**

Reference	Approach	Scale $\mu$	$\langle \xi^2 \rangle_\mu$	$\langle \xi^4 \rangle_\mu$	$\langle \xi^6 \rangle_\mu$	$\langle \xi^8 \rangle_\mu$	$\langle \xi^{10} \rangle_\mu$
(This paper)	CGC[0.74] fit	$\sim 1$ GeV	0.227	0.105	0.062	0.041	0.029
(This paper)	CGC[0.63] fit	$\sim 1$ GeV	0.229	0.107	0.063	0.042	0.030
[234]	FSSat fit	$\sim 1$ GeV	0.227	0.105	0.062	0.041	0.029
(This paper)	Old BG prediction	$\sim 1$ GeV	0.181	0.071	0.036	0.021	0.014
[242]	GenSR	1 GeV	0.227(7)	0.095(5)	0.051(4)	0.030(2)	0.020(5)
[243]	SR	1 GeV	0.26	0.15			
[241]	SR	1 GeV	0.26(4)				
[244]	SR	1 GeV	0.254				
[245]	SR	1 GeV	$0.23 \pm_{-0.02}^{+0.03}$	$0.11 \pm_{-0.02}^{+0.03}$			
[246]	Lattice	2 GeV	0.24(4)				
	$6z(1-z)$	$\infty$	0.2	0.086	0.048	0.030	0.021

Table 6. Our extracted values for  $\langle \xi^n \rangle_\mu$ , compared to predictions based on the QCD sum rules (SR), Generalised QCD Sum Rules (GenSR) or lattice QCD.

compare our DAs with that predicted by Ball and Braun [241], at a scale  $\mu = 1$  GeV. The agreement is reasonable given that in reference [241], the expansion in Gegenbauer polynomials is truncated at low order, which is pre-sumably responsible for the local minimum at  $z = 1/2$ . Certainly all 4 distributions distributions are broader than the asymptotic prediction  $\sim 6z(1-z)$ .

**Conclusions:** We have used the current HERA data on diffractive  $\rho$  production to extract information on the  $\rho$  light-cone wavefunction. We find that the corresponding leading twist-2 DA is broader than the asymptotic shape and agrees very well with the expectations of QCD sum rules and the lattice. We also find that the data prefer a transverse wavefunction with end-point enhancement although the degree of such an enhancement is model-dependent.

*Acknowledgments:* We thank H. Kowalski and C. Marquet for useful discussions. R.S. also thanks the organisers for their invitation and for making this workshop most enjoyable.

## 3 Nuclear Effects Across the $x - Q^2$ plane

### 3.1 Nuclear Quarks and Gluons

#### 3.1.1 Introduction

*Rodolfo Sassot, Marco Stratmann, Pia Zurita*

In spite of the remarkable phenomenological success of QCD as the theory of strong interactions, a detailed understanding of the role of quark and gluon degrees of freedom in nuclear matter is still lacking and poses great challenges for the theory. Ever since the discovery that quark and gluons in bound nucleons exhibit momentum distributions noticeably different from those measured in free or loosely bound nucleons [247] more than two decades ago, the precise determination of nuclear parton distribution functions (nPDF) has attracted growing attention, driving both increasingly accurate and comprehensive nuclear structure functions measurements [248] and a more refined theoretical understanding of the underlying physics.

The precise knowledge of nPDFs is not only required for a deeper understanding of the mechanisms associated with nuclear binding from a QCD improved parton model perspective, but is also a crucial input for the theoretical interpretation and analyses of a wide variety of ongoing and future high energy physics experiments, such as, for instance, heavy ion collisions at BNL-RHIC [249], proton-nucleus collisions to be performed at the CERN-LHC [250], or neutrino-nucleus interactions in long baseline neutrino experiments [251]. Consequently, the kinematic range and the accuracy at which nPDFs are known has evolved into a key issue in many areas of hadronic and particle physics.

The standard description of DIS processes off nuclear targets is customarily done in terms of the hard scale  $Q$  set by the virtuality of the exchanged photon and a scaling variable  $x_A \equiv Q^2/(2p_A \cdot q)$ , analogue to the Bjorken variable used in DIS off nucleons. Here,  $p_A$  is the target nucleus momentum, and, consequently,  $x_A$  is kinematically restricted to  $0 < x_A < 1$ , just like the standard Bjorken variable. Alternatively, one can define another scaling variable  $x_B \equiv Ax_A$ , where  $A$  is the number of the nucleons in the nucleus. Under the assumption that the nucleus momentum  $p_A$  is evenly distributed between the nucleons  $p_N = p_A/A$ , this variable resembles the Bjorken variable corresponding to the scattering off free nucleons,  $x_B \equiv Q^2/(2p_N \cdot q)$ . However, in nuclear scattering context it spans the interval  $0 < x_B < A$ , by definition, reflecting the fact that a parton may in principle carry more than the average nucleon momentum.

In the most naive picture, parton distributions in a nucleus are simply given by the incoherent sum or superposition of the parton distributions in the  $Z$  protons and  $(A - Z)$  neutrons that constitute the nucleus. In that case, the ratios between the structure functions or cross sections of two isoscalar nuclei (with the same proportion of protons and neutrons, such as carbon and deuteron) should be just proportional to the ratio of their respective number of nucleons (or to unity if we normalize the structure functions by the number of nucleons  $A$ ).

If we take into account Fermi motion effects, one would expect that in the larger nuclei, the cross section extends up to larger  $x_B$ , so the rates should typically grow to larger than unity at high  $x_B$ . What the EMC experiment found was that in addition to this motion effect, there was a significant and quite unexpected drop in the rates between approximately  $x_B \approx 0.3$  and  $x_B \approx 0.7$ . In Figure 53 we show a precise measurement performed recently at JLab [252] that illustrates both effects. Later on, it was found that the situation was even

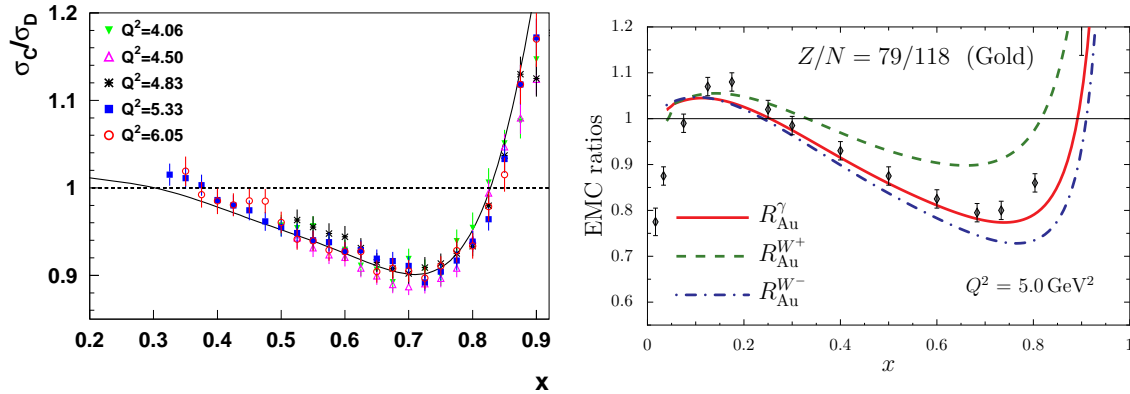


Figure 53. *Left:* EMC effect and Fermi motion as measured at JLab [252]. *Right:* The experimental results of Ref. [253] are illustrated for a gold target. The solid line is the result from Ref. [254] for the usual EMC effect and the dashed and dashed-dotted lines are respectively the EMC effects in the  $F_2^{W+}$  and  $F_2^{W-}$  structure functions. In both panels,  $x \equiv x_B$  as defined in the text.

worse for the naive picture outlined above, because at lower  $x_B$  values, the rates showed again non-trivial patterns of suppression and enhancement. These effects are called shadowing and anti-shadowing, respectively. The phenomenon has been measured at different  $Q^2$  and basically persists at higher  $Q^2$  but with a particular dependence, specific for each  $x_B$  region. In the following years different explanations, mechanisms, and QCD inspired models have been put forward.

After more than 30 years of experimental and theoretical studies, a standard picture of nuclear modifications of structure functions and parton densities has not yet emerged. This is a clear target for detailed studies at the EIC, which have a large potential to qualitatively improve the current situation.

### 3.1.2 The EMC effect at an EIC

*Ian C. Cloët*<sup>1</sup>

The EMC effect has an immediate parton model interpretation, which is that the valence quarks in nuclei carry a smaller momentum fraction than the valence quarks in a free nucleon. There have been numerous attempts to explain the EMC effect, for example nuclear structure [255], nuclear pion enhancement [256], dynamical rescaling and inter-nucleon color conductivity [257–259], point like configurations [260] and the medium modifications to the bound nucleons [261–264]. However, after more than a quarter of a century since the original EMC experiment there still no universally accepted explanation of the EMC effect. Therefore, it appears likely that to gain a deeper insight into the origins of the EMC effect we require new experimental information that is not accessed in traditional lepton deep inelastic scattering (DIS).

An electron ion collider (EIC) provides excellent opportunities to access different aspects of the EMC effect, which are not as accessible with traditional fixed target experiments. A standout example is  $W$ -production via the DIS processes

$$\begin{aligned}\ell^- + A &\longrightarrow W^- + \nu_\ell + A \longrightarrow \nu_\ell + X, \\ \ell^+ + A &\longrightarrow W^+ + \bar{\nu}_\ell + A \longrightarrow \bar{\nu}_\ell + X.\end{aligned}$$



Extraction of the target structure functions from these reactions is possible at an EIC because of the unique ability to reconstruct the final state and therefore avoid the need to directly determine the outgoing momentum of the neutrino or anti-neutrino. The parton model expressions for the  $F_2$  structure functions that characterize these processes are [265]

$$F_{2A}^{W^+}(x) = \bar{u}_A(x) + d_A(x) + s_A(x) + \bar{c}_A(x), \quad (140)$$

$$F_{2A}^{W^-}(x) = u_A(x) + \bar{d}_A(x) + \bar{s}_A(x) + c_A(x), \quad (141)$$

where  $u_A(x)$ ,  $\bar{u}_A$ , ... are the various quark distributions of the target. In the valence quark region these  $W^\pm$  structure functions are completely dominated by quark distributions of a single flavour, and hence a measurement of these structure functions provides direct access to the flavour decomposition of the nuclear parton distributions functions in this region. The flavour dependence of the EMC effect can then be determined, which will provide extremely important new information on the nature of this important phenomena.

The EMC effect ratio can be defined as

$$R^i = \frac{F_{2A}^i}{Z F_{2p}^i + N F_{2n}^i}, \quad \text{where } i \in \gamma, W^\pm, \quad (142)$$

and  $F_{2p}^i$ ,  $F_{2n}^i$ ,  $F_{2A}^i$  are respectively the proton, neutron and target structure functions. The atomic number of the target is labelled by  $Z$  and  $N$  is the target neutron number. Using the nuclear matter quark distribution results from Ref. [254] we can construct the usual EMC effect associated with the exchange of a virtual photon and also the EMC effect in the  $W^\pm$  structure functions. These results are illustrate in Fig. 53 for a gold nucleus.

Therefore measurements of  $F_{2A}^{W^\pm}(x)$  for various nuclei, for example carbon, iron, gold and lead would provide important new information on the flavour dependence of the EMC effect. Which in Ref. [254] is predicted to be large for nuclei like lead and gold. It is also claimed that a significant part and the NuTeV anomaly may also be explained by this isovector EMC effect [254]. Therefore, these measurements present an excellent opportunity for an EIC and will undoubtedly help us understand the origins of the EMC effect, which is essential if we are to ever have a QCD based description of nuclei.

### 3.1.3 Nuclear gluons

*Hans J. Pirner*

Historically, the very accurate NMC measurements of DIS on Tin and Carbon nuclei has allowed one to extract the gluon distribution from the scaling violation in  $F_2(A)$ . This has been done by Gousset and myself [266] for the first time. That analysis shows an enhancement of 10% i.e. antishadowing for  $x \approx 0.1$  and the same amount of shadowing, namely also 10% at  $x \approx 0.01$ . A high experimental accuracy is demanded, therefore only a trend could be established. The asymptotic calculation of heavy charmonium production on nuclei is often proposed as another method to extract the nuclear gluon distribution based on the gluon-gluon fusion process. As shown in various papers by Kopeliovich this production is more complicated, especially for  $J/\Psi$ , because of initial and final state effects. Measurements of the gluon distribution would give an experimental window on the importance of gluonic effects in nuclear binding. Very little is known about the role of gauge fields in nuclei.

To gain insight on gluons in abundant nucleons system, we have studied an abelian QED model [267] where the nucleon is replaced by an atom and the nucleus by a molecule, *i.e.*, we have analysed the structure function of the photon in the  $H_2$ -molecule and compared it with the structure function in the  $H$ -atom. The electron orbits of the hydrogen atoms in the molecule are polarized and modified by the electron exchange interaction leading to a suppression of photons at small  $x$ . At the momentum corresponding to the relative distance of the two protons a small antishadowing peak is visible [267]. In analogy, gluon antishadowing in the region  $x = 0.1$  may indicate the distance  $\Delta r \approx 2$  fm between the centers of the nucleons which act as color sources of common gluon fields between nucleons. A covalent binding of quarks may manifest itself as a density dependent lack of long range gluons at  $x < 0.1$  similarly to the deformation of the photon cloud in the hydrogen molecule. In addition, in non-abelian QCD one expects at small  $x$  that the gluons from different nucleons overlap and merge. Both of these effects have also an interpretation in the nuclear rest frame in terms of the absorption of various partonic components in the wave function of the photon.

During the last ten years the few available data have been used to manufacture nuclear parton distributions and evolve them to high  $Q^2$ , as reviewed below. In a careful analysis one has to respect the large errors of the starting distribution at low  $Q^2$  for the nuclear gluon distributions and also the larger  $x$  region has to be included correctly - at least the fact that the nuclear gluon distribution [268] is more strongly affected by Fermi-motion of the nucleons than the quark distribution, since it has a stronger decrease at large  $x$ . Enhancement of the nuclear gluon distribution sets in already at  $x = 0.5$  which may be of importance for charmonium production at JLab [268]. An EIC, with its large  $Q^2$  range and high luminosity, would allow for the first time a very detailed study of nuclear gluons from the lowest  $x$ , up to the very interesting  $x \gtrsim 0.1$  range where gluon antishadowing, EMC and Fermi motion effects take place. It will be very instructive to measure and understand the differences with respect to the same effects on quarks.

### 3.1.4 Global fits of nuclear PDFs: current status

*Rodolfo Sassot, Marco Stratmann, Pia Zurita*

From the point of view of perturbative QCD (pQCD), the extraction of nPDF can be performed in close analogy to what is routinely done for free nucleons: they are considered as non-perturbative inputs, to be inferred from data, whose relation to the measured observables and their energy scale dependence can be computed order by order in perturbation theory. Although one cannot discard potentially larger higher-twist or power corrections than in the case of free nucleons, or non-linear nuclear recombination effects, standard QCD factorization and universality of nPDFs are found to hold to a very good approximation in the kinematical range covered by present experiments.

At variance with PDFs for free nucleons, which, driven by the demand for increasingly precise predictions of standard model “banned an impressive degree of accuracy and refinement, extractions of nPDFs are done at a considerably lower level of sophistication. Not only the number, variety, kinematical coverage, and precision of nuclear data are much more limited, but the precise parameterization of nPDFs is also much more involved as it depends not only on the energy scale  $Q$  and the parton’s momentum fraction  $x$  but also on the size of the nucleus characterized by the atomic number  $A$ . In the following, we present a brief summary of the current status of nPDFs and outline limitations in the analyses

imposed by the data available so far.

Thanks to its variable beam energy, the possibility to run with different nuclei, and the envisioned large luminosities, an EIC will add invaluable novel information on nPDF from studies of the inclusive structure functions  $F_{2,L}$ . It will extend the kinematic range toward lower values of  $x$  as well as higher scales  $Q$ , allow a precise gluon determination scaling violations of  $F_2$ , permit the flavor separation of the quark sea and the study the onset of non-linear saturation effects at small  $x$  (see Section 2.2.3), which eventually spoil the factorized pQCD approach.

**Status of Nuclear Parton Densities.** From the point of view of pQCD and a factorized approach, the description of nuclear DIS can be viewed as follows. In a DIS processes off a nuclear target, we also have a hard momentum scale  $Q$  that allows one to factorize the measured cross section into a point-like partonic cross section and non-perturbative parton densities, characteristic of partons seen in that nucleus. These “effective” parton densities factorize and encode all the non-perturbative information, including the details about the nuclear structure, and every mechanism, interaction, or effect we can imagine. Since the hard partonic cross sections are just the same as those appearing in the factorization for free nucleons, the nuclear parton densities will evolve with scale in the same way as ordinary parton densities. For similar reasons, the approach could be extended to higher orders. What is clearly not obvious within this line of reasoning is why, or how, one could split the non-perturbative effective nuclear parton density into a piece containing only the effects related to quarks and gluons belonging to single nucleon from those related to the nucleons bound in the nuclei. No field theoretical tool gives us a precise prescription of how to achieve this. It is important to keep in mind that even in lepton-nucleon scattering standard PDFs are not just naive probability densities; they are non-trivial, though perfectly well defined, objects which depend on the choice of factorization scheme and contain other ingredients such as gauge links.

What can be done, of course, is to follow a program of global QCD analyses completely analogous to the one carried out for PDFs, i.e., to extract the nPDFs and their  $A$  dependence from data. In doing so one can explore if the basic properties of factorization and universality still hold in a nuclear environment. The first QCD extractions of nPDFs defined in this way were done at the end of the 90’s by two pioneering groups who performed leading order (LO) analyses of nuclear DIS data (EKS98, HKM01) [124, 269, 270].

When introducing nPDF, the usual approach was to propose a very simple relation between the parton distribution of a proton bound in the nucleus,  $f_i^A$ , and those for free protons  $f_i$ ,

$$f_i^A(x_B, Q_0^2) = R_i(x_B, Q_0^2, A, Z) f_i(x_B, Q_0^2), \quad (143)$$

in terms of a multiplicative nuclear correction factor  $R_i(x_B, Q^2, A, Z)$ , specific to a given nucleus  $(A, Z)$ , parton flavor  $i$ , and initial energy scale  $Q_0^2$ . Such a description is convenient since the ratio  $R_i(x_B, Q^2, A, Z)$  compares directly the parton densities with and without nuclear effects, and is closely related to the most common nuclear DIS observables, which are the ratios between the nuclear and deuterium structure functions. In Ref. [271] the alternative to relate nPDFs to standard PDFs by means of a convolution was introduced. The convolution approach implements straightforwardly effects related to rescalings or shifts in the parton’s momentum fraction due to interactions with the nuclear medium. In addition, convolution integrals are the most natural language for parton dynamics beyond the LO and allow for the straightforward application of the Mellin transform techniques, convenient for

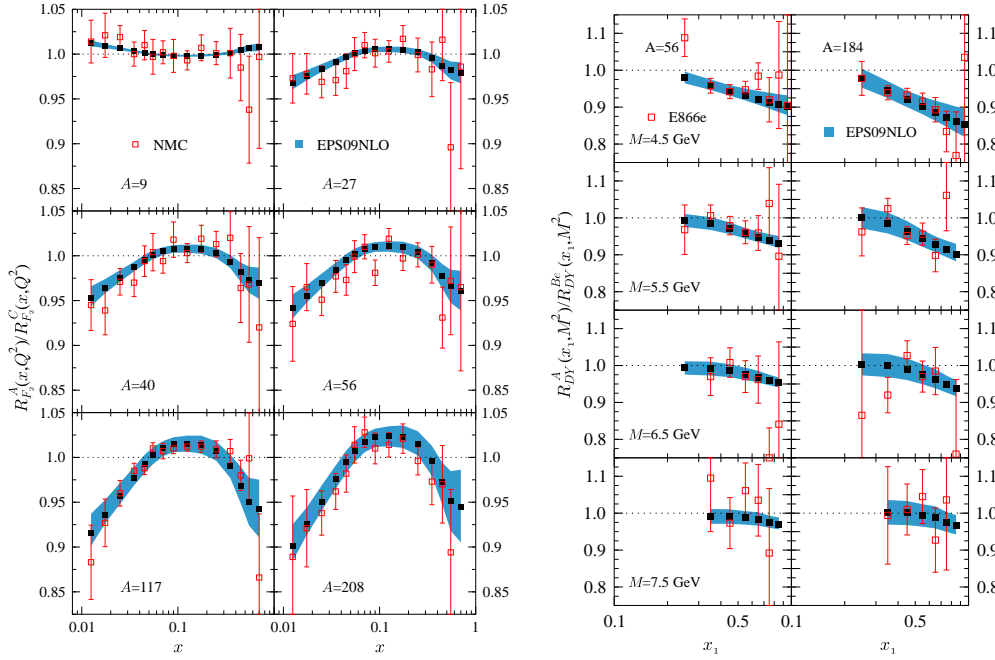


Figure 54. Quality of the fit to nuclear DIS and Drell-Yan data; taken from Ref. [126].

a numerical fast and accurate computation of the scale dependence of PDFs and relevant cross section estimates.

Following the developments for standard PDFs, nPDFs analyses subsequently incorporated various improvements such as a consistent next-to-leading order (NLO) framework (nDS) [271], a thorough uncertainty analysis (HKN04 LO) [272], and periodical updates of the different sets in order to incorporate new data (EKPS07 LO) [273], up to NLO accuracy (HKN07 NLO, EPS09 NLO) [126, 274]. In the latest sets [126, 275] particular attention has been paid to the possible impact of  $d+Au$  collision data from RHIC and neutrino DIS data on the global fits. A typical comparison to nuclear DIS and Drell-Yan data is shown in Fig. 54.

It is worth noticing that the inclusion of  $d+Au$  data in nPDFs fits, although neglecting any nuclear modifications in the hadronization process, leads to significantly larger gluon shadowing and antishadowing, as it has been pointed by [126]. The same data, however, can be described with much more moderate nuclear gluon PDFs, but including medium modified nFFs [276], see Section 4.1.4.

Regarding the impact of neutrino data, Schienbein et al. [275] claim that within their analysis it is not possible to reproduce simultaneously the trend of the data coming from electromagnetic nuclear DIS and some observables derived from neutrino DIS measurements. Of course, these conclusions are reached under rather stringent assumptions such as a very specific parameterization for nuclear effects and those implicit in the derivation of the neutrino DIS rates to deuteron, which have not been actually measured yet. On the other hand, using the EPS09 analysis and neutrino DIS data, Paukkunen and Salgado [277] find no traces of such tension, besides some energy dependent fluctuations in the NuTeV data. A typical comparison to neutrino data is given in Fig. 55.

Different recent extractions of nPDFs are shown in Fig. 56. A general shortcoming of

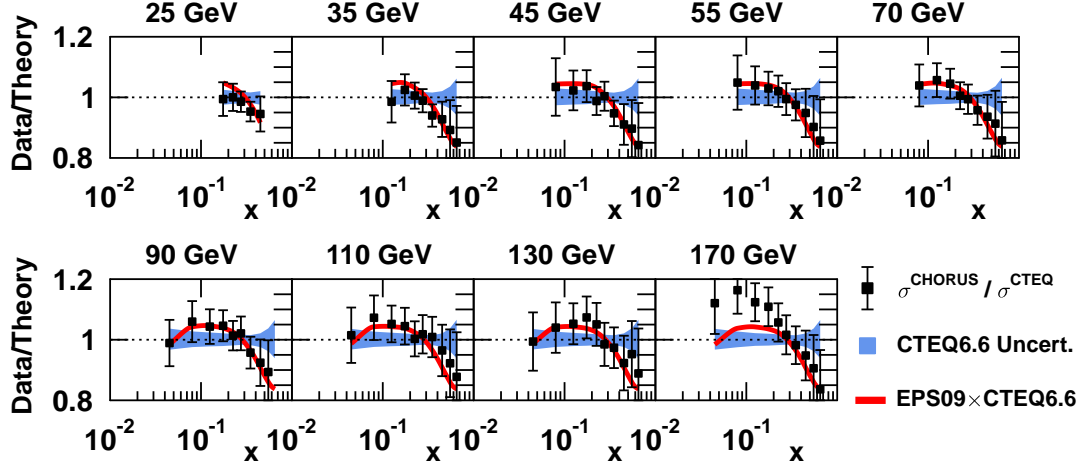


Figure 55. Comparison to neutrino data; taken from Ref. [277].

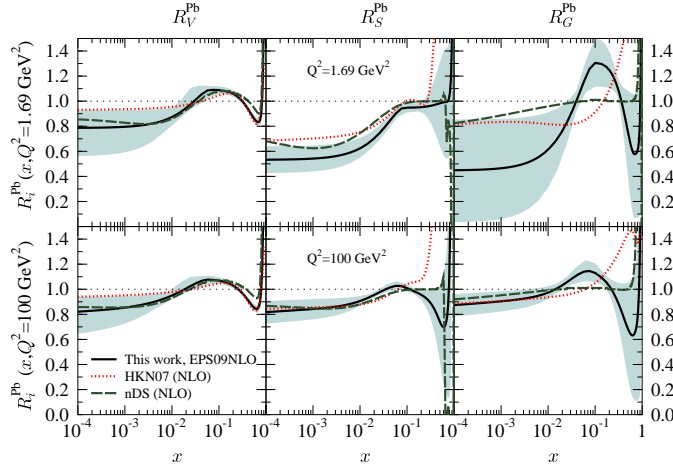


Figure 56. Comparison between different sets of nPDFs from [278].

all present fits is that independent nuclear modification factors can be determined only for gluons, valence, and sea quarks without distinguishing different quark flavors. Also, present fixed-target data do not constrain nPDFs below about  $x_B \simeq 0.01$ , and the curves shown at smaller values of  $x_B$  are mere extrapolations. Uncertainties on nPDFs are large, in particular for the nuclear gluon distribution. There is clearly a need for more precise data covering also the small  $x_B$  region.

**Conclusions.** In the last few years our knowledge of the way that both parton densities and fragmentation probabilities are modified in a nuclear environment have improved significantly. Different studies performed so far have clearly demonstrated that pQCD factorization and universality are extremely good approximations within the precision and kinematic range of the available data. Although the uncertainties and differences between different QCD global analysis are still large, the availability of more data for different processes, and their subsequent inclusion in the analyses will certainly help to reduce them further. Ultimately, the EIC will be required for precise quantitative studies and to explore

the small  $x_B$  regime where novel non-linear recombination and saturation phenomena are expected. A preliminary study of the capabilities of the EIC in these respects has been presented in Section 2.2.3: the EIC has the potential to determine gluon and quark nPDFs to a precision comparable to the nucleon PDFs down to  $x \sim 10^{-3}$ , and indeed to detect saturation effects as a deviation from DGLAP linear evolution.

### 3.1.5 HKN nuclear parton distribution functions

*Shunzo Kumano*

The Hirai, Kumano and Nagai (HKN) nuclear PDFs [272, 274] are determined by a global analysis of world data on charged-lepton DIS and Drell-Yan processes with nuclear targets. Since the PDFs of the nucleon are relatively well determined, it is appropriate to parametrize the nPDFs at the initial  $Q_0^2 = 1 \text{ GeV}^2$  using Eq. (143) and

$$R_i(x_B, Q_0^2, A, Z) = 1 + \left(1 - \frac{1}{A^\alpha}\right) \frac{a_i + b_i x + c_i x^2 + d_i x^3}{(1-x)^{\beta_i}}, \quad (144)$$

The determined  $u_v$ ,  $\bar{q}$ , and  $g$  nPDFs from the HKN07 analysis [274] are shown for the calcium nucleus in Fig. 57 at  $Q^2=1 \text{ GeV}^2$ . LO and NLO results are shown with uncertainty bands, showing that nPDFs are determined more accurately at NLO. We obtain  $\chi_{min}^2/\text{d.o.f.}=1.35$  and 1.21 for the LO and NLO fits, respectively.

The valence-quark modifications are well determined because of accurate measurements on the  $F_2$  ratios at medium  $x$ . The small- $x$  region is fixed by the baryon-number and charge conservations together with the modifications in the medium- and large- $x$  regions. The antiquark modifications are also determined well at small  $x$  due to measurements on  $F_2$  shadowing, and they are also fixed at  $x \sim 0.1$  because of Fermilab Drell-Yan measurements. However, the region at  $x > 0.2$  is not determined at all. The E906/SeaQuest collaboration is currently measuring this medium- $x$  region, and there is also a possibility to measure this region with an experiment at J-PARC. In the near future, the uncertainty bands should be significantly reduced for the antiquark.

The gluon distribution has the largest uncertainties since it contributes to the  $F_2$  and Drell-Yan ratios only as higher-order effects, and the  $Q^2$  dependence of  $F_2^A/F_2^{A'}$  is not measured accurately on nuclear targets, which makes it difficult to pin down the gluon modifications measured by scaling violations of  $F_2$ .

The small- $x$  nPDFs are dominated by huge gluon distributions, so that it is essential to determine them accurately for new discoveries by high-energy heavy-ion experiments. There-

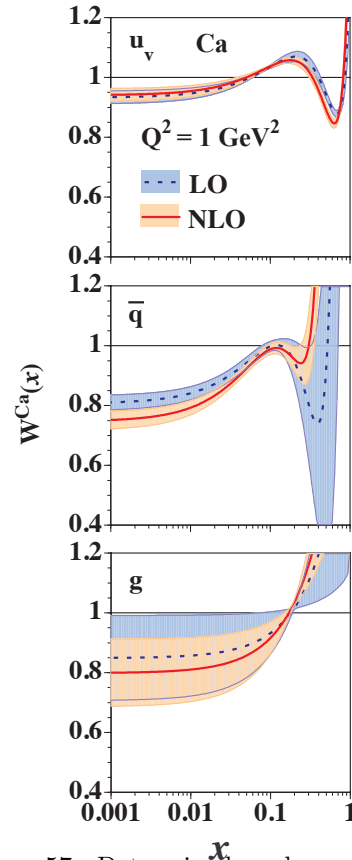


Figure 57. Determined nuclear modifications in Ca [274].

fore, it is important to measure  $Q^2$  dependence of  $F_2^A/F_2^{A'}$  at EIC for determining nuclear gluon distributions.

In the HKN07, the nPDFs are also investigated for the deuteron. In obtaining the “nucleonic” PDFs, deuteron data are used after crude nuclear corrections. Since the current PDFs could possibly contain nuclear effects, appropriate nuclear corrections should be applied in future for excluding such effects. Our codes for calculating the nPDFs and their uncertainties are available at the web site [279]. The technical details are explained in Refs. [272, 274] and within the subroutine.

## 3.2 Colour Transparency

### 3.2.1 Colour transparency phenomena

*B. Z. Kopeliovich*

The nuclear medium is more transparent for colorless hadronic wave packets than predicted by the Glauber model. One can treat this phenomenon either in the hadronic basis as a results of Gribov’s inelastic corrections [83], or in QCD as a result of color screening [72], an effect called color transparency (CT). Although the two approaches are complementary, the latter interpretation is more intuitive and straightforward. Indeed, a point-like colorless object cannot interact with external color fields, therefore its cross section vanishes as  $\sigma(r) \propto r^2$  when  $r \rightarrow 0$  [72]. When a colorless wave packet propagates through a nucleus, the fluctuations with small size have an enhanced survival probability which leads to a non-exponential attenuation  $\propto 1/L$  [72], where  $L$  is the path length in nuclear matter.

Diffraction electroproduction of vector mesons off nuclei is affected by shadowing and absorption which are different phenomena. Final state absorption of the produced meson exists even in the classical probabilistic approach which relates nuclear suppression to the survival probability  $W(z, b)$  of the vector meson produced at the point with longitudinal coordinate  $z$  and impact parameter  $\vec{b}$ ,

$$W(z, b) = \exp \left[ - \sigma_{in}^{VN} \int_z^\infty dz' \rho_A(b, z') \right], \quad (145)$$

where  $\rho_A(b, z)$  is the nuclear density and  $\sigma_{in}^{VN}$  is the inelastic  $VN$  cross section. Shadowing, is also known to cause nuclear suppression. In contrast to final state absorption, it is a pure quantum-mechanical effect which results from destructive interference of the amplitudes for which the interaction takes place on different bound nucleons. It can be interpreted as a competition between the different nucleons participating in the reaction: since the total probability cannot exceed one, each participating nucleon diminishes the chances of others to contribute to the process. The interplay between absorption and shadowing is controlled by the two time scales introduced for the case of charmonium in Eqs. (114)-(115). They are defined similarly for other hadrons.

In the low-energy limit of short  $l_c < l_f \ll R_A$  (shorter than the mean nucleon spacing  $\sim 2$  fm) only final state absorption matters. The ratio of the quasielastic  $\gamma^* A \rightarrow V X$  and  $\gamma^* N \rightarrow V X$  cross sections reads,

$$R_{inc} \Big|_{l_c, l_f \ll R_A} \equiv \frac{\sigma_V^{*A}}{A \sigma_V^{*N}} = \frac{1}{A} \int d^2b \int_{-\infty}^\infty dz \rho_A(b, z) \exp \left[ - \sigma_{in}^{VN} \int_z^\infty dz' \rho_A(b, z') \right] \quad (146)$$

In the limit of long  $l_c \gg R_A$  it takes a different form; in the Glauber approximation,

$$R_{inc} \Big|_{l_c \gg R_A} = \int d^2b T_A(b) \exp \left[ -\sigma_{in}^{VN} T_A(b) \right] , \quad (147)$$

One can see that the  $V$  meson attenuates along the whole nucleus thickness in Eq. (147), but only along roughly half of that length in Eq. (146). The exact expression beyond VDM which interpolates between the two regimes (146) and (147) can be found in [230].

The effects of color transparency lead to deviation from this expression. These effects, which can be understood as Gribov inelastic corrections lead to Equation (116), which should be used to study the effects of color transparency.

**Light-cone distribution functions for the photons and vector mesons.** In what follows we rely on the dipole description and need to know the distribution functions for the photon and vector mesons. To be self-consistent we should use the same light-cone potential for describing both. In the equation (32) for the Green function we chose the real part of the potential of the  $\bar{q}q$  dipole as in Refs. [87, 218]. Solving Eq. (32) for the Green function with this potential and assuming a similar spin structures for the vector mesons and photons, one can obtain an explicit formula for the vector meson light-cone wave function [218], depending on a “width” and a “quark mass” phenomenological parameters that were fitted to data in [240].

**Cross section on a proton.** Now we are in a position to calculate the forward electro-production diffractive amplitudes, which have the following form, The forward scattering amplitude reads,

$$\begin{aligned} \mathcal{M}_{\gamma^* N \rightarrow V N}^T(s, Q^2) \Big|_{t=0} &= N_C Z_q \sqrt{\alpha_{em}} \int d^2r \sigma_{\bar{q}q}(\vec{r}, s) \int_0^1 d\alpha \left\{ m_q^2 \Phi_0(\epsilon, \vec{r}, \lambda) \Psi_V^T(\vec{r}, \alpha) \right. \\ &\quad \left. + [\alpha^2 + (1 - \alpha)^2] \vec{\Phi}_1(\epsilon, \vec{r}, \lambda) \cdot \vec{\nabla}_r \Psi_V^T(\vec{r}, \alpha) \right\} \end{aligned} \quad (148)$$

$$\begin{aligned} \mathcal{M}_{\gamma^* N \rightarrow V N}^L(s, Q^2) \Big|_{t=0} &= 4 N_C Z_q \sqrt{\alpha_{em}} m_V Q \int d^2r \sigma_{\bar{q}q}(\vec{r}, s) \\ &\quad \times \int_0^1 d\alpha \alpha^2 (1 - \alpha)^2 \Phi_0(\epsilon, \vec{r}, \lambda) \Psi_V^L(\vec{r}, \alpha) . \end{aligned} \quad (149)$$

These amplitudes are normalized as  $|\mathcal{M}^{T,L}|^2 = 16\pi d\sigma_N^{T,L}/dt \Big|_{t=0}$ . In what follows we calculate the cross sections  $\sigma = \sigma^T + \epsilon \sigma^L$  assuming that the photon polarization is  $\epsilon = 1$ .

For HERA data, the normalization of the cross section and its energy and  $Q^2$  dependence are remarkably well reproduced, see [218] This is important, since the absolute normalization is usually much more difficult to reproduce than nuclear effects, which we switch to in the next section.

As a cross-check for the choice of the  $\rho^0$  wave function in Eqs. (??) - (??) we also calculated the total  $\rho^0$ -nucleon cross section, which is usually expected to be roughly similar to the pion-nucleon cross section  $\sigma_{tot}^{\pi N} \sim 25$  mb. For the dipole cross section we adopt the KST parameterization [87], which has been used above, and is designed to describe low- $Q^2$  data. Then, at  $\nu = 100$  GeV we obtain  $\sigma_{tot}^{\rho^0 N} = 27$  mb which is quite a reasonable number.



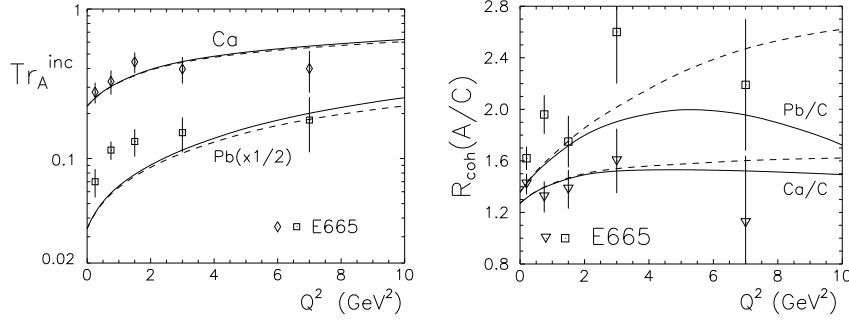


Figure 58. Comparison of the dipole approach with E665 data [280] for nuclear effect in electroproduction of  $\rho$ -mesons. *Left panel:*  $Q^2$ -dependence of nuclear transparency for lead and calcium. Solid and dashed curves show the results of using the Green function approach and the “frozen” approximation respectively. *Right panel:*  $Q^2$ -dependence of the total cross section ratio  $R_{coh}(A/C) = 12\sigma_{coh}/A\sigma_{coh}$ .

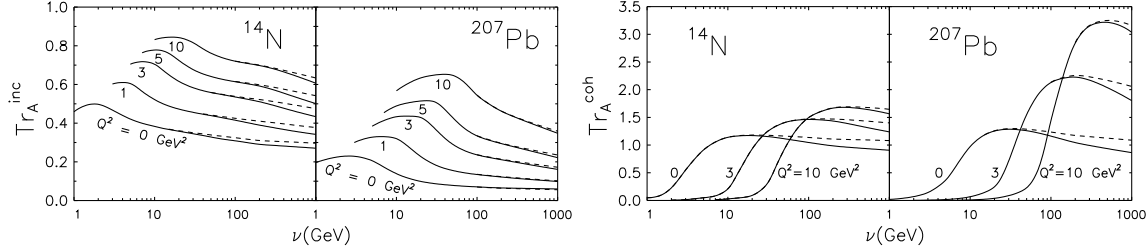


Figure 59. Nuclear transparency for incoherent and coherent electroproduction of  $\rho^0$  on nitrogen and lead as function of energy. Solid and dashed curves correspond to calculations with and without gluon shadowing, respectively. *Left two panels:* Incoherent production at  $Q^2 = 0, 1, 3, 5, 10$  GeV<sup>2</sup>. *Right two panels:* Coherent production at  $Q^2 = 0, 3, 10$  GeV<sup>2</sup>.

**Diffraction electroproduction on nuclei.** In the high energy regime of  $l_c \gg R_A$  one can rely on Eq. (119) for incoherent electroproduction of  $\rho$ -mesons (with different quark mass and meson wave function). As a manifestation of color transparency, the nuclear ratio, also called nuclear transparency,  $Tr_A^{inc} \equiv R_{inc}$  defined in (118), was predicted in [281] to rise as function of  $Q^2$ . Indeed, the mean size of the  $q\bar{q}$  component of the virtual photon decreases with  $Q^2$ , so the nucleus becomes more transparent. The results of the E665 experiment at Fermilab [280] depicted in Fig. 58 are in a good accord with the predicted behavior. The calculations performed in the “frozen” approximation ( $l_c \gg R_A$ ) are presented with dashed curves. The more realistic results including finiteness of  $l_c$  and  $l_f$  are plotted by solid curves. While the “frozen” approximation is rather accurate for incoherent production, the deviation from its expectation for coherent process at the energy of the E665 experiment is significant.

The predicted energy dependence of the nuclear ratios in incoherent and coherent  $\rho$  production on nitrogen and lead are depicted in Fig. 59. As was expected, the nucleus becomes more opaque with energy for incoherent production. This happens because when the hadronic fluctuations of the virtual photon live longer, they propagate through the whole nucleus and attenuate more. On the other hand, in incoherent production the phase shifts between the amplitudes of  $\rho$  production on different nucleons must be very small in order the nucleus remained intact. This is why the nuclear ratio depicted in the bottom part of Fig. 59 is so suppressed at low energies.

At high energies, such as at an EIC, gluon shadowing causes an additional nuclear suppression of  $\rho$  production. This correction is calculated as was described in Sect. 2.1.5 and the final results are plotted in Fig. 59 by solid curves. As was expected, the effect of gluon shadowing is not significant.

### 3.2.2 From color transparency to color opacity

*Mark Strikman*

Color transparency (CT) phenomena play several roles. They probe both the high energy dynamics of strong interaction and the minimal small size components of the hadrons. In the case when some of the produced particles have energies smaller than 10 GeV in the nucleus rest these processes could be also used to study the space-time evolution of small wave packets - a question relevant for interpretation of heavy ion collisions. They also provide an important link to the hard QCD black disk regime - the regime of strong absorption for the processes which at lower energies exhibit the CT regime, and determine the kinematics where factorization can be applied to generalized parton distribution studies.

The basic feature of CT is the suppression of interaction of small size color singlet configurations: for a dipole of transverse size  $d$  perturbative QCD gives

$$\sigma(d, x_N) = \frac{\pi^2}{3} \alpha_s(Q_{eff}^2) d^2 [x_N G_N(x_N, Q_{eff}^2) + 2/3 x_N S_N(x_N, Q_{eff}^2)], \quad (150)$$

where  $Q_{eff}^2 \propto 1/d^2$ ,  $x_N = Q_{eff}^2/W^2$ , and the second term is due to the contribution of quark exchanges which is important for intermediate energies [282]. There are two critical requirements for CT phenomena: *squeezing*, i.e., selection of small size configurations, and *freezing*, i.e., selection of high enough energies to allow squeezed configuration to live long enough.

At high energies one can select CT processes by selecting special final states: for example, diffraction of pion into two high  $p_t$  jets, or a small initial state  $\gamma_L^*$  such as in exclusive production of mesons. QCD factorization theorems [282, 283] were proven for these processes based on the CT property of QCD. The space time picture of these processes in the nucleus rest frame is as follows: long before the target, the projectile pion or virtual photon fluctuates into  $q\bar{q}$  configuration with transverse separation  $d$ , which elastically scatters off the target with an amplitude which for  $t = 0$  is given by Eq. (150) (up to small corrections due to different off shellness of the  $q\bar{q}$  pair in the initial and final states), followed by the transformation of the pair into two jets or a vector meson. With a slight simplification, the amplitude for dijet diffractive production can be written as

$$A(\pi N \rightarrow 2 jets + N)(z, p_t, t = 0) \propto \int d^2 d \psi_\pi^{q\bar{q}}(d, z) \sigma_{q\bar{q}-N(A)}(d, s) e^{i p_t d}, \quad (151)$$

where  $z$  is the light-cone fraction of the pion momentum carried by a quark, and  $\psi_\pi^{q\bar{q}}(z, d) \propto z(1-z)_{d \rightarrow 0}$  is the quark-antiquark Fock component of the meson light cone wave function. The presence of the plane wave factor in the final state leads to an expectation of an earlier onset of scaling than in the case of the vector meson production, where the vector meson wave function appears instead. CT was observed in the pion diffraction into two jets [284] confirming predictions of [285]. The HERA data on exclusive vector meson production are also well described.

## Investigations at the EIC.

Studies at the EIC will require investigation of different exclusive meson production channels as a function of  $x, Q^2$ . In the CT limit and  $-t \geq 0.1 \text{ GeV}^2$  where coherence effects are negligible one expects

$$\sigma_{\gamma_L^* A \rightarrow \text{"meson"} A^*}^{incoh}(t) = Z \sigma_{\gamma_L^* p \rightarrow \text{"meson"} N}(t) N \sigma_{\gamma_L^* n \rightarrow \text{"meson"} N}(t) \quad (152)$$

In the EIC kinematics the coherence length is  $\gg 2R_A$  so deviations from the CT prediction could be due to the leading twist effects - leading twist shadowing, and higher twist effects of multiple interactions of the  $q\bar{q}$  pair with the target nucleus. There are two distinctive regimes:  $x \geq 0.03$  where nuclear PDFs are practically linear in A, and  $x \leq 0.01$  where a significant LT shadowing of nPDFs is expected (see discussion in section 2.1.6).

**The  $x \geq 0.03$  region.** Multiple interactions should reduce the cross section. At the EIC it would be possible to perform a scan as a function of  $Q^2$ . For low  $Q^2$  and especially for  $\sigma_T$  one expects a hadron like regime in which absorption is strong and  $\sigma_{\gamma_L^* A \rightarrow \text{"meson"} A^*}^{incoh}(t) \propto A^{1/3}$ . With increase of  $Q^2$  one expects a transition from the soft dynamics with Gribov-Glauber type screening to the CT regime without significant LT gluon shadowing. In the case of  $J/\psi$  production one expects CT regime already at low  $Q^2$  while for the light mesons the onset of CT can be much slower as essential transverse sizes of  $q\bar{q}$  decrease rather slowly with  $Q^2$  [286] as manifested in the slow convergence of the t-slope of  $\rho$ -meson production to the t-slope of  $J/\psi$  production with increase of  $Q^2$ .

**The  $x \leq 0.01$  region.** In this regime one expects a large shadowing due to the LT mechanisms both for the incoherent contribution and for coherent contribution in which case [287] - perturbative color opacity:

$$\frac{d\sigma_{\gamma_L A \rightarrow VMA}}{dt} / \frac{d\sigma_{\gamma_L N \rightarrow VMN}}{dt} = G_A^2(x, Q_{eff}^2) / G_N^2(x, Q_{eff}^2) \cdot F_A^2(t), \quad (153)$$

where  $F_A(t)$  is the nucleus form factor. Typical results for the expected suppression effect are given in Fig. 60. Note here that effective  $Q^2$  which enters in Eq.153 is much smaller than  $Q^2$  in the electroproduction of light vector mesons. For example for  $\rho$  meson case  $Q_{eff}^2 \sim 3 \text{ GeV}^2$  for  $Q^2 \sim 10 \text{ GeV}^2$ . For  $J/\psi$  photoproduction  $Q_{eff}^2 \sim 3 \div 4 \text{ GeV}^2$  and slowly grows with  $Q^2$  [288]. Hence for the top of the EIC energies one expects reduction of the coherent  $J/\psi$  photo/electro production of at least a factor of two. Numerically the LT shadowing mechanism leads to a larger screening effect for the interaction of the small dipoles than the HT dipole eikonal models (cf. [286]).

The incoherent cross section,  $\sigma_{incoh}$  is shadowed somewhat stronger than the coherent cross section,  $\sigma_{coh}$ . Effect grows with increase of the strength of the elementary interaction. As a result the ratio  $B_{\gamma^* N \rightarrow VM^* N}^{-1} \cdot \sigma_{incoh} / \sigma_{coh}$  of incoherent and coherent cross sections integrated over  $t$  and divided by the slope of the elementary cross section is expected to decrease slowly with decrease of  $x$  at fixed  $Q^2$  (cf. Fig.43 in [289]). For example, for  $B = 4 \text{ GeV}^{-2}$ ,  $R \equiv \sigma_{incoh} / \sigma_{coh}$  changes from  $R \approx 0.3$  in the impulse approximation limit to  $R \approx 0.18$  in the regime of strong absorption (strength of dipole interaction of the order  $\sigma_{tot}(\pi N)$ ). Simultaneous measurements of coherent and incoherent diffraction will allow to test the underlying dynamics in a greater detail.

Note that it will be feasible to measure coherent cross section at  $t \sim 0$  due to the very steep  $t$  dependence of coherent peak and ability to kill most of the incoherent diffraction

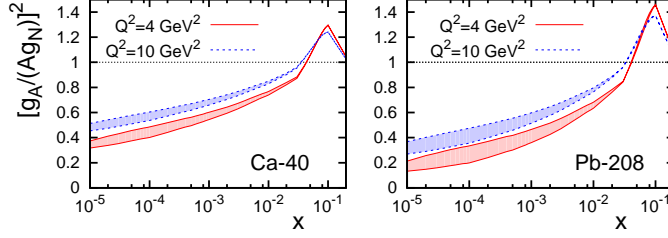


Figure 60. Leading twist shadowing effect for coherent vector meson production off Ca and Pb. Bands reflect the range of predictions given by the FGS10\_L and FGS10\_H parametrizations of the gluon LT shadowing.

using ZDC veto. At the same time measurements of the  $t$  dependence of coherent diffraction beyond the first minimum,  $t_1 \equiv t_{first\,minimum}$ , will be hardly possible (except for the lightest nuclei like  ${}^4\text{He}$ ) due to the dominance of processes of the nuclear excitations for  $-t \geq -t_1$  (one would have to measure very soft photons at rather large opening angles - see discussion in [290] to eliminate this contribution). Note that cross section of inelastic diffraction with production of hadrons in the nucleus fragmentation region is comparable to that of quasielastic diffraction. One would have to use studies of the  $t$ -dependence of the meson production and/or hadron production in the nucleus fragmentation region to separate these two processes.

**Testing onset of the black disk regime.** Study of the vector meson production provides also a fine probe to test the onset of high density color opacity regime where LT approximation breaks down - the black disk regime in which interaction of small dipoles with heavy nuclei becomes completely absorptive. In this limit one can derive [291] a model independent prediction for the cross section of the vector meson production

$$\frac{d\sigma^{\gamma^*+A \rightarrow V+A}}{dt} = \frac{M_V^2}{Q^2} \frac{d\sigma^{\gamma_L^*+A \rightarrow V+A}}{dt} = \frac{(2\pi R_A^2)^2}{16\pi} \frac{3\Gamma_V M_V^3}{\alpha(M_V^2 + Q^2)^2} \frac{4 |J_1(\sqrt{-t}R_A)|^2}{-tR_A^2}, \quad (154)$$

where  $\Gamma_V$  is the electronic decay width  $V \rightarrow e^+e^-$ ,  $\alpha$  is the fine-structure constant. Eq. (154) corresponds to a drastically different result: a factor of  $Q^4$  slower  $Q^2$  dependence of the cross section than the LT result.

**Other directions of studies.** Recently a number of novel processes were suggested to check the interplay between CT and color opacity phenomena as well as to use CT to understand dynamics of various elementary processes.

1. It was demonstrated that it is possible to trace small dipoles through the center of the nucleus by selecting large  $t$  VM production with rapidity gap  $\gamma^*A \rightarrow VM + gap + Y$  for  $x_g = -t/(-t + M_V^2)$  [292].
2. It was suggested that amplitudes of high energy  $2 \rightarrow 3$  branching processes:  $a + b \rightarrow c + d + e$ , where  $t = (p_b - p_e)^2$  is small,  $t' = (p_a - p_c)^2$ ,  $s' = (p_c + p_e)^2$  are large, and  $t'/s' = const$  can be written in a factorized form as a convolution of different nucleon quark GPDs and hard  $2 \rightarrow 2$  amplitudes [293]. Several examples of such processes are depicted in Fig. 61. In the case of the  $ep$  collider one would be able to study both the nucleon GPDs and GPDs of the real (virtual photon). Also it will be possible to study

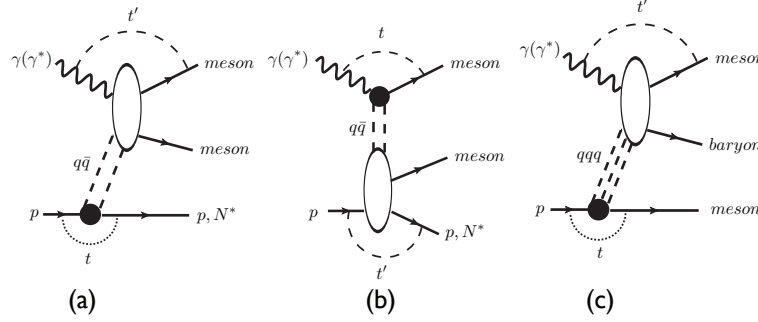


Figure 61. Examples of  $2 \rightarrow 3$  processes probing (a) nucleon GPDs and large angle  $\gamma^*(q\bar{q}) \rightarrow \pi\pi(\pi\rho)$  scattering; (b) photon GPDs and large angle  $nucleon(q\bar{q}) \rightarrow \pi N$  scattering, (c) nucleon  $\rightarrow$  meson GPD and large angle  $\gamma^*(qqq) \rightarrow \pi N$  scattering.

large angle  $\gamma(\gamma^*) + (q\bar{q}) \rightarrow meson_1 + meson_2$  and  $\gamma(\gamma^*) + (qqq) \rightarrow meson + baryon$  reactions.

3. Embedding these processes in the nuclei, for example by studying the process  $\gamma + A \rightarrow \pi^+\pi^+A^*$  it will be possible to determine at what  $p_T$  of the pions CT sets in and hence determine minimal  $p_T$  for which these processes could be used to study various quark GPDs. The nuclear transparency for these processes is very sensitive to the size of the meson  $\bar{q}$  configurations [294]. Hence it maybe possible to determine characteristic transverse size of  $q\bar{q}$  involved in the hard process using Eq. (150). Also by studying the transparency as a function of  $s$  for fixed  $s', t, t'$  one could measure in a great detail the rate and the pattern of the space time evolution of small  $q\bar{q}$  wave packets.

**Conclusions.** In summary, it would be possible to study color transparency and color opacity dynamics at the EIC in a variety of nuclear processes. Observation of CT will play a crucial role in determining the kinematics where studies of the GPDs will be possible at the EIC.

### 3.3 Nuclear quark and gluon GPDs

Vadim Guzey, Mark Strikman

Generalized parton distributions (GPDs) parameterize the response of hadronic targets (nucleon, nucleus) when probed by hard probes in exclusive reactions. The QCD factorization theorems state the GPDs are universal distributions that can be accessed in a wide range of hard exclusive processes: deeply virtual Compton scattering (DVCS) [295], electroproductions of mesons by longitudinal virtual photons [283], time-like Compton scattering, etc. GPDs are fundamental and rigorously-defined quantities that encode information on: (i) the distributions and correlations of partons in hadrons that is much richer than that contained in usual diagonal parton distributions and elastic form factors (in a certain sense, GPDs provide a three-dimensional parton imaging), (ii) parton total angular momentum (thus, GPDs are believed to help resolve the so-called proton spin crisis), etc. For the detailed discussion of GPDs, see section "Imaging QCD Matter"

.....  
 ..... (to be edited by the conveners to have the correct reference).....  
 .....

While what has been said above holds true for any hadronic target, nuclear GPDs are also interesting in their own right:

- (i) Nuclear GPDs give an access to both proton and neutron GPDs [296–300]. Incoherent reactions (with nuclear break-up) can be used to study quasi-free neutron GPDs [301].
- (ii) Traditional nuclear effects—off-diagonal EMC effect [302, 303], nuclear shadowing and antishadowing [99, 304, 305]—have been predicted to be more prominent than in the diagonal case.
- (iii) Nuclear GPDs may be a good tool to study such not well-established/controversial and novel nuclear effects as the medium modifications of bound nucleon GPDs [303, 306] and presence of non-nucleonic degrees of freedom [307].

### 3.3.1 Medium $x_B > 0.05$

The cleanest way to study GPDs is deeply virtual Compton scattering (DVCS),  $\gamma^* + A \rightarrow \gamma + A'$ . Nuclear DVCS is more complex and versatile than that with the free proton because the nuclear target  $A$  can have various spins (the number of GPDs increases with the spin of the target) and many different final states  $A'$  can be produced ( $A' = A, A^*, A + \pi, A - 1 + N$ , etc.). In the situation when the final nuclear state cannot be detected, one can sum over all final states  $A'$  assuming their completeness and obtain for the nuclear DVCS cross section [299]:

$$\sigma_{\text{DVCS}} = A(A - 1)\sigma_{\text{DVCS}}^{\text{coh}} + A\sigma_{\text{DVCS}}^N. \quad (155)$$

In this expression, the first term is the coherent-dominated contribution (without nuclear break-up or excitation) which is proportional to the nuclear form factor squared,  $F_A^2$ , and significant only at the small momentum transfer  $t$ . The second term is the incoherent contribution whose  $t$  dependence is governed by that of the nucleon GPDs; this term dominates at large  $t$ .

Similarly to Eq. (155), the expressions interpolating between the coherent and incoherent regimes can also be derived for the interference between DVCS and Bethe-Heitler (BH) amplitudes and BH cross section. For instance, the coherent-dominated contribution to the interference between DVCS and BH amplitudes scales as  $Z(A - 1)$  and that to the BH cross section scales as  $Z(Z - 1)$  ( $Z$  is the nuclear charge). Therefore, one immediately and model-independently predicts the enhancement of the ratio of the nuclear to free proton DVCS beam-spin asymmetries at small  $t$ ,  $A_{\text{LU}}^A/A_{\text{LU}}^p \sim (A - 1)/(Z - 1)$  [298, 299]. At large  $t$  the cross section is dominated by the incoherent contribution, no nuclear enhancement is expected, and  $A_{\text{LU}}^A/A_{\text{LU}}^p \sim 1$  (in fact, the neutron contribution somewhat suppresses the ratio and makes  $A_{\text{LU}}^A/A_{\text{LU}}^p < 1$  [300]). While the Hermes analysis of nuclear DVCS with  $^4\text{He}$ ,  $^{14}\text{N}$ ,  $^{20}\text{Ne}$ ,  $^{84}\text{Kr}$ , and  $^{132}\text{Xe}$  targets supports that  $A_{\text{LU}}^A/A_{\text{LU}}^p \sim 1$  at large  $t$  and  $A$ -independent at all  $t$ , it finds that at small  $t$ ,  $A_{\text{LU}}^A/A_{\text{LU}}^p = 0.91 \pm 0.19$  [308].

Quark nuclear GPDs in the kinematic region of the off-diagonal EMC effect,  $0.1 < x_B < 0.3$ , will be constrained with high precision by the analysis of the completed Jefferson Lab (CLAS) experiment on DVCS on  $^4\text{He}$  [309]. The experiment measured purely coherent nuclear DVCS (the recoiled nucleus was detected using the BoNuS spectator tagger) and also the DVCS on a quasi-free proton. The latter will probe possible nuclear medium modifications of the bound proton quark GPDs [306]. Gluon GPDs in nuclei can be accessed best in hard exclusive production of heavy vector mesons. For instance, coherent  $J/\psi$  production for  $x_B > 0.1$  can be used to learn about the off-diagonal EMC effect in the gluon

channel. The incoherent production of  $J/\psi$  can be used to probe medium modifications of the gluon GPD of the bound nucleon.

The EIC will be the only other accelerator beside JLab 12 GeV to study GPDs in  $e + A$  collisions, and will contribute considerably to their knowledge. In particular, it will access sea quark and gluon distributions, which are hard to measure at JLab due to the limited  $x$  and  $Q^2$  range, and open dedicated channels like  $J/\Psi$  diffractive production.

### 3.3.2 Small $x_B < 0.05$ : leading twist shadowing and exclusive diffraction

The EIC will open the way to experimental measurements of nuclear GPDs at small  $x_B$ , where nuclear shadowing is known to occur for PDFs. The leading twist theory of nuclear shadowing (see section 2.1.6) allows one also to predict the impact parameter dependence of nuclear PDFs [95, 97–99]. The resulting impact parameter dependent nuclear PDFs,  $f_{j/A}(x, Q^2, b)$  ( $b$  is the two-dimensional vector of the impact parameter) are nothing else but the corresponding nuclear generalized parton distributions (GPDs) in the  $\xi \rightarrow 0$  limit and in the impact parameter space [305]:

$$f_{j/A}(x, Q^2, b) = H_A^j(x, \xi = 0, b, Q^2). \quad (156)$$

GPDs depend on two light-cone fractions  $x$  and  $\xi$ ;  $\xi$  is fixed by the external kinematics,  $\xi = x_B/(2 - x_B)$ , where  $x_B$  is the standard Bjorken  $x$ . The number of GPDs depends on the spin of the target; we shall consider only spinless targets characterized by one twist-two chirally-even GPD  $H^j$  ( $j$  is the parton flavor).

Using the predictions of the leading twist theory of nuclear shadowing for the impact parameter dependence of nuclear PDFs (Eq. (35)) and the connection of Eq. (156), one can obtain the nuclear GPD  $H_A^j$  at small  $x$  in the  $\xi = 0$  limit. The final result for the GPDs in the momentum space is

$$\begin{aligned} H_A^j(x, \xi = 0, t, Q^2) = & AF_A(t) f_{j/N}(x, Q^2) \\ & - \frac{A(A-1)}{2} 16\pi \Re e \left\{ \frac{(1-i\eta)^2}{1+\eta^2} \int d^2b e^{i\vec{\Delta}_\perp \cdot \vec{b}} \int_{-\infty}^{\infty} dz_1 \int_{z_1}^{\infty} dz_2 \int_x^{0.1} dx_P \rho_A(b, z_1) \right. \\ & \times \rho_A(b, z_2) e^{im_N x_P (z_1 - z_2)} e^{-\frac{A}{2}(1-i\eta)\sigma_{\text{soft}}^j(x, Q^2) \int_{z_1}^{z_2} dz' \rho_A(b, z')} \frac{1}{x_P} f_j^{D(4)}(\beta, Q^2, x_P, t_{\min}) \Big\}, \end{aligned} \quad (157)$$

where the notation is the same as in eqs. (34) and (35).

Figure 62 presents our predictions for the ratio  $H_A^j(x, \xi = 0, t, Q^2)/[AF_A(t)f_{j/N}(x, Q^2)]$  for  $^{208}\text{Pb}$  as a function of  $x$  for different values of  $t$ . The left panel corresponds to the ratio of the  $\bar{u}$ -quark distributions; the right panel corresponds to the gluon distributions. All curves correspond to  $Q^2 = 4 \text{ GeV}^2$  and model FGS10\_H (see details in section 2.1.6). Since the  $t$  dependence of the shadowing correction to  $H_A^j(x, \xi = 0, t)$  (second term in Eq. (157)) is somewhat slower than that of the impulse approximation (the first term), the effect of nuclear shadowing expectedly increases as  $|t|$  is increased.

Experimental observables measured in hard exclusive processes such as, *e.g.*,  $\gamma^* + A \rightarrow \gamma(J/\Psi, \rho, \dots) + A$ , probe the GPD  $H_A^j(x, \xi, t, Q^2)$  integrated over the entire region of the light-cone variable  $x$ ,  $0 \leq x \leq 1$ . However, at high energies (small  $\xi$  or  $x_B$ ), the situation simplifies: the predominantly imaginary  $\gamma^* + A \rightarrow \gamma(J/\Psi, \rho, \dots) + A$  scattering amplitudes are expressed solely in terms of the GPDs at the  $x = \xi$  cross-over line,  $H_A^j(\xi, \xi, t, Q^2)$  (to the

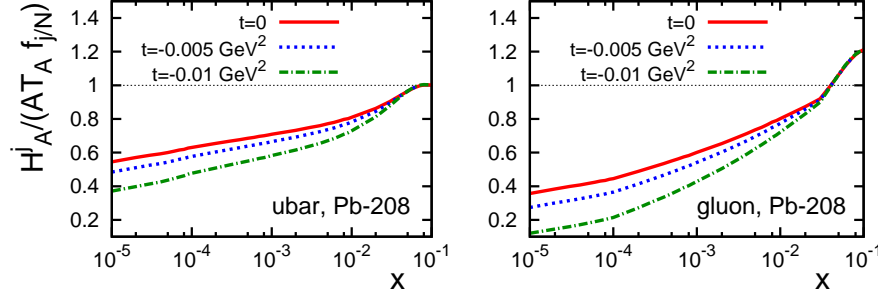


Figure 62. The ratio of the gluon and  $\bar{u}$ -quark  $H_A^j(x, \xi = 0, t)/[AF_A(t)f_{j/N}(x, Q^2)]$  for  $^{208}\text{Pb}$  as a function of  $x$  for different values of  $t$ . All curves correspond to  $Q^2 = 4 \text{ GeV}^2$  and model FGS10\_H.

leading order in the strong coupling constant  $\alpha_s$ ). In addition, it was shown in [310] that at high energies and in the leading logarithmic approximation (LLA), GPDs at an input scale  $Q_0^2 \sim \text{few GeV}^2$  can be approximated well by the usual parton distributions, i.e., it is safe to neglect the effect of the skewness  $\xi$ . Therefore, for instance, for the imaginary part of the coherent nuclear deeply virtual Compton scattering (DVCS) amplitude ( $\gamma^* + A \rightarrow \gamma + A$ ), we have at the leading order in  $\alpha_s$ :

$$\begin{aligned} \Im m \mathcal{A}_{\text{DVCS}}(\xi, t, Q^2) &= -\pi \sum_q e_q^2 [H_A^q(\xi, \xi, t, Q^2) + H_A^{\bar{q}}(\xi, \xi, t, Q^2)] \\ &\approx -\pi \sum_q e_q^2 [H_A^q(\xi, \xi = 0, t, Q^2) + H_A^{\bar{q}}(\xi, \xi = 0, t, Q^2)] , \end{aligned} \quad (158)$$

where  $e_q$  are the quark charges;  $H_A^q(\xi, \xi = 0, t, Q^2)$  are given by Eq. (157).

The cleanest way to access GPDs is via DVCS. At the photon level, the  $\gamma^* + A \rightarrow \gamma + A$  cross section reads, see, e.g., [311]:

$$\frac{d\sigma_{\text{DVCS}}}{dt} = \frac{\pi \alpha_{\text{em}}^2 x^2 (1 - \xi^2)}{Q^4 \sqrt{1 + \epsilon^2}} |\Im m \mathcal{A}_{\text{DVCS}}(\xi, t, Q^2)|^2 , \quad (159)$$

where  $\alpha_{\text{em}}$  is the fine-structure constant;  $\epsilon^2 = 4x^2 m_N^2 / Q^2$ ;  $\Im m \mathcal{A}_{\text{DVCS}}$  is given by Eq. (158).

The DVCS process interferes and competes with the purely electromagnetic Bethe-Heitler (BH) process. The BH cross section at the photon level can be written in the following form [311]:

$$\frac{d\sigma_{\text{BH}}}{dt} = \frac{\pi \alpha_{\text{em}}^2}{4Q^2 t (1 + \epsilon)^{5/2} (1 - y - y^2/2)} \int_0^{2\pi} \frac{d\phi}{2\pi} \frac{1}{\mathcal{P}_1(\phi) \mathcal{P}_2(\phi)} |\mathcal{A}_{\text{BH}}(\xi, t, Q^2, \phi)|^2 , \quad (160)$$

where  $y = (q \cdot P_A)/(k \cdot P_A) = Q^2/(xs)$  ( $k$  is the incoming lepton momentum,  $q$  is the momentum of the virtual photon,  $P_A$  is the momentum of the incoming nucleus,  $s$  is the total invariant energy squared);  $\phi$  is the angle between the lepton and hadron scattering planes;  $\mathcal{P}_1(\phi)$  and  $\mathcal{P}_2(\phi)$  are proportional to the lepton propagators;  $|\mathcal{A}_{\text{BH}}(\xi, t, Q^2)|^2$  is the BH amplitude squared. The expressions for  $\mathcal{P}_{1,2}(\phi)$  and  $|\mathcal{A}_{\text{BH}}(\xi, t, Q^2)|^2$  can be found in [311]. Note that  $|\mathcal{A}_{\text{BH}}(\xi, t, Q^2)|^2$  is proportional to the nuclear electric form factor squared,  $|F_A(t)|^2$ , and the nucleus charge squared,  $Z^2$ .

Integrating the differential cross sections in Eqs. (159) and (160) over  $t$ , one obtains the corresponding  $t$ -integrated cross sections between  $t_{\min} \approx -x^2 m_N^2$ ;  $t_{\max} = -1 \text{ GeV}^2$ :

$$\sigma_{\text{DVCS (BH)}} = \int_{t_{\max}}^{t_{\min}} dt \frac{d\sigma_{\text{DVCS (BH)}}}{dt} . \quad (161)$$



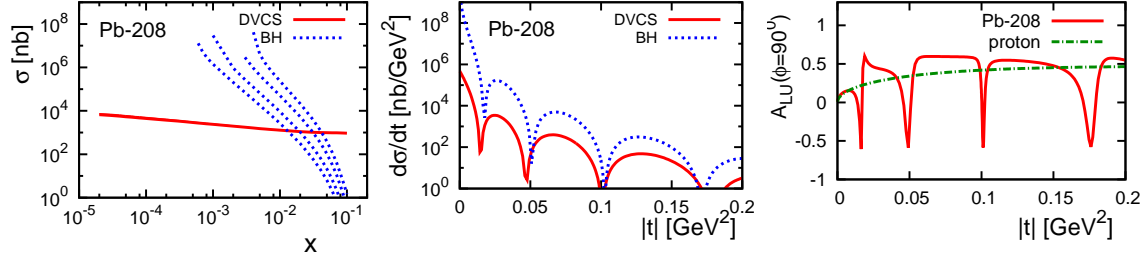


Figure 63. The DVCS (solid curves) and Bethe-Heitler (dot-dashed curves) cross sections for  $^{208}\text{Pb}$  at  $Q^2 = 4 \text{ GeV}^2$ . *Left panel:*  $t$ -integrated cross sections vs.  $x$ . The four BH curves correspond, from left to right, to  $\sqrt{s} \sqrt{s} = (32, 44, 66, 90) \text{ GeV}$ . *Middle panel:* differential cross sections vs.  $|t|$  at fixed  $x = 5 \times 10^{-3}$ ; the BH curve corresponds to  $\sqrt{s} = 32 \text{ GeV}$ . *Right panel:* beam-spin asymmetry  $A_{LU}$ .

In Figure 63 we present our predictions for a  $^{208}\text{Pb}$  target: in the left plot, the DVCS and BH cross sections at  $Q^2 = 4 \text{ GeV}^2$ , in the middle plot the differential cross sections as a function of  $|t|$  at fixed  $x = 5 \times 10^{-3}$ , and in the left plot the  $A_{LU}$  asymmetry.

In the considered kinematics, the  $t$ -integrated BH cross section is much larger than the DVCS cross section for  $x < 10^{-2}$  due to the dramatic enhancement of the BH cross section at small  $t \approx t_{\min}$  by the factor  $1/t$ , see Eq. (160). Therefore, in order to extract a small DVCS signal on the background of the dominant BH contribution for such  $x$ , one needs to consider the observable differential in  $t$ . The  $t$  dependence of the DVCS and BH differential cross sections has the characteristic shape of the nuclear form factor squared, with distinct minima and maxima. However, the minima of the DVCS cross section are slightly shifted towards smaller  $t$ : this is the effect of the leading twist nuclear shadowing in quark nuclear GPDs. The small shift of the minima toward smaller  $t$  can be interpreted as an increase of the transverse size of the distributions of quarks in nuclei. One can enhance the effect by using lighter nuclei (e.g.,  $^4\text{He}$  and  $^{12}\text{C}$ ) or by considering observables sensitive to the interference between the BH and DVCS amplitudes. For instance, the DVCS beam-spin asymmetry at  $A_{LU}(\phi = 90^\circ)$ , dramatically oscillates as a function of  $|t|$  [305], and the sole reason for these oscillations is the leading twist nuclear shadowing.

Another possibility to study nuclear shadowing in DVCS is offered by processes with nuclear break-up. In this case, the nuclear modification (suppression due to shadowing) of the DVCS break-up cross section (as compared to the impulse approximation) is as large—or even bigger—as that for the coherent case. At the same time, in the impulse approximation, the relative contribution of the DVCS and BH cross sections is enhanced by  $A/Z$  compared to the  $ep$  case. It allows one to observe the DVCS signal on the large BH background down to much smaller  $x$  than in the  $ep$  case, see the discussion in section “Imaging”

.....  
 ..... (to be edited by the conveners to have the correct reference).....  
 .....

The leading twist theory of nuclear shadowing allows one also to make predictions for certain observables in exclusive electroproduction of heavy vector mesons ( $J/\psi$ ,  $\Upsilon$ ) with nuclear targets which probe the nuclear gluon distribution. The pattern of nuclear modifications due to the leading twist nuclear shadowing (strong and  $t$ -dependent shadowing and shift of the minima of the cross section towards smaller  $t$ ) is similar to what we already discussed for small- $x$  nuclear DVCS [99]. See also the discussion by M.Strikman in Section 3.2.2.

### 3.4 Nuclear TMDs

*Jian-Hua Gao, Zuo-tang Liang, Xin-Nian Wang, Jian Zhou*

Transverse momentum dependent distributions (TMDs) are a generalization of parton distribution functions (PDFs) that extend our knowledge of the nucleon structure by including the information on parton transverse momentum distribution inside nucleon/nucleus. The exploration of the nucleon TMDs may also shed light on the issues about spin-orbit correlations and quantum interference effects. On the other side, nuclear TMDs play the important role in studying the final/initial state multiple rescattering effect. Indeed, the leading power nuclear effect comes from the gauge link appearing in the nuclear TMDs, in which the rescattering effect is encoded.

The extraction of the TMDs from high energy scattering data relies on TMD factorization theorems, established in the  $e^+e^-$  annihilation process [312] and semi-inclusive deep-inelastic (SIDIS) lepton-nucleon scattering [313]. It is not so clear whether TMD factorization still holds in the SIDIS off large nucleus target. In our recent work [314], we simply assume that it does. Correspondingly, one can introduce leading power unpolarized nuclear TMD. For simplicity, we restrict our discussion to the light cone gauge,  $A^+ = 0$  [315], where

$$f_q^A(x, \vec{k}_\perp) = \int \frac{dy^-}{2\pi} \frac{d^2 y_\perp}{(2\pi)^2} e^{ixp^+ y^- - i\vec{k}_\perp \cdot \vec{y}_\perp} \langle A | \bar{\psi}(0, \vec{0}_\perp) \frac{\gamma^+}{2} \mathcal{L}_\perp(0, y) \psi(y^-, \vec{y}_\perp) | A \rangle, \quad (162)$$

and the transverse gauge link is  $\mathcal{L}_\perp \equiv P \exp \left[ -ig \int_{0_\perp}^{\vec{y}_\perp} d\vec{\xi}_\perp \cdot \vec{A}_\perp(\infty, \vec{\xi}_\perp) \right]$ . This gauge link is not only crucial to ensure the gauge invariance of the TMD parton distribution functions, but also leads to physical consequences such as single-spin asymmetry in SIDIS and Drell-Yan process in  $e+p$  collisions [316–318]. For DIS off a nucleus target, it should also contain information on the quark transverse momentum broadening due to multiple scattering inside the nucleus [314].

In the study of either cold or hot nuclear matter, parton transverse momentum broadening plays a crucial role in unraveling the medium properties. One important parameter that controls parton energy loss is the parton transport parameter  $\hat{q}$ , *i.e.*, the transverse momentum broadening squared per unit of propagation length [319]. Therefore, calculation and measurement of the jet transport parameter is an important step toward understanding the intrinsic properties of the QCD medium. Much effort has been devoted to the study of transverse momentum broadening in high energy collisions within different approaches [319–326].

In this contribution, we start from the matrix element definition of the nuclear TMD and identify the gauge link as the main source of leading nuclear effects. The broadened distribution has a Gaussian form, as found in earlier studies [325], and suppresses the azimuthal asymmetry in SIDIS off nuclear targets. This in turns gives a direct experimental access to the cold nuclear matter transport coefficient  $\hat{q}$ , and offers a way to determine the relative magnitude of the intrinsic transverse momentum in various *nucleon* TMDs.

**Nuclear TMDs and nucleon TMDs.** The effect of final state interaction that leads to the transverse momentum broadening can be encoded in the gauge link. In fact, the nuclear dependent part of the quark TMD can be isolated from the gauge link, so that the nuclear TMD can be expressed as a convolution of the Gaussian broadening and the nucleon TMD. Assuming a weakly bound nucleon, neglecting the correlation between different nucleons,

and keeping only the matrix elements with nuclear enhancement one obtains the nuclear TMD,

$$f_q^A(x, \vec{k}_\perp) = \frac{A}{\pi \Delta_{2F}} \int d^2 \ell_\perp e^{-(\vec{k}_\perp - \vec{\ell}_\perp)^2 / \Delta_{2F}} f_q^N(x, \vec{\ell}_\perp) , \quad (163)$$

as a convolution of the nucleon TMD and a Gaussian with a width  $\Delta_{2F}$  given by the total transverse momentum broadening squared,

$$\Delta_{2F} = \frac{1}{A f_q^N(x)} \int d^2 k_\perp k_\perp^2 \left[ f_q^A(x, \vec{k}_\perp) - f_q^N(x, \vec{k}_\perp) \right] = \int d\xi_N^- \hat{q}_F(\xi_N) . \quad (164)$$

where the quark transport parameter  $\hat{q}_F(\xi_N)$  is defined as

$$\hat{q}_F(\xi_N) = -\frac{g^2}{2N_c} \rho_N^A(\xi_N) \int \frac{d\xi^-}{2p^+} \langle N | F_{+\sigma}(0) F_+^\sigma(\xi^-) | N \rangle = \frac{2\pi^2 \alpha_s}{N_c} \rho_N^A(\xi_N) [x f_N^g(x)]_{x=0}, \quad (165)$$

with  $\rho_N^A(\xi_N)$  is the spatial nucleon density inside the nucleus and  $f_g^N(x)$  is the gluon distribution function in a nucleon. Eq. (163) is our main result.

**Nuclear dependence of azimuthal asymmetry in SIDIS.** One can generalize the above approach to nuclear modification of higher twist TMD parton distributions. The case of twist-3 and twist-4 TMDs [327–329], which account for the  $\cos \phi$  and  $\cos 2\phi$  azimuthal asymmetries in SIDIS, has been recently investigated in Ref. [330, 331]. Here we review the nuclear dependent  $\cos \phi$  azimuthal asymmetry in the two kinematic regions: at small transverse momentum  $P_{h\perp} \sim \Lambda_{QCD}$  and intermediate transverse momentum  $\Lambda_{QCD} \ll P_{h\perp} \ll Q$ , where  $Q$  is the virtual photon momentum. The central ingredient of the treatment in Ref. [330] is the relation between the nucleon twist-3 TMDs and nuclear ones. If we look at the jet production in SIDIS, the azimuthal asymmetry is solely determined by one twist-3 TMD distribution  $f^\perp(x, k_\perp)$ . The ratio of the asymmetry between the SIDIS off nucleon and nuclei is

$$\frac{\langle \cos \phi \rangle_{eA}}{\langle \cos \phi \rangle_{eN}} = \frac{f_\perp^A(x, k_\perp) / f^A(x, k_\perp)}{f_\perp^N(x, k_\perp) / f^N(x, k_\perp)} \quad (166)$$

The ratio depends on how the twist-3 TMD distributions  $f_\perp^A$  is enhanced/suppressed due to the stronger final state interaction taking place inside a nucleus. Following the same approach applied to the twist-2 TMD distribution, we relate the function  $f_\perp^A$  to  $f_\perp^N$ ,

$$f_\perp^A(x, k_\perp) \approx \frac{A}{\pi \Delta_{2F}} \int d^2 \ell_\perp \frac{(\vec{k}_\perp \cdot \vec{\ell}_\perp)}{k_\perp^2} e^{-(\vec{k}_\perp - \vec{\ell}_\perp)^2 / \Delta_{2F}} f_\perp^N(x, \ell_\perp) \quad (167)$$

Given the TMDs  $f^N(x, k_\perp)$  and  $f_\perp^N(x, k_\perp)$ , one will be able to calculate the ratio (167). To illustrate the nuclear dependence of the asymmetry qualitatively, we consider an ansatz of the Gaussian distributions in  $k_\perp$  for both TMDs,

$$f^N(x, k_\perp) = \frac{1}{\pi \alpha} f_q^N(x) e^{-k_\perp^2 / \alpha} , \quad f_\perp^N(x, k_\perp) = \frac{1}{\pi \beta} f_{q\perp}^N(x) e^{-k_\perp^2 / \beta} . \quad (168)$$

As shown in Fig. 64, the azimuthal asymmetry is suppressed in  $e + A$  SIDIS as compared to that in  $e + N$  SIDIS. Note also that the suppression pattern as a function of  $k_\perp$  is sensitive to the relative magnitude of the intrinsic transverse momentum in the *nucleon* TMDs.

Now let us discuss the asymmetry at intermediate transverse momentum. The fact that TMDs are perturbative calculable when  $p_\perp \gg \Lambda_{QCD}$  or  $k_\perp \gg \Lambda_{QCD}$  allows us to reduce

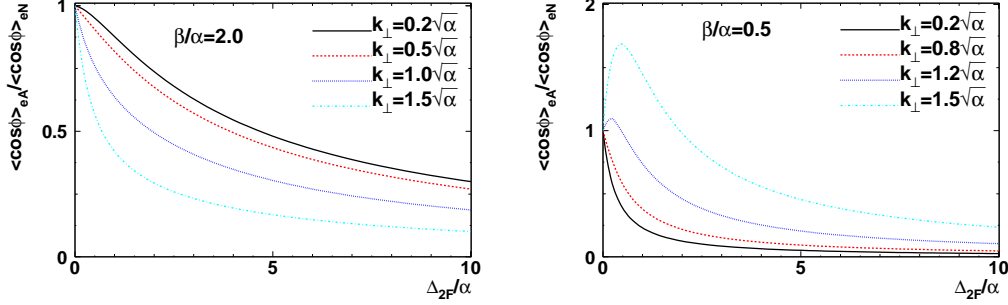


Figure 64. Ratio  $\frac{\langle \cos \phi \rangle_{eA}}{\langle \cos \phi \rangle_{eN}}$  as a function of  $\Delta_{2F}$  for different  $k_{\perp}$  and the relative width  $\beta/\alpha$ .

the theoretical uncertainty, since the twist-3 TMDs are poorly known so far. In the parton model, the azimuthal asymmetry for hadron production in SIDIS can be expressed as a convolution of a few TMD distributions and TMD fragmentation functions [327, 328]. It turns out that fragmentation functions  $H_{\perp}^{\perp}$  and  $\tilde{H}$  are power suppressed compared to  $\tilde{D}_{\perp}$  and  $D$  at large  $p_{\perp}$  [332–334]. Therefore, at intermediate transverse momentum, the leading power terms are proportional to  $f_1 \tilde{D}_{\perp}$  and  $f_{\perp} D$ . In the current fragmentation region, where  $p_{\perp}$  is large, we make collinear expansion around  $p_{\perp} = q_{\perp}$  in terms of the power  $k_{\perp}/q_{\perp}$  and keep the quadratic terms  $k_{\perp}^2/q_{\perp}^2$  in order to extract the nuclear dependent contributions. After carrying out the integrals over  $p_{\perp}$ , we find the nuclear dependent azimuthal asymmetry is related to the term  $D(z) \int \frac{k_{\perp}^2}{q_{\perp}^2} f_1(x, k_{\perp}) d^2 k_{\perp}$ . Therefore, the difference of the  $\cos \phi_h$  azimuthal asymmetry is proportional to the transverse momentum broadening.

$$\langle \cos \phi_h \rangle_{eA} - \langle \cos \phi_h \rangle_{eN} \propto \int \frac{k_{\perp}^2}{q_{\perp}^2} [f_1^A(x, k_{\perp}) - f_1^N(x, k_{\perp})] = \frac{\Delta_{2F}}{q_{\perp}^2} \quad (169)$$

**Conclusions.** In summary, we can get a direct handle on the crucial transport parameter  $\hat{q}$ , which described the properties of the QCD medium, by measuring the nuclear dependent azimuthal asymmetry at intermediate transverse momentum. Conversely, the target nucleus can be used as a filter to study nucleon TMDs, *e.g.*, to determine the relative magnitude of the intrinsic transverse momentum of  $f^N$  and  $f_{\perp}^N$ .

*Acknowledgments:* J.Z. thanks A. Metz and M. Diehl for helpful discussion.

## 4 Parton Propagation and Hadronization

### 4.1 Current Fragmentation

#### 4.1.1 Introduction and the role of $e + A$ collisions

*Raphaël Dupré and Alberto Accardi*

The fragmentation process, by which hard partons turn into hadrons, is only partly known due to its non perturbative nature. Fragmentation functions, which encode the probability that a parton fragments into a hadron, have been obtained by fitting experimental data covering large kinematic ranges and numerous hadron species, see Section 4.1.4. However, knowledge about the dynamics of hadronization remains fragmentary: this process has been studied in a number of model calculations, but lacks a first-principles description in QCD. However, a rough general picture can be established from general considerations, see Figure 65 as an example for DIS. At LO the virtual photon strikes a quark, which then propagates quasi-freely emitting gluons; after a time called *production time*, the quark neutralizes its color and gluon emission stops. The quark becomes a pre-hadron, which will eventually form a hadron at the *formation time*. In fact, a color string connects the struck quark to its nucleon, and hadrons can be formed all along this string, but we focus our attention on the hadron that contains the struck parton. In nuclear DIS, the hadronization process happens at least in part in the target nucleus (cold nuclear matter). Thus the quark is subject to energy loss by medium-induced gluon *brehmsstrahlung*, and the prehadron (as well as the hadron) can have inelastic interactions with the surrounding nucleons, leading to attenuation and broadening of the produced particle spectra. The relative weight of one mechanism compared to the other is determined by the magnitude of the color neutralization time. For full reviews, see Refs. [335, 336].

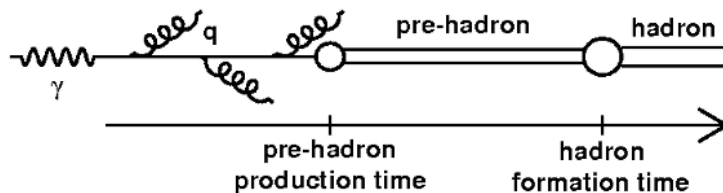


Figure 65. Sketch of the hadronization process.

These nuclear effects are both a chance to study hadronization and nuclear properties, and a misfortune as they introduce uncertainty in many nuclear measurements. For example, in neutrino experiments nuclei are used to maximize cross section, and the kinematics is reconstructed from the hadronic final state, so that a poor knowledge of hadron attenuation leads to a tangible systematic error. In heavy ion collisions, hadrons are produced in hot and expanding nuclear matter, whose properties can be measured, among other methods, by the modifications of high-energy particle spectra compared to proton-proton and proton-nucleus collisions. It is clear that the details and the time scales of the hadronization process can profoundly modify the interpretation of the data, see Fig. 2.

**The role of  $e + A$  collisions.** Nuclear deep inelastic scattering (nDIS) provides a known and stable cold nuclear medium and a low-multiplicity final state with strong experimental control on the kinematics of the hard scattering. This permits one to use nuclei as

femtometer-scale detectors and study the time scales of the hadronization process and calibrate theoretical models for parton energy loss and prehadronic scattering, that can then be applied, e.g. to the study of the QGP, see Figure 2. Initial state parton energy loss can furthermore be studied in isolation from hadronization in Drell-Yan lepton pair production in  $p + A$  collisions, where however it can be masked by nuclear modification of the target wave function such as antishadowing and the EMC effect. So, an interplay of nuclear DIS and nuclear Drell-Yan can help isolating hadronization effects on one hand, and on the other to clarify the differences in quark and anti-quark antishadowing. Perhaps more interestingly, the study of hadronization in nuclear DIS can give direct information about the gluon structure of the nuclei. For example, one can link energy loss and transverse momentum broadening to the gluon density [337] or more directly to the saturation scale [93]. In models like GiBUU [338], focussing on hadron absorption, access to the pre-hadron evolution and its color transparency evolution is possible. All these physical interpretation of the data are model dependent and based on very different assumptions about the relative importance of the interaction mechanisms, therefore they are fragile and need to be carefully validated and calibrated with precise data.

The typical observables used to explore hadronization in nuclear DIS are the multiplicity ratio and the transverse momentum broadening, in both cases they are comparison of deuterium with heavier nuclei. The multiplicity ratio, representing the production rate of a hadron  $h$  in a nuclear target  $A$  compared to Deuterium, is defined as:

$$R_A^h(Q^2, \nu, z_h, p_T^2) = \frac{N_A^h(Q^2, \nu, z_h, p_T^2)/N_A^e(Q^2, \nu)}{N_D^h(Q^2, \nu, z_h, p_T^2)/N_D^e(Q^2, \nu)} \quad (170)$$

with  $N_t^e$  and  $N_t^h$  respectively the number of electron and the number of semi-inclusive hadrons  $h$  from a target  $t$ .  $1 - R_A^h$  is the attenuation of the hadron production on a nuclear target of atomic mass  $A$ . This ratio minimizes the influence of nuclear PDF modifications, which have been shown to cancel to a large degree up to NLO. The hadron transverse momentum broadening, representing the increase of transverse momentum in a nuclear target  $A$  compared to Deuterium, is defined by

$$\Delta\langle p_T^2 \rangle = \langle p_T^2 \rangle_A - \langle p_T^2 \rangle_D \quad (171)$$

with  $\langle p_T^2 \rangle_t$  the average hadron transverse momentum measured in a target  $t$ . When integrated on large kinematic range, these observables they are dominated by the geometry of the nuclei and are do not discriminate well between the models. One needs to also consider more differential observables, including a multi-dimensional analysis of  $R_M$  and  $\Delta\langle p_T^2 \rangle$ , and hadron-hadron and photon-hadron correlations.

Another possibility is to use experimental settings in which we can isolate the involved processes. In the case of EIC, the high energy boost imparted to the struck quark in events with large  $\nu$  can increase dramatically the production length, which leads to pre-hadron production far outside the nuclei and an experimental isolation of pure parton energy loss effects. Since the pre-hadron production time is expected to roughly be inversely proportional to the mass squared of the hadron, measuring attenuation and  $p_T$ -broadening of many meson and baryon species, together with the large  $\nu$  leverage afforded by the EIC, will give another important handle in the exploration of the hadronization mechanism. Finally, new features will be available at the EIC, the high rate for heavy flavor production ( $D$  and  $B$  mesons) will allow the measurement of heavy quark energy loss. Finally, jet production, will open the possibility to study the dynamics of parton showers and the detailed transport

properties of cold nuclear matter using specific jet observables.

**Overview of theoretical models.** Three processes are typically included in theoretical descriptions of in-medium hadronization: quark energy loss, prehadron absorption and modified fragmentation functions. The models in the literature are usually based on one or two of those and neglect the others. In this section we will discuss a few examples to give an idea of the abundant existing literature; for a detailed review, including models specific to heavy ion collision experiments, see Ref. [335].

Pure quark energy loss model assume a very long production time and are typically used to describe hadron suppression in the hot nuclear matter produced in heavy-ion collision. In a few cases they have been applied to nDIS data as well [339, 340] permitting a common interpretation of hadron suppression in cold and hot nuclear matter. In these models, hadron suppression is due to the lower energy of the quark when it fragments, so that hadrons are produced in lower number and at lower energy. The differences in the models depend on the way calculations of medium-induced gluon radiation are performed, on the modeling of the medium, and on assumptions about its coupling to the hard parton.

Typically, parton energy loss is determined by the transport coefficient  $\hat{q}$ , which is defined as the transverse momentum square transfered to a quark after propagating through a length of nuclear matter and is a characteristic property of that matter. It is expected to be much larger in a Quark-Gluon Plasma than in the target nucleus of a nDIS experiment, which is what is observed from the analysis of experimental data from RHIC and HERMES [339–342]. The  $\hat{q}$  transport coefficient is directly related to the observed broadening of the  $p_T$  distribution of hadrons in nDIS; it follows that the main challenge for these pure energy loss models is to make a coherent picture of both multiplicity ratios and hadron  $p_T$  broadening. In particular, for some of the models, the  $\hat{q}$  extracted from multiplicity ratio is bigger by an order of magnitude than what one would estimate from the hadron transverse momentum broadening. This has led some authors [343] to the conclusion that quark energy loss is not enough to explain the observed nuclear effects; nevertheless, the variation between theoretical models is still too big for a definitive statement.

The GiBUU model [338] is an absorption model based on Boltzmann equation including only hadronic and pre-hadronic interactions, see Section 4.1.3. It assumes short productions times obtained from the Lund string model and neglects gluon brehmstrahlung from the partonic stage. It can describe very well most of the hadron multiplicity ratios measured at HERMES and EMC using a linear growth of the pre-hadron cross section between production time and formation time. Other pure absorption models [344–346] are also successful in describing hadron attenuation. However, the transverse momentum broadening remains a challenge for this kind of models; some progress within GiBUU has been presented during the meeting by Kai Gallmeister.

To resolve the problems of the previous “pure” models, Kopeliovich *et al.* [343] describe hadronization including both quark energy loss and hadron absorption. In their model, the transverse momentum broadening is linked to quark energy loss and the multiplicity ratio suppression is explained by hadron absorption, therefore the two processes can be independently quantified. This model describes HERMES data to a large extent, and highlights the fact several processes are involved and need to be disentangled.

Recently, HERMES data have also been described by assuming factorization and universality to hold at the nuclear level not only for parton distributions but also for fragmentation functions, and a set of nuclear Fragmentation Functions have been fitted to experimental data using both  $e + A$  interactions and  $d + Au$  collisions at RHIC. In this case no dynam-

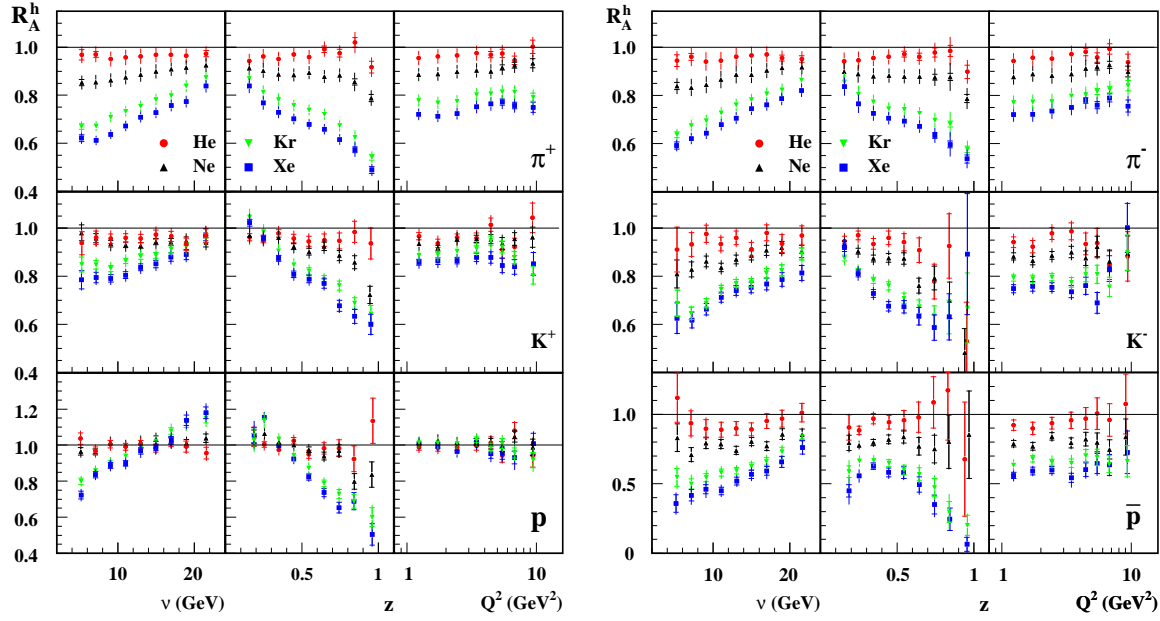


Figure 66. Multiplicity ratio of positively charged hadrons (left) and negatively charged hadrons (right) from the HERMES experiment [353]

ical assumption is made on the physical mechanism for nuclear modifications of hadron production, which is effectively subsumed into the nuclear FFs, see Section 4.1.4.

A number of other models exist using different variants of the discussed mechanisms, and most of them are able to describe the existing data to a good extent: no consensus is reached yet on which mechanisms are dominant, and indeed this is the main motivation for future precise measurements of hadronization at Jefferson Lab [347]. These low-energy experiments will be completed by the time EIC starts its operations, and will help settle some of the issues related to prehadron formation and interaction in cold nuclear matter, such as the scale of the production time.

**Previous measurements and open questions.** Unidentified charged hadron multiplicity ratios in nuclei were measured in numerous lepton facilities, the earlier results were by Osborne *et al.* [348] at SLAC, Hand *et al.* [349] and the E665 collaboration [350] at FNAL, and the European Muon Collaboration [351, 352] at CERN. Those measurements revealed a general picture: hadron suppression is stronger at low  $\nu$  and high  $z$ . On the opposite side, at low  $z$ , an increase of the number of hadron is observed.

In the more recent data from the HERMES collaboration [353, 354] several hadrons are studied individually (Fig. 66), and new observable such as transverse momentum broadening (figures 69 and 70) and two hadrons multiplicity ratios [355] are measured. Because of their improved precision and the large number of hadron species, these data provide us today with a much more detailed picture, which leads to new questions. The behavior of the kaons, for example, is very interesting:  $K^+$  are less suppressed than pions, but  $K^-$  have the same behavior than pions (figure 66). This difference is not reproduced by existing models, showing that the relatively simple phenomenological models utilized so far cannot fully describe the data. Furthermore, the introduction by HERMES of precise and flavor dependent  $\Delta p_T^2$  measurement [354] has revealed another strange behavior: the  $p_T$  broadening of  $K^+$  is



larger than for the pion (Figure 69 right). This seems to indicate more interaction for kaons, and yet they are less suppressed. To solve this apparent incongruity, one may have to consider models based on different processes involved at different stages of hadronization, like in Reference [343], reinforcing the indications coming from kaon suppression. Furthermore, no model is able to describe the  $z$  dependence of the  $p_T$  broadening, highlighting once again the need for a more detailed theoretical understanding of hadronization. Finally, proton observables are very different from anti-protons (figure 66), and no model is yet able to reproduce them correctly, although few attempts have been made [338, 356]. At the low energies of HERMES part of the problem may be due to protons coming from the target fragmentation region, which is interesting in its own right. The collider geometry and the large energy range of EIC will permit to experimentally separate clearly target and current fragmentation, allowing to address hadronization in either region. Indeed developing a consistent picture within a given model for both current and target fragmentation would be a great theoretical progress.

To complete the review of existing data, we should mention the preliminary results on pion and kaon production from the CLAS collaboration at Jefferson Lab, where electrons up to 5 GeV scatter on fixed targets ranging from Carbon to Lead [357, 358].

#### 4.1.2 Studying Hadronization at EIC

*Raphaël Dupré and Alberto Accardi*

The experimental study of the hadronization process using nDIS is well established; however the high energy available at the EIC creates novel opportunities. The main interest in going at higher energy is to insure that hadron formation occurs outside of the nuclei, in order to isolate in-medium parton interactions and energy loss. Furthermore EIC will permit, for the first time in  $e + A$  collisions, to study hadronization of the open charm and eventually open bottom mesons. Recent results from RHIC [359, 360] are showing unexpected results for open charm and bottom suppression in  $A + A$  collisions, and several contrasting explanations have already been suggested, with more detailed experiments planned at RHIC. However, due to the intricate interplay of the many variables in  $A + A$  collisions and to the poorly known nature of the Quark-Gluon Plasma partons, the  $e + A$  input seems necessary to confirm any interpretation. Also, the considerable energy leverage offered by an EIC is a chance to map precisely the  $Q^2$  evolution of parton energy loss, and determine possible nuclear modifications of DGLAP evolution. The high luminosity will also facilitate study of two particle correlations (such as hadron-hadron or photon-hadron) on a wide energy range, largely improving recent HERMES measurements, and complementing the low-energy measurements planned at CLAS. Finally, high energy permits to access jets, which give an opportunity to use new observables with improved sensitivity to quark energy loss and the medium modification of fragmentation functions, see Section 4.2. They also facilitate a detailed determination of the cold nuclear matter transport coefficients, which encode basic information on the non perturbative gluonic structure of the nuclei and can be calculated from first principles, e.g., in lattice QCD [361].

To illustrate the possibilities offered by EIC, we show projections done using the PYTHIA Monte-Carlo generator to evaluate cross sections at  $s = 200$  or  $1000 \text{ GeV}^2$ , and  $L = 200 \text{ fb}^{-1}$ . We apply a series of cuts on the generated events to ensure the DIS nature of the interaction ( $Q^2 > 1 \text{ GeV}^2$  and  $W^2 > 4 \text{ GeV}^2$ ), to limit radiative corrections ( $y < 0.85$ ), to insure that we can detect the scattered electron ( $y > 0.1$ ) and to limit di-parton production

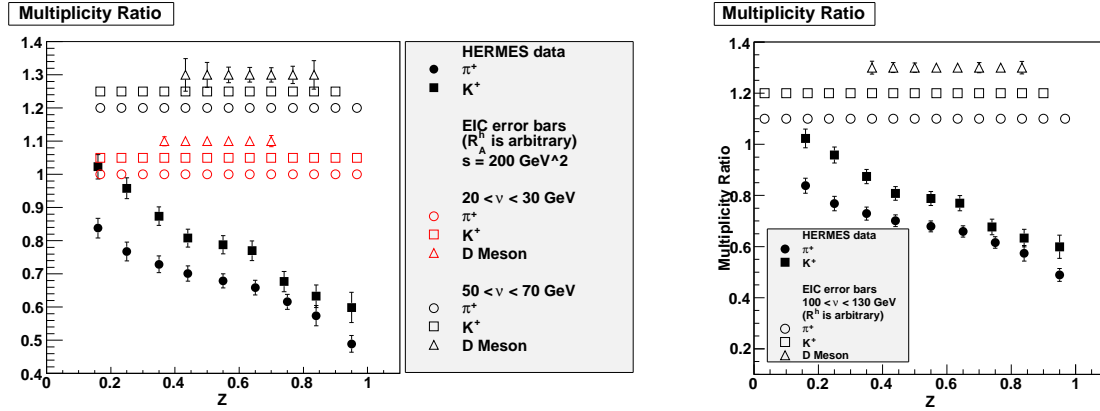


Figure 67. Multiplicity ratio in function of  $z$  for various  $\nu$  bins. Full points are data from HERMES [353], empty are projections for statistical errors at the EIC, at arbitrary vertical position. The left panel shows EIC measurements at  $s = 200 \text{ GeV}^2$ , for 2 different  $\nu$  cuts ( $20 < \nu < 30 \text{ GeV}$  and  $50 < \nu < 70 \text{ GeV}$ ); the right panel at  $s = 1000 \text{ GeV}^2$  with  $100 < \nu < 130 \text{ GeV}$ .

in the hard scattering of the virtual photon ( $x_{Bj} > 0.1$ ). Finally we assume an acceptance of 50% for pions, eta meson and kaons, and, an acceptance of 2% for heavy mesons. The acceptance is set low for heavy mesons to account for the small number of decay channels that can be effectively detected. EIC observables are plotted on arbitrary vertical scales, and include statistical errors only.

EIC is the perfect tool for precise measurement of quark energy loss and transverse momentum broadening. One may object that the higher EIC energies, because of the large  $\nu \gtrsim 150 \text{ GeV}$ , the relative effect on the quark momentum is too little to produce an appreciable hadron attenuation. This is true at least for the pions, as shown by EMC data. However, attenuation may in fact disappear at a yet higher value of  $\nu$  for large  $z$  or for heavier particles, because of reduced production times, or for large  $Q^2$ , because of a faster evolution in virtuality as discussed in Section 4.2.2. Anyway, because of the EIC kinematic flexibility, interesting multiplicity ratios can be measured. For example, Figure 67 shows projections for light and heavy flavors, which would shed light on the heavy quarks at RHIC, where they unexpectedly display a similar suppression compared to their light counterparts. It is also interesting to compare mesons of different mass but same valence quark contents, such as  $\pi^0$  vs.  $\eta$ , and  $K^0$  vs.  $\Phi$ . Figure 68 shows projections for the former case compared to calculations in a pure energy loss or pure prehadron absorption scenario. The sensitivity of such measurement to the hadronization time scales is obvious.

Changing observable, measurements of the hadron transverse momentum broadening permit to get around the smallness of hadron attenuation at large energies. Indeed the  $p_T$  broadening to first approximation is independent of  $\nu$ , and even very little effects can be experimentally observed; moreover, the induced transverse momentum has a theoretical interpretation in terms of transport coefficients. However, one should keep in mind that  $\Delta\langle p_T^2 \rangle$  of pions or other hadrons is not a direct measurement of  $\hat{q}$ , which is the parton transverse momentum broadening, and that it is essential to use dependences in  $\nu$  and  $z$  to make a model independent extraction of  $\hat{q}$ . One may also access  $\hat{q}$  thorough nuclear modifications of hadron azimuthal asymmetries, see Section 3.4. The importance of this topic, especially in the scope of EIC other measurements, is enhanced by the connection between  $\hat{q}$  and the saturation scale [93], enabling an independent large- $x$  measurement of the

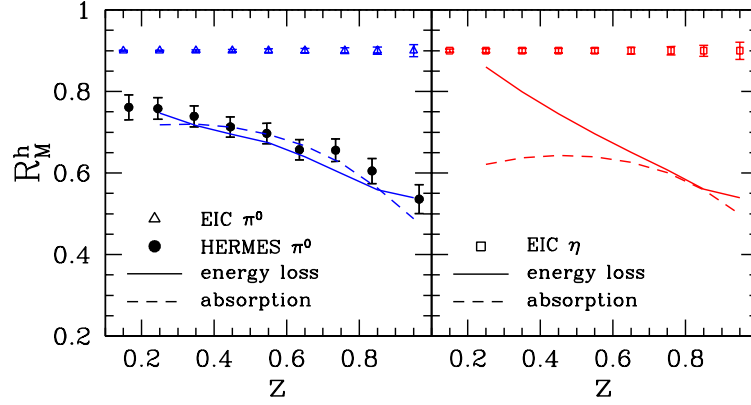


Figure 68. Multiplicity ratio for  $\pi^0$  and  $\eta$  mesons compared to pure energy loss and pure prehadron absorption computations.

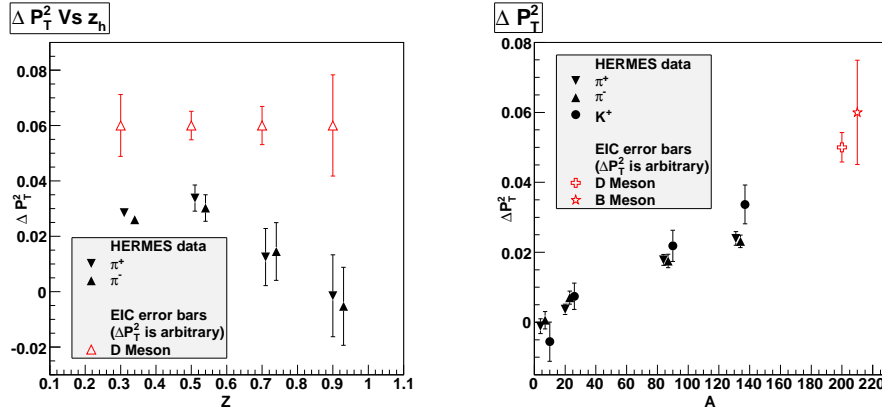


Figure 69. Transverse momentum broadening in function of  $z$  (left) and  $A$  (right), empty triangles and star are projections for EIC at  $s = 1000\text{GeV}^2$ , full points are HERMES data.

latter, complementary to the more traditional small- $x$  measurements discussed in Section 2. EIC will not only allow one to make those measurements with pions but also, and uniquely compared to previous e+A facilities, with heavy mesons (see figures 69).

The  $Q^2$  evolution of hadron attenuation is not clearly understood: HERMES data indicate a small rise of the transverse momentum broadening, but the  $Q^2$  coverage is not large enough to make a definite statement. An EIC can do a far better job as shown in figure 70 and provide a unique probe to detect any modification of the DGLAP evolution in nuclear medium.

The scaling of the hadronization times and the quark energy loss with the mass of quarks is an important question that can be used to reveal pQCD effects in parton energy loss and non perturbative effects in hadronization [362, 363]. Many measurements to explore this at the EIC are possible, as the figures in this section illustrate.

To achieve the discussed measurement the key experimental requirement are good particle ID in general; for heavy flavors one needs in particular a very good vertex detector resolution, which needs to be of the order of few tens of micrometer, and high luminosity to reach a statistical precision allowing unambiguous theoretical interpretations. Having a  $\nu$  range covering low values for studies of hadronization and large values for studies of parton

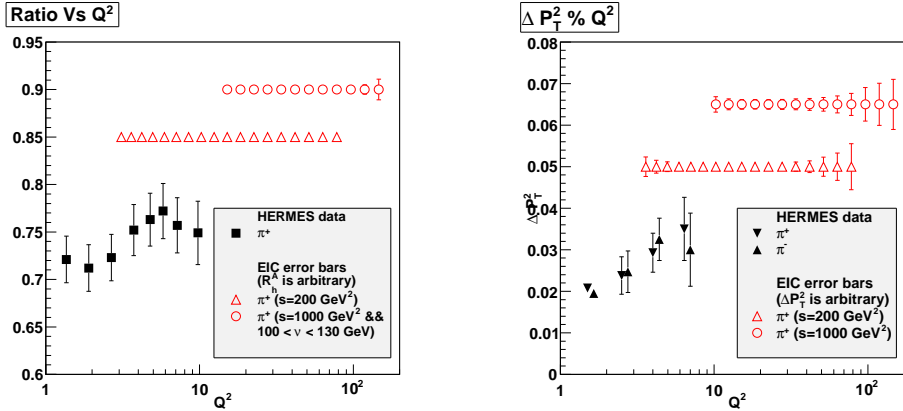


Figure 70. Multiplicity ratio (left) and transverse momentum broadening (right) in function of  $Q^2$ , empty markers are projections for EIC at  $s = 200\text{GeV}^2$  (triangles) and at  $s = 1000\text{GeV}^2$  (circles), full markers are HERMES data.

propagation and energy loss will require energies spanning  $s = 200 - 1000 \text{ GeV}^2$ . The lowest required energy can be increased provided measurements of  $y < 0.1$  can be achieved for SIDIS observables.

Finally, the high energy of EIC provides the chance, for the first time in  $e + A$ , to study hadronization through jet observables. Jets are a new and independent way to access transport coefficient  $\hat{q}$  and confirm other measurements, to explore in detail the medium induced gluon radiation and transport properties of cold nuclear matter, and to study the conversion of the parton shower into hadrons, see Section 4.2.

#### 4.1.3 Hadronization in $e + A$ collisions within GiBUU

*Kai Gallmeister and Ulrich Mosel*

The study of the interaction of hadrons, produced by elementary probes in a nucleus, with the surrounding nuclear medium can help to investigate important topics, such as color transparency and hadronization time scales. We investigate this by means of the semiclassical GiBUU transport code [364], which not only allows for absorption of newly formed hadrons, but also for elastic and inelastic scattering as well as for side feeding through coupled channel effects. A study of parton interactions in cold, ordinary nuclear matter of known properties is important to disentangle effects of the interaction of partons from those of the medium in which they move.

We summarize here the main features of our model, for details see [338]. The model relies on a factorization of hadron production into the primary interaction process of the lepton with a nucleon, essentially taken to be the free one, followed by an interaction of the produced hadrons with nucleons. We have modeled the prehadronic interactions such that the description is applicable at all energy regimes and describes the transition from high to low energies correctly. For the first step we use the PYTHIA model, that has been proven to very successfully describe hadron production, also at the low values of  $Q^2$  and  $\nu$  treated in our studies. This model contains not only string fragmentation but also direct interaction processes such as diffraction and vector-meson dominance. In this first step we take nuclear effects such as Fermi motion, Pauli blocking and nuclear shadowing into account [365]. The relevant production and formation times [338] are obtained directly from PYTHIA [366].

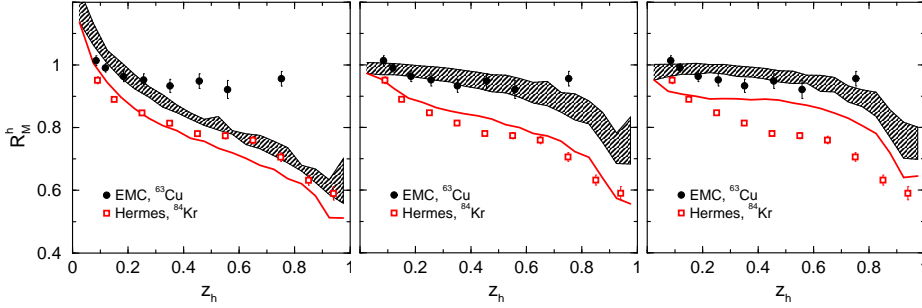


Figure 71. Nuclear modification factor for charged hadrons. Experimental data are shown for HERMES at 27 GeV and for EMC at 100-280 GeV. The cross section scenarios are (from left to right): constant, linear and quadratic increase with time after production.

In the second step we introduce prehadronic interactions between the production and the formation time and the full hadronic interactions after the hadron has been formed.

The actual time dependence of the prehadronic interactions presents an interesting problem in QCD. Dokshitzer et al. [367] have pointed out that QCD and quantum mechanics lead to a time-dependence somewhere between linear and quadratic. We also note that a linear behavior has been used by Farrar et al. [368] in their study of quasi-exclusive processes. In our calculations we work with different time-dependence scenarios, among them a constant, lowered prehadronic cross section, a linearly rising one, and a quadratically rising one. In addition, we study a variant of the latter two, where the cross section for leading hadrons, i.e., hadrons that contain quarks of the original target nucleon, starts from a pedestal value  $\sim 1/Q^2$ , thus taking into account possible effects of color transparency.

Fig. 71 shows a comparison of these various model assumptions to HERMES and EMC data on unidentified charged hadron attenuation. A good description of both data sets simultaneously is obtained only with a linear time dependence of the cross sections. Furthermore, a nearly perfect agreement is seen in comparisons with data taken by the HERMES collaboration for pions, kaons, and protons, which give the attenuation  $R_M$  as a function of energy transfer  $\nu$ , relative energy  $z_h = E_h/\nu$ , momentum transfer  $Q^2$  and the squared transverse momentum  $p_T^2$  [353]. The rise of  $R_M$  with  $\nu$  is mainly an acceptance effect, as we have shown in [365], whereas the weaker rise of  $R_M$  with  $Q^2$  reflects the pedestal value  $\sim 1/Q^2$  of the prehadronic cross sections.

In Fig. 4.1.3 we show the average formation time for different particle species as a function of the boson energy  $\nu$ . One realizes a smooth transition from CLAS at 5 GeV up to EMC at 280 GeV for all particle species. One observes a somehow larger formation time for pions than for all other, the heavier particles. Nevertheless, this effect, being somewhere on a 50% level, is much smaller than mass ratios would suggest:  $m_N/m_\pi \sim 7$ . Thus, recalling the basic boost relation,  $t_h = \gamma_h \tau_h = (E_h/m_h)\tau_h$ , the factor  $\tau_h$  and the factor  $m_h$  in the nominator/denominator cancel each other. We therefore conclude, that within our model the formation time of a hadron in its rest frame is proportional to its mass,  $\tau_f \propto m_H$ , contrary to common assumptions of a constant formation time for all hadron species, which can also be obtained from uncertainty principle considerations [335, 362].

**Hadron Attenuation at EIC: Strong  $Q^2$  Dependence.** One may now look at hadron attenuation at EIC. Fig. 73 shows the expected attenuation for different hadron species within several  $Q^2$  bins as function of  $\nu$  and  $z$  for a collider setup  $(3 + 30)$  GeV, which is

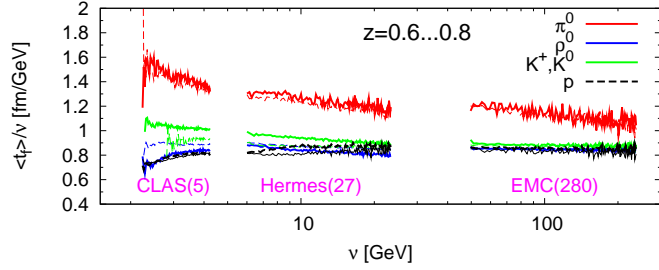


Figure 72. The average formation time of different particles divided by  $\nu$  as a function of  $\nu$  for several experimental setups.

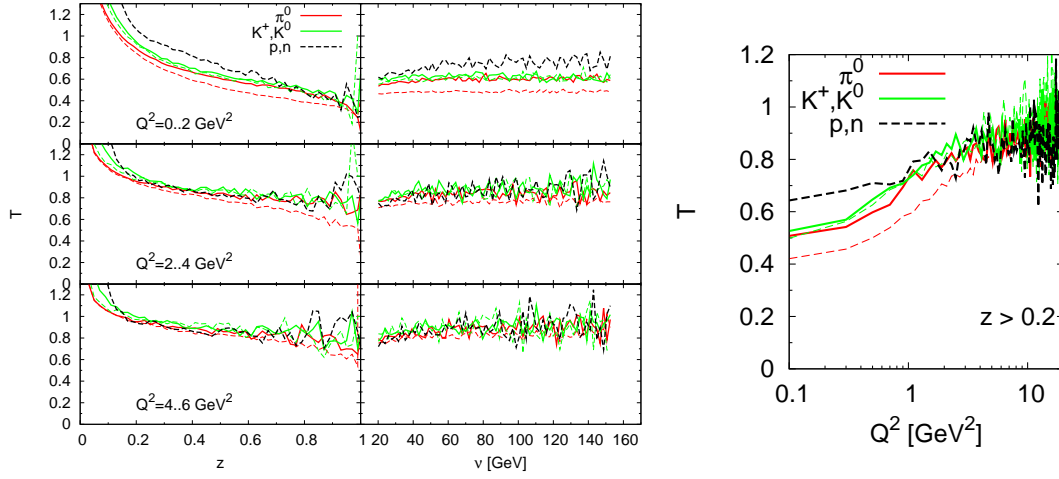


Figure 73. The hadron attenuation for different hadron species within several  $Q^2$  bins as function of  $z$  (left panel) and  $\nu$  (for  $z > 0.2$ , right panel) for a collider setup (3 + 30) GeV.

close to former EMC conditions. One observes a large  $Q^2$  dependence: while for low  $Q^2$  values, the attenuation of all hadron species decreases to approx. 0.5 at  $z \rightarrow 1$ , the attenuation is only approx. 0.8 for  $Q^2 > 4$  GeV<sup>2</sup>. This is also shown in Fig. 73, where the same attenuation is shown, but now as a function of  $Q^2$  and integrated over all  $\nu$  and  $z > 0.2$  values. It is worthwhile to mention, that there is nearly no  $\nu$  dependence for all  $Q^2$  bins visible in our calculations.

**Hadron Attenuation at EIC:  $\pi^0$  vs.  $\eta$ .** As already seen in Fig. 73, some differences in the resulting attenuation ratio show up for different hadron species. In Section 4.1.2, it has been suggested that a comparison of  $\eta$  and  $\pi^0$  attenuation ratios will distinguish between energy-loss models and absorption models. In Fig. 74 we show our results for the attenuation of these two particle species. Both attenuation signals are close to each other, but showing a somehow stronger absorption for  $\pi^0$  than for  $\eta$  mesons, in which case the discriminatory power would be weaker. In Fig. 74 we also show the hadronic interaction cross section of pions and eta mesons with nucleons. For laboratory momenta larger than 2 GeV, these are nearly identical. Thus differences in the attenuation are due to formation time effects.

#### 4.1.4 A global fit of nuclear fragmentation functions

Rodolfo Sassot, Marco Stratmann, Pia Zurita

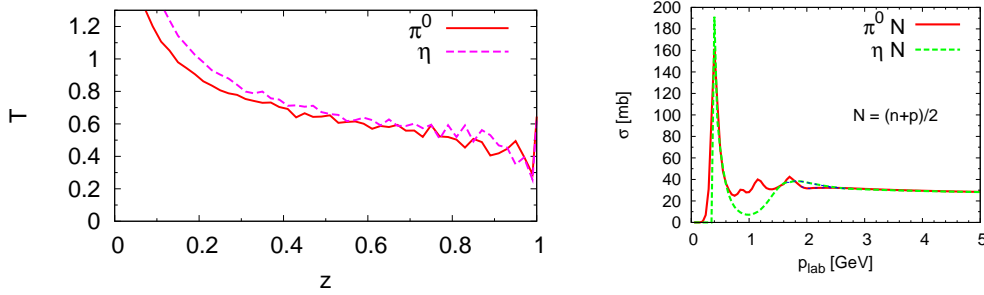


Figure 74. Left panel: The hadron attenuation for  $\pi^0$  and  $\eta$  mesons for a collider setup of 3+30 GeV. Right panel: The hadronic interaction cross section of  $\pi^0$  and  $\eta$  mesons with nucleons at rest as a function of the meson momentum.

Similarly to modifications of PDFs in nuclei, the production of hadrons in the final-state is known to be affected when occurring in a nuclear environment. For example, semi-inclusive deep-inelastic scattering (SIDIS) off large nuclear targets shows significant differences as compared to hadron production off light nuclei or proton targets, as reviewed in Section 4.1.1.

The past few years have seen a significant improvement in the pQCD description of hadron production processes, and, more specifically, in the precise determination of vacuum fragmentation functions (FFs), including estimates of their uncertainties [369]. FFs carry the details of the non-perturbative hadronization process, factorized from the hard scattering cross section in the same way as for PDFs. The most important result of these studies is that the standard pQCD framework not only reproduces data on electron-positron annihilation into hadrons, but it describes with remarkable precision also other processes like semi-inclusive deep-inelastic scattering and hadron production in proton-proton collisions. It is then quite natural to ask if pQCD factorization can be also generalized to final-state nuclear effects, i.e., to introduce medium modified or nuclear fragmentation functions (nFFs), and to assess how good such an approximation works or to determine where and why it breaks down. From theoretical considerations alone, the answer is, however, not obvious since on the one hand, interactions with the nuclear medium may spoil the requirements of the factorization theorems, but, on the other hand, any estimates of possible factorization breaking effects are strongly model dependent.

Within the factorization ansatz, nFFs should contain (factorize) all the non-perturbative details related to hadronization in a nuclear environment, would be exchangeable from one process to another (universal), and would allow for QCD estimates at any given order in perturbation theory in a well defined and unified framework. These features can be explicitly tested using data from an increasing but still limited number of experiments that have performed precise measurements of hadron production off nuclear targets, for instance, in SIDIS by HERMES [353] or in deuteron-gold collisions studied at RHIC [370, 371]. Both type of processes are compatible with a universal nuclear modification of the hadronization mechanism in the currently accessible kinematic regime. The inclusion of next-to-leading order QCD corrections and the possibility to use different observables have been proven to be crucial for an accurate parametrization of nFFs [276].

In addition to the primary goal of testing the factorization properties of nFFs and to constrain them from different data sets in a consistent theoretical framework (for further comparison with the different model estimates), a thorough analysis of nFFs also serves as

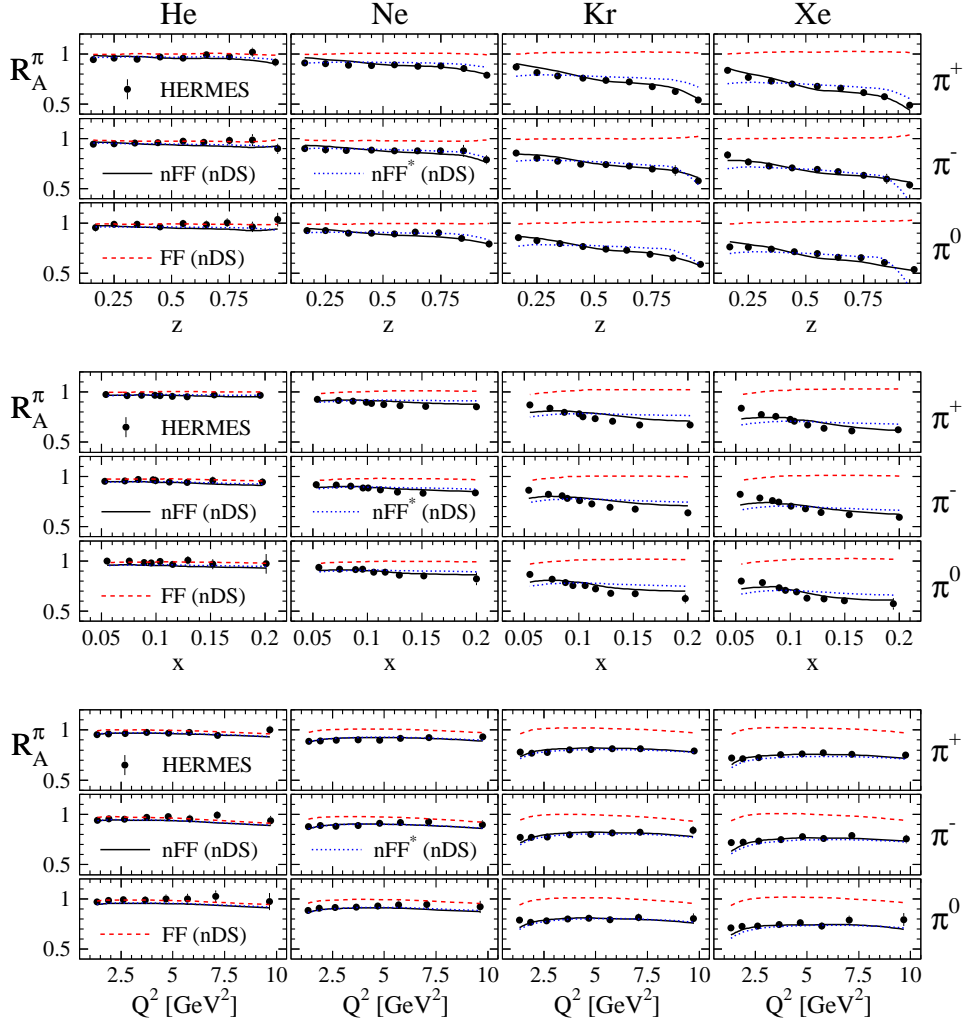


Figure 75. Quality of the nFF fit to nuclear SIDIS data from HERMES.

a baseline for ongoing studies of hadron production processes in heavy ion collisions performed at RHIC and the LHC [372]. In the following, we present a brief summary of the first global fit of nFFs and outline limitations in the analysis imposed by the data available so far.

**Medium Modified Fragmentation Functions.** Even though nuclear effects in the hadronization process have been known to be significant for quite some time, only recent experiments have become precise enough and selective from a kinematical point of view to allow for more detailed and quantitative studies. Specifically, the HERMES collaboration has performed a series of measurements of pion, kaon and proton attenuation on different nuclear targets as a function of the hadron momentum fraction  $z$  and the photon virtuality  $Q^2$ , which both are used to characterize fragmentation functions, as well as the virtual photon energy  $\nu$ , that can be related to the nucleon momentum fraction  $x$  carried by initial-state parton, see Fig. 66.

Single-inclusive identified hadron yields obtained in  $d + Au$  collisions at mid-rapidity at BNL-RHIC, which show a characteristic nucleae suppression and enhancement pattern as



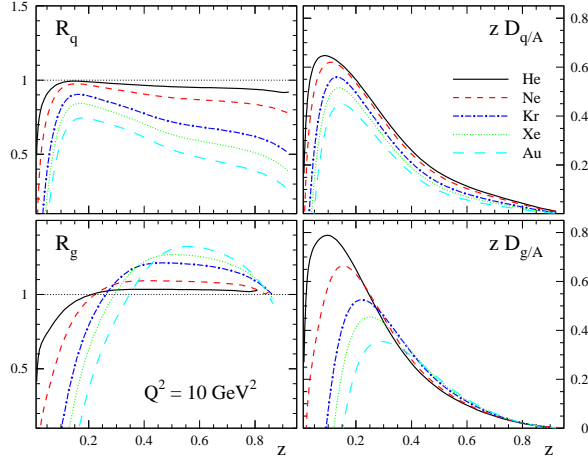


Figure 76. of medium modified and standard FFs.

a function of the hadron transverse momentum  $p_T$ , are another source of information on nuclear modification effects in the hadronization process. These measurements are often seen as “control experiments” associated with the heavy-ion program at RHIC to explore the properties of nuclear matter under extreme conditions. However, in view of the evidence for strong medium induced effects in the fragmentation process found in SIDIS,  $d + Au$  data are also of a particular relevance for extracting nFFs and testing the assumed factorization and universality properties.

To perform global nFF fits, it was proposed in Ref. [276] to relate the medium modified fragmentations to the standard ones in a convolution approach with a very simple ansatz for the weight functions. The fits give a very good description of the full kinematic dependence of the HERMES data as can be seen in Fig. 75 while an approach which ignores all final-state nuclear effects clearly fails. The same set of nFFs that account for nuclear modification in SIDIS also reproduce the main features of the  $d + Au$  data from RHIC. The peculiar  $p_T$  dependence of the effects is found to come from an interplay between quark and gluon fragmentation as a function of  $p_T$  in the hadron production cross section. It is interesting to notice that there seems to be no visible conflict between the standard  $Q^2$  dependence assumed for the nFFs and the data. In this respect, there have been many interesting suggestions and model dependent calculations at the LO level, motivating the use of medium modified evolution equations. However, in the range of  $Q^2$  covered by present SIDIS and  $d + Au$  data, there is no evidence for any significant departure from standard time-like evolution equations [373–376].

The pattern of medium induced modifications is rather different for quarks and for gluons, see Fig. 76. The dominant role of quark fragmentation in SIDIS leads to a suppression, i.e.,  $R_q^\pi < 1$ , increasing with nuclear size  $A$  as dictated by the pattern of hadron attenuation found experimentally. The enhancement of hadrons observed in  $d + Au$  collisions for  $p_T \approx 10$  GeV, along with the dominant role of gluon fragmentation at low values of  $p_T$  explains that  $R_g^\pi > 1$  for  $z \rightarrow 0.2$ . Below  $z \simeq 0.2$ , where all the data used in the fit have very limited or no constraining power, both quark and gluon nFFs drop rapidly. For the time being, the behavior in this region could easily be an artifact of the currently assumed functional form for the parameterization.

**The role of an EIC.** Thanks to its variable beam energy, the possibility to run with different nuclei, and the envisioned large luminosities, an EIC will add invaluable novel information both on nFFs from studies of semi-inclusive gadron production. In particular, the extended  $Q^2$  range where measurements will be possible will allow one to accurately test the factorization assumption for nFFs, which is at the basis of the presented approach to nuclear modifications of hadron production.

#### 4.1.5 Heavy quarks and quarkonia in a nuclear environment

*B. Z. Kopeliovich*

**Time dependence of vacuum radiation.** The color field of a quark originated from a hard reaction (DIS, high- $p_T$ ,  $e^+e^-$ , etc.) is stripped off, *i.e.*, such a quark is lacking a color field up to transverse frequencies  $q \lesssim Q$ , and starts regenerating its field by radiating gluons, *i.e.*, forming a jet. This can be described by means of an expansion of the initial "bare" quark over the Fock states containing a physical quark and different number of physical gluons with different momenta. Originally this is a coherent wave packet equivalent to a single bare quark  $|q\rangle$ . However, different components have different invariant masses and they start gaining relative phase shifts as function of time. As a result, the wave packet is losing coherence and gluons are radiated in accordance with their coherence times. The required time is to the jet energy, since the radiation time (or length) depends on the gluon energy and transverse momentum  $k$  (relative to the jet axis),

$$l_c = \frac{2E}{M_{qg}^2 - m_q^2} = \frac{2Ex(1-x)}{k^2 + x^2 m_q^2}. \quad (172)$$

Here  $x$  is the fractional light-cone momentum of the radiated gluon;  $m_q$  is the quark mass;  $M_{qg}^2 = m_q^2/(1-x) + k^2/x(1-x)$  is the invariant mass squared of the quark and radiated gluon.

One can trace how much energy is radiated over the path length  $L$  by the gluons which have lost coherence during this time interval [343, 377–380],

$$\Delta E(L) = E \int_{\Lambda^2}^{Q^2} dk^2 \int_0^1 dx x \frac{dn_g}{dx dk^2} \Theta(L - l_c), \quad (173)$$

where  $Q \sim p_T$  is the initial quark virtuality; the infra-red cutoff is fixed at  $\Lambda = 0.2 \text{ GeV}$ . The radiation spectrum reads

$$\frac{dn_g}{dx dk^2} = \frac{2\alpha_s(k^2)}{3\pi x} \frac{k^2[1 + (1-x)^2]}{[k^2 + x^2 m_q^2]^2}, \quad (174)$$

where  $\alpha_s(k^2)$  is the running QCD coupling, which is regularized at low scale by replacement  $k^2 \Rightarrow k^2 + k_0^2$  with  $k_0^2 = 0.5 \text{ GeV}^2$ . In the case of heavy quark the  $k$ -distribution Eq. (174) peaks at  $k^2 \approx x^2 m_q^2$ , corresponding to the polar angle (in the small angle approximation)  $\theta = k/xE = m_q/E$ . This is known as the dead cone effect [381, 382].

The step function in Eq. (173) creates another dead cone [380]: since the quark is lacking a gluon field, no gluon can be radiated unless its transverse momentum is sufficiently high,  $k^2 > 2Ex(1-x)/L - x^2 m_q^2$ . This bound relaxes with the rise of  $L$  until it reaches  $k^2 \sim x^2 m_q^2$ , characterizing the heavy quark dead cone at  $L_q = E(1-x)/xm_q^2$ . The radiation of such a

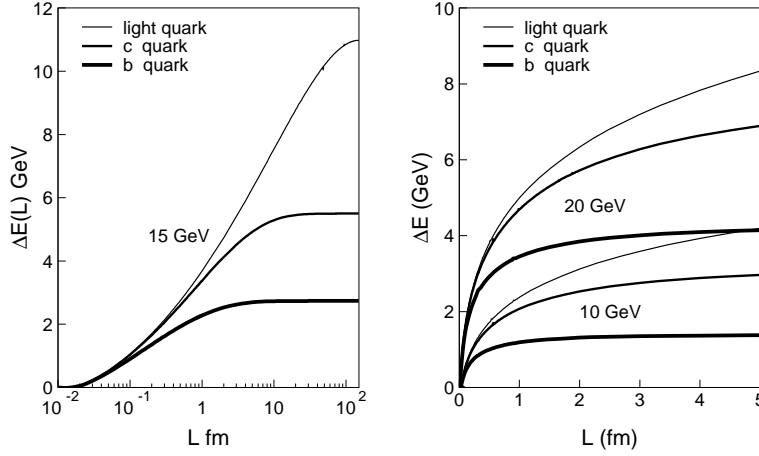


Figure 77. *Left panel:* Vacuum energy loss by light ( $m_q = 0$ ), charm ( $m_c = 1.5$  GeV) and bottom ( $m_b = 4.5$  GeV) quarks with  $E = 15$  GeV and virtuality  $Q \sim E$  as function of path length. *Right panel:* The same, but for energies 10 (three upper curves) and 20 GeV (three bottom curves), and zoomed in at short path lengths.

”naked” quark has its own dead cone controlled by its virtuality  $Q^2 \gg m_q^2$ , and is much wider than the one related to the quark mass. Therefore, there is no mass dependence of the radiation until the quark virtuality cools down to  $Q^2 \Rightarrow Q^2(L) \sim m_q^2$ : at the early stage of hadronization, when  $Q^2(L) \gg m_q^2$ , all quarks radiate equally, and the results of [382] for a reduced energy loss of heavy quarks should be applied with a precaution. The numerical results demonstrating this behavior are depicted in Fig. 77.

One can see that a substantial difference between radiation of energy by the charm and light quarks onsets at rather long distances, above 10 fm. However the  $b$ -quark radiation is suppressed already at a short distance, less than one fermi. Moreover, it completely regenerates the color field already at a distance of the order of 1 fm and does not radiate any more. Of course, this  $b$ -quark still may have a medium induced radiation, which is very weak according to [382]. Notice that the interference between vacuum and induced radiations is absent because they occur on different time scales.

**Production and formation length.** One should clearly distinguish between the production time scales for a colorless dipole (pre-hadron) and the final hadron. The former signals color neutralization, which stops the intensive energy loss caused by vacuum radiation following the hard process, while the latter is a much longer time taken by the dipole to gain the needed hadronic mass, i.e. to develop the hadron wave function. While the former is proportional to  $1 - z_h$  and contracts at large fractional momentum  $z_h$  of the hadron, the latter keeps rising proportional to  $z_h$ . These two time scales are frequently mixed up. The shortness of the production lengths at large  $z_h$  is dictated by energy conservation. Indeed, a parton originated from a hard reaction intensively radiates losing energy, and this cannot last long, otherwise the parton energy will drop below the energy of the detected hadron. Only creation of a colorless pre-hadron, which does not radiate gluons any more, can stop the dissipation of energy. Thus, energy conservation imposes a restriction on the color neutralization time [383]:

$$l_p \leq \frac{E_q}{\langle dE/dz \rangle} (1 - z_h) . \quad (175)$$

which must vanish at  $z_h \rightarrow 1$ . One should also distinguish between the mean hadronization time of a jet, whose energy is shared between many hadrons, and specific events containing a leading hadron with  $z_h \rightarrow 1$ . Production of such a hadron in a jet is a small probability fluctuation, usually associated with large rapidity gap events. The space-time development

of such an unusual jet is different from the usual averaged jet. It is illustrated in Fig. 78. Notice that one should not mix up the production time with the time scale evaluated in [384], Eq. (2), which is just the well known coherence time. This is not the time of duration of hadronization which we are interested in. If hadronization were lasting as long as the coherence time, energy conservation would be broken. Besides, a pre-hadron does not have any certain mass, since according to the uncertainty relation it takes time, called formation time, to resolve between the ground and excited states, which have certain masses. Therefore, one cannot evaluate the production time of a pre-hadron relying on the mass of the hadron.

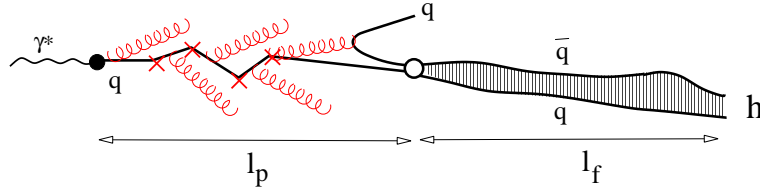


Figure 78. Two-step process of leading hadron production. On the production length  $l_p$  the quark is hadronizing experiencing multiple interactions broadening its transverse momentum and inducing an extra energy loss. Eventually the quark color is neutralized by picking up an antiquark. The produced color dipole (pre-hadron) is attenuating in the medium and developing the hadron wave function over the formation path length  $l_f$ .

Since the produced pre-hadron strongly attenuates in the nuclear medium, the position of the color neutralization point is crucial for the resulting nuclear suppression. Notice that such a picture of space-time development of hadronization is classical. In quantum mechanics one cannot say with certainty whether the pre-hadron is produced inside or outside the medium: the inside-outside interference term is significant [385].

**Heavy flavored hadrons.** The production length distribution calculated for light quarks [343, 377, 379] should be similar to that for charm quarks, which have a similar vacuum radiation during first several fermi. However, a bottom quark, according to Fig. 77, dissipates considerably less energy, moreover, its vacuum radiation ceases at the distance of about 1 fm, because the quark completely restores its color field. Of course confinement does not allow a colored quark, even with a restored field, propagate freely. It keeps losing energy via nonperturbative mechanisms [379], like in the mentioned above string (flux tube) model. Surprisingly, nonperturbative dynamics is more involved into hadronization of heavy compared with light quarks. However, one should remember that this is true only for jets which end up with production of leading hadrons with  $z_h \rightarrow 1$ .

A high-energy heavy quark always escapes from the medium and produces an open flavor hadron with no suppression. Therefore a break-up of a light-heavy dipole propagating in a medium should not lead to a suppression, unless the fractional momentum  $z_h$  of the detected hadron is fixed at a large value. In such a case break up of the dipole ignites continuation of vacuum energy loss, which slows down the quark to smaller values of  $z_h$ . This is why a quark should stop radiating at a distance  $l \sim l_p$  and produce a colorless dipole, which then survives through the medium.

It is interesting that the produced heavy-light,  $c-q$  or  $b-q$  dipoles expand their sizes faster than a light  $\bar{q}q$  dipole. This happens because of the very asymmetric sharing of the longitudinal momentum in such dipoles. Minimizing the energy denominator one gets the fractional momentum carried by the light quark,  $\alpha \sim \frac{m_q}{m_Q}$ , which indeed is very small, about

0.1 for charm and 0.03 for bottom. Then according to [380, 386] the dipole size is evolving with time as

$$r_T^2(t) = \frac{2t}{\alpha(1-\alpha)E} + r_0^2, \quad (176)$$

where  $r_0$  is the initial dipole separation: the  $b$ - $q$  dipole is expanding much faster than  $\bar{q}q$ .

**Conclusions.** The hadronization of charm and bottom quarks ends up at a short distance  $l_p$  with production of a colorless dipole. These dipoles are expanding similar, or even faster than a light  $\bar{q}q$  dipole, therefore they are strongly absorbed by the medium. This may explain why both of them are strongly suppressed in  $AA$  collisions. Studies of light *vs.* heavy meson productions at the EIC will clearly be able to validate the discussed effects.

## 4.2 Jets

### 4.2.1 Jets, in-medium parton propagation and nuclear gluons

*Alberto Accardi, Matthew C. Lamont, and Gregory Soyez*

Preliminary results from the SLAC E665 fixed target experiment have demonstrated jet production in  $e + A$  collisions at  $s \approx 1000 \text{ GeV}^2$  [387, 388]. Thus, the start of the jet study programme should be feasible in a Phase-I EIC. This can be confirmed by further simulations, required to study the capabilities in a collider experiment as opposed to a fixed-target experiment like E665.

As will be discussed in detail in the next 2 contributions, nuclear modification of production 1+1 jets production, i.e., 1 jet from current fragmentation and 1 from target fragmentation, is of great interest to study parton propagation through cold nuclear matter, in order to extract cold nuclear transport coefficients, and probing soft gluons in nuclei. In addition, the nucleus can be used as a femtometer-scale detector of the evolution of parton showers, allowing to test their perturbative descriptions (*e.g.*,  $k_T$ -ordering *vs.* rapidity ordering) and Monte-Carlo implementations, which are used pervasively in all fields of high-energy physics to analyze experimental data.

The case of 2+1 jets is also interesting. Indeed, the cross section for this process reads

$$\frac{d^2\sigma_{2+1}}{dx_p dQ^2} = A_q(x_p, Q^2) q_A(x_p, Q^2) + A_g(x_p, Q^2) g_A(x_p, Q^2), \quad (177)$$

where the two terms correspond to the quark-initiated and gluon-initiated processes respectively, and the coefficients  $A_q$  and  $A_g$  are matrix elements that can be computed at given order in perturbation theory. Unlike the 1+1 case which is dominated by quark initiated processes, the 2+1 cross section is now also sensitive to nuclear gluons, and offers yet another way to measure them.

Since the outgoing jets have to travel in the medium, the coefficients  $A_q$  and  $A_g$  will be affected by in-medium propagation. We shall assume here that the measurements of 1+1 jet cross-sections allow to control in medium quark jets, hence  $A_q$ . Then, by tagging or vetoing gluon jets in 2+1 events one can study, respectively, gluon jets in-medium propagation and the nuclear gluon distributions. In Fig. 79, we show the expected kinematic reach of the gluon measurements for a phase-I and phase-II EIC, and for various cuts on the jet transverse momentum  $p_T$ . Details can be found in [389].

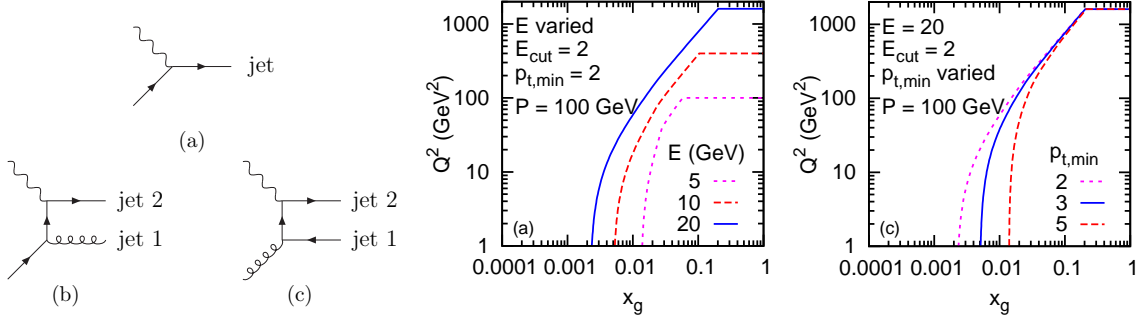


Figure 79. *Left:* Parton-level processes that contribute (a) to the 1+1 and (b,c) 2+1 jet cross-section. *Middle and Center:* Accessible kinematic range in  $x_p$  and  $Q^2$  for the 2+1 jets scenario. The accessible region is plotted for different energies  $E$  of the electron beam and hadron beam energy  $E_p = 100$  GeV, corresponding to a phase-I and phase-II EIC, for different jet transverse momentum cuts  $p_T > p_{T,min}$  at fixed jet energy cut  $E_{cut}$ .

Detailed simulations are planned to study the feasibility and physics reach of these jet studies.

#### 4.2.2 Monte-Carlo for hard jets in e+A collisions

*A. Majumder*

The production and modification of hard jets produced in lepton nucleus collisions is considered. The assumption of factorization of the hard scattering cross section from the structure functions and final fragmentation function allow one to compute the final medium modified fragmentation function in both cold nuclear matter and in a hot Quark-Gluon-Plasma (QGP) in an identical formalism. This allows for both a cross check of the basic energy loss formalism used in these reactions, and a comparative study of the partonic sub-structure of these different phases of QCD matter. Detailed descriptions are provided via a Monte-Carlo simulation of such calculations. We compare the results of analytical calculations in these two regimes and present preliminary Monte-Carlo simulations for jets produced in deep-inelastic collisions.

**Introduction to in-medium DGLAP.** Collision processes which involve a hard scale can be factorized into separate probabilities of hard and soft processes which are convoluted via a single dimensionless variable [1]. For example for the case of single hadron inclusive production in deep-inelastic-scattering (DIS), the differential cross section may be expressed as,

$$\frac{d\sigma}{dz} = \int dx G(x, Q^2) \otimes \frac{d\hat{\sigma}}{dQ^2} \otimes D(z, Q^2), \quad (178)$$

where,  $G(x, Q^2)$  represents the parton distribution function,  $\frac{d\hat{\sigma}}{dQ^2}$  represents the electron quark scattering cross section via single photon exchange. And  $D(z, Q^2)$  represents the fragmentation function to produce a hadron with a momentum  $z\nu$  from the fragmentation of the outgoing quark jet. The structure functions and fragmentation functions are defined and factorized from the hard cross sections at a given scale  $\mu^2$  which in this case is chosen to be equal to the hard scale of the process  $Q^2$ . They only need to be measured at a

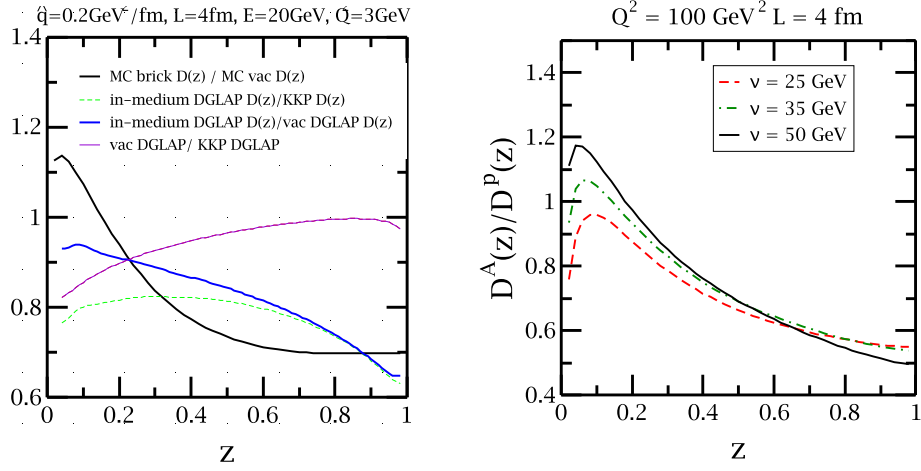


Figure 80. *Left:* A comparison of the results of an analytic DGLAP evolution calculation and a Monte-Carlo shower calculation for the same choice of input parameters. *Right:* Results of a set of Monte-Carlo simulations of a jet propagating through a 4 fm brick.

single scale, and the change of these functions with scale is given by the DGLAP evolution equations [153]. For fragmentation functions these equations read

$$\frac{\partial D(z, Q^2)}{\partial \ln Q^2} = \frac{\alpha_S}{2\pi} \int \frac{dy}{y} P(y) D\left(\frac{z}{y}, Q^2\right), \quad (179)$$

where,  $P(y)$  is the gluon splitting function and represents the probability for a quark to radiate a gluon and retain a fraction  $y$  of its light cone momentum.

In the case of DIS on a large nucleus, one may simply include the entire effect of the medium by including a length dependent multiplicative factor to the gluon splitting function [390], which accounts for the fact that the radiated gluon will scatter in the medium influencing its radiation amplitude, i.e.,  $P(y) \rightarrow P(y)K(y, q^-, L^-, Q^2)$ . The medium dependent factor given as [391],

$$K(y, q^-, L^-, Q^2) = \int_0^{L^-} d\zeta^- \frac{\hat{q}}{Q^2} \left[ 2 - 2 \cos\left(\frac{Q^2 \zeta^-}{2p^+ q^- y(1-y)}\right) \right] \quad (180)$$

In the equation above,  $L^-$  is the maximum possible length traversed in the medium in the course of one emission. In an evolution equation, the formation time of the final radiation is chosen to be larger than the maximum medium length. This restricts the length to be no larger than  $q^-/Q_{min}^2$ , where  $Q_{min}$  is the minimum allowed virtuality on exit from the medium. In an analytic solution to the DGLAP equation, one requires an input fragmentation function. The most unambiguous input is to use the known vacuum fragmentation function at the scale  $Q_{min}^2$  where we have stipulated that the jet has emerged from the medium. This is then evolved in  $Q^2$  up to the hard scale of the process using the medium modified evolution equation which includes the kernel of Eq. (180).

Results from such an in-medium DGLAP evolution are plotted in Fig. 80. The input distribution in vacuum is taken from KKP at an input scale of  $\mu_{in}^2 = 1 \text{ GeV}^2$  and evolved up to  $Q^2$ . Its ratio to the KKP fragmentation at the scale  $Q^2$  is plotted as the green dashed line in Fig. 80. Note that our numerical implementation of the DGLAP equation is different from that of KKP and so for comparison, we plot the ratio of the vacuum evolved fragmentation

function in our implementation versus that in the KKP where both calculations start from the same input distribution i.e. the KKP function at the scale  $\mu_{in}^2$ , and are compared at the higher scale of  $Q^2$ . The ratio is plotted as the magenta curve in Fig. 80. While over the range of  $z$  considered, the curve is close to unity, it may deviate by up to 20% at lower values of  $z$ .

The solid blue line in Fig. 80 represents the ratio of the medium modified fragmentation function to the vacuum fragmentation function, where both numerator and denominator are calculated using the same numerical routine (for the vacuum FF we simply use  $\hat{q} = 0$ ). This ratio can be approximately compared to the ratio of hadron yields in a DIS experiments. It should be pointed out that in all the calculations reported in this article, the medium is assumed to be static and uniform with a fixed length. This fixed length is travelled by each jet. Realistic geometries will be considered in the future.

**Monte-Carlo implementation.** In any realistic calculation of jet modification in an extended medium a variety of approximations need to be made. For example, in the in-medium DGLAP evolution equations reported in the previous sections we assumed that the entirety of the parton shower exits the medium and fragments in vacuum. This is obviously not the case. In reality, a large portion of the shower is trapped in the medium and does not undergo vacuum fragmentation. Such effects cannot be treated in a DGLAP setup where the input is the final vacuum fragmentation. Note that such effects may be included with a position dependent input fragmentation function. However, such input is always ambiguous and the computation of the evolution of a position, energy and obviously  $z$ -dependent fragmentation functions are prohibitively numerically intensive.

The obvious solution to this is to use a Monte-Carlo jet routine. Unlike analytic in-medium DGLAP calculations which evolve upwards, numerical Monte-Carlo routines evolve downwards in virtuality. As such, they are a more natural calculation which reconstructs the shower forwards in time. One starts with the original produced hard virtual parton and then constructs the Sudakov factor

$$\Delta(Q^2, \mu^2) = \exp \left[ -\frac{\alpha_S}{2\pi} \int_{\mu^2}^{Q^2} \frac{dq^2}{q^2} \int dy P(y) \{1 + K(y^-, q^-, L^-, q^2)\} \right], \quad (181)$$

which yields the probability of no resolvable emission between  $Q^2$  and  $\mu^2$  and uses this to numerically estimate the probability of the initial parton being produced with a maximum virtuality of  $\mu^2$ . One then samples the splitting function to estimate the probability that the produced partons have fractions  $y$  and  $1 - y$  of the parent parton. Unlike the case of the vacuum Sudakov factor, the equation above also contains in addition the medium dependent kernel  $K$  defined in Eq. (180). This means that at each point, the shower may undergo either a vacuum split or a medium induced split. It also clearly demonstrates how the probability of splitting increases in the medium. At each point, we estimate the location of the parton based on its formation time, which may be easily obtained from its virtuality and its energy.

This showering routine is repeated to obtain partons with lower and lower virtuality. We terminate the shower when the virtuality of the parton reaches  $\Lambda_0 = 1$  GeV. If at this point the parton is found outside the medium, then it is convoluted with a vacuum fragmentation function. If it is found inside the medium then it is removed from the final shower. We point out again that the medium in all these calculations is not a real nucleus, but rather a static brick. Once the shower is calculated in the medium, it is then repeated in vacuum. Thus



both numerator and denominator of the ratio of fragmentation functions are calculated by an identical routine.

Using this implementation we may repeat our calculations in the HERMES like systematics of Fig. 80. The results of the Monte-Carlo is represented by the black solid line. We should mention in passing that the fragmentation function used in the Monte-Carlo calculation is BKK while that in the DGLAP is KKP. We note that the ratio of fragmentation functions are rather similar. The Monte-Carlo results are for the most part below the DGLAP calculation. This is because of the mechanism by which we can systematically remove the partons which fragment in the medium, which can only be done in the MC calculation. The excess at lower  $z$  is partially due to the use of a different fragmentation function and partially due to some of these partons having a long formation time.

Having tested the Monte-Carlo calculation in HERMES like systematics  $E = 20$  GeV and  $Q^2 = 3$  GeV<sup>2</sup>, we apply the MC calculation to the EIC like systematics  $E = 25, 35, 50$  GeV and  $Q^2 = 100$  GeV<sup>2</sup>. First off, we note that even with the larger energies there is a considerable amount of suppression. This is due to the larger  $Q^2$  of the produced jet. Such jets tend to shower a lot and thus end up being considerably affected by the medium. This goes beyond what is known at HERMES that increasing the energy reduces the observed suppression. We also find a kind of universal suppression at large  $z$  which is independent of energy. This kind of universal suppression was also noted in the DGLAP calculations performed for comparison with the HERMES data. In the earlier DGLAP calculations, the reason for the scaling was due to the vanishing of the real part of the evolution equation, leaving the same virtual corrections for different energies. It is difficult to state at this point if the scaling observed in the Monte-Carlo calculations is due to a similar reason, i.e., the vanishing of the real part of the equivalent DGLAP calculation.

If the results reported here are verified by a future EIC, this would represent an interesting observation: to find an almost 50% suppression in the large  $z$  yield even for 50 GeV jets. Such high  $Q^2$  jets should be describable using perturbation theory over a large part of their lifetime and would thus yield deep probes of the medium through which they propagate. This would allow for a much clearer understanding of the gluonic structure of nucleons inside nuclei. It would also greatly facilitate our understanding of how jets are modified in a dense extended environment, which would allow for more refined probes of matter produced in heavy-ion collisions.

### 4.2.3 Jet evolution in hot and cold matter

*Hans J. Pirner*

High energy probes may be used to analyse the matter which they transverse. Jet tomography has become very popular in heavy ion physics where the plasma as the transient product of the collision of two relativistic nuclei is the object of analysis. We call this matter hot, since the plasma has temperatures of more than 200 MeV, i.e. above the critical or cross over temperature from hadronic degrees of freedom to quark-gluon degrees of freedom. Electron-nucleus jet production can help to test our understanding of jet propagation in cold matter, which should be addressed in a similar way. We will discuss jet propagation in hot matter first.

A common interpretation of the large pion attenuation in  $Au + Au$  collisions at RHIC is partonic energy loss, where hadronization occurs outside of the hot zone and is not affected by the medium. There is no doubt that gluon radiation plays an important role for the

energy loss and the parton evolution at RHIC and the LHC. The respective virtualities of partons are around  $Q = 20 \text{ GeV}$  and  $Q = 100 \text{ GeV}$ . In our modeling of jet evolution [392, 393] the parton shower is treated together with the propagation of the parton in the medium which is more realistic because of the relevant time scales. A typical shower at RHIC lasts about  $\tau_{\text{evo}} = 2 \text{ fm}$ . The non-perturbative part of hadronization involves the decay of the resonances at the preconfinement scale  $Q_0 = 1 - 2 \text{ GeV}$  into 3-4 pions. The lifetime of the plasma can be estimated  $\tau_c = 3.3 \text{ fm}$ . Comparing the two time estimates, we see that at the end of the evolution at RHIC resonances interact with hadronic resonance matter. This process can be described by a hadronic theory with cross sections slightly larger than hadronic cross sections in vacuum. Because of these large cross sections, absorptive effects play a decisive role in the observed suppression of hadrons in RHIC experiments. We have advocated two scenarios. Scenario 1 uses the conservative radiative energy loss obtained from QCD and includes prehadron formation and resonance absorption. Scenario 2 neglects the resonance phase but tunes up the energy loss parameter to fit the data.

In more detail, our model [392] works as follows: The parton produced in a hard process radiates successively to reduce its virtuality and become on mass-shell. This parton shower is modified by scattering in the medium. Because both terms enter the same equation one cannot separate scattering and radiation. This equation includes truly radiative energy loss, but without coherence. Quark fragmentation at RHIC and gluon fragmentation at LHC should give the essential results. The indices on the fragmentation functions and the splitting functions can then be dropped and the formalism becomes simpler. For the in-medium fragmentation function  $D^m(x, Q^2)$  we include into the DGLAP evolution the scattering term  $S(x, Q^2)$ .

$$\frac{\partial D^m(x, Q^2)}{\partial \ln Q^2} = \frac{\alpha_s(Q^2)}{2\pi} \int_x^1 \frac{dz}{z} P(z) D^m\left(\frac{x}{z}, Q^2\right) + S(x, Q^2) \quad (182)$$

with

$$S(x, Q^2) \simeq f \frac{n_g \sigma \langle q_\perp^2 \rangle}{2m_s Q^2} \left( D(x, Q^2) + x \frac{\partial D}{\partial x}(x, Q^2) \right). \quad (183)$$

The quantity appearing in the scattering term is the jet transport parameter  $\hat{q} \simeq \bar{n} \bar{\sigma} \langle q_\perp^2 \rangle$ , which describes the mean acquired transverse momentum of the parton per unit length.

To allow a direct fit of experimental data with only parton energy loss, we introduce a possible enhancement factor  $f$  in the scattering term. The scattering term is most relevant at small virtualities  $Q \simeq Q_0$  and consequently we have used the scale  $Q_0$  in  $\alpha_s$  to arrive at an upper boundary for  $\hat{q}$ . More explicitly, these expressions give  $\hat{q} = 0.5 \text{ GeV}^2 / \text{fm}$  for a temperature of  $T = 0.3 \text{ GeV}$  for RHIC and  $\hat{q} = 5.2 \text{ GeV}^2 / \text{fm}$  for  $T = 0.5 \text{ GeV}$  corresponding to LHC. As shown in ref. [392] we can fit the RHIC data including prehadron absorption in the final state resonance gas. The prediction for LHC gives an  $R_{AA} \approx 0.4$ . If we use an enhancement factor  $f = 8$  which is beyond any higher order QCD correction, the measurement of hadrons with high transverse momentum would be totally suppressed at LHC.

Let us now discuss jets in cold matter i.e. jets resulting from DIS on nuclei. Electron scattering on a fixed target at intermediate Bjorken  $x$  can be treated along similar lines as the DGLAP evolution of the quark jet in the cold medium, whereas electron-nucleus scattering at low  $x$ , in principle necessitates the evolution of the quark and antiquark produced from photon-gluon fusion. It is not clear whether the cascades from the two reaction products behave independently when they propagate through the target. In the Ariadne model two

strings result from the quark and antiquark produced by photon-gluon fusion. The first string connects the antiquark with the quark which emitted the gluon. The second string combines the quark with the remnant diquark of the proton. Because of the aligned jet configuration one of the two strings only contains few low momentum particles and perhaps may be neglected in first approximation. The evolution equation outlined above can then be applied to jet propagation in cold matter, and applications to the EIC are planned. Scattering partners of the quark are nucleons and the quantity  $\langle \sigma q_{\perp}^2 \rangle$  can be derived from the dipole cross section on nucleons. The resulting transport parameter at HERMES energies is very small  $\hat{q} = 0.035 \text{ GeV}^2 / \text{fm}$  and has been tested in hadronic broadening of the produced hadrons [394]. For a high energy machine with an electron-nucleon energy  $E_{cm} = 100 \text{ GeV}$  the transport parameter will be larger due to the increasing dipole cross section, we estimate that the transport parameter will increase to about  $\hat{q} = 0.1 \text{ GeV}^2 / \text{fm}$ . So effects should well be observable, but smaller than at RHIC.

### 4.3 Target Fragmentation

#### 4.3.1 Fragmentation of nuclei - a critical tool for novel QCD phenomena

*Mark Strikman*

The main focus of the discussions on quark propagation through the nuclei has been on current fragmentation processes, *e.g.*, the suppression of the leading hadron spectrum,  $p_t$  broadening and jet propagation in nuclear matter. So far very little attention has been paid to the nuclear fragmentation in DIS. To some extent this is due to the lack of experimental data, as such measurements are very challenging. However, while nuclear effects in the current fragmentation region decrease with increasing  $Q^2$  at fixed  $x$ , the nuclear effects in the fragmentation region persist in this limit, and are likely to depend on  $x$ . They may allow to address a number of important questions:

- Are color tubes formed in propagation of quarks through nuclear media?
- How different are propagation of gluons and quarks through the nuclear media?
- How different are propagation of a quark and a dipole?

To visualize these questions it is convenient to consider the process in the nuclear rest frame and distinguish three kinematic regions: (a) For  $x \geq 0.1$  a quark is knocked out (or a gluon if we consider for example leading dijet or charm production in DIS), (b) for  $0.1 > x \geq 1/(2R_{Am_N})$  the virtual photon converts to a  $q\bar{q}$  pair inside a heavy nucleus, and (c) for  $x < 1/2R_{Am_N}$   $\gamma^* \rightarrow q\bar{q}$  transition occurs predominantly before the target, see Fig. 81

In the case of  $x > 0.1$  and large  $Q^2$  corresponding to knock out of a quark, a color triplet  $qq$  system is left inside the nucleus and it is typically moving along the virtual photon momentum direction with a relatively small velocity. The knocked out quark fragments into partons/hadrons at the longitudinal distances  $y \geq 2p_q/\Delta m^2 \gg R_A$ , where  $\Delta m^2 \sim 1 \text{ GeV}^2$  can be estimated based on the current DIS data [338]. It is similar to that for color transparency processes. As a result, the leading hadron spectrum at large  $Q^2$  approaches the universal limit given by pQCD. This pattern is consistent with the experimental data. Differently from the naive expectations of the parton model an A-dependent  $p_t$  broadening

in present in this limit. Naively the hadrons produced in the fragmentation of the quark are formed at the distances given by  $y \geq 2p_h/\Delta m^2$ , so that there should be a depletion in the spectrum at  $p_h^{crit} \sim \Delta m^2 R_A/2$  followed by the enhancement at rapidities close to the nuclear rapidity (a hadron pileup). Since for heavy nuclei  $p_h^{crit} \sim 10 \div 20$  GeV/c one would expect a strong deformation of the hadron spectrum with a large increase of multiplicity for  $|y - y_A| \leq 2 \div 3$  for  $A \sim 200$ . In particular, it would be manifested in the strong break up of the heavy nuclei which is associated with emission of many soft neutrons. One should also expect an increase of the multiplicity of soft neutrons with an increase of  $p_t$  of the leading hadron, since large  $p_t$  selects events with extra Coulomb exchanges which are more likely for longer quark paths inside the nucleus and should result in a larger number of wounded nucleons. These may also lead to creation of large unscreened color regions in the nucleus - see Fig.82. An open question is how these expectations could be affected by a high degree of coherence in the emission of the partons in pQCD. Such a coherence may lead to strong screening effects in the formation of the final state and in particular a reduction of  $\Delta m^2$  away from the current fragmentation region. Also, if the color tube is very narrow, a chance that the tube intersects with other nucleons maybe significantly reduced.

For intermediate  $x \sim 0.05$ , the virtual photon also penetrates any point in the nucleus but it can hit either quark or antiquark, so in principle, by studying the properties of the leading hadron one can compare the structure of the final state interaction for the removal of quark and antiquark which maybe different, for example since  $\bar{q}$  can belong to a color singlet  $q\bar{q}$  cluster.

For small enough  $x \leq 0.03$  the virtual photon predominantly transforms into a  $q\bar{q}$  pair before the target nucleus. In the aligned jet model one would expect that the number of wounded nucleons would be given by  $A\sigma(eN)/\sigma(ep)$  with the hadrons formed at the similar distances as in the large  $x$  case. Hence naively one would expect that many nucleons will be wounded in a heavy nucleus, leading to a strong excitation of the nucleus which is known to be associated with a multiple neutron emission, emission of protons with momenta of  $\geq 300$  MeV/c, see also Section 4.3.3 .

The process of the neutron emission in DIS off lead was studied by the E665 collaboration at FNAL for average  $x \sim 0.05$  and  $Q^2 \sim \text{few GeV}^2$  [395]. The results of the measurement are compared the theoretical calculation of [396] in Fig. 82. Calculations using a Monte Carlo event generator tuned to reproduce the neutron emission in the proton-nucleus scattering reproduces both the neutron multiplicity and the neutron momentum distribution, provided only recoil nucleons with energy smaller than 1 GeV are allowed to interact in the nucleus. Taken at face value, this suggests a very strong reduction of the final state interactions at large energies which is consistent with the trend of the E665 data to have a smaller neutron multiplicity for larger  $\nu$ .

At very small  $x$  and moderate  $Q^2$  one may reach the black disk regime. In this regime the leading hadron spectrum is reduced, and the pQCD factorization for the parton frag-

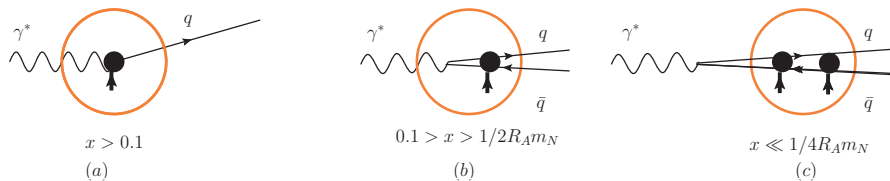


Figure 81. Space-time picture of DIS in the nucleus rest frame for different  $x$

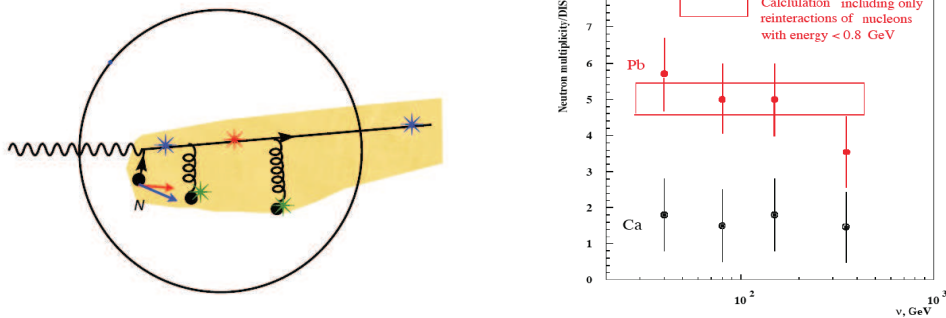


Figure 82. *Left*: Coulomb exchanges may lead to formation of extended spatial regions where color is not screened. *Right*: The E665 data [395] for the soft neutron multiplicity compared with the calculation of [396].

mentation breaks down in a gross way [291], see also Section 3.2.2. In this limit, selection of events with enhanced activity in the nuclear fragmentation region should lead to reduction of the forward spectrum: this would provide a clear signal for a new regime, since no such correlation is possible in the leading-twist pQCD regime.

In summary, hadron production in the nuclear fragmentation region is very sensitive to the dynamics of space-time evolution of the triplet and octet color tubes as well as of color dipoles. This is one of the unexplored frontiers where the collider kinematics will allow a qualitative improvements in the data, and likely lead to the discovery a series of new regularities. This may include a much higher degree of coherence in the fragmentation (hinted at by the E665 data) than suggested by the current models. Understanding of the fragmentation dynamics will be also of great help for understanding the dynamics in the nuclear fragmentation region in heavy ion collisions, where high density quark-gluon systems may be produced.

#### 4.3.2 In-medium hadronization and EMC effects in nuclear SIDIS

*C. Ciofi degli Atti, L. P. Kaptari, B. Z. Kopeliovich, and C. B. Mezzetti*

The SIDIS process  $A(e, e'(A-1))X$  in which, instead of the leading hadron, a nucleus  $(A-1)$  in the ground or in low excitation states is detected in coincidence with the scattered electron, can provide new information about the mechanism of hadronization and the origin of the EMC effect [397–401]. Two main advantages of the new SIDIS process over the classical SIDIS [335] and inclusive  $A(e, e')X$  scattering [402] are worth being mentioned here. First, it can provide a new insight into the space-time development of hadronization at the early stage, which can be probed only by placing additional scattering centers at microscopic distances, i.e. by using nuclear targets. Detecting a jet produced on a nuclear target, one can get information about its time development, but in a rather indirect and complicated way, since cascading inside the nuclear medium essentially modifies the observables. Measuring the recoil nucleus supplies additional and cleaner information about the dynamics of hadronization; in particular, this process is free of the uncertainties caused by cascading, and the survival probability of the recoil nucleus is extremely sensitive to the multiparticle components of the jet [397]. Secondly, a proper ratio of the cross sections on a nucleus  $A$  taken at different values of the Bjorken scaling variable  $x_{Bj}$  provides information on the nucleon structure functions in the medium,  $F_2^{N/A}$ . Several experimental projects to

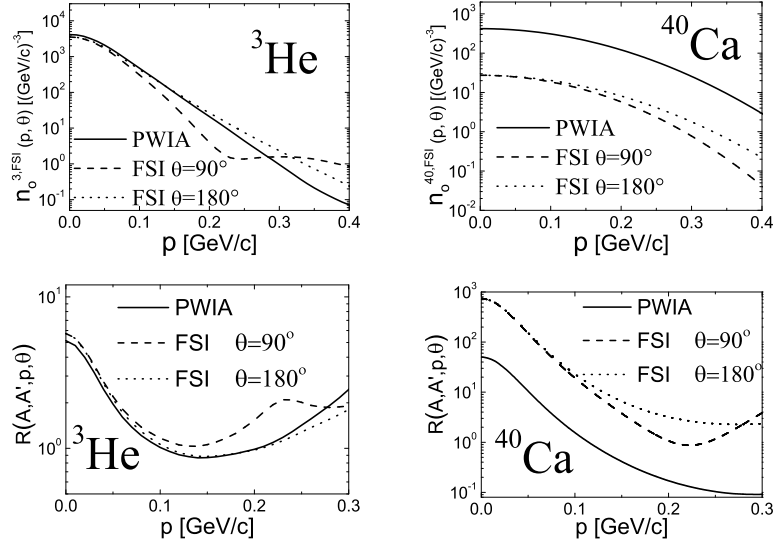


Figure 83. *Top panels:* the distorted momentum distributions  $n_0$  with  $\theta = \theta_{\widehat{\mathbf{P}_{A-1}\mathbf{q}}}$  and  $p \equiv |\mathbf{P}_{A-1}|$  for  ${}^3\text{He}$  and  ${}^{40}\text{Ca}$ . *Bottom panels:* The ratio  $R(A, A')$  of Eq. 187 with  $A = 2$ , and  $A' = {}^3\text{He}$  or  ${}^{40}\text{Ca}$ .

investigate the new process at 12 GeV Jlab have been proposed thanks to the development of proper recoil detectors [403], and the experiment on Deuteron targets has already been performed [404].

The basic ingredients of the theoretical calculation are the nuclear momentum distributions, the nucleon structure function  $F_2^{N/A}$  in the medium, and the effective cross section of interaction between the hadronizing nucleon debris and the spectator nucleons. This last reads [397]

$$\sigma_{eff}(z, x_{Bj}, Q^2) \equiv \sigma_{eff}(z) = \sigma_{tot}^{NN} + \sigma_{tot}^{\pi N} [n_M(z) + n_G(z)] \quad (184)$$

where  $\sigma_{tot}^{NN}$  and  $\sigma_{tot}^{\pi N}$  are the total nucleon-nucleon ( $NN$ ) and pion-nucleon ( $\pi N$ ) cross sections, and the  $Q^2$ - and  $x_{Bj}$ -dependent quantities  $n_M(z)$  and  $n_G(z)$  denote the pion multiplicities due to the breaking of the color string and to gluon radiation, respectively. Their explicit form directly follows from the hadronization mechanism proposed in Ref. [405], leading to a satisfactory description of the grey track production in DIS off nuclei [356].

The cross section of the  $A(e, e'(A-1))X$  process [397, 399] schematically reads

$$\frac{d\sigma^{A,FSI}}{dx_{Bj}dQ^2d\mathbf{P}_{A-1}} = F_2^{N/A}(x_A, Q^2, k^2) \otimes n_0^{A,FSI}(\mathbf{P}_{A-1}) \quad (185)$$

where  $x_A = x_{Bj}/z_1^{(A)}$ ,  $z_1^{(A)} = (M_A k \cdot q)/(m_N P_A \cdot q)$ ,  $k$  is the four-momentum of the bound nucleon and  $P_A$  of the target nucleus. In this Equation,  $n_0^{A,FSI}(\mathbf{P}_{A-1})$  is the distorted momentum distribution of the bound nucleon after final state interaction (FSI) with the debris nucleon ( $\mathbf{k}_1 = -\mathbf{P}_{A-1}$  in Plane Wave Impulse Approximation):

$$n_0^{A,FSI}(\mathbf{P}_{A-1}) = \frac{1}{2J_A + 1} \sum_{\mathcal{M}_A, \mathcal{M}_{A-1}} \left| \int d\mathbf{r}'_1 e^{i\mathbf{P}_{A-1}\mathbf{r}'_1} \langle \Psi_{J_{A-1}, \mathcal{M}_{A-1}}^0 | S_{FSI}^{XN} | \Psi_{J_A, \mathcal{M}_A}^0 \rangle \right|^2 \quad (186)$$

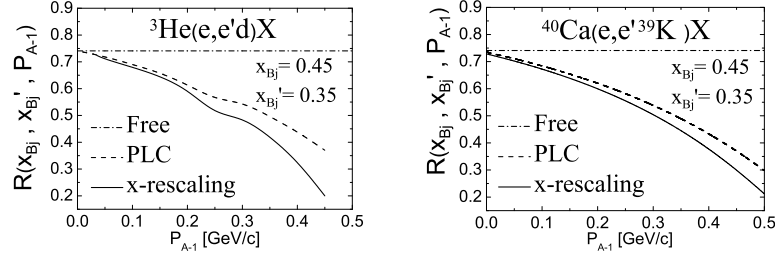


Figure 84. The ratio  $R(x_{Bj}, x'_{Bj})$  of Eq. (188) for the process  ${}^3\text{He}(e, e'd)X$  and  ${}^{40}\text{Ca}(e, e'{}^{39}\text{K})X$  calculated with different nucleon structure functions: i) free structure function; ii) off mass-shell (x-rescaling) structure function; iii) with suppression of point-like configurations (PLC) in the medium depending upon the nucleon virtuality [409] ( $P_{A-1} \equiv |\mathbf{P}_{A-1}|$ ).

where  $S_{FSI}^{XN}$  is the debris-nucleon eikonal scattering  $S$ -matrix which differs from the Glauber form [406] because of the  $z$  dependence of  $\sigma_{eff}$ . The results of some calculations are presented in what follows, using for Deuteron and  ${}^3\text{He}$  realistic wave functions [407] corresponding to the AV18 interaction [408], and for heavy nuclei single particle mean field wave functions. A good agreement between our parameter-free calculation [401] and the experimental JLab data for  ${}^2\text{H}(e, e'p)X$  around  $\theta \simeq 90^\circ$  is exhibited.

The distorted momentum distributions of  ${}^3\text{He}$  and  ${}^{40}\text{Ca}$  at kinematics more appropriate for EIC are shown in Fig. 83; as already pointed out, the FSI is governed by the details of  $\sigma_{eff}$  and strongly affects the survival probability of  $(A-1)$ , as it can be seen by comparing the results for  ${}^3\text{He}$  and  ${}^{40}\text{Ca}$ . Let us denote the cross section (185) by  $\sigma^{A,FSI}$ . Then, if our description is correct, the ratio of cross sections on different nuclei,

$$R(A, A', \mathbf{P}_{A-1}) = \frac{\sigma^{A,exp}(x_{Bj}, Q^2, |\mathbf{P}_{A-1}|, z_1^{(A)}, y_A)}{\sigma^{A',exp}(x_{Bj}, Q^2, |\mathbf{P}_{A-1}|, z_1^{(A')}, y_{A'})} \rightarrow \frac{n_0^{(A,FSI)}(\mathbf{P}_{A-1})}{n_0^{(A',FSI)}(\mathbf{P}_{A-1})} \quad (187)$$

should be governed only by the FSI, as shown in Fig. 83.

In order to tag bound nucleon structure functions, whose nuclear modification is one of the causes of the EMC effect, one has to get rid of the distorted nucleon momentum distributions and other nuclear structure effects. This can be achieved by considering the ratio of the cross sections on a nucleus  $A$  measured at two different values of the Bjorken scaling variable,  $x_{Bj}$  and  $x'_{Bj}$ , leaving unchanged all other quantities in the two cross sections, i.e., the ratio

$$R(x_{Bj}, x'_{Bj}, |\mathbf{P}_{A-1}|) = \frac{\sigma^{A,exp}(x_{Bj}, Q^2, |\mathbf{P}_{A-1}|, z_1^{(A)}, y_A)}{\sigma^{A,exp}(x'_{Bj}, Q^2, |\mathbf{P}_{A-1}|, z_1^{(A)}, y_A)} \approx \frac{F_2^{N/A}(x_A, Q^2, k^2)}{F_2^{N/A}(x'_A, Q^2, k^2)} \quad (188)$$

which depends only upon the nucleon structure function  $F_2^{N/A}$ . Calculations of the ratio (188) have been performed [401] using three different structure functions, namely, the free one, giving no EMC effect, and two medium dependent structure functions, yielding only a few percent difference in the inclusive cross section. It can be seen from Fig. 84 that the discrimination of different models of the medium dependence of  $F_2^{N/A}(x_A, Q^2, k^2)$  can indeed be achieved, especially at large  $P_{A-1} \equiv |\mathbf{P}_{A-1}|$ .

In conclusion, from what shown here and in the original papers [397–401] it appears that the SIDIS process  $A(e, e'(A-1))X$ , with detection of a complex nucleus  $(A-1)$ , would be extremely useful to clarify the origin of the EMC effect and to study the early

stage of hadronization at short formation times. At EIC kinematics (large  $Q^2$  and  $W_X^2$ ) the theoretical assumptions underlying Eqs.(184)-(186) are expected to be of higher validity than at JLab energy. The problem remains as to whether experiments of the kind we are discussing, i.e. the detection of low-momentum light nuclei at specific angles, could be performed at an Electron Ion Collider. We have calculated the process  ${}^3\text{He}(e, e'd)X$  at various EIC kinematics and found that, e.g. at  $Q^2 \simeq 30 \text{ GeV}^2$  and  $x_{Bj} \simeq 0.7$ , when the Deuteron is emitted at about  $90^\circ$  in the target rest frame, this corresponds to about  $1^\circ$  in the direction of the incident nucleus in the collider CM frame.

### 4.3.3 Slow Neutrons and Final-State-Interaction Length

*Kai Gallmeister, Ullrich Mosel*

Within collider kinematics, it is very elucidating to look at “slow” nucleons of energy less than 10 GeV, considered slow with respect to the (fast) target nucleon [396], see also Section 4.3.1. Performing some exploratory simulations within the GiBUU framework (see Section 4.1.3) we are confronted with a lot of complications. In Fig. 85 we show some distributions of slow neutrons as a function of energy for different production points in the longitudinal axis, normalized to the corresponding number of scattered electrons. This result is to be considered as preliminary, since we learned that we need a more accurate treatment of Pauli-blocking and binding effects in the few MeV region. In addition, we need to take into account the production of slow nucleons via evaporation and fragmentation. This work is currently in progress by inclusion of a multi-fragmentation framework (SMM) [410] and correcting for effects of the large energy gap between initial interaction and fragmenting nucleons.

It has been proposed by Ciofi degli Atti and coworkers in many papers (see Section 4.3.2) that the interaction cross section of the jet particles within a SIDIS event with the debris of the target nucleus shows interesting formation length dependencies. We see a large potential for our GiBUU model to study all these questions.

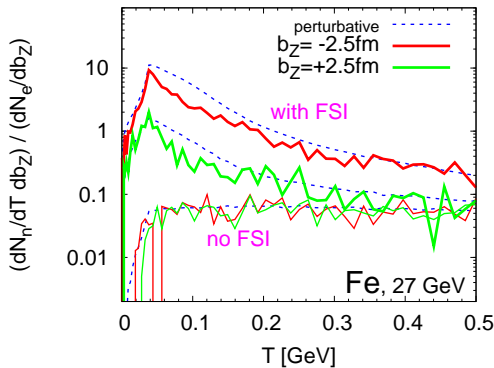


Figure 85. Production cross section of neutrons with low momenta for different longitudinal production points, normalized to the corresponding number of events. (Calculations have to be considered as preliminary; work in progress.)

## 4.4 Bose-Einstein Correlations at the Electron-Ion Collider

*G. P. Gilfoyle*

QCD directs the formation of hadrons from quarks and gluons in hard scattering. However, our understanding of this process is *ad hoc*; there is no full, QCD-based theory to



explain hadronization and fragmentation. To probe these processes we propose to take advantage of an iconic quantum mechanical effect: the symmetrization of the wave function required for bosons. Particles formed near one another will have overlapping wave functions and the interference of the wave functions produces correlations in the intensity and momentum dependence of the final particles. These Bose-Einstein Correlations (BEC) (or the Hanbury-Brown Twiss effect) are examples of intensity interferometry and can be used to study the space-time extent of the source of the particles and/or learn about the dynamics of their formation. They have been used to investigate hot nuclear matter, but there are only a few cases where  $e + A$  interactions have been studied. That work revealed that BECs can be used to study the QCD string in hard scattering and our simulations show we will be able to make precise measurements of the BEC source size at the EIC.

Bose-Einstein Correlations arise when two identical bosons are detected and their joint wave function  $|p_1 p_2\rangle$  ( $p_i$  is the particle 4-momentum) must be symmetric under particle exchange. In other words, when the two bosons are detected from different points in space-time, the observer cannot distinguish the origin of each particle so their amplitudes must add. This requirement gives rise to interference terms in the intensity that do not exist for non-identical particles. In fact, for identical fermions there would be an anti-correlation between the particles. The BEC in energy-momentum space is related to the extent of the source in its spatial dimensions and the correlation function can be written as

$$R(Q_{12}) = \frac{dN/dQ_{12}}{dN_{ref}/dQ_{12}} \quad (189)$$

where  $Q_{12} = \sqrt{-(p_1 - p_2)^2}$  is the Lorentz-invariant momentum difference between the identical bosons and  $N_{ref}$  is a reference spectrum constructed with no BECs. The correlation function is often parameterized at

$$R(Q_{12}) = \alpha (1 + \lambda \Omega(Q_{12} r_{12})) (1 + \beta Q_{12}). \quad (190)$$

In static models of particle sources,  $\Omega(Q_{12} r_{12})$  can be interpreted as the Fourier transform of the spatial distribution of the emission region of bosons with overlapping wave functions and is characterized by the size parameter  $r_{12}$  of the source. It is typically treated as a Gaussian ( $e^{-Q_{12}^2 r_{12}^2}$ ) or an exponential ( $e^{-Q_{12} r_{12}}$ ). The parameter  $\lambda$  measures the coherence of the source,  $\alpha$  is a normalization factor, and  $\beta$  accounts for long range correlations.

**Existing measurements.** There is a long history of the study of BECs in particle and nuclear physics going back to 1960 when two-pion correlations were measured in  $p\bar{p}$  collisions [412]. They have been used to study geometric properties in  $e + p$  reactions [411], the space-time extent of hot nuclear matter in  $Au + Au$  collisions [413, 414], and the dynamical properties of hadrons extracted from  $Au + Au$  collisions [415]. Figure 86 shows the two-pion correlation function from Ref. [411] for  $e + p$  reactions measured at the DESY collider for an electron momentum  $p_e = 27.6$  GeV and proton momenta  $p_p = -820$  GeV and  $p_p = -920$  GeV. It shows several of the important features seen in many correlation functions. There is a clear correlation that is maximal at  $Q_{12} = 0$  and drops rapidly to unity and below with increasing momentum difference. The height of the correlation function at  $Q_{12} = 0$  measures the coherence in the source. At moderate  $Q_{12}$  the correlation drops below one reflecting the usual practice of requiring the integral of the entire correlation function to go to one. There is a steady rise in  $R$  at larger  $Q_{12}$  due to long-range effects. Recall the denominator Eq. (189); It should be free of the correlations arising from Bose-Einstein

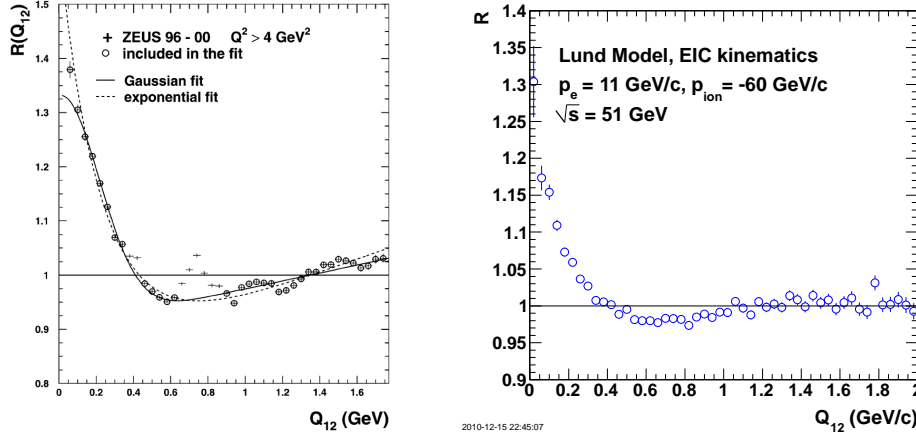


Figure 86. *Left*: the measured Bose-Einstein correlation function,  $R(Q_{12})$ , together with Gaussian and exponential fits [411]. The error bars show the statistical uncertainties. The data points included in the fit are marked with the circles. The other points are excluded from the fit because the correlation is dominated by resonance effects. *Right*: Pythia simulation of  $\pi^+\pi^+$  Bose-Einstein correlations (BEC) at Electron-Ion Collider kinematics. The BEC parameters were taken from Ref. [411]. The Lund fragmentation model was used.

statistics, but will not be free of all correlations: momentum conservation will push  $R$  up at large  $Q_{12}$ . The width of the peak at  $Q_{12} = 0$  reflects the size of the source of the two bosons, *i.e.* large width in momentum space implies a small spatial source. The width of  $R$  in Fig. 86 corresponds to  $r_{12} \approx 0.9 \text{ fm}$  for an exponential fit and is largely independent of  $Q^2$ , the square of the four-momentum transfer.

**BECs at the EIC.** Measurements with the CLAS detector at Jefferson Lab of a different type of correlations (*i.e.*, two protons) have been performed on nuclear targets. Some of the results are shown in the left-hand panel of Fig. 87 [416]. The figure shows the effects on the source size  $r_{rms}$  (extracted from the correlation) of the average pair momentum ( $p = |\vec{p}_1 + \vec{p}_2|/2$ ) and the nuclear size on the correlation function. At low average pair momentum  $r_{rms}$  increases for the heavier nuclei and approaches the nuclear size; implying the possible dominance of proton rescattering. The density of the source was extracted in Ref. [416] and found to be about 2-3 times the nuclear density in helium.

In the right-hand panel of Fig. 87 we show preliminary results from Jefferson Lab for BECs from  $\pi^+\pi^+$  pairs on several nuclear targets [420]. Below  $Q_{12} \approx 0.15 \text{ GeV/c}$  the correlations from all nuclei rise to a large positive correlation. Above  $Q_{12} \approx 0.15 \text{ GeV/c}$  the correlation functions overlap one another within the statistical uncertainty.

Measurement of Bose-Einstein correlations at the EIC will provide a new portal to studies of cold, high-density nuclear matter and the process of hadronization. The ground-state properties of nuclei are now well understood. *Ab initio* calculations of the nuclear ground state are successful for nuclei up to  $A = 8$  and higher [421, 422] and lattice QCD calculations continue to make progress toward a fundamental understanding of the nucleon [423]. However, the high-momentum components of the nuclear ground state are only now being revealed. These high-momentum nucleons are often paired with another, nearby neutron or proton forming regions of cold, dense nuclear matter. Short-range correlations have shown the importance of high-density components and the influence of the tensor force

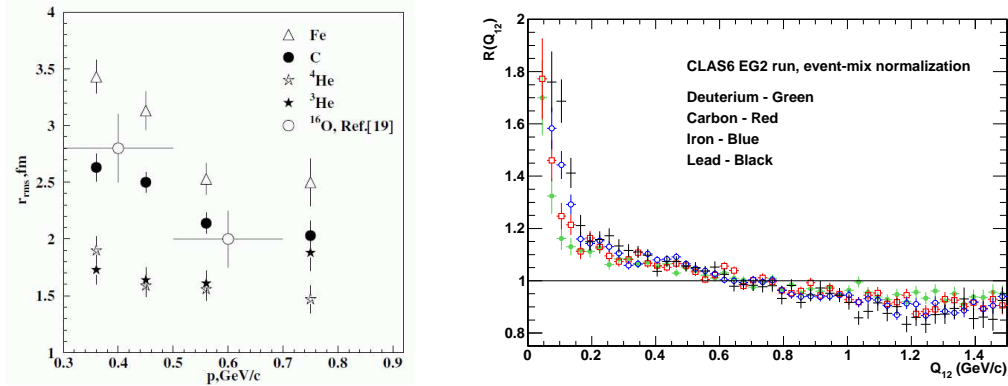


Figure 87. Left panel: The size parameter  $r_{rms}$  as a function of the mean pair momentum  $p = |\vec{p}_1 + \vec{p}_2|/2$  is shown for different nuclear targets [416]. Data from Refs [417–419] are shown which correspond to  $e - ^{16}\text{O}$  interactions at initial energy of 5 GeV and  $Q^2 < 0.1(\text{GeV}/c)^2$  are shown for comparison. Right panel: Preliminary correlation functions for  $\pi^+\pi^+$  from the CLAS detector at Jefferson Lab [420].

[424, 425]. The results of Ref. [416] (left-hand panel of Fig. 87) demonstrated the use of correlations to extract density information. Measurements at the EIC could also help us understanding neutron stars [426] and the EMC effect [427].

Hadronization and fragmentation (the formation of hadrons in hard scattering and the breaking of a QCD ‘string’) are fundamental processes described by QCD. Considerable data have been collected on these processes and the data have been parameterized and used as inputs to the analysis of high-energy data (*e.g.* the Large Hadron Collider (LHC)). However, there is no microscopic, QCD-based, underlying theory to explain the data. Recent results from RHIC, HERMES, Jefferson Lab, and other facilities are starting to reveal the properties of quarks as they propagate through nuclear and hadronic matter [335, 428]. Understanding these results and resolving questions like the competition between prehadron absorption and gluon radiation continue to be a challenge. A new era will open with the Jefferson Lab 12-GeV upgrade and later with the EIC. The higher luminosity will make multidimensional analysis accessible ( $Q^2$ ,  $\nu$ ,  $z$ ) along with other production channels ( $K$ ,  $\eta$ ,  $\pi^0$ ,  $\Lambda$ ) to probe the physics. As one moves to higher  $Q^2$  the stretching of the QCD color string in the direction of propagation may become evident. Calculations of BECs in  $e^+ + e^-$  annihilation reveal that information about the string tension can be obtained even at low  $Q^2$  where the source is roughly spherical [429].

**Simulations.** We have simulated Bose-Einstein correlations for  $\pi^+\pi^+$  pairs at the kinematics of the Electron-Ion Collider to investigate the feasibility of measuring BECs at the EIC. For our starting point we used the results for  $\pi^+\pi^+$  correlations from  $ep$  reactions at DESY that are shown in Fig. 86 [411]. That measurement covered the range  $Q^2 = 4 - 8000 (\text{GeV}/c)^2$  and there was limited  $Q^2$  dependence in the BEC parameters they extracted. It is reasonable to believe those parameters may also apply to the EIC kinematics. We chose the  $\pi^+\pi^+$  channel because we expect them to be abundant and there is data from other experiments that enable us to make comparisons. We took advantage of several existing tools to perform the simulations. The Pythia program [430] was used to generate events with either Lund string model or independent fragmentation. The code also

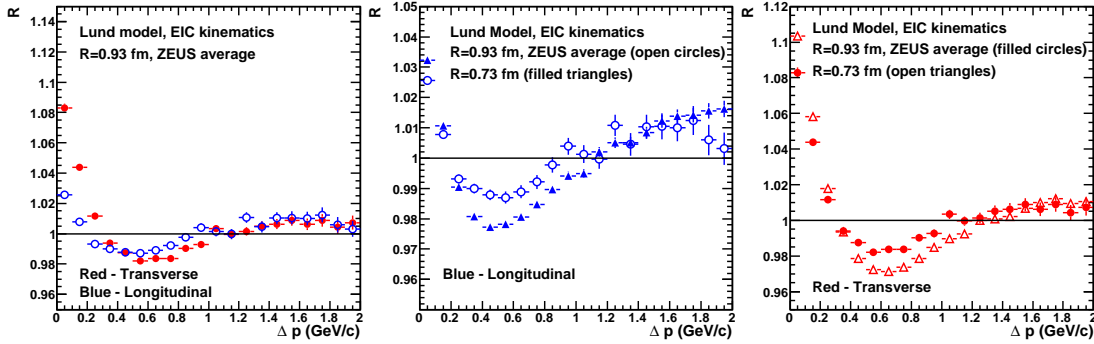


Figure 88. Longitudinal and transverse ( $LT$ ) correlation functions calculated with Pythia. The left-hand panel shows the correlations functions using the Ref. [411] parameters. The other two panels show a comparison between those results and ones from a calculation with a smaller source size  $r_{12}$ .

includes a feature to simulate Bose-Einstein correlations [431, 432]. The algorithm for the BECs starts with the usual fragmentation simulation and then pairs of identical particles (*i.e.*  $\pi^+\pi^+$ ) are selected. For these pairs the relative 4-momentum  $Q_{12}$  is modified according to the desired parameterization (see discussion of Eq. (190) above) with the constraint that the total 3-momentum of the pair remains the same in the center-of-mass (CM). The overall effect of applying the algorithm is to preserve momentum conservation, but reduce the energy. To compensate for the energy reduction, the CM momentum vectors are then rescaled.

We now discuss the results of our simulations. First, as a consistency check, we compared the simulated correlation function  $R$  for  $\pi^+\pi^+$  pairs with the measurements from DESY shown in Fig. 86. The simulated correlation was weaker than the measured one,  $R(Q_{12} = 0) = 1.2$  (simulated) versus  $R(Q_{12} = 0) = 1.38$  (measured), and not as wide, but still experimentally significant. Since we are studying the possibility of observing BECs, the parameters from Ref. [411] will provide a more conservative (and safer) test. We also simulated the BECs at the same kinematics as the preliminary results from Jefferson Lab shown in the right-hand panel of Fig. 87 ( $p_e = 5$  GeV and fixed target). Here we found the simulated correlation disappeared entirely. The multiplicity of the events generated by Pythia dropped significantly at these kinematics reflecting the limitations of the code at these lower energies.

At EIC kinematics ( $p_e = 11$  GeV/c,  $p_{ion} = -60$  GeV/c,  $\sqrt{s} = 51$  GeV), we used the BEC parameters from the ZEUS paper [411]. Since the EIC will run at energies lower than at HERA, but above the current ones at Jefferson Lab, our estimates of the BECs are again conservative ones. Our simulation of  $R$  at EIC kinematics is shown in the right panel of Fig. 86. There is, like in the Ref. [411] data, a sizable correlation at  $Q_{12} = 0$ , a decrease in  $R$  with width  $\approx 0.2$  GeV/c, a dip below unity (recall discussion of Fig. 86) and then the data approach one at high  $Q_{12}$ . The Lund model was used here for the fragmentation and a calculation using the independent fragmentation model in Pythia yielded similar results. This result shows we can expect sizable correlation functions at the EIC.

One of the possible effects we may see at the EIC is the stretching of the QCD color string at high  $Q^2$  and/or changes in the string tension (recall Ref. [429]). The fragmentation region may not be spherical as observed in Ref. [429], but may have different sizes in the longitudinal and transverse directions. Such a difference was measured in Ref. [411] where

the longitudinal radius was  $0.26 \pm 0.03$  fm bigger than the transverse one. To search for such an effect in our simulation requires a different approach to extracting  $R$ . We worked in the longitudinal Center-of-Mass System (LCMS), where the longitudinal components of the pair momentum add to zero and extracted the transverse and longitudinal 3-momentum differences  $\Delta p$ . Our initial results are shown in the left-hand panel of Fig. 88. The transverse (red, filled circles) and longitudinal (blue, open circles) produce the characteristic shapes seen above for  $R$ , but with significant quantitative differences between the two. The transverse correlation is about twice the longitudinal one at  $Q_{12} = 0$  and the widths are similar. The large difference between the correlations functions suggests this may be a useful tool for studying space-time properties of the emission source. To delve deeper into this question, we considered the sensitivity of the  $LT$  distributions to changes in the size parameter in the BEC parameterization. The middle and right-hand panels in Fig. 88 show a comparison of the same  $LT$  correlation functions shown in the left-hand panel with ones calculated with a smaller size parameter ( $r_{12} = 0.73$  fm versus  $r_{12} = 0.93$  fm from Ref. [411]). The smaller radius amplifies the shape of the correlation functions (the maximum at  $Q_{12} = 0$  increases and the dip at  $Q_{12} \approx 0.6$  GeV/c is deeper. We can clearly separate the two distributions within the Monte Carlo statistics shown here. We expect the statistical uncertainties for an EIC measurement to be better than the Monte Carlo statistical uncertainties shown here. The cross sections for these reactions (from Pythia) multiplied by the EIC luminosity suggest a production rate of  $10^5$  Hz. We also fitted the correlation functions with Eq. (190) and obtained uncertainties on the size parameter  $r_{12}$  less than 0.15 fm which is comparable to the precision of the results in Ref. [411]. Thus, we will be able to discriminate between different size parameters at least at the 0.2 fm level.

**Conclusions.** Bose-Einstein correlations will be an important tool at the Electron-Ion Collider for studying high-density nuclear matter, the dynamics of the QCD string in hard scattering, and to gain a deeper understanding of fragmentation and hadronization. Our simulations have shown us that we can expect large (20%) effects in the correlation function at small  $Q_{12}$ . The longitudinal-transverse correlations are sensitive to the size parameter to a fraction of a  $fm$ . Finally, the large  $\pi^+\pi^+$  BECs observed at JLab that are not reproduced in our simulations hold the promise of new physics to be uncovered with the EIC.

## 5 e+A Monte Carlo Simulation Tools

### 5.1 A Monte Carlo Generator for Diffractive Events in e+A Collisions

*Tobias Toll and Thomas Ullrich*

Monte Carlo (MC) event generators are a crucial and widely used tool for both particle and high energy nuclear physics. Any successful generator attempts to include models of all of our knowledge and understanding regarding the processes being studied, and thus allows us to test the feasibility of the relevant measurements. Designing the EIC is no exception. While there is a rich set of event generators for  $e + p$  collisions available (*e.g.* PYTHIA6 [433], HERWIG++ [434], LEPTO [435], PEPSI [436], RAPGAP [437], ARIADNE [438], CASCADE [439], SHERPA [440]), the situation for  $eA$  collisions is less favorable. The exception is DPMJET [441] which attempts to describe deep-inelastic  $eA$  events but does not include the rich physics accessible via diffractive events.

In strong interactions, diffractive events can be interpreted as resulting from scattering via the exchange of a pomeron that carries the quantum numbers of the vacuum, as discussed in 2.3.2. It was a surprise to see that a large fraction (approximately 15%) of all  $e+p$  events at HERA were diffractive. Calculations predict this fraction to be even larger in  $e+A$  collisions where the large nuclei remain intact  $\sim 25\text{-}30\%$  of the time (*e.g.* [120, 121]).

Studies at an EIC will allow us to directly probe the nature of the pomeron and will provide definitive tests of strong gluon field dynamics in QCD. In fact diffractive events are considered the most sensitive means of studying saturation since the dipole scattering amplitude is proportional to the square of the gluon momentum distribution  $xg(x, Q^2)$ . Another fascinating aspect of the study of diffractive events at an EIC is that it would allow us to measure the intensity and the *spatial* distribution of the strong field that binds the nucleus together [187].

For all the above measurements the most important process to study is the production of exclusive diffractive vector mesons, such as  $J/\Psi$ ,  $\phi$ , and  $\rho$  mesons, as well as Deeply Virtual Compton Scattering (DVCS) photons. These processes give very clean final states, consisting of the scattered electron and nucleus and one extra particle: a vector meson or a real photon. This is a process which is dominated by small momentum fractions  $x < 10^{-2}$ .  $J/\Psi$  production is particularly well suited for studies of the spatial gluon distribution inside nuclei due to its well known wave function, narrow decay width, and its large branching ratio for electromagnetic decays  $J/\Psi \rightarrow e^+ + e^-$  (or  $\mu^+ + \mu^-$ ).

The measurement of exclusive vector meson production in diffractive events will be one of the key measurements at an EIC. Therefore these processes have been the starting point in our efforts to realise a new multi-purpose MC generator.

**The Dipole Model:** The dipole model is an important tool in investigations of diffractive processes and for the purpose of applying it to  $e+A$  collisions, we needed an impact parameter dependent model as starting-point. Two known models fulfil this requirement: bSat (or IPSat)[118] and bCGC [118, 119]. They are the underlying building blocks used in the generator. In what follows, we will concentrate on the bSat model and not discuss the technical details of the generator but focus on how the dipole models are applied with emphasis on the extension to  $e+A$  collisions.

The parameters of the dipole models described below have been tuned to inclusive HERA data, and they describe a wide variety of HERA measurements exceptionally well [118, 119].

**The Dipole Model in  $e + p$ :** The production of exclusive vector mesons and DVCS photons at small  $x$  for  $ep$  collisions,  $e + p \rightarrow e' + p' + V/\gamma$ , in the dipole model has been extensively studied [118, 119]. Here the virtual photon splits into a quark-antiquark dipole which interacts with the target diffractively via one or many two-gluon pomeron exchanges (see Fig. ??). The amplitude for this process is:

$$\mathcal{A}_{T,L}^{\gamma^* p \rightarrow V p}(x, Q, \Delta) = i \int dr \int \frac{dz}{4\pi} \int d^2\mathbf{b} (\Psi_V^* \Psi)(r, z) 2\pi r J_0([1-z]r\Delta) e^{-i\mathbf{b} \cdot \Delta} \frac{d\sigma_{q\bar{q}}^{(p)}}{d^2\mathbf{b}}(x, r, \mathbf{b}) \quad (191)$$

Here  $T$  and  $L$  represent the transverse and longitudinal polarizations of the virtual photon,  $r$  is the size of the dipole,  $z$  the energy fraction of the photon taken by the quark,  $\Delta = \sqrt{-t}$  is the transverse part of the four-momentum difference of the outgoing and incoming proton, and  $\mathbf{b}$  is the impact parameter of the dipole. The wave function of the produced vector meson or real photon is  $\Psi_V$  while that of the incoming photon that splits into the dipole is  $\Psi$ . The dipole cross-section  $d\sigma_{q\bar{q}}^{(p)}/d^2\mathbf{b}(x, r, \mathbf{b})$  is defined as

$$\frac{d\sigma_{q\bar{q}}^{(p)}}{d^2\mathbf{b}}(x, r, \mathbf{b}) \equiv 2\mathcal{N}^{(p)}(x, r, \mathbf{b}) = 2[1 - \Re(S)] \quad (192)$$

where  $\mathcal{N}$  is the scattering amplitude which is a number between 0 and 1, which is 1 minus the real part of the  $S$ -matrix.

In the bSat model the dipole cross-section is:

$$\frac{d\sigma_{q\bar{q}}^{(p)}}{d^2\mathbf{b}} = 2 \left[ 1 - \exp \left( -\frac{\pi^2}{2N_C} r^2 \alpha_S(\mu^2) x g(x, \mu^2) T(b) \right) \right] \quad (193)$$

where  $\mu^2 = 4/r^2 + \mu_0^2$  and  $\mu_0^2$  is a cut-off scale in the DGLAP evolution of the gluons  $g(x, \mu^2)$ . The nucleon shape function  $T^{(p)}(b) = 1/(2\pi B_G) \exp(-b^2/(2B_G))$ . The parameter  $B_G$  is determined through fits to HERA data [118]. We use  $B_G = 4 \text{ GeV}^{-2}$ . It should be noted that bSat is a model of multiple two-gluon exchanges and does not contain any gluon-gluon recombinations. It is however, by construction, a model that obeys unitarity, so in this respect it is a saturation model.

Figure 89(a) shows the dipole cross-section as a function of  $r$  for different impact parameters. Figure 89(b) and (c) depict the wave overlap,  $(\Psi_V^* \Psi)(r, z)$ , for  $J/\Psi$  (b) and  $\rho$  mesons (c) [118] used in Eq. 191. It should be noted that the  $J/\psi$  is not necessarily the best suited vector meson for probing saturation effects. Studying saturation implies probing large dipole radii  $r \gtrsim 2 \text{ GeV}^{-1}$  (0.4 fm). However, the wave overlap with the  $J/\Psi$  vanishes almost entirely for these dipole sizes. The lighter vector mesons  $\rho$  and  $\phi$  certainly appear more suited in this case. Unfortunately the wave functions of the lighter vector mesons are less well known than that of the  $J/\Psi$  increasing the uncertainties in model-data comparisons. This can be overcome in the future by improving our knowledge of the light vector meson wave functions.

**Phenomenological Corrections to the Cross-Section:** In the derivation of the dipole amplitude (eq. (191)) only the real part of the  $S$ -matrix is taken into account, making the amplitude purely imaginary. The real part of the amplitude can be included by multiplying the cross-section by a factor  $(1 + \beta^2)$ , where  $\beta$  is the ratio of real to imaginary part of the

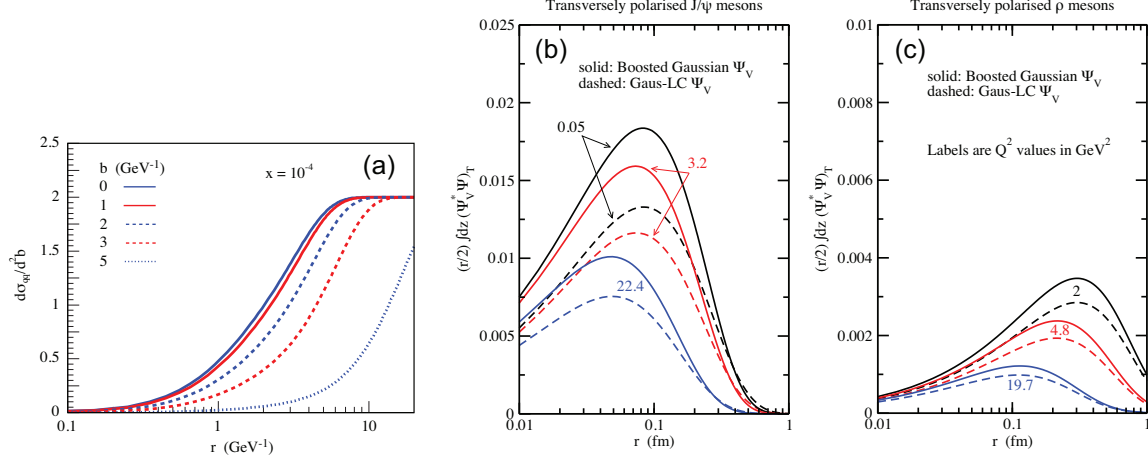


Figure 89. (a) shows the dipole cross-section for various impact parameters as a function of dipole size in the bSat model. (b) and (c) depict the wave overlap functions for  $J/\psi$  and  $\rho$  mesons respectively as a function of  $r$  for various  $Q^2$  for transversely polarized photons (from [118]).

amplitude. It is calculated using:

$$\beta = \tan\left(\lambda \frac{\pi}{2}\right), \quad \text{where } \lambda \equiv \frac{\partial \ln\left(\mathcal{A}_{T,L}^{\gamma^*p \rightarrow Vp}(x, Q, \Delta)\right)}{\partial \ln(1/x)} \quad (194)$$

Also, the two gluons interacting in each event do not carry the same momentum fraction  $x$ . In the leading  $\ln(1/x)$  limit, this skewedness effect disappears, but can still be accounted for by a factor  $R_g(\lambda)$ , where:

$$R_g(\lambda) = \frac{2^{2\lambda+3}}{\sqrt{\pi}} \frac{\Gamma(\lambda + 5/2)}{\Gamma(\lambda + 4)} \quad (195)$$

$R_g$  is multiplied to the gluon distribution  $xg(x, \mu^2)$  and  $\lambda$  is defined as the derivative of  $\ln(xg(x, \mu^2))$  with respect to  $\ln(1/x)$ . It should be noted that while the correction of the real part of the amplitude is on firm theoretical footing, the skewedness correction should be viewed as a purely phenomenological correction. Also, the correction variable  $\lambda$  is only well behaving for small values of  $x < 10^{-2}$ . The combined magnitude of both corrections is  $x$  dependent and is typically of the order of 10 – 60%.

**Extending the Dipole Model from  $e + p$  to  $e + A$ :** When going from  $ep$  to  $eA$  scattering we will use the independent scattering approximation:

$$1 - \mathcal{N}^{(A)} = \prod_{i=1}^A \left(1 - \mathcal{N}^{(p)}(x, r, |\mathbf{b} - \mathbf{b}_i|)\right) \quad (196)$$

where  $\mathbf{b}_i$  is the position of each nucleon in the nucleus. Here, these positions are generated according to the Wood-Saxon potential. Combining equations (192), (193) and (196) the bSat dipole cross-section for  $eA$  becomes:

$$\frac{d\sigma_{q\bar{q}}^{(A)}}{d^2\mathbf{b}}(x, r, \mathbf{b}, \Omega) = 2 \left[ 1 - \exp\left(-\frac{\pi^2}{2N_C} r^2 \alpha_S(\mu^2) xg(x, \mu^2) \sum_{i=1}^A T^{(p)}(\mathbf{b} - \mathbf{b}_i)\right) \right] \quad (197)$$



At small gluon momentum fractions,  $x < 10^{-2}$ , the dipole interacts coherently with large volumes of the nucleus. Therefore the configuration of nucleons in the nucleus is not an observable. To obtain the total cross-section, these nucleon configurations have to be averaged over:

$$\frac{d\sigma_{\text{total}}}{dt} = \frac{1}{16\pi} \left\langle |\mathcal{A}(x, Q^2, t, \Omega)|^2 \right\rangle_{\Omega} \quad (198)$$

where  $\Omega$  denotes nucleon configurations.

One defines two different kinds of diffractive events in  $eA$ : coherent and incoherent. In incoherent diffractive processes the nucleus breaks up into two or more color neutral fragments, something not possible in diffractive  $ep$ . If the nucleus stays intact the diffractive processes are coherent. In the Good-Walker picture [442] (also found in [187]) the incoherent cross-section is proportional to the variance of the amplitude with respect to the initial nucleon configurations  $\Omega$  of the nucleus:

$$\frac{d\sigma_{\text{incoherent}}}{dt} = \frac{1}{16\pi} \left( \left\langle |\mathcal{A}(x, Q^2, t, \Omega)|^2 \right\rangle_{\Omega} - |\langle \mathcal{A}(x, Q^2, t, \Omega) \rangle_{\Omega}|^2 \right) \quad (199)$$

where the first term on the R.H.S is the total cross-section and the second term is the coherent part of the cross-section.

**The Generator:** The Monte Carlo event generator is implemented in C++ through a set of modular classes. A rich set of input parameters let the user select beam energy and species (A), wave function model, dipole model, kinematic range and the final state particle to study:  $\rho$ ,  $\pi$ ,  $J/\Psi$ , or  $\gamma$  (DVCS). Internally, the variables  $t$ ,  $Q^2$ , and  $W^2$  are generated following a probability density function (pdf). From these three variables, the complete final state consisting of the scattered electron, the scattered proton or nucleus, and the produced vector meson or photon can be unambiguously calculated.

**Generating Events for  $ep$ :** The variables are generated from a probability density function which for  $ep$  is:

$$\text{pdf}(Q^2, W^2, t) = \frac{\partial^3 \sigma_{\text{tot}}}{\partial Q^2 \partial W^2 \partial t} = \frac{1}{16\pi} \sum_{T,L} f_{T,L}^{\gamma*}(Q^2, W^2) \left| \mathcal{A}_{T,L}^{\gamma^* p \rightarrow Vp}(W^2, Q^2, t) \right|^2 \quad (200)$$

where  $f_{T,L}^{\gamma*}$  is the photon flux for transversely and longitudinally polarized photons. The user may also choose to include the corrections for the real part of the amplitude and/or the skewedness effect as described above.

**Generating Events for  $eA$ , the MC-Glauber Approach:** For  $eA$  the pdf is:

$$\frac{\partial^3 \sigma_{\text{total}}}{\partial Q^2 \partial W^2 \partial t}(Q^2, W^2, t) = \frac{1}{16\pi} \sum_{T,L} f_{T,L}^{\gamma*}(Q^2, W^2) \left\langle \left| \mathcal{A}_{T,L}^{\gamma^* A \rightarrow V A}(Q^2, W^2, t, \Omega) \right|^2 \right\rangle_{\Omega} \quad (201)$$

Here the average of an observable  $\mathcal{O}$  with respect to the initial nucleon configurations  $\Omega$  is defined as follows:

$$\langle \mathcal{O} \rangle_{\Omega} \equiv \frac{1}{C_{\text{max}}} \sum_{j=1}^{C_{\text{max}}} \mathcal{O}(\Omega_j) \quad (202)$$

where a number of  $C_{\max}$  configurations  $\Omega_j$  are generated and summed over. This sum will converge to the true average for large  $C_{\max}$ . We call this way of performing the average the MC-Glauber approach. It should be noticed that this method of averaging the initial nucleon configurations is different than in previous publications, *e.g.* in [121] and [187].

For each event, the coherent part of the cross-section is calculated simultaneously with the total cross-section, by averaging the amplitude before squaring it. It is then decided probabilistically that the nucleus breaks up if:

$$\left( \frac{\partial^3 \sigma_{\text{total}}}{\partial Q^2 \partial W^2 \partial t} - \frac{\partial^3 \sigma_{\text{coherent}}}{\partial Q^2 \partial W^2 \partial t} \right) \bigg/ \frac{\partial^3 \sigma_{\text{total}}}{\partial Q^2 \partial W^2 \partial t} > R \quad (203)$$

where  $R$  is a random number from a uniform distribution on  $[0 - 1[$ . When this happens, the final state does not contain a scattered nucleus but rather the decay products resulting from the break-up of the nucleus.

**Generating Events for  $eA$ , the Optical Approach:** A simpler and faster way of doing the average over the initial nucleon configurations is what we call the optical approach. Here the average is done implicitly in the dipole cross-section which becomes [121]:

$$\left\langle \frac{d\sigma_{q\bar{q}}^A}{d^2\mathbf{b}} \right\rangle_{\Omega, \text{Optical}} = 2 \left[ 1 - \left( 1 - \frac{T_A(\mathbf{b})}{2} \sigma_{q\bar{q}}(x, r) \right)^A \right]. \quad (204)$$

For processing speed reasons we approximate the integrated dipole cross-section using the GBW approximation [112]:

$$\sigma_{q\bar{q}}^{\text{GBW}}(x, r) = \sigma_0 \left( 1 - \exp \left( -\frac{r^2 Q_s^2(x)}{4} \right) \right) \quad (205)$$

where  $Q_s^2(x) = (x_0/x)^\lambda$ . Here,  $\sigma_0 = 23.9$  mb,  $\lambda = 0.287$  and  $x_0 = 1.1 \cdot 10^{-4}$  [118].  $T_A$  is the projection of the Woods-Saxon potential in the transverse plane. This approximation is valid for large nuclei. In the optical approach, *only* the coherent part of the cross-section can be calculated, since it gives the average of the amplitude, but not of the amplitude squared. It is implemented in the program as a fast alternative to the more accurate but CPU-time intensive MC-Glauber approach.

**Results:** In the following we only show results from the  $e+A$  part of the generator. In Figure 90, the coherent part of the cross-section for  $e + A \Rightarrow e' + A' + J/\Psi$  is shown as a function of  $|t|$ , with  $Q^2 = 10^{-4} \text{ GeV}^2$  and  $x_p = 0.006$ . The nucleus used is gold with  $A=197$ . The cross-section is calculated for different numbers of averaged nucleon configurations  $C_{\max}$ . The target is probed by the dipole at a scale  $\Delta$  which means that at large  $|t|$  the cross-section is much more sensitive to smaller variations in the positions of the nucleons than it is for small  $|t|$ . Therefore, for small  $|t|$ , the sum over configurations converges quickly, while for larger  $|t|$ , more configurations are needed for the sum to converge. As indicated in Fig. 90 approximately 100 configurations are needed to describe  $eA$  scatterings up to  $|t| \approx 0.2 \text{ GeV}^2$ . In Figure 90 the total cross-section and the incoherent part of the cross-section are shown as averaged over 500 nuclear configurations. The  $t$ -slope of the incoherent cross-section is close to  $6 \text{ GeV}^{-2}$ . This is a bit steeper than is found in [122], where the impact parameter dependence was factorized out in the dipole cross-section and therefore the  $t$ -slope =  $B_G = 4 \text{ GeV}^{-2}$ .

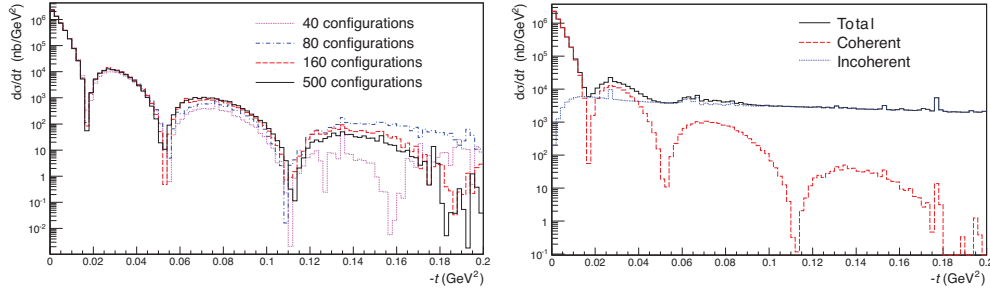


Figure 90. *Left plot.* The coherent part of the cross-section as a function of  $|t|$  for electron-gold scattering at  $Q^2 = 10^{-4} \text{ GeV}^2$  and  $x_p = 0.006$  averaged over 40, 80, 160 and 500 configurations respectively. *Right plot.* The total, coherent, and incoherent cross-sections as a function of  $|t|$  for  $e\text{Au}$  scattering at  $Q^2 = 10^{-4} \text{ GeV}^2$  and  $x_p = 0.006$  averaged over 500 configurations.

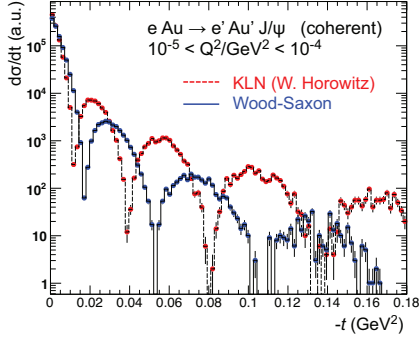


Figure 91. The coherent part of the cross-section of  $e+A \rightarrow e'+A' + J/\psi$  for two different distributions of the initial nucleon configurations: Woods-Saxon and KLN (from [445]).

In order to measure the spatial distribution of gluons inside the nucleus, the coherent cross-section has to be well measured as a function of  $t$ . The inverse Fourier transformation of this will then give the transverse spatial dependence of the amplitude. To do this the position of the several coherent maxima in the  $t$ -distribution have to be measured accurately.

Experimentally, this requires the suppression of the large incoherent fraction, which is of course also of great interest in itself [120]. Coherent and incoherent processes can be separated by detecting the nuclear-breakup, i.e., detecting the nuclear fragments. While this is experimentally straight forward in fixed target experiments it is rather challenging at an EIC since the charged fragments are transported along the ion beam line. The most promising approach is the measurement of emitted neutrons via zero-degree-calorimeters, a technique used extensively at RHIC. Preliminary studies using de-excitation models (e.g. Gemini++ [443] and SMM [444]) and a realistic layout of an EIC interaction region showed that rejection factors of larger than  $10^5$  can be achieved.

In Fig. 90, the nucleon configurations have been explicitly generated according to the Woods-Saxon configuration. Fig. 5.1 shows the same Woods-Saxon distribution in the optical approach compared with a KLN distribution motivated by the CGC as discussed in [445]. It can be seen that the difference when using different initial nucleon distributions within the nucleus is considerable and easily measurable by an EIC. It also demonstrates the flexibility of the generator in adapting different models at all stages of the generation process.

**Summary and Outlook:** A new event generator for the generation of diffractive events in  $ep$  and  $eA$  collisions has been implemented based on an impact parameter dependent

dipole model. It describes the coherent and incoherent contributions to the cross-sections. In its current version it is limited to the production of exclusive vector mesons and DVCS photons. We intend to include more general diffractive processes in the same framework,  $e + p/A \rightarrow e' + p'/A' + X$  where  $X$  is a general final state consisting of two or more hadrons. When completed it will be the first diffractive event generator for  $eA$  collisions with a broad range of processes relevant for the physics of a future EIC.

*Acknowledgments:* The authors would like to thank the INT for their hospitality and support. Also many thanks to G. Beuf, M. Diehl, A. Dumitru, W. Horowitz, H. Kowalski, T. Lappi, and R. Venugopalan for many helpful discussions.

## 5.2 Parton propagation and hadronization simulations: overview

*Alberto Accardi*

The “Parton Propagation and Fragmentation” working group is currently working on several Monte Carlo simulations to address hadronization in the cold nuclear medium. More information, references and links are available on the PPF working group wiki [446].

- **PyQM.** The “Pythia Quenching Model” is an energy-loss simulation based on Pythia, see Section 5.3. The partons created in the hard scattering are allowed to lose energy according to the Salgado-Wiedemann quenching weights, and then fed into the Lund string fragmentation Pythia module. The goal is to determine if the Lund string fragmentation leads to observable differences compared to using Fragmentation Functions to describe leading hadron attenuation (as implemented e.g. in PQM, see below), and to provide a simulation for a broader range of hadron flavors.
- **Q-Pythia extension to DIS.** Q-Pythia is an energy loss simulation by Armesto, Cunqueiro and Salgado based on medium-modified DGLAP evolution equations. Currently, only energy loss in the QGP is implemented, and we are working on implementing energy loss in the cold nuclear target. Pursuing this simulation is likely to have a very big pay-off: it will allow to study jet nuclear modifications, the effects of medium modified DGLAP evolution on hadron observables, and compare this to the BDMPs energy loss formalism in the integrated PQM simulation, and the implementation of the Higher-Twist energy loss formalism. Comparison to simulations done with Q-Herwig, would also allow one to gauge the effects of cluster vs. Lund string hadronization.
  - **PQM.** The “Parton Quenching Model” is a simulation by Dainese, Loizides and Paic, which uses Pythia as a parton level generator, and then applies the Salgado-Wiedemann quenching weights to determine the parton energy loss before using Fragmentation Functions to determine single hadron attenuation. It has been integrated in Q-Pythia by C. Loizides.
  - **PyQM integration.** It will be interesting to integrate PyQM in Q-Pythia, to provide a direct comparison between hadronization performed according to the Lund string model and using Fragmentation Functions.
- **Higher-Twist energy loss.** The Higher-Twist energy loss formalism has recently been extended to include a resummation of all higher-twist contributions, and implemented in a Monte-Carlo simulation, see Section 4.2.2.

- **GiBUU.** This is (among other things) a simulation of nuclear modifications of hadron production in DIS based on the Lund string model and BUU coupled-channel transport equation for the (pre)hadrons, and completely neglects energy loss, see Section 4.1.3. It has been extensively tested on HERMES and EMC data, and is ready to use at the EIC energy. It will be interesting to implement the few variations in the space-time prehadron production schemes available on the market and investigate possible observable differences. Inclusion of target fragmentation is currently in progress in the multi-fragmentation framework (SMM) [410] and correcting for effects of the large energy gap between initial interaction and fragmenting nucleons.

### 5.3 PyQM: a pure energy loss Monte-Carlo simulation

*Raphaël Dupré and Alberto Accardi*

Pure quark energy loss models are widely used to describe jet quenching in relativistic heavy ion collisions (RHIC), however most of the calculations were never applied to the nDIS experiments, which are usually at lower energy, making any comparison difficult. EIC is the chance to have data of both processes at similar kinematic, in this context it is natural to develop PyQM, a pure energy-loss Monte-Carlo simulation for nDIS based on the Salgado-Wiedemann quenching weights formalism [447] widely used to analyze RHIC data. This simulation will be utilized as a tool to evaluate the future EIC capabilities concerning quark energy loss measurement; since it also provides rate estimates and the kinematics of particles to detect, this information will be used to discuss the relevance and interest of various observables and the accelerator and detector requirements to access them.

The PyQM Monte-Carlo simulation is based on PYTHIA [430] for the DIS interaction and the fragmentation process, which is described by the Lund string model. Between the initial hard scattering and string fragmentation, we apply quark energy loss on the struck parton, using a nuclear density profile [448] to estimate the quantity of matter the quark has to go through, and the Salgado-Wiedemann quenching weights [449] to calculate the energy loss itself. To account for the geometry of the nuclei, we follow Ref. [450], and pick randomly the interaction point according to the nuclear density distribution; the thickness of the nuclear matter seen by the parton is then given by

$$R = \frac{2\bar{\omega}_C^2(\vec{b}, y)}{\int_y^\infty dz \hat{q}_A(\vec{b}, z)} \quad (206)$$

with  $y$  the position along the propagation direction with its origin at the interaction point, and  $\vec{b}$  the transverse position of the  $y$  axis relative to the center of the nucleus. The

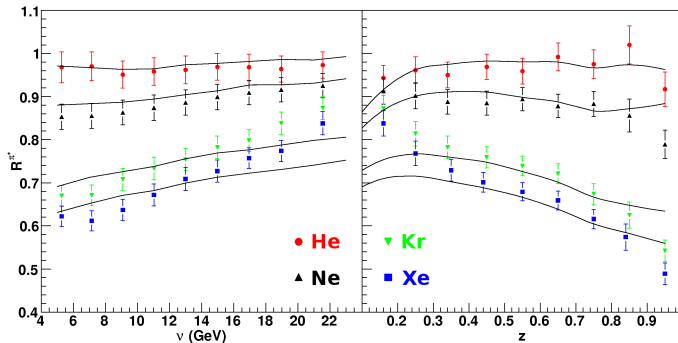


Figure 92. Multiplicity ratio of positive pions from HERMES[353] (points) compared to the PyQM pure energy loss simulation (lines).

characteristic energy  $\omega_C$ , and the local transport coefficient  $\hat{q}$  are given by

$$\omega_C(\vec{b}, y) = \int_y^\infty dz(z - y)\hat{q}_A(\vec{b}, z) \quad \hat{q}_A(\vec{b}, y) = \frac{\hat{q}_0}{\rho_0}\rho_A(\vec{b}, y) \quad (207)$$

Then the only free parameter for the quenching weights, and indeed for the whole simulation, is  $\hat{q}_0$ , the transport coefficient at the center of the nucleus. This is found to be  $\hat{q}_0 = 0.6 \text{ GeV}^2 \text{ fm}^{-1}$  from a fit of the HERMES data [353] (figure 92), in agreement with the analytic calculations of [335, 450]. A full description of the results of this simulation compared to HERMES would be beyond the scope of this presentation; here we note that its results are satisfactory for the multiplicity ratio, but require a seemingly too large  $\hat{q}$  compared to HERMES data on pion  $p_T$ -broadening. We are currently working on an implementation of  $p_T$ -broadening in our simulation, which, puzzlingly, appears instead to produce the right amount of integrated  $p_T$  broadening as a function of  $A$ . This issue is directly linked to the quenching weight calculation and work is in progress to better understand it.

## 6 Connections to Other Fields

### 6.1 Gluon Tomography in Nuclei - The Heavy Ion Collision Initial State

*William A. Horowitz*

The main purpose of colliding large nuclei is the creation and study of the quark-gluon plasma (QGP), the deconfined state of QCD matter at high temperatures ( $T \sim 200$  MeV) and low baryon chemical potential ( $\mu \sim 0$ ). Measuring the properties of the QGP is interesting as it is one of the few expected phases of the strong force, one of the only four known forces in Nature. The QGP is fascinating from a theoretical standpoint as there exists the possibility of experimentally measuring the emergent many-body properties of the non-linear, non-Abelian QCD field theory. It was hoped that the collision of large, ultra-relativistic nuclei in a heavy-ion collision (HIC) might provide an experimental window with which to observe the properties of the QGP, and it appears that just such a novel phase of matter has been created at RHIC [451–455].

But what are the properties of this QGP that has been created? Qualitatively: is the medium strongly or weakly coupled; what are its relevant degrees of freedom; does viscous relativistic hydrodynamics describe the bulk physics of the QGP; does either pQCD or the phenomenological string theory methods of the AdS/CFT correspondence or neither describe the physics of either the bulk medium or the high momentum probes of the medium? Quantitatively: what is the viscosity of the medium; what are the values of its transport coefficients? Is the QGP at RHIC the most perfect fluid created by mankind? The difficulty faced when trying to answer these questions is that a heavy-ion collision is an incredibly complex event. It is useful to think about a HIC, as currently best understood, as a series of separate stages: 1)  $t = -\infty$ , the time before overlap, when the nuclei are boosted to 200 GeV per nucleon at RHIC; 2)  $t = 0$ , the actual collision of the nuclei and creation of large chromodynamic fields; 3)  $0 \lesssim t \lesssim 1$  fm/c, the initial large chromodynamic fields rapidly thermalize; 4)  $1 \lesssim t \lesssim 3$  fm/c, evolution as a QGP; 5)  $3 \lesssim t \lesssim 4$  fm/c, hadronization; 6)  $4 \text{ fm/c} \lesssim t \rightarrow \infty$ , evolution as a hadron gas. A cartoon of a typical central heavy ion collision is shown in figure 93.

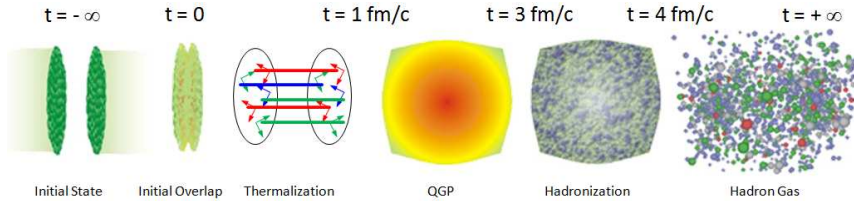


Figure 93. Cartoon of the stages of a heavy ion collision. Timescales are approximate.

As one can see, the system is in the QGP phase for only a brief period of its entire space-time evolution! Really only the time spent in a hadron gas is under reasonable theoretical control; the other times are important to understand not only because they are interesting in their own right—What are the non-linear evolution effects on the color charge density of highly boosted nuclei? How do very large chromodynamic fields thermalize so rapidly? How does hadronization occur?—but also because the interpretation of experimental observables associated with the QGP is sensitive to the details of the physics of the other stages of a HIC. Any new means of experimentally extending our understanding of these other stages would provide a qualitative leap forward in our understanding of the QGP created at RHIC.

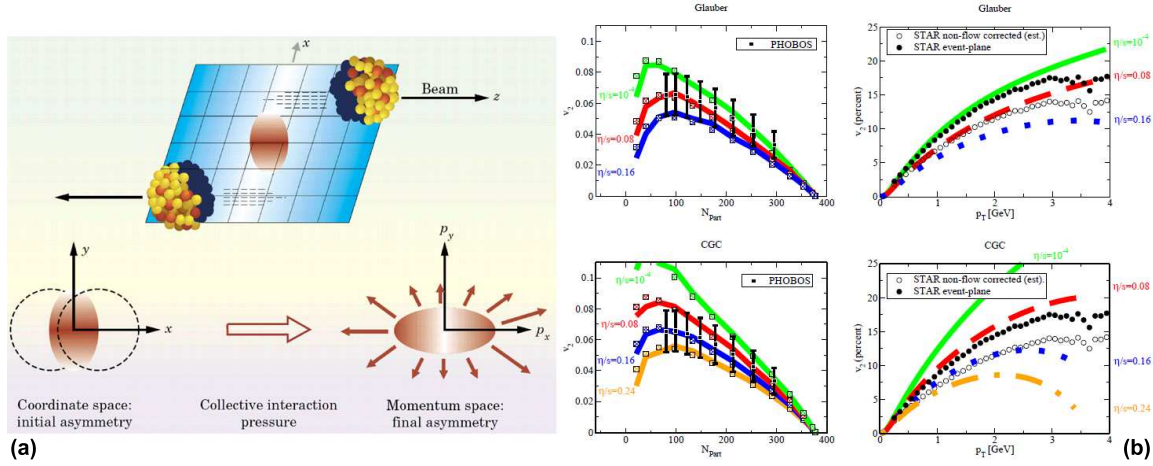


Figure 94. (a) Initial spatial anisotropy evolves into momentum anisotropy in non-central heavy ion collisions. Hydrodynamics aims to quantitatively model this process to gain information on the medium and its properties. (b) Comparison of data and theoretical predictions using viscous relativistic hydrodynamics for  $v_2^h(N_{part})$  (left) and  $v_2^h(p_T)$  (right). Viscous hydrodynamics predictions use Glauber-like initial conditions (top) or a simplified implementation of color glass condensate (CGC) physics (bottom). Note the 100% difference in extracted  $\eta/s$  from the two naive geometry models. figures adapted from [182, 456].

Of particular importance are the initial conditions of a heavy-ion collision, from  $t = -\infty$  to  $t \sim 1$  fm/c, from the time before the collision up through thermalization. An electron-ion collider that probes gluons at  $x \sim 10^{-3}$  could provide precisely this qualitatively new physics understanding of the initial conditions.

The two most striking discoveries of the RHIC heavy-ion program so far are perfect fluidity and jet suppression. The naive interpretation of the measured flow of low momentum particles is that the QGP is a strongly coupled fluid whose properties are described by AdS/CFT; the naive interpretation of the measured jet suppression is that the QGP is a weakly coupled plasma whose properties are described by pQCD. These two interpretations are both mutually exclusive and highly dependent upon the initial conditions of HIC.

**Hydrodynamics.** The stunning success of ideal relativistic hydrodynamics at RHIC as compared to its failure in lower energy machines [181, 457, 458], led to the proclamation of the creation of a perfect fluid at RHIC [459–461]. In HIC particle spectra are often conveniently reported as

$$\frac{dN^h}{dp_T}(p_T, \phi, N_{part}) = \frac{dN^h}{dp_T}(p_T, N_{part}) \left( 1 + 2v_2^h(p_T, N_{part}) \cos 2\phi + \dots \right), \quad (208)$$

where  $\phi$  is the angle of the observed particle with respect to the semiminor axis of the overlap region; see figure 94 (a). As pictured in figure 94 (a) the  $v_2^h$  develops from pressure gradients that build up as a result of the spatial anisotropy created in the initial overlap of the two nuclei.

The nearly ideal fluid flow as surmised from hydrodynamics is exciting because the extracted value of  $\eta/s$ , the shear viscosity to entropy ratio, is smaller than for any other known substance [462]. From a theoretical standpoint, this nearly ideal flow is a huge success for string phenomenology: the lower bound for  $\eta/s$  in a strongly-coupled liquid as computed using the AdS/CFT correspondence is  $1/4\pi$ , in natural units. This value of  $1/4\pi \simeq 0.1$



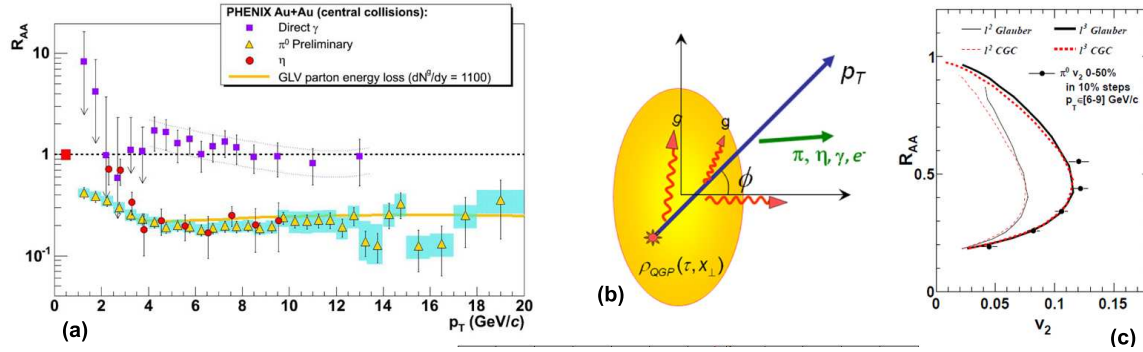


Figure 95. (a) A plot of the early success of pQCD energy loss calculations in describing  $R_{AA}(p_T)$ , Eq. 209. (b) Cartoon of the energy loss from a high- $p_T$  parton in the QGP medium. The longer the pathlength  $L$  the greater the energy loss: the spatial anisotropy manifests as a suppression anisotropy, which is represented by  $v_2^h$ . (c) pQCD ( $\Delta E \sim L^2$ ) energy loss significantly underpredicts the anisotropy while AdS/CFT ( $\Delta E \sim L^3$ ) loss is consistent. The simultaneous description of  $R_{AA}$  and  $v_2$  seems to require both  $L^3$  energy loss and a CGC-like initial state. figures adapted from [185, 465].

should be compared to the naive estimate from pQCD,  $\eta/s \sim 1$ . Conservative estimates of the extracted value of  $\eta/s$  from comparison between theoretical calculations and experimental data yield  $\eta/s \sim 0.1 - 0.5$  [462]. Hydrodynamics is a set of partial differential equations: initial conditions, for which hydrodynamics can tell us nothing, must be supplied. Figure 94 (b), in which a 2+1D viscous hydrodynamics calculation is compared with data, shows the at least factor of 2 uncertainty in the extracted value of  $\eta/s$  that arises from the poorly constrained mean value of the initial geometry. The uncertainty from fluctuations [463], in which hot and cold spots appear in the initial conditions, might also be very large [464]. This very large range of  $\eta/s$  means that one cannot definitively claim that the medium is better understood as strongly coupled and near the lower bound set by AdS/CFT or weakly coupled, with pQCD providing a good physical description.

**High- $p_T$  Physics.** Originally, high- $p_T$  particles were hoped to provide a tomographic probe of the QGP medium produced at RHIC. Jet tomography, then, would provide a means, independent of hydrodynamics, for determining many medium properties; most important, jet tomography could be a tool to investigate the initial geometry of the HIC. While early work showed great promise, see figure 95 (a), there are several observables for which the perturbative energy loss calculations do not provide a good description of the data (see, e.g., figure 95(c)). There is currently not much theoretical control over the in-medium energy loss experienced by high- $p_T$  partons: different assumptions about the best physics approximations have yielded very different energy loss calculations (see, e.g., [336, 466]), and all these calculations suffer from large, mostly unquantified uncertainties due to simplifying mathematical approximations [467]. Nevertheless, qualitatively fascinating discoveries can be made from high- $p_T$  observables. In particular, one may compare the results of strong coupling calculations derived using the AdS/CFT correspondence to those derived using traditional pQCD methods; in this way, energy loss holds out the possibility of rigorously investigating, independent of hydrodynamics, whether RHIC creates a strongly-coupled perfect fluid or a weakly-coupled plasma.

High-energy particle spectra are often reported as normalized by the  $p + p$  spectrum

multiplied by  $N_{coll}(N_{part})$ , where  $N_{coll}(N_{part})$  is the expected number of  $p + p$ -like hard collisions in an  $A + A$  collision with a given number of participants:

$$R_{AA}^h(p_T, \phi, N_{part}) = \frac{dN_{AA}^h(p_T, \phi)}{dp_T} \bigg/ N_{coll}(N_{part}) \frac{dN_{pp}^h(p_T)}{dp_T}, \quad (209)$$

where  $h$  is the measured hadron species and  $\phi$  is the same angle as was defined in the discussion of hydrodynamics. This ratio is also often reported as a Fourier expansion, with  $v_2^h$  again representing twice the first Fourier coefficient (the same  $v_2^h$  as in hydrodynamics). However the physical understanding of the origin of the high- $p_T$   $v_2^h$  is very different from the hydrodynamics physics which dominates the generation of the low- $p_T$   $v_2^h$ . For high- $p_T$  observables,  $v_2^h$  comes from high- $p_T$  partons traversing a medium asymmetric from the initial geometry: less energy loss occurs for partons traveling the short direction of the almond-shaped overlap region compared to those partons that travel the long direction. A cartoon of this physical picture is shown in figure 95 (b). The size of  $v_2^h$  is then an entangled measure of the geometry of the medium and the pathlength dependence of the energy loss mechanism: perturbative elastic energy loss, which goes as  $L^1$ , produces less  $v_2^h$  for a given geometry than perturbative inelastic energy loss, which goes as  $L^2$ , which produces less  $v_2^h$  than strong-coupling energy loss, which, for light partons, goes as  $L^3$  and as  $\exp(-L)$  for heavy partons.  $v_2^h$  is of particular interest because it was recently measured out to  $p_T \sim 13$  GeV, well beyond momentum scales where hadronization effects might be important. That the observed  $v_2^h$  is significantly larger than that predicted by perturbative methods, shown in figure 95 (c), is perhaps the best high- $p_T$  experimental evidence that AdS/CFT, as opposed to pQCD, is the best approximation to the relevant physics at RHIC.

As the theoretical prediction of high- $p_T$   $v_2^h$  comes directly from the azimuthal anisotropy of the QGP medium, knowledge and constraint of the initial geometry is crucially important for a rigorous scientific conclusion to be made: the sharper the produced medium the larger the  $v_2^h$ , regardless of energy loss mechanism. As one can see from figure 95, there are reasonable initial conditions for which no known energy loss calculation describes the data. And just as in hydrodynamics, fluctuations may play an important, even outsized, role.

**Measuring the Initial State.** From the above discussion it is clear that knowledge of the initial conditions at RHIC is crucial for interpreting the experimental data. The density of the charged and neutral matter density of nuclei at rest is well understood from diffraction pattern experiments (see, e.g., [468]). Knowledge of the rest frame density of protons and neutrons in nuclei has been used extensively in estimating the initial matter density created in HIC. Matter production in HIC, though, depends on the distribution of quarks and, especially, gluons in the nuclear wavefunction. Below some value of Bjorken  $x$  that is not yet precisely known non-Abelian, non-linear QCD evolution effects become important. The (mostly) gluonic initial state medium at midrapidity at RHIC consists of particles of  $x \sim p_T/\sqrt{s} \sim 10^{-3}$ , which is at the order of magnitude for which small- $x$  physics likely becomes relevant. Unfortunately the theory of small- $x$  physics in  $A + A$  collisions is very complicated, and current knowledge is incomplete. Additionally, the aforementioned theoretical calculations of  $v_2^h$  are in fact most sensitive to the quantitative shape of the edge of the initial nuclear overlap in HIC; it is just in this region that many of the theoretical tools developed for small- $x$  physics study break down. It turns out, though, that through careful measurements, diffraction patterns may be measured at an electron-ion collider using deeply-virtual Compton scattering and vector meson production. These diffraction patterns, in turn, may be inverted to constrain the initial gluonic and quarkonic

densities of the highly boosted nuclei. Fortunately, these experimental measurements give the most sensitive determination of these densities at the edge of the nucleus, the region of the overlap which hydrodynamics and energy loss calculations are most sensitive to.

## 6.2 Constraining initial conditions in A+A collisions

*Adrian Dumitru*

Understanding small- $x$  gluon production in the *initial* state of relativistic A+A collisions constrains the amount of additional entropy produced via “final-state” interactions such as parton thermalization / QGP formation [469] and its subsequent hydrodynamic expansion. If these processes provide a significant contribution, then that should presumably show in the centrality dependence of the multiplicity in the final state: final state interactions should be much more prevalent for a head-on collision of two large nuclei than for a grazing shot or p+A or (minimum bias) p+p collisions. It is therefore very important to test models for initial particle production over a broad range of centralities – perhaps down to the level of p+p collisions – in order to constrain entropy production due to thermalization and viscous hydrodynamic expansion [470].

To compute the number of small- $x$  gluons released from the wavefunctions of the colliding nuclei, one frequently employs the  $k_\perp$ -factorization formalism [34, 471],

$$\frac{dN}{d^2\mathbf{r}_\perp dy} = \mathcal{N} \frac{N_c}{N_c^2 - 1} \times \int \frac{d^2 p_\perp}{p_\perp^2} \int^{p_\perp} d^2 k_\perp \alpha_s(Q^2) \phi_A(x_1, \frac{(\mathbf{p}_\perp + \mathbf{k}_\perp)^2}{4}; \mathbf{r}_\perp) \phi_B(x_2, \frac{(\mathbf{p}_\perp - \mathbf{k}_\perp)^2}{4}; \mathbf{r}_\perp), \quad (210)$$

where  $N_c = 3$  is the number of colors, and  $p_\perp$ ,  $y$  are the transverse momentum and the rapidity of the produced gluons, respectively.  $x_{1,2} = p_\perp \exp(\pm y) / \sqrt{s_{NN}}$  denote the light-cone momentum fractions of the colliding gluon ladders,  $\sqrt{s_{NN}}$  is the collision energy, and typically one chooses  $Q^2 = \max((\mathbf{p}_\perp + \mathbf{k}_\perp)^2, (\mathbf{p}_\perp - \mathbf{k}_\perp)^2) / 4$ . The normalization factor  $\mathcal{N}$  can be fixed from peripheral collisions, where final-state interactions should be suppressed. It effectively also absorbs NLO corrections and the contribution from sea (anti-)quarks. The unintegrated gluon distribution  $\phi$  is related to the dipole scattering amplitude in the adjoint representation,  $N_G$ , through a Fourier transform [472]:

$$\phi(x, k_\perp^2; \mathbf{r}_\perp) = \frac{C_F}{\alpha_s(k_\perp) (2\pi)^3} \int d^2 \mathbf{s}_\perp e^{-i\mathbf{k}_\perp \cdot \mathbf{s}_\perp} \nabla_{\mathbf{s}_\perp}^2 N_G(x, s_\perp; \mathbf{r}_\perp). \quad (211)$$

**The multiplicity in heavy-ion collisions.** Fig. 96 (left) shows the centrality dependence of particle production for heavy-ion collisions at 200 GeV and 2760 GeV, respectively, obtained by integrating eq. (210) over the transverse overlap of the colliding nuclei. The unintegrated gluon distributions are solutions of the *local* (impact parameter independent) Balitsky-Kovchegov (BK) equation with running-coupling corrections according to the Balitsky prescription [43]. The impact parameter dependence is due entirely to the initial condition where it has been assumed that essentially  $Q_s^2(x_0; \mathbf{r}_\perp) = Q_0^2 \sigma_0 T_A(\mathbf{r}_\perp)$  increases in proportion to the thickness of the nucleus ( $Q_0$  and  $\sigma_0$  denote constant scales; for details see ref. [199]). Neglecting the impact parameter dependence of the dipole scattering amplitude  $N_G$  in a nucleon relies on the scale separation  $R_A \gg R_N \gg Q_s^{-1}$  where  $R_A$  is the size of the overlap region in the collision [475].

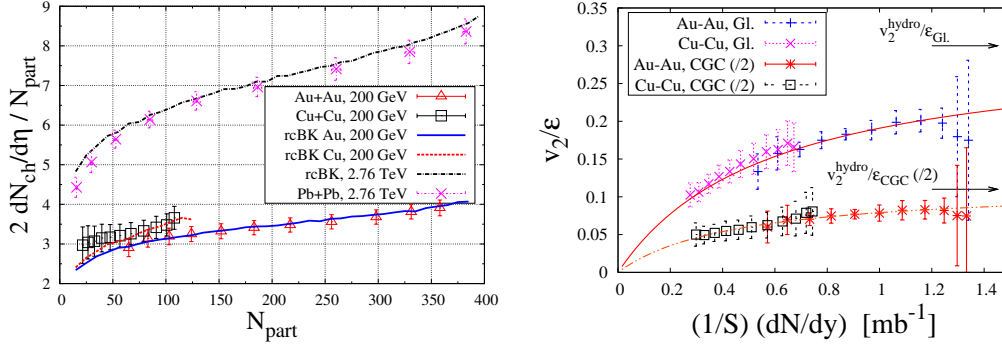


Figure 96. Left: Centrality dependence of the multiplicity at 200 GeV and 2760 GeV, respectively, from  $k_{\perp}$  factorization with running-coupling BK unintegrated gluon distributions (see [199] for details). PHOBOS data: [194] (Au+Au), [473] (Cu+Cu); ALICE data from ref. [197]. Right:  $v_2/\epsilon$  versus the transverse particle density [474];  $v_2/\epsilon_{CGC}$  has been scaled by 1/2 for better visibility.

Apparently, the model calculation describes both the centrality and the energy dependence of particle production fairly well. If so, this constrains final-state entropy production and correlates the thermalization time and the shear viscosity to entropy density ratio: extremely rapid thermalization and/or  $\eta/s \gtrsim 0.3$  would be excluded by stringent entropy production bounds [470].

Several caveats remain. As already mentioned above, the absolute normalization of the gluon density at small  $x$  (alternatively, the factor  $\mathcal{N}$  in the  $k_{\perp}$  factorization formula) can be fixed in practice only from very peripheral A+A or p+p collisions<sup>9</sup>. For p+p collisions, however, the impact parameter dependence of the dipole scattering amplitude over distance scales  $\sim R_N$  can not be neglected, see for example ref. [476].

Furthermore, it may be important to consider in more detail the structure of running coupling corrections to the  $k_{\perp}$ -factorization formula (210) [200] and the effect of a full NLO treatment of BK evolution. Indeed, if such corrections modify the centrality dependence of particle production in A+A collisions then they will also affect entropy production constraints and thus the fundamental understanding of the thermalization processes and time scales as well as estimates of the shear viscosity of thermal QCD.

**The eccentricity in heavy-ion collisions.** Other quantities of relevance for the interpretation of heavy-ion collisions exhibit even greater sensitivity to the actual *distribution* of produced gluons in the transverse  $\mathbf{r}_{\perp}$  plane than its integral  $dN/dy$ . A collision of two heavy ions at non-zero impact parameter, neglecting fluctuations of the local density of participant nucleons, leads to a momentum asymmetry called “elliptic flow”,  $v_2 \sim \langle \cos 2\phi \rangle$ , as described in section 6.1. In the absence of any scales (such as the freeze-out temperature  $T_f$ , the phase transition temperature  $T_c$ , or a non-vanishing mean free path  $\lambda$ ), hydrodynamics predicts that  $v_2$  is proportional to the eccentricity  $\epsilon$  of the overlap area [477],  $\epsilon = \langle y^2 - x^2 \rangle / \langle y^2 + x^2 \rangle$ . The average is taken with respect to the distribution of produced gluons in the transverse  $x$ - $y$  plane. Clearly,  $\epsilon$  involves large cancellations of the contributions of gluons produced near the center  $r_{\perp} \sim 0$  of the overlap zone and so is more sensitive to particle production in the periphery.

A simple geometry based initial condition assumes that by analogy to the Glauber model

<sup>9</sup>Small- $x$  partons do not contribute significantly to the momentum sum rule and a precise matching to the parton distributions at large  $x$  and low  $Q^2$  is lacking.

for soft particle production  $dN/dy d^2r_\perp \sim \rho_{\text{part}}^{\text{ave}}(r_\perp) \equiv (\rho_{\text{part}}^A(r_\perp) + \rho_{\text{part}}^B(r_\perp))/2$ , where  $\rho_{\text{part}}^i$  is the density of participants of nucleus  $i$  per unit transverse area. High-density QCD (the “Color-Glass Condensate”) predicts a somewhat different distribution of gluons in the transverse plane, corresponding to a higher eccentricity  $\varepsilon$ . In particular, in the “p+A limit” when one of the nuclei is very dense while the other is dilute, the number of produced particles is proportional only to the density of the dilute collision partner, whose partons add up linearly. Hence, *in the reaction plane*,  $dN/dy d^2r_\perp \sim \min(Q_{s,A}^2, Q_{s,B}^2) \sim \min(\rho_{\text{part}}^A, \rho_{\text{part}}^B)$  drops more rapidly as one moves towards the edge of the overlap zone than  $dN/dy d^2r_\perp \sim \rho_{\text{part}}^{\text{ave}}$  [478]. Thus, a higher eccentricity is a generic effect due to a dense target or projectile. Specific numerical estimates rely on an accurate determination of the unintegrated gluon distribution, however. Ref. [199] finds that the energy dependence of  $\varepsilon$  from RHIC to LHC is very weak.

Fig. 96 (right) shows the elliptic flow  $v_2$  measured in heavy-ion collisions at RHIC scaled by the eccentricity  $\varepsilon$  of the overlap zone [474]. As already mentioned above, in the absence of any scales such as a non-zero mean free path,  $v_2/\varepsilon$  would be independent of the transverse density of particles. Indeed, if the  $v_2$  data is scaled by the eccentricity obtained from a CGC model implementation then the required breaking of scale invariance is lower than for purely geometry based (Glauber-like) initial conditions. Actual solutions of viscous hydrodynamics (for  $v_2$ ) appear to confirm this simple observation in that the *slope* of  $v_2/\varepsilon$  versus transverse density is sensitive to the distribution of produced particles [479].

More recent studies attempt to understand also the relation of higher moments of anisotropic flow  $v_n$  to corresponding moments of the initial eccentricity  $\varepsilon_n$  – such as the “triangularity” [184, 480–483], which is non-zero because of fluctuations of the large- $x$  sources in the transverse impact parameter plane before the collision. A quantitative interpretation of the “response”  $v_n$  of the Quark-Gluon Plasma medium to the initial geometry will also rely on a good understanding of particle production in high-energy QCD.

### 6.3 Particle production at low- $x$ and gluon saturation: from $p+A$ to $e+A$

*Kirill Tuchin*

In the beginning of the RHIC era, the  $p(d)+A$  program was perceived as merely a useful baseline reference for the heavy-ion program. It very soon turned out that due to a wise choice of colliding energy, RHIC probes the transition region to a new QCD regime of gluon saturation. While the first hints of gluon saturation were observed in DIS experiments at HERA, it is fair to say that gluon saturation was discovered in  $dA$  collisions at RHIC. At present, as we are heading toward the era of EIC, it is important to review what we have learned at RHIC and how it can be used to optimize the EIC program. The purpose of this section is to review phenomenological studies of gluon saturation at RHIC.

The reason why  $pA$  and  $eA$  high energy physics programs are closely related is provided by the Pomeronchuk theorem, which states that all high energy scattering processes are mediated by the exchange of a collective gluon state – known as a Pomeron – that has vacuum quantum numbers. For this reason, inclusive processes in both programs share many similarities in the low  $x$  region. The main distinction arises from the difference in the characteristic scales of the projectile: in protons it is a soft scale  $\Lambda$ , while in virtual photons, it is the photon virtuality  $Q^2$ , which depends on the electron kinematics. A possibility to control the  $Q^2$  is a great advantage of DIS. In particular, it allows one to study the total cross sections/structure functions. However, in practice, the requirement to keep  $x$  low

significantly restricts the range of  $Q^2$ 's available for low  $x$  studies.

The relation between  $pA$  and  $eA$  scattering at low- $x$  becomes particularly apparent in the framework of the dipole model [29]. In the dipole model, the cross section for  $eA \rightarrow X$  or  $pA \rightarrow X$  scattering, where  $X$  is an arbitrary final state, can be represented as

$$d\sigma_{p(\gamma^*)+A \rightarrow X} = \int d^2r_\perp \Phi^{p(\gamma^*)}(r_\perp) d\sigma_{\mathfrak{d}+A \rightarrow X}(r_\perp), \quad (212)$$

where  $\mathfrak{d}$  stands for color dipole (letter  $d$  is reserved for deuteron) of size  $r_\perp$  in the transverse plane. Eq. (212) is based on the separation of scales: the interaction length  $\ell_i \sim R_A$  (in the target rest frame) is much smaller than the coherence length  $\ell_c = \gamma/M_N$ , where  $\gamma \gg 1$  is the Lorentz factor and  $M_N$  is the nucleon mass.  $\Phi^{p(\gamma^*)}(r_\perp)$  is the light-cone “wave function” describing the Fourier decomposition of a projectile into dipoles; it can be calculated in QED (for  $\gamma^*$ ), or modeled (for proton), see e.g. [484, 485]. The main theoretical concern in low  $x$   $pA/eA$  scattering is calculation of the dipole-nucleus cross section, which is universal for both processes. With this observation in mind, we are going to consider some of the  $pA$  processes at RHIC that are of relevance for low- $x$  physics at EIC.

**Inclusive hadron production:**  $p + A \rightarrow h + X$ . The cornerstone for phenomenological applications of the Color Glass Condensate (CGC), which is the theory of gluon saturation, is the factorization theorem proved in [472], where the cross section was derived that resums all leading logarithmic contributions  $\alpha_s \ln(1/x) \sim 1$  (LLA) for a heavy nucleus in the quasi-classical limit  $\alpha_s^2 A^{1/3} \sim 1$ . A similar result was reported in [486–488]. One does not expect that any of the hard perturbative QCD (hpQCD) factorizations apply in this case because higher twist interactions of valence quarks and gluons give contributions of order unity. Nevertheless, despite the fact that individual diagrams break factorization in covariant and light-cone gauges, the final re-summed expression can be cast in the  $k_T$ -factorized form. Unlike in hpQCD, the physical quantity that is factorized – the unintegrated gluon distribution  $\varphi(x, Q^2)$  – can be calculated perturbatively owing to the existence of a hard scale  $Q_s \gg \Lambda_{\text{QCD}}$ . Another surprising fact is that contrary to naive expectations,  $\varphi(x, Q^2)$  is related not to the momentum space Fourier-image of the nucleus gluon-field correlation function  $\langle A_\perp(0_\perp) \cdot A_\perp(x_\perp) \rangle$ , but rather to the Fourier-image of  $\nabla_r^2 N(r_\perp, b_\perp, y)$ , where  $N(r_\perp, b_\perp, y)$  is the imaginary part of the forward elastic scattering amplitude of a color dipole of size  $r_\perp$  at impact parameter  $b_\perp$  and rapidity  $y = \ln(1/x)$  in the heavy nucleus. Although the inclusive gluon production in  $pA$  collisions is the only known case where  $k_T$ -factorization holds, factorization of the multipoles in the transverse coordinate space is a general feature of the low- $x$  cross sections. It must be stressed that this multipole factorization does not imply hpQCD factorizations ( $k_T$  or collinear ones) and neither opposite is generally true.

The  $k_T$ -factorization formula derived in [472] led to successful phenomenology of inclusive hadron production in  $dA$  collisions at RHIC, where the suppression of hadrons at forward rapidities and Cronin enhancement at mid-rapidity were qualitatively predicted [489, 490] and then quantitatively described in the CGC framework [491–493]. The production of valence quarks in the forward direction gives an important contribution to inclusive hadron production at large- $x$  of the proton and was discussed in [494–496].

By integrating the gluon spectrum over  $p_\perp$ , one arrives at the total hadron yield as a function of rapidity  $y$ . It is rather weakly dependent on the details of the gluon distributions. Therefore, a simple model suggested in [497] is able to describe inclusive hadron yield

with remarkable accuracy.

**Open charm (beauty) production:**  $p + A \rightarrow D + X$ . The production of heavy quarks in  $pA$  collisions at low- $x$  was calculated in [208, 498, 499]. One expects that the hpQCD factorization is applicable if the saturation momentum is much smaller than the quark mass  $m$  [500]. At RHIC,  $Q_s \sim m$  for charm and bottom, hence factorization is broken in both cases. Indeed, analysis of [501] indicates that semi-classical calculations of [208] disagree with  $k_T$ -factorization by about 10% at the  $t$ -channel gluon transverse momenta around  $m$ . hpQCD factorization is restored in the kinematic region where the operator product expansion is applicable, i.e. at transverse momenta much higher than the saturation momentum.

The phenomenology of open heavy quark production at RHIC was developed in [502], where it was found that the production pattern of heavy quarks is qualitatively similar to that of light quarks and gluons, although the magnitude of nuclear effects (Cronin and suppression) slowly decrease with increasing quark mass. These qualitative features are in good agreement with preliminary data.

**Inclusive production of  $J/\Psi$ :**  $p + A \rightarrow J/\Psi + X$ . In addition to the scales  $\ell_i$  and  $\ell_c$  mentioned earlier, the production of a charmonium state is characterized by another scale: formation length  $\ell_f = \gamma/\Delta M$ , where  $\Delta M$  is its binding energy. The key theory observation is strong ordering of the scales at high energies:  $\ell_i \ll \ell_c \ll \ell_f$  [287, 503]. Consequently, we can distinguish three stages of  $J/\Psi$  production. (i)  $g^* \rightarrow c\bar{c}$  described by the light-cone amplitude  $\psi^g(k_\perp, z)$  often referred to as gluon's light-cone wave function, (ii) interaction of the gluon or the  $c\bar{c}$  with the target depending on whether the splitting has occurred after or before the interaction, and (iii) formation of charmonium wave function. Unlike stages (i) and (ii), which can be described using perturbation theory owing to the weakness of the strong interaction at the  $J/\Psi$ -mass scale, stage (iii) is non-perturbative because  $\Delta M \ll M$ . This, however, does not preclude us from using perturbation theory for calculating the  $J/\Psi$  production cross section, since the fragmentation process is independent of energy and atomic weight ( $\ell_f \gg R_A$ ). In other words, fragmentation happens in the vacuum long after any interaction with the target.

Thus, the problem of calculating the  $J/\Psi$  production cross-section reduces to the calculation of the cross section of  $\mathfrak{d} + A \rightarrow [c\bar{c}(1^{--})] + X$  dipole-nucleus scattering. This calculation was done in [504, 505]. Note, that interaction depends on the quantum state of the  $c\bar{c}$  pair, which must be in the  $1^{--}$  color singlet state. Therefore, only those higher twist contributions may be taken into account that lead to this quantum state, and which are also enhanced by  $\alpha_s^2 A^{1/3} \sim 1$ . At the lowest order in  $\alpha_s$ , the projectile gluon in the proton wave-function has two interaction possibilities: (i) leading twist processes  $g + g \rightarrow J/\Psi + g$ , which is of order  $\mathcal{O}(\alpha_s^5 A^{1/3})$  and (ii) higher twist process  $g + g + g \rightarrow J/\psi$  (initial gluons come from different nucleons), which is of the order  $\mathcal{O}(\alpha_s^6 A^{2/3})$ . Since  $\alpha_s^2 A^{1/3} \sim 1$ , the higher twist mechanism (ii) is parametrically enhanced. Notice, that this leading contribution explicitly breaks  $k_T$ -factorization as it is proportional to  $xG(x_1)[xG(x_2)]^2$ . Results reported in [504, 505] show strong coherence effects consistent with expectations of CGC theory.

**Electromagnetic probes.** The main advantage of electromagnetic probes, such as photons and dileptons, is that they are directly observable without an intermediate hadronization process, in contrast to quarks and gluons. Therefore, they are a cleaner probe of

low- $x$  nuclear matter. Their disadvantage is a low production rate due to the smallness of electromagnetic coupling. Prompt photon production in  $pA$  collisions was considered in [506] through the process  $qA \rightarrow \gamma qX$ . The production of di-leptons in a similar process  $qA \rightarrow l^+l^-qX$  was addressed in [507–509]. At higher energies, gluons become much more abundant than quarks in the central rapidity region which implies that photon (dilepton) production will go via the process  $g^*A \rightarrow q\bar{q}X\gamma(l^+l^-)$ . It is suppressed by  $\alpha_s$  but enhanced by a positive power of energy. There have been no detailed phenomenological studies of electromagnetic probes in  $pA$  collisions at RHIC.

**Double inclusive hadron production and correlations.** Azimuthal correlations are an important tool to investigate properties of QCD at low  $x$ . In [510] it was proposed that azimuthal correlations of hadrons produced at large rapidity separation ( $\Delta y \gg 1$ ) may be depleted due to a quasi-classical nature of the saturated gluon fields. Unfortunately, accurate theoretical calculations in the region of large but finite  $\Delta y$  are challenging as they must involve complicated NLO BFKL effects. Important progress has been made in the investigation of azimuthal correlations at smaller  $\Delta y$ .

It has been suggested in [511] that correlations at small  $\Delta y$  in the forward direction can be effectively used to study gluon saturation. Indeed, the forward direction corresponds to low  $-x$  of the nucleus where gluon saturation effects are strongest. Theory predicts that back-to-back correlations are suppressed due to gluon saturation. Phenomenological models based on the CGC were suggested in [511, 512] and [513] and rely on different approximations. An approach of [511, 512] is based on the dipole model [29] in which double inclusive gluon [514], quark–anti-quark [208, 498, 499] and valence quark – gluon [511] cross sections were calculated. Another approach [513] is based on an approximate  $k_T$ -factorization and relies on calculation of double-inclusive production based on NLO BFKL [515, 516].

Both models give a reasonable quantitative description of experimental data. However, in order to use azimuthal correlations to study low- $x$  physics in the most effective way, much phenomenological work remains to be done to reconcile the existing approaches and reduce model-dependencies in calculations. Measurements of forward azimuthal correlations in  $eA$  will have a clear advantage over that in  $pA$  due to much better theoretical control of the projectile current.

**Diffraction.** One of the most sensitive probes of low- $x$  QCD is diffraction. This is because scattering in the high energy limit of QCD is mediated by the same collective gluon state (Pomeron) as the diffractive scattering. Saturation effects on diffractive processes in  $pA$  collisions were investigated in [484, 485, 517–519] where the main focus was on diffractive hadron production. (In [520, 521] this work was extended to DIS).

In diffraction on nuclear targets, it is important to distinguish two processes: coherent and incoherent diffraction, depending on the final state of the target. Coherent diffractive hadron production in  $pA$  collisions is a process  $p + A \rightarrow X + h + [LRG] + A$ , where  $[LRG]$  stands for Large Rapidity Gap. Coherent diffractive production exhibits a much stronger dependence on energy and atomic number than the corresponding inclusive process. Indeed, the diffractive amplitude is proportional to the square of the inelastic one. At asymptotically high energies, coherent diffractive events are expected to constitute up to a half of the total cross section, the other half being all inelastic processes. Therefore, coherent diffraction is a powerful tool for studying the low- $x$  dynamics of QCD.

In all phenomenological applications of the CGC formalism, one usually relies on the



mean-field approximations in which only the lowest order Green's functions are relevant. Although corrections to the mean-field approximation, i.e. quantum fluctuations about the classical solution, are assumed to be small in  $pA$  collisions at RHIC, their detailed phenomenological study is absent. An observable that is directly sensitive to quantum fluctuations is incoherent diffraction:  $p + A \rightarrow X + h + [LRG] + A^*$ , where  $A^*$  denotes excited nucleus that subsequently decays into a system of colorless protons, neutrons and nuclei debris. Incoherent diffraction measures fluctuations of the nuclear color field. Calculations show that unlike the nuclear modification factor for coherent diffractive gluon production, the nuclear modification factor for incoherent diffraction is not expected to exhibit a significant rapidity and energy dependence [519]. Therefore, the two diffractive processes can in principle be experimentally distinguished and yield unique information about low- $x$  QCD. Unfortunately, the study of diffraction in  $pA$  collisions at RHIC is a virgin subject in part due to technical difficulties associated with measurements at very small forward angles.

**Instead of a summary.** Studying particle production in DIS at low  $x$  has two main advantages: (i) one has much better theoretical understanding of the forward kinematic region owing to the weakness of the QED coupling and (ii) new kinematic regions open up for investigation depending on values of momentum scales  $Q^2$ ,  $k_\perp^2$  and  $Q_s^2$ , where  $Q^2$  is photon virtuality,  $Q_s^2$  is saturation scale and  $k_\perp$  is transverse momentum of produced hadron.

## 6.4 Small- $x$ dynamics in ultraperipheral heavy ion collisions at the LHC

*Mark Strikman*

Experiments at HERA have demonstrated that reactions with quasi real photons provide an effective tool of probing pQCD which complements studies of DIS processes. In the near future it will be possible to extend these studies to ultra-high energy photon - nucleus collisions via the study of ultra-peripheral collisions (UPCs) of heavy ions (protons and ions) at the LHC. The feasibility and the possible reach of these investigations was explored in a five year long study undertaken by the collaboration of theorists and experimentalists. The results of the study were published as a volume of Physics Reports [289]. Due to the high energy of the colliding nuclei and very good acceptance of the CMS and ATLAS detectors at large rapidities, UPCs at the LHC allows to study a wide range of the processes sensitive to the small- $x$  dynamics for  $W_{\gamma N} \leq 1 - 2$  TeV. This would extend the  $x$  range probed at HERA down by at least by a factor of ten. A further advantage for the search for non-linear effects will be the use of the nuclear targets.

The kinematic range for which studies of several processes of interest will be feasible is presented in Fig.97 (taken from [289]) as a function of  $x$  and  $Q$  which is the typical gluon virtuality which, as the transverse momentum of the jet or leading pion, sets the scale for dijet and  $\pi\pi$  production respectively. The typical gluon virtuality scale for exclusive quarkonium photoproduction is shown for  $J/\psi$  and  $\Upsilon$ . Below we list some of the directions of the planned studies.

**Dijet production.** Dijet production in the discussed kinematic range is dominated by photon - gluon fusion. Estimates of the counting rates including cuts due to the acceptance of the CMS detector were performed in [522]. It was found that measurements of the nuclear gluon pdfs will be feasible down to  $x \sim 10^{-4}$  via study of several channels: dijet,

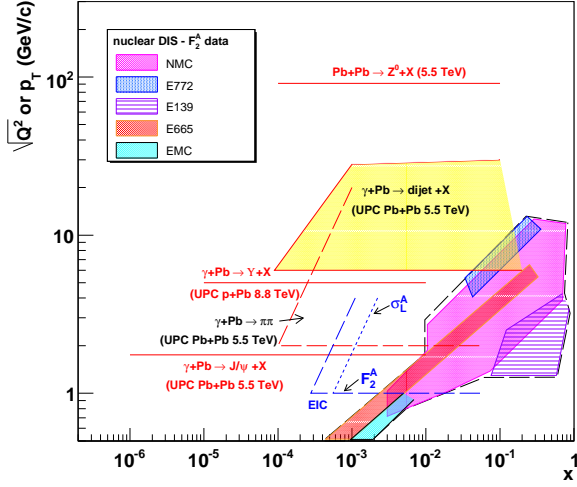


Figure 97. The kinematic range in which UPCs at the LHC can probe gluons in protons and nuclei in quarkonium production, dijet and dihadron production. For comparison, the kinematic ranges for  $J/\psi$  at RHIC,  $F_2^A$  and  $\sigma_L^A$  at eRHIC and  $Z^0$  hadroproduction at the LHC are also shown.

charm, beauty jets, providing a number of cross checks. Use of the zero degree calorimeters (ZDCs) will also allow the separation of diffractive events and hence measure the nuclear gluon diffractive pdfs in the same kinematics. Hence, it will be possible to test a prediction of the leading twist theory of nuclear shadowing that the probability of the gluon induced coherent diffraction at large  $p_T$  and small  $x$  should be of the order 10 – 15% [104].

The cutoff  $p_t(jet) \geq 6 - 8$  GeV/c (necessary for selecting dijet production) reduces non-linear effects in dijet production. The parameter which governs non-linear effects is  $R_{NL} = C_F^2 \alpha_s(Q) x G_T(x, Q^2) / \pi r_T^2 Q^2$ , where  $C_F^2$  is the Casimir operator, equal to 4/3 for  $q\bar{q}$  and 3 for  $gg$ , and  $r_T$  is the transverse area of the target. For the smallest  $x, p_T$  corner,  $R_{NL}$  for the UPC processes  $R_{NL}$  is about the same as for  $F_{2A}(x, Q^2 \sim 2 - 4 \text{ GeV}^2)$  for the lowest  $x$  which could be reached at the EIC.

It will be also possible to reach larger  $R_{NL}$  at smaller virtualities and  $x \sim 10^{-4}$  using leading pion production in the central detectors  $|y| \leq 2.4$  - see dashed area in Fig.97. This is a kinematics similar to the production of two forward pions in d+Au collisions at RHIC. Within the mechanism of fractional energy losses [291, 523], one expects a strong suppression of the two pion yield as compared to the single pion yield which would allow one to perform clean tests of the onset of the black disk regime (BDR).

Another sensitive probe of the onset of BDR would be exclusive diffractive production of two jets in the process  $\gamma + A \rightarrow 2 \text{ jets} + A$ . In the case of light quark jets, this process is strongly suppressed in the pQCD regime, while it is a dominant contribution to the diffractive mechanism in the BDR [291].

**The interaction of small dipoles with nuclear media.** In the leading twist approximation, the suppression of onium coherent production is given by the square of the ratio of the gluon densities in the nucleus and the proton gluon pdfs. It will be feasible to investigate the suppression of coherent  $J/\psi, \Upsilon$  production in nucleus-nucleus collisions down to  $x \sim m_{onium}/2(E_A/A)$  corresponding to production at the central rapidities. At rapidities away from zero, photons of smaller energies dominate in the production of  $J/\psi$ , making it very difficult to probe smaller  $x$  for virtualities  $\sim 3 \text{ GeV}^2$  characteristic for  $J/\psi$  coherent photoproduction. However, the use of incoherent diffractive onium production appears to solve this problem as one can use production of soft neutrons to determine which of the nuclei emitted a photon and which was involved in the strong interaction [289]. As a result,

there is a potential for probing  $J/\psi$  production down to  $x \sim 10^{-6}$ , see Fig.97.

A complementary method of tracking a small dipole through the nuclear media will be provided by the  $J/\psi$  production in the  $-t \geq \text{few GeV}^2$  process  $\gamma + A \rightarrow J/\psi + \text{rapidity gap} + Y$  [292]. It is possible in this case to select the kinematics where  $x_g$  of the gluon involved in the hard process is  $x_g \geq 0.01$ . In this case, scattering at central impact parameters dominates and one can probe the propagation of a small dipole through  $\sim 10$  fm of the nuclear media up to  $W_{\gamma N} \sim 1$  TeV.

In conclusion, it appears that UPC studies to be performed at the LHC in the next few years will allow for the search of several signals of the onset of the BDR. However, it will not be possible to perform a precision scan of the range of moderate  $Q^2$  sensitive to the transition between non-linear and linear regimes in the  $x$  range to be covered by the EIC. Hence the UPC - LHC and EIC programs will nicely complement each other.

## List of Authors

Alberto Accardi

*Theory Center, Jefferson Lab, Newport News, VA, USA*

Jochen Bartels

*II. Institute of Theoretical Physics, Hamburg University, Germany*

Guillaume Beuf

*Department of Physics, Brookhaven National Laboratory, Upton, NY 11973, USA*

Ian C. Cloët

*Department of Physics, University of Washington, Seattle, WA 98195-1560, USA*

Giovanni A. Chirilli

*Nuclear Science Division, Lawrence Berkeley National Laboratory, Berkeley, CA 94720, USA*

Claudio Ciofi degli Atti

*Department of Physics, University of Perugia, Perugia, I-06123, Italy*

*Istituto Nazionale di Fisica Nucleare, Sezione di Perugia, Perugia, I-06123, Italy*

Fabio Dominguez

*Department of Physics, Columbia University, New York, NY 10027, USA*

Adrian Dumitru

*Department of Natural Sciences, Baruch College, New York, NY 10010, USA*

*RIKEN BNL Research Center, Brookhaven National Laboratory, Upton, NY 11973, USA*

Raphaël Dupré

*Physics Division, Argonne National Laboratory, Argonne, IL 60439, USA*

*Université de Lyon, Lyon, France*

Jeffrey R. Forshaw

*Particle Physics Group, University of Manchester, UK*

Kai Gallmeister

*Institute for Theoretical Physics, Giessen University, Giessen, Germany*

J.-H. Gao

*Department of Modern Physics, University of Science and Technology of China, Hefei, Anhui 230026, China*

François Gelis

*Institut de Physique Théorique, CEA/Saclay, 91191 Gif-sur-Yvette Cedex, France*

Gerard P. Gilfoyle

*Physics Department, University of Richmond, Richmond, VA, USA*

*Krzysztof Golec-Biernat*

*Institute of Nuclear Physics, Polish Academy of Sciences, Cracow, Poland*

*Institute of Physics, University of Rzeszów, Rzeszów, Poland*

*Victor P. Gonçalves*

*Instituto de Física e Matemática, Universidade Federal de Pelotas, Pelotas, RS, Brazil*

*Vadim Guzey*

*Theory Center, Jefferson Lab, Newport News, VA, USA*

*William A. Horowitz*

*Department of Physics, University of Cape Town, Rondebosch 7701, South Africa*

*Department of Physics, The Ohio State University, Columbus, OH 43210, USA*

*Leonid P. Kaptari*

*Department of Physics, University of Perugia, Perugia, I-06123, Italy*

*Instituto Nazionale di Fisica Nucleare, Sezione di Perugia, Perugia, I-06123, Italy*

*Bogoliubov Lab. Theor. Phys., 141980, JINR, Dubna, Russia*

*Boris Z. Kopeliovich*

*Departamento de Física, Universidad Técnica Federico Santa María, Valparaíso, Chile*

*Instituto de Estudios Avanzados en Ciencias e Ingeniería, Valparaíso, Chile*

*Centro Científico-Tecnológico de Valparaíso, Valparaíso, Chile*

*Yuri V. Kovchegov*

*Department of Physics, The Ohio State University, Columbus, OH 43210, USA*

*Shunzo Kumano*

*KEK Theory Center, Institute of Particle and Nuclear Studies, KEK, Tsukuba, Japan*

*Department of Particle and Nuclear Studies, Graduate University for Advanced Studies,*

*Tsukuba, Japan*

*Matthew Lamont*

*Brookhaven National Laboratory, Upton, NY, USA*

*Tuomas Lappi*

*Department of Physics, 40014 University of Jyväskylä, Finland*

*Helsinki Institute of Physics, 00014 University of Helsinki, Helsinki, Finland*

*Z.-T. Liang*

*Department of Physics, Shandong University, Jinan, Shandong 250100, China*

*Abhijit Majumder*

*Department of Physics, The Ohio State University, Columbus, OH 43210, USA*

*Cyrille Marquet*

*Physics Department, Theory Unit, CERN, CH-1211 Genève 23, Switzerland*

Chiara B. Mezzetti

*Department of Physics, University of Perugia, Perugia, Italy  
Istituto Nazionale di Fisica Nucleare, Sezione di Perugia, Italy*

Ulrich Mosel

*Institute for Theoretical Physics, Giessen University, Giessen, Germany*

Lezsek Motyka

*Institute of Physics, Jagiellonian University, Cracow, Poland*

Hans J. Pirner

*Institute of Theoretical Physics, Heidelberg University, Heidelberg, Germany*

Juan Rojo

*Dipartimento di Fisica, Università di Milano, Milano, Italy  
Istituto Nazionale di Fisica Nucleare, Sezione di Milano, Milano, Italy*

Ruben Sandapen

*Département de Physique et d'Astronomie, Université de Moncton, Canada*

Rudolfo Sassot

*Instituto de Física de Buenos Aires, Buenos Aires, Argentina  
Departamento de Física, Universidad de Buenos Aires, Buenos Aires, Argentina*

Gregory Soyez

*Institut de Physique Théorique, CEA Saclay, CNRS URA 2306, France*

Anna M. Staśto

*Physics Department, Pennsylvania State University, State College, PA 16802, USA  
RIKEN BNL Research Center, Brookhaven National Laboratory, Upton, NY 11973, USA  
Institute of Nuclear Physics, Polish Academy of Sciences, Cracow, Poland*

Marco Stratmann

*Physics Department, Brookhaven National Laboratory, Upton, NY, USA*

Mark Strikman

*Physics Department, Pennsylvania State University, State College, PA 16802, USA*

Tobias Toll

*Brookhaven National Laboratory, Upton, NY, USA*

Kirill Tuchin

*Department of Physics and Astronomy, Iowa State University, Ames, IA 50011, USA*

Thomas Ullrich

*Brookhaven National Laboratory, Upton, NY, USA*

Xin-Nian Wang  
*Nuclear Science Division, Lawrence Berkeley National Laboratory, Berkeley, CA 94720, USA*

Bo-Wen Xiao  
*Physics Department, Pennsylvania State University, State College, PA 16802, USA*

Feng Yuan  
*Nuclear Science Division, Lawrence Berkeley National Laboratory, Berkeley, CA 94720, USA*  
*RIKEN BNL Research Center, Brookhaven National Laboratory, Upton, NY 11973, USA*

J. Zhou  
*Department of Physics, Temple University, Philadelphia, PA 19122, USA*

P. Zurita  
*Instituto de Física de Buenos Aires, Buenos Aires, Argentina*  
*Departamento de Física, Universidad de Buenos Aires, Buenos Aires, Argentina*

## Acknowledgments

A. Dumitru is supported in part by the DOE Office of Nuclear Physics through Grant No. DE-FG02-09ER41620 and by The City University of New York through the PSC-CUNY Research Award Program, grant 63382-00 41.

M. Strikman is supported by DOE grant No. DE-FG02-93ER40771.

The research of Y.Kovchegov is sponsored in part by the U.S. Department of Energy under Grant No. DE-SC0004286.

B. Z. Kopeliovich was supported in part by Fondecyt (Chile) grant 1090291, by DFG (Germany) grant PI182/3-1, and by Conicyt-DFG grant No. 084-2009.

V. P. Gonçalves was partially financed by the Brazilian funding agencies CNPq and FAPERGS.

T. Lappi is supported by the Academy of Finland, project 126604.

A. Accardi is supported by the DOE contract DE-AC05-06OR23177, under which Jefferson Science Associates, LLC operates Jefferson Lab, and NSF awards No. 0653508 and No. 1002644.

G. A. Chirilli is supported in part by the U.S. Department of Energy under contracts DE-AC02- 05CH11231.

G. Beuf's contribution has been authored under the Contract No. DE-AC02-98CH10886 with the U.S. Department of Energy.

W. H. Horowitz was sponsored in part by the U.S. Department of Energy under Grant No. DESC0004286.

R. Sandapen thanks the Institute for Nuclear Theory (INT) and the Faculté des Études Supérieures et de la Recherche (FESR) of the Université de Moncton for financial support.

J. R. Forsahw is supported by the UK's STFC.

B.-W. Xiao and F. Yuan have been supported in part by the U.S. Department of Energy under the contracts DE-AC02-05CH11231, DE-AC02-98CH10886 and DOE OJI grant No. DE-SC0002145.

Raphaël Dupré is supported under DOE contract DE-AC02-06CH11357.

The work of T. Ullrich was supported in part by the U. S. Department of Energy under Contract No. DE-AC02-98CH10886.

T. Toll is supported through BNL-LDRD 10-042, project 02847.

A. Majumder was supported in part by the U.S. Department of Energy under grant no.



DE-SC0004286.

## References

- [1] J. C. Collins, D. E. Soper, and G. F. Sterman, Nucl. Phys. **B261**, 104 (1985).
- [2] J. C. Collins, D. E. Soper, and G. F. Sterman, Nucl. Phys. **B308**, 833 (1988).
- [3] S. Moch, J. A. M. Vermaseren, and A. Vogt, Nucl. Phys. **B688**, 101 (2004).
- [4] S. Moch, J. A. M. Vermaseren, and A. Vogt, Phys. Lett. **B606**, 123 (2005).
- [5] A. Vogt, S. Moch, and J. A. M. Vermaseren, Nucl. Phys. **B691**, 129 (2004).
- [6] J. Collins and H. Jung, (2005), arXiv:0508280 [hep-ph].
- [7] A. D. Martin, W. J. Stirling, R. S. Thorne, and G. Watt, Eur. Phys. J. **C63**, 189 (2009).
- [8] P. M. Nadolsky, Phys. Rev. **D78**, 013004 (2008).
- [9] F. Caola, S. Forte, and J. Rojo, Phys. Lett. **B686**, 127 (2010).
- [10] R. D. Ball *et al.*, Nucl. Phys. **B809**, 1 (2009).
- [11] R. D. Ball *et al.*, Nucl. Phys. **B823**, 195 (2009).
- [12] E. A. Kuraev, L. N. Lipatov, and V. S. Fadin, Sov. Phys. JETP **45**, 199 (1977).
- [13] I. I. Balitsky and L. N. Lipatov, Sov. J. Nucl. Phys. **28**, 822 (1978).
- [14] V. S. Fadin and L. N. Lipatov, Phys. Lett. **B429**, 127 (1998).
- [15] M. Ciafaloni and G. Camici, Phys. Lett. **B430**, 349 (1998).
- [16] M. Ciafaloni, D. Colferai, G. P. Salam, and A. M. Stasto, Phys. Rev. **D68**, 114003 (2003).
- [17] M. Ciafaloni, D. Colferai, and a. A. M. S. G. P. Salam, Phys. Lett. **B587**, 87 (2004).
- [18] M. Ciafaloni, D. Colferai, G. Salam, and A. Stasto, JHEP **0708**, 046 (2007).
- [19] G. Altarelli, R. D. Ball, and S. Forte, Nucl.Phys. **B742**, 1 (2006).
- [20] G. Altarelli, R. D. Ball, and S. Forte, Nucl.Phys. **B674**, 459 (2003).
- [21] L. D. McLerran and R. Venugopalan, Phys. Rev. **D49**, 2233 (1994).
- [22] L. D. McLerran and R. Venugopalan, Phys. Rev. **D50**, 2225 (1994).
- [23] L. D. McLerran and R. Venugopalan, Phys. Rev. **D49**, 3352 (1994).
- [24] Y. V. Kovchegov, Phys. Rev. **D54**, 5463 (1996).
- [25] J. Jalilian-Marian, A. Kovner, L. D. McLerran, and H. Weigert, Phys. Rev. **D55**, 5414 (1997).
- [26] G. P. Lepage and S. J. Brodsky, Phys. Rev. **D22**, 2157 (1980).
- [27] N. N. Nikolaev and B. G. Zakharov, Z. Phys. **C49**, 607 (1991).
- [28] Y. V. Kovchegov and L. D. McLerran, Phys. Rev. **D60**, 054025 (1999).
- [29] A. H. Mueller, Nucl. Phys. **B335**, 115 (1990).
- [30] Y. V. Kovchegov, Phys. Rev. **D55**, 5445 (1997).
- [31] L. D. Landau and E. M. Lifshitz, *Quantum mechanics, non-relativistic theory, Vol. 3* (Butterworth-Heinemann, 2003).
- [32] I. Balitsky, Nucl. Phys. **B463**, 99 (1996).
- [33] Y. V. Kovchegov, Phys. Rev. **D60**, 034008 (1999).
- [34] L. V. Gribov, E. M. Levin, and M. G. Ryskin, Phys. Reports **100**, 1 (1983).
- [35] A. H. Mueller and J. w. Qiu, Nucl. Phys. **B268**, 427 (1986).

- [36] J. Jalilian-Marian, A. Kovner, A. Leonidov, and H. Weigert, Phys. Rev. **D59**, 014014 (1998).
- [37] E. Iancu, A. Leonidov, and L. D. McLerran, Nucl. Phys. **A692**, 583 (2001).
- [38] I. Balitsky, (1997), hep-ph/9706411.
- [39] Y. V. Kovchegov, Phys. Rev. **D61**, 074018 (2000).
- [40] M. Braun, Eur. Phys. J. **C16**, 337 (2000).
- [41] K. Golec-Biernat, L. Motyka, and A. M. Stasto, Phys. Rev. **D65**, 074037 (2002).
- [42] K. Rummukainen and H. Weigert, Nucl. Phys. **A739**, 183 (2004).
- [43] J. L. Albacete and Y. V. Kovchegov, Phys. Rev. **D75**, 125021 (2007).
- [44] A. M. Stasto, K. Golec-Biernat, and J. Kwiecinski, Phys. Rev. Lett. **86**, 596 (2001).
- [45] A. Freund, K. Rummukainen, H. Weigert, and A. Schäfer, Phys. Rev. Lett. **90**, 222002 (2003).
- [46] E. Levin and K. Tuchin, Nucl. Phys. **B573**, 833 (2000).
- [47] E. Iancu, K. Itakura, and L. McLerran, Nucl. Phys. **A708**, 327 (2002).
- [48] J. Jalilian-Marian, A. Kovner, A. Leonidov, and H. Weigert, Nucl. Phys. **B504**, 415 (1997).
- [49] J. Jalilian-Marian, A. Kovner, A. Leonidov, and H. Weigert, Phys. Rev. **D59**, 014014 (1999).
- [50] J. Jalilian-Marian, A. Kovner, A. Leonidov, and H. Weigert, Phys.Rev. **D59**, 034007 (1999).
- [51] J. Jalilian-Marian, A. Kovner, and H. Weigert, Phys. Rev. **D59**, 014015 (1999).
- [52] A. Kovner, J. G. Milhano, and H. Weigert, Phys. Rev. **D62**, 114005 (2000).
- [53] H. Weigert, Nucl. Phys. **A703**, 823 (2002).
- [54] E. Iancu, A. Leonidov, and L. D. McLerran, Phys. Lett. **B510**, 133 (2001).
- [55] E. Ferreira, E. Iancu, A. Leonidov, and L. McLerran, Nucl. Phys. **A703**, 489 (2002).
- [56] F. Gelis and R. Venugopalan, Nucl.Phys. **A776**, 135 (2006).
- [57] F. Gelis and R. Venugopalan, Nucl.Phys. **A779**, 177 (2006).
- [58] E. Iancu, A. Leonidov, and L. McLerran, (2002), hep-ph/0202270.
- [59] E. Iancu and R. Venugopalan, *Quark Gluon Plasma 3* (World Scientific, 2004), hep-ph/0303204.
- [60] Y. V. Kovchegov, J. Kuokkanen, K. Rummukainen, and H. Weigert, Nucl. Phys. **A823**, 47 (2009).
- [61] J.-P. Blaizot, E. Iancu, and H. Weigert, Nucl.Phys. **A713**, 441 (2003).
- [62] I. Balitsky, Nucl.Phys. **B463**, 99 (1996).
- [63] S. Jeon and R. Venugopalan, Phys.Rev. **D70**, 105012 (2004).
- [64] S. Jeon and R. Venugopalan, Phys.Rev. **D71**, 125003 (2005).
- [65] Y. Hatta, E. Iancu, K. Itakura, and L. McLerran, Nucl. Phys. **A760**, 172 (2005), hep-ph/0501171.
- [66] Y. V. Kovchegov, L. Szymanowski, and S. Wallon, Phys.Lett. **B586**, 267 (2004).
- [67] L. D. McLerran and R. Venugopalan, Phys.Rev. **D59**, 094002 (1999).
- [68] R. Venugopalan, Acta Phys.Polon. **B30**, 3731 (1999).
- [69] F. Gelis, T. Lappi, and R. Venugopalan, Phys.Rev. **D78**, 054019 (2008).
- [70] F. Gelis, T. Lappi, and R. Venugopalan, Phys.Rev. **D78**, 054020 (2008).

- [71] F. Gelis, T. Lappi, and R. Venugopalan, Phys.Rev. **D79**, 094017 (2009).
- [72] B. Z. Kopeliovich, L. I. Lapidus, and A. B. Zamolodchikov, JETP Lett. **33**, 595 (1981).
- [73] N. Nikolaev and B. G. Zakharov, Z. Phys. **C53**, 331 (1992).
- [74] J. Kogut and D. Soper, Phys. Rev. **D1**, 2901 (1970).
- [75] J. Bjorken, J. Kogut, and D. Soper, Phys. Rev. **D3**, 1382 (1971).
- [76] S. Brodsky and A. Mueller, Phys. Lett. **B206**, 685 (1988).
- [77] J. B. K. J. M. Bjorken, Phys. Rev. **D8**, 1341 (1973).
- [78] J. Kopeliovich and B. Povh, Z. Phys. **A356**, 467 (1997).
- [79] B. Kopeliovich, J. Raufeisen, and A. Tarasov, Phys. Lett. **B440**, 151 (1998).
- [80] K. Golec-Biernat and M. Wüsthoff, Phys. Rev. **D59**, 014017 (1999).
- [81] [NMC Collaboration], M. Arneodo *et al.*, Nucl. Phys. **B481**, 3 (1996).
- [82] [NMC Collaboration], P. Amaudruz *et al.*, Nucl. Phys. **B441**, 3 (1995).
- [83] V. Gribov, Sov. Phys. JETP **29**, 483 (1969).
- [84] A. B. Kaidalov, Phys. Rept **50**, 157 (1979).
- [85] Y. M. Kazarinov, B. Z. Kopeliovich, L. I. Lapidus, and I. K. Potashnikova, Sov. Phys. JETP **43**, 598 (1976).
- [86] B. Z. Kopeliovich, A. V. Tarasov, and A. Schäfer, Phys. Rev. **C59**, 1609 (1999).
- [87] B. Kopeliovich, A. Schäfer, and A. Tarasov, Phys. Rev. **D62**, 054022 (2000).
- [88] A. DiGiacomo and H. Panagopoulos, Phys. Lett. **B285**, 133 (1992).
- [89] T. Schäfer and E. V. Shuryak, Rev. Mod. Phys. **70**, 323 (1998).
- [90] B. Z. Kopeliovich, I. K. Potashnikova, B. Povh, and I. Schmidt, Phys. Rev. **D76**, 094020 (2007).
- [91] B. Z. Kopeliovich, J. Nemchik, A. Schäfer, and A. V. Tarasov, Phys. Rev. **C65**, 035201 (2002).
- [92] J. L. Albacete, N. Armesto, J. G. Milhano, C. A. Salgado, and U. A. Wiedemann, Phys. Rev. **D71**, 014003 (2005).
- [93] B. Z. Kopeliovich, I. K. Potashnikova, and I. Schmidt, Phys. Rev. **C81**, 035204 (2010).
- [94] B. Z. Kopeliovich, E. Levin, I. K. Potashnikova, and I. Schmidt, Phys. Rev. **C79**, 064906 (2009).
- [95] L. Frankfurt and M. Strikman, Eur. Phys. J. **A5**, 293 (1999).
- [96] V. A. Abramovsky, V. N. Gribov, and O. V. Kancheli, Sov. J. Nucl. Phys. **18**, 308 (1974).
- [97] L. Frankfurt, V. Guzey, and M. Strikman, Phys. Rev. **D71**, 054001 (2005).
- [98] V. Guzey and M. Strikman, Phys. Lett. **B687**, 167 (2010).
- [99] L. Frankfurt, V. Guzey, and M. Strikman, to be submitted to Phys. Rep .
- [100] J. C. Collins, Phys. Rev. **D61**, 019902 (2000).
- [101] [H1 Collaboration], A. Aktas *et al.*, Eur. Phys. J. **C48**, 715 (2006).
- [102] A. Donnachie and P. V. Landshoff, Phys. Lett. **B296**, 227 (1992).
- [103] N. Armesto, A. B. Kaidalov, C. A. Salgado, and K. Tywoniuk, Eur. Phys. J. **C68**, 447 (2010).
- [104] L. Frankfurt, V. Guzey, and M. Strikman, Phys. Lett. **B586**, 41 (2004).

- [105] H. Abramowicz, L. Frankfurt, and M. Strikman, *Surveys High Energ. Phys.* **11**, 51 (1997).
- [106] A. I. Shoshi, F. D. Steffen, and H. J. Pirner, *Nucl. Phys.* **A709**, 131 (2002).
- [107] A. I. Shoshi, F. D. Steffen, H. G. Dosch, and H. J. Pirner, *Phys. Rev.* **D66**, 094019 (2002).
- [108] J. Nian and H. J. Pirner, *Nucl. Phys.* **A833**, 119 (2010).
- [109] H. J. Pirner and F. Yuan, *Phys. Rev.* **D66**, 034020 (2002).
- [110] J. Bartels, K. Golec-Biernat, and L. Motyka, *Phys. Rev.* **D81**, 054017 (2010), 0911.1935.
- [111] K. J. Golec-Biernat and M. Wusthoff, *Phys. Rev.* **D59**, 014017 (1998).
- [112] K. J. Golec-Biernat and M. Wusthoff, *Phys. Rev.* **D60**, 114023 (1999).
- [113] J. L. Albacete, N. Armesto, J. G. Milhano, and C. A. Salgado, *Phys. Rev.* **D80**, 034031 (2009).
- [114] J. L. Albacete, N. Armesto, J. G. Milhano, P. Q. Arias, and C. A. Salgado, (2010).
- [115] J. Bartels, K. J. Golec-Biernat, and H. Kowalski, *Phys. Rev.* **D66**, 014001 (2002).
- [116] A. P. Bukhvostov, G. V. Frolov, L. N. Lipatov, and E. A. Kuraev, *Nucl. Phys.* **B258**, 601 (1985).
- [117] H. Kowalski and D. Teaney, *Phys. Rev.* **D68**, 114005 (2003).
- [118] H. Kowalski, L. Motyka, and G. Watt, *Phys. Rev.* **D74**, 074016 (2006).
- [119] G. Watt and H. Kowalski, *Phys. Rev.* **D78**, 014016 (2008).
- [120] H. Kowalski, T. Lappi, C. Marquet, and R. Venugopalan, *Phys. Rev.* **C78**, 045201 (2008).
- [121] H. Kowalski, T. Lappi, and R. Venugopalan, *Phys. Rev. Lett.* **100**, 022303 (2008).
- [122] T. Lappi and H. Mantysaari, (2010), arXiv:1011.1988.
- [123] R. D. Ball *et al.*, *Nucl. Phys.* **B838**, 136 (2010).
- [124] K. J. Eskola, V. J. Kolhinen, and C. A. Salgado, *Eur. Phys. J.* **C9**, 61 (1999).
- [125] S. Forte, *Acta Phys. Polon.* **B41**, 2859 (2010).
- [126] K. J. Eskola, H. Paukkunen, and C. A. Salgado, *JHEP* **04**, 065 (2009).
- [127] G. Altarelli, R. D. Ball, and S. Forte, *Nucl. Phys.* **B799**, 199 (2008).
- [128] F. Caola, S. Forte, and J. Rojo, *Nucl. Phys.* **A854**, 32 (2011).
- [129] E. R. Cazaroto, F. Carvalho, V. P. Goncalves, and F. S. Navarra, *Phys. Lett.* **B669**, 331 (2008).
- [130] I. Balitsky, *Phys. Rev.* **D75**, 014001 (2005).
- [131] Y. V. Kovchegov and H. Weigert, *Nucl. Phys.* **A784**, 188 (2007).
- [132] I. Balitsky and G. A. Chirilli, *Phys. Rev.* **D77**, 014019 (2008).
- [133] V. S. Fadin, E. A. Kuraev, and L. N. Lipatov, *Phys. Lett.* **B60**, 50 (1975).
- [134] I. Balitsky and G. A. Chirilli, *Nucl. Phys.* **B822**, 45 (2009).
- [135] I. Balitsky and G. A. Chirilli, *Phys. Rev.* **D79**, 031502 (2009).
- [136] I. Balitsky and G. A. Chirilli, *Phys. Rev.* **D83**, 031502 (2011).
- [137] I. Balitsky, (2001), hep-ph/0101042.
- [138] A. H. Mueller and J.-w. Qiu, *Nucl. Phys.* **B268**, 427 (1986).
- [139] A. H. Mueller, *Nuclear Physics* **B335**, 115 (1990).

- [140] L. Cornalba, M. S. Costa, and J. Penedones, JHEP **03**, 133 (2010).
- [141] J. Bartels and A. Kyrieleis, Phys. Rev. **D70**, 114003 (2004).
- [142] J. Bartels, D. Colferai, S. Gieseke, and A. Kyrieleis, Phys. Rev. **D66**, 094017 (2002).
- [143] J. Bartels, S. Gieseke, and A. Kyrieleis, Phys. Rev. **D65**, 014006 (2002).
- [144] I. Balitsky and G. A. Chirilli, Phys. Lett. **B687**, 204 (2010).
- [145] G. A. Chirilli, L. Szymanowski, and S. Wallon, Phys. Rev. **D83**, 014020 (2011).
- [146] S. J. Brodsky, G. P. Lepage, and P. B. Mackenzie, Phys. Rev. **D28**, 228 (1983).
- [147] E. Gardi, J. Kuokkanen, K. Rummukainen, and H. Weigert, Nucl. Phys. **A784**, 282 (2007).
- [148] Y. V. Kovchegov and H. Weigert, Nucl. Phys. **A789**, 260 (2007).
- [149] J. L. Albacete, Phys. Rev. Lett. **99**, 262301 (2007).
- [150] M. A. Braun, Phys. Lett. **B348**, 190 (1995).
- [151] E. Levin, Nucl. Phys. **B453**, 303 (1995).
- [152] V. Gribov and L. Lipatov, Sov.J.Nucl.Phys. **15**, 438 (1972).
- [153] G. Altarelli and G. Parisi, Nucl. Phys. **B126**, 298 (1977).
- [154] Y. L. Dokshitzer, Sov. Phys. JETP **46**, 641 (1977).
- [155] L. Lipatov, Sov.J.Nucl.Phys. **23**, 338 (1976).
- [156] K. J. Golec-Biernat, L. Motyka, and A. M. Stasto, Phys. Rev. **D65**, 074037 (2002).
- [157] J. L. Albacete, N. Armesto, J. G. Milhano, C. A. Salgado, and U. A. Wiedemann, Phys. Rev. **D71**, 014003 (2005).
- [158] A. H. Mueller and D. N. Triantafyllopoulos, Nucl. Phys. **B640**, 331 (2002).
- [159] S. Munier and R. B. Peschanski, Phys. Rev. Lett. **91**, 232001 (2003).
- [160] S. Munier and R. B. Peschanski, Phys. Rev. **D69**, 034008 (2004).
- [161] S. Munier and R. B. Peschanski, Phys. Rev. **D70**, 077503 (2004).
- [162] M. Bramson, Mem. Am. Math. Soc. **44**, 285 (1983).
- [163] U. Ebert and W. van Saarloos, Physica **D146**, 1 (2000).
- [164] J. Berger and A. Stasto, Phys. Rev. **D83**, 034015 (2011).
- [165] G. Beuf, (2010), arXiv:1008.0498 [hep-ph].
- [166] A. H. Mueller, Nucl. Phys. **A724**, 223 (2003).
- [167] K. Dusling, F. Gelis, T. Lappi, and R. Venugopalan, Nucl. Phys. **A836**, 159 (2010).
- [168] M. Froissart, Phys. Rev. **123**, 1053 (1961).
- [169] K. J. Golec-Biernat and A. M. Stasto, Nucl. Phys. **B668**, 345 (2003).
- [170] C. Marquet and L. Schoeffel, Phys. Lett. **B639**, 471 (2006).
- [171] A. Bialas and R. B. Peschanski, Phys. Lett. **B378**, 302 (1996).
- [172] A. Bialas and R. B. Peschanski, Phys. Lett. **B387**, 405 (1996).
- [173] C. Marquet, Phys. Rev. **D76**, 094017 (2007).
- [174] C. J. Bomhof, P. J. Mulders, and F. Pijlman, Eur. Phys. J. **C47**, 147 (2006).
- [175] F. Dominguez, B.-W. Xiao, and F. Yuan, Phys. Rev. Lett. **106**, 022301 (2011).

- [176] Y. V. Kovchegov and A. H. Mueller, Nucl. Phys. **B529**, 451 (1998).
- [177] M. Anselmino *et al.*, Eur. Phys. J. **A39**, 89 (2009).
- [178] C. Marquet, B.-W. Xiao, and F. Yuan, Phys. Lett. **B682**, 207 (2009).
- [179] V. P. Goncalves, M. S. Kugeratski, and F. S. Navarra, Phys. Rev. **C81**, 065209 (2010).
- [180] Particle Data Group, K. Nakamura *et al.*, J. Phys. **G37**, 075021 (2010).
- [181] T. Hirano, U. W. Heinz, D. Kharzeev, R. Lacey, and Y. Nara, Phys. Lett. **B636**, 299 (2006).
- [182] M. Luzum and P. Romatschke, Phys. Rev. **C79**, 039903 (2009).
- [183] J. Jia and R. Wei, Phys. Rev. **C82**, 024902 (2010).
- [184] B. Schenke, S. Jeon, and C. Gale, (2010), arXiv:1009.3244 [hep-ph].
- [185] J. Jia, W. A. Horowitz, and J. Liao, (2011), arXiv:1101.0290 [nucl-th].
- [186] S. Munier, A. M. Stasto, and A. H. Mueller, Nucl. Phys. **B603**, 427 (2001).
- [187] A. Caldwell and H. Kowalski, Phys. Rev. **C81**, 025203 (2010).
- [188] R. D. Woods and D. S. Saxon, Phys. Rev. **95**, 577 (1954).
- [189] T. Hirano and Y. Nara, Nucl. Phys. **A743**, 305 (2004).
- [190] A. Kuhlman, U. W. Heinz, and Y. V. Kovchegov, Phys. Lett. **B638**, 171 (2006).
- [191] J. Jalilian-Marian and Y. V. Kovchegov, Prog. Part. Nucl. Phys. **56**, 104 (2006).
- [192] [ZEUS Collaboration], S. Chekanov *et al.*, Eur. Phys. J. **C24**, 345 (2002).
- [193] B. Hahn, D. G. Ravenhall, and R. Hofstadter, Phys. Rev. **101**, 1131 (1956).
- [194] [PHOBOS Collaboration], B. B. Back *et al.*, Phys. Rev. **C65**, 061901 (2002).
- [195] PHENIX, S. S. Adler *et al.*, Phys. Rev. **C71**, 034908 (2005).
- [196] PHOBOS, B. Alver *et al.*, Phys. Rev. **C80**, 011901 (2009).
- [197] [ALICE Collaboration], K. Aamodt *et al.*, (2010), arXiv:1012.1657 [nucl-ex].
- [198] [ALICE Collaboration], K. Aamodt *et al.*, Phys. Rev. Lett. **106**, 032301 (2011).
- [199] J. L. Albacete and A. Dumitru, (2010), arXiv:1011.5161 [hep-ph].
- [200] W. A. Horowitz and Y. V. Kovchegov, (2010), arXiv:1009.0545 [hep-ph].
- [201] J. R. Forshaw, R. Sandapen, and G. Shaw, Phys. Rev. **D69**, 094013 (2004).
- [202] C. Marquet, R. B. Peschanski, and G. Soyez, Phys. Rev. **D76**, 034011 (2007).
- [203] R. Enberg, J. R. Forshaw, L. Motyka, and G. Poludniowski, JHEP **09**, 008 (2003).
- [204] G. G. Poludniowski, R. Enberg, J. R. Forshaw, and L. Motyka, JHEP **12**, 002 (2003).
- [205] A. Deshpande, R. Milner, R. Venugopalan, and W. Vogelsang, Ann. Rev. Nucl. Part. Sci. **55**, 165 (2005), hep-ph/0506148.
- [206] L. D. McLerran and R. Venugopalan, Phys.Rev. **D49**, 3352 (1994).
- [207] H. Fujii, Nucl.Phys. **A709**, 236 (2002).
- [208] J. P. Blaizot, F. Gelis, and R. Venugopalan, Nucl. Phys. **A743**, 57 (2004).
- [209] F. Dominguez, C. Marquet, and B. Wu, Nucl.Phys. **A823**, 99 (2009).
- [210] C. Marquet, R. B. Peschanski, and G. Soyez, Nucl. Phys. **A756**, 399 (2005).
- [211] H. G. Dosch, T. Gousset, G. Kulzinger, and H. J. Pirner, Phys. Rev. **D55**, 2602 (1997).

- [212] G. Kulzinger, H. G. Dosch, and H. J. Pirner, Eur. Phys. J. **C7**, 73 (1999).
- [213] [ZEUS Collaboration], S. Chekanov *et al.*, Nucl. Phys. **B695**, 3 (2004).
- [214] A. Caldwell and H. Kowalski, (2009), arXiv:0909.1254 [hep-ph].
- [215] E. Iancu, K. Itakura, and S. Munier, Phys. Lett. **B590**, 199 (2004).
- [216] G. Soyez, Phys. Lett. **B655**, 32 (2007).
- [217] M. Alvioli, H. J. Drescher, and M. Strikman, Phys. Lett. **B680**, 225 (2009).
- [218] B. Z. Kopeliovich, J. Nemchik, A. Schafer, and A. V. Tarasov, Phys. Rev. **C65**, 035201 (2002).
- [219] J. Hufner, Y. P. Ivanov, B. Z. Kopeliovich, and A. V. Tarasov, Phys. Rev. **D62**, 094022 (2000).
- [220] E. Eichten, K. Gottfried, T. Kinoshita, K. D. Lane, and T.-M. Yan, Phys. Rev. **D21**, 203 (1980).
- [221] W. Buchmuller and S. H. H. Tye, Phys. Rev. **D24**, 132 (1981).
- [222] C. Quigg and J. L. Rosner, Phys. Lett. **B71**, 153 (1977).
- [223] A. Martin, Phys. Lett. **B93**, 338 (1980).
- [224] M. V. Terent'ev, Sov. J. Nucl. Phys. **24**, 106 (1976).
- [225] P. Hoyer and S. Peigné, Phys. Rev. **D61**, 031501(R) (2000).
- [226] H. J. Melosh, Phys. Rev. **D9**, 1095 (1974).
- [227] J. Hufner and B. Z. Kopeliovich, Phys. Lett. **B426**, 154 (1998).
- [228] B. Z. Kopeliovich and B. G. Zakharov, Phys. Rev. **D44**, 3466 (1991).
- [229] Y. P. Ivanov, B. Z. Kopeliovich, A. V. Tarasov, and J. Hufner, Phys. Rev. **C66**, 024903 (2002).
- [230] J. Hufner, B. Kopeliovich, and J. Nemchik, Phys. Lett. **B383**, 362 (1996).
- [231] V. P. Goncalves, M. S. Kugeratski, M. V. T. Machado, and F. S. Navarra, Phys. Rev. **C80**, 025202 (2009).
- [232] E. R. Cazaroto, F. Carvalho, V. P. Goncalves, M. S. Kugeratski, and F. S. Navarra, Phys. Lett. **B696**, 473 (2011).
- [233] A. H. Mueller and B. Patel, Nucl. Phys. **B425**, 471 (1994).
- [234] J. R. Forshaw and R. Sandapen, JHEP **11**, 037 (2010).
- [235] [ZEUS Collaboration], S. Chekanov *et al.*, PMC Phys. **A1**, 6 (2007).
- [236] J. R. Forshaw and G. Shaw, JHEP **12**, 052 (2004).
- [237] L. Motyka, K. Golec-Biernat, and G. Watt, (2008), arXiv:0809.4191 [hep-ph].
- [238] [H1 Collaboration], F. D. Aaron *et al.*, JHEP **05**, 032 (2010).
- [239] J. R. Forshaw, R. Sandapen, and G. Shaw, JHEP **11**, 025 (2006).
- [240] J. Nemchik, N. N. Nikolaev, E. Predazzi, and B. G. Zakharov, Z. Phys. **C75**, 71 (1997).
- [241] P. Ball and V. M. Braun, Phys. Rev. **D54**, 2182 (1996).
- [242] A. P. Bakulev and S. V. Mikhailov, Phys. Lett. **B436**, 351 (1998).
- [243] V. L. Chernyak and A. R. Zhitnitsky, Phys. Rept. **112**, 173 (1984).
- [244] P. Ball, V. M. Braun, and A. Lenz, JHEP **08**, 090 (2007).
- [245] P. Ball and R. Zwicky, Phys. Rev. **D71**, 014015 (2005).
- [246] [RBC Collaboration], P. A. Boyle *et al.*, PoS **LATTICE2008**, 165 (2008).



- [247] [European Muon Collaboration], J. J. Aubert *et al.*, Phys. Lett. **B123**, 275 (1983).
- [248] M. Arneodo, Phys. Rept. **240**, 301 (1994).
- [249] PHENIX, S. S. Adler *et al.*, Phys. Rev. Lett. **91**, 172301 (2003).
- [250] A. Accardi *et al.*, (2004), hep-ph/0308248.
- [251] E. A. Paschos and J. Y. Yu, Phys. Rev. **D65**, 033002 (2002), hep-ph/0107261.
- [252] J. Seely *et al.*, Phys. Rev. Lett. **103**, 202301 (2009).
- [253] J. Gomez *et al.*, Phys. Rev. **D49**, 4348 (1994).
- [254] I. C. Cloet, W. Bentz, and A. W. Thomas, Phys. Rev. Lett. **102**, 252301 (2009), 0901.3559.
- [255] R. P. Bickerstaff and A. W. Thomas, J. Phys. **G15**, 1523 (1989).
- [256] E. L. Berger and F. Coester, Phys. Rev. **D32**, 1071 (1985).
- [257] F. E. Close, R. G. Roberts, and G. G. Ross, Phys. Lett. **B129**, 346 (1983).
- [258] O. Nachtmann and H. Pirner, Z.Phys. **C21**, 277 (1984).
- [259] H. J. Pirner and J. P. Vary, (2010), arViv:1008.4962 [hep-ph].
- [260] L. L. Frankfurt and M. I. Strikman, Nucl. Phys. **B250**, 143 (1985).
- [261] G. A. Miller and J. R. Smith, Phys. Rev. **C65**, 015211 (2002), nucl-th/0107026.
- [262] J. R. Smith and G. A. Miller, Phys. Rev. **C65**, 055206 (2002), nucl-th/0202016.
- [263] I. C. Cloet, W. Bentz, and A. W. Thomas, Phys. Rev. Lett. **95**, 052302 (2005), nucl-th/0504019.
- [264] I. C. Cloet, W. Bentz, and A. W. Thomas, Phys. Lett. **B642**, 210 (2006), nucl-th/0605061.
- [265] Particle Data Group, C. Amsler *et al.*, Phys. Lett. **B667**, 1 (2008).
- [266] T. Gousset and H. J. Pirner, Phys. Lett. **B375**, 349 (1996).
- [267] M. Kaluza, A. G. Schneider-Neureither, and H.-J. Pirner, Phys.Rev. **C48**, 877 (1993).
- [268] H. Merabet, J. Mathiot, J. Dolejsi, and H. Pirner, Phys.Lett. **B307**, 177 (1993).
- [269] K. J. Eskola, V. J. Kolhinen, and P. V. Ruuskanen, Nucl. Phys. **B535**, 351 (1998).
- [270] M. Hirai, S. Kumano, and M. Miyama, Phys. Rev. **D64**, 034003 (2001).
- [271] D. de Florian and R. Sassot, Phys. Rev. **D69**, 074028 (2004).
- [272] M. Hirai, S. Kumano, and T. H. Nagai, Phys. Rev. **C70**, 044905 (2004).
- [273] K. J. Eskola, V. J. Kolhinen, H. Paukkunen, and C. A. Salgado, JHEP **05**, 002 (2007).
- [274] M. Hirai, S. Kumano, and T. H. Nagai, Phys. Rev. **C76**, 065207 (2007).
- [275] I. Schienbein *et al.*, Phys. Rev. **D80**, 094004 (2009).
- [276] R. Sassot, M. Stratmann, and P. Zurita, Phys. Rev. **D81**, 054001 (2010).
- [277] H. Paukkunen and C. A. Salgado, (2010), arXiv:1009.3143 [hep-ph].
- [278] H. Paukkunen, C. A. Salgado, and K. J. Eskola, (2010), arXiv:1009.3142 [hep-ph].
- [279] The HKN-NPDF code is available at <http://research.kek.jp/people/kumanos/nuclp.html>.
- [280] [E665 Collaboration], M. Adams *et al.*, Phys.Rev.Lett. **74**, 1525 (1995).
- [281] B. Z. Kopeliovich, J. Nemchick, N. N. Nikolaev, and B. G. Zakharov, Phys. Lett. **B309**, 179 (1993).

- [282] L. Frankfurt, G. A. Miller, and M. Strikman, Phys. Rev. **D65**, 094015 (2002).
- [283] J. C. Collins, L. Frankfurt, and M. Strikman, Phys. Rev. **D56**, 2982 (1997).
- [284] E791 Collaboration, E. Aitala *et al.*, Phys.Rev.Lett. **86**, 4773 (2001).
- [285] L. Frankfurt, G. Miller, and M. Strikman, Phys.Lett. **B304**, 1 (1993).
- [286] L. Frankfurt, W. Koepf, and M. Strikman, Phys. Rev. **D54**, 3194 (1996).
- [287] S. J. Brodsky, L. Frankfurt, J. F. Gunion, A. H. Mueller, and M. Strikman, Phys. Rev. **D50**, 3134 (1994).
- [288] L. Frankfurt, W. Koepf, and M. Strikman, Phys. Rev. **D57**, 512 (1998).
- [289] A. J. Baltz *et al.*, Phys. Rept. **458**, 1 (2008).
- [290] S. White and M. Strikman, (2010), arXiv:1003.2196 [nucl-ex].
- [291] L. Frankfurt, V. Guzey, M. McDermott, and M. Strikman, Phys. Rev. Lett. **87**, 192301 (2001).
- [292] L. Frankfurt, M. Strikman, and M. Zhalov, Phys. Rev. Lett. **102**, 232001 (2009).
- [293] S. Kumano, M. Strikman, and K. Sudoh, Phys. Rev. **D80**, 074003 (2009).
- [294] S. Kumano and M. Strikman, Phys. Lett. **B683**, 259 (2010).
- [295] J. C. Collins and A. Freund, Phys. Rev. **D59**, 074009 (1999).
- [296] E. R. Berger, F. Cano, M. Diehl, and B. Pire, Phys. Rev. Lett. **87**, 142302 (2001).
- [297] F. Cano and B. Pire, Nucl. Phys. **A711**, 133 (2002).
- [298] A. Kirchner and D. Mueller, Eur. Phys. J. **C32**, 347 (2003).
- [299] V. Guzey and M. Strikman, Phys. Rev. **C68**, 015204 (2003), hep-ph/0301216.
- [300] V. Guzey, Phys. Rev. **C78**, 025211 (2008).
- [301] Jefferson Lab Hall A, M. Mazouz *et al.*, Phys. Rev. Lett. **99**, 242501 (2007), 0709.0450.
- [302] S. Scopetta, Phys. Rev. **C70**, 015205 (2004).
- [303] S. Liuti and S. K. Taneja, Phys. Rev. **C72**, 032201 (2005).
- [304] A. Freund and M. Strikman, Eur. Phys. J. C **33**, 53 (2004), hep-ph/0309065.
- [305] K. Goeke, V. Guzey, and M. Siddikov, Phys. Rev. **C79**, 035210 (2009).
- [306] V. Guzey, A. W. Thomas, and K. Tsushima, Phys. Lett. **B673**, 9 (2009).
- [307] V. Guzey and M. Siddikov, J. Phys. **G32**, 251 (2006).
- [308] [HERMES Collaboration], A. Airapetian *et al.*, Phys. Rev. **C81**, 035202 (2010).
- [309] H. Egiyan *et al.*, 2008, Jefferson Lab Experiment E08-024.
- [310] L. Frankfurt, A. Freund, V. Guzey, and M. Strikman, Phys. Lett. **B418**, 345 (1998).
- [311] A. V. Belitsky, D. Mueller, and A. Kirchner, Nucl. Phys. **B629**, 323 (2002).
- [312] J. C. Collins and D. E. Soper, Nucl. Phys. **B194**, 445 (1982).
- [313] X.-d. Ji, J.-p. Ma, and F. Yuan, Phys. Rev. **D71**, 034005 (2005).
- [314] Z.-t. Liang, X.-N. Wang, and J. Zhou, Phys. Rev. **D77**, 125010 (2008).
- [315] A. V. Belitsky, X. Ji, and F. Yuan, Nucl. Phys. **B656**, 165 (2003).
- [316] D. W. Sivers, Phys.Rev. **D41**, 83 (1990).
- [317] S. J. Brodsky, D. S. Hwang, and I. Schmidt, Phys. Lett. **B530**, 99 (2002).

- [318] J. C. Collins, Phys. Lett. **B536**, 43 (2002).
- [319] R. Baier, Y. L. Dokshitzer, A. H. Mueller, S. Peigne, and D. Schiff, Nucl.Phys. **B484**, 265 (1997).
- [320] G. T. Bodwin, S. J. Brodsky, and G. Lepage, Phys.Rev. **D39**, 3287 (1989).
- [321] M. Luo, J.-w. Qiu, and G. F. Sterman, Phys.Lett. **B279**, 377 (1992).
- [322] X.-f. Guo, Phys. Rev. **D58**, 114033 (1998).
- [323] U. A. Wiedemann, Nucl. Phys. **B588**, 303 (2000).
- [324] R. J. Fries, Phys. Rev. **D68**, 074013 (2003).
- [325] A. Majumder and B. Muller, Phys. Rev. **C77**, 054903 (2008).
- [326] F. D'Eramo, H. Liu, and K. Rajagopal, (2010), 1006.1367.
- [327] P. J. Mulders and R. D. Tangerman, Nucl. Phys. **B461**, 197 (1996).
- [328] A. Bacchetta *et al.*, JHEP **02**, 093 (2007).
- [329] Z.-t. Liang and X.-N. Wang, Phys. Rev. **D75**, 094002 (2007).
- [330] J.-H. Gao, Z.-t. Liang, and X.-N. Wang, Phys. Rev. **C81**, 065211 (2010).
- [331] Y.-k. Song, J.-h. Gao, Z.-t. Liang, and X.-N. Wang, (2010), 1012.4179.
- [332] X. Ji, J.-W. Qiu, W. Vogelsang, and F. Yuan, Phys. Rev. Lett. **97**, 082002 (2006).
- [333] A. Bacchetta, D. Boer, M. Diehl, and P. J. Mulders, JHEP **08**, 023 (2008).
- [334] F. Yuan and J. Zhou, Phys. Rev. Lett. **103**, 052001 (2009).
- [335] A. Accardi, F. Arleo, W. K. Brooks, D. D'Enterria, and V. Muccifora, Riv. Nuovo Cim. **32**, 439 (2010).
- [336] A. Majumder and M. V. Leeuwen, (2010), arXiv:1002.2206 [hep-ph].
- [337] F. Arleo, JHEP **11**, 044 (2002).
- [338] K. Gallmeister and U. Mosel, Nucl. Phys. **A801**, 68 (2008).
- [339] E. Wang and X.-N. Wang, Phys. Rev. Lett. **89**, 162301 (2002).
- [340] A. Accardi, Eur. Phys. J. **C49**, 347 (2007).
- [341] PHENIX, A. Adare *et al.*, Phys. Rev. **C77**, 064907 (2008).
- [342] S. A. Bass *et al.*, Phys. Rev. **C79**, 024901 (2009).
- [343] B. Z. Kopeliovich, J. Nemchik, E. Predazzi, and A. Hayashigaki, Nucl. Phys. **A740**, 211 (2004).
- [344] A. Accardi, V. Muccifora, and H.-J. Pirner, Nucl.Phys. **A720**, 131 (2003), nucl-th/0211011.
- [345] A. Accardi, D. Grunewald, V. Muccifora, and H. J. Pirner, Nucl. Phys. **A761**, 67 (2005).
- [346] A. Accardi, D. Grunewald, V. Muccifora, and H. J. Pirner, (2005).
- [347] K. H. *et al.*, Jefferson Lab experiment E12-06-117, [http://www.jlab.org/exp\\_prog/proposals/06/PR12-06-117.pdf](http://www.jlab.org/exp_prog/proposals/06/PR12-06-117.pdf).
- [348] L. S. Osborne *et al.*, Phys. Rev. Lett. **40**, 1624 (1978).
- [349] L. Hand *et al.*, Z. Phys. **C1**, 139 (1979).
- [350] E665, M. R. Adams *et al.*, Z. Phys. **C65**, 225 (1995).
- [351] European Muon Collaboration, A. Arvidson *et al.*, Nucl. Phys. **B246**, 381 (1984).

- [352] European Muon Collaboration, J. Ashman *et al.*, Z. Phys. **C52**, 1 (1991).
- [353] HERMES, A. Airapetian *et al.*, Nucl. Phys. **B780**, 1 (2007).
- [354] HERMES, A. Airapetian *et al.*, Phys. Lett. **B684**, 114 (2010).
- [355] HERMES, A. Airapetian *et al.*, Phys. Rev. Lett. **96**, 162301 (2006).
- [356] C. Ciofi degli Atti and B. Z. Kopeliovich, Phys. Lett. **B606**, 281 (2005).
- [357] CLAS, K. Hicks and A. Daniel, Proceedings of the XVII International Workshop on Deep-Inelastic Scattering and Related Topics (DIS2009), Madrid, Spain, April 2009, <http://dx.doi.org/10.3360/dis.2009.85>.
- [358] W. K. Brooks and H. Hakobyan, Nucl. Phys. **A830**, 361c (2009).
- [359] PHENIX, A. Adare *et al.*, Phys. Rev. Lett. **98**, 172301 (2007).
- [360] STAR, B. I. Abelev *et al.*, Phys. Rev. Lett. **98**, 192301 (2007).
- [361] A. Majumder, (2010), [http://www.int.washington.edu/talks/WorkShops/int\\_10\\_3](http://www.int.washington.edu/talks/WorkShops/int_10_3).
- [362] I. Vitev, J. Phys. **G35**, 104011 (2008).
- [363] W. A. Horowitz and M. Gyulassy, J. Phys. **G35**, 104152 (2008).
- [364] GiBUU homepage: <http://gibuu.physik.uni-giessen.de/GiBUU/>.
- [365] T. Falter, *Nuclear reactions of high energy protons, photons and leptons*, PhD thesis, Justus-Liebig-Universität Gießen, 2004, available online at <http://theorie.physik.uni-giessen.de/>.
- [366] K. Gallmeister and T. Falter, Phys. Lett. **B630**, 40 (2005).
- [367] Y. L. Dokshitzer, V. A. Khoze, A. H. Mueller, and S. Troian, (1991).
- [368] G. Farrar, H. Liu, L. Frankfurt, and M. Strikman, Phys.Rev.Lett. **61**, 686 (1988).
- [369] D. de Florian, R. Sassot, and M. Stratmann, Phys. Rev. **D75**, 114010 (2007).
- [370] [PHENIX Collaboration], S. S. Adler *et al.*, Phys. Rev. Lett. **98**, 172302 (2007).
- [371] [STAR Collaboration], J. Adams *et al.*, Phys. Lett. **B637**, 161 (2006).
- [372] N. Armesto, (2009), arXiv:0903.1330 [hep-ph].
- [373] X.-f. Guo and X.-N. Wang, Phys. Rev. Lett. **85**, 3591 (2000).
- [374] A. Majumder, E. Wang, and X.-N. Wang, Phys. Rev. **C73**, 044901 (2006).
- [375] N. Armesto, L. Cunqueiro, C. A. Salgado, and W.-C. Xiang, JHEP **02**, 048 (2008).
- [376] S. Albino, B. A. Kniehl, and R. Perez-Ramos, Nucl. Phys. **B819**, 306 (2009).
- [377] B. Kopeliovich, J. Nemchik, and E. Predazzi, (1995), nucl-th/9607036.
- [378] B. Kopeliovich, J. Nemchik, and I. Schmidt, Nucl.Phys. **A782**, 224 (2007).
- [379] B. Kopeliovich, H.-J. Pirner, I. Potashnikova, and I. Schmidt, Phys.Lett. **B662**, 117 (2008).
- [380] B. Z. Kopeliovich, I. K. Potashnikova, and I. Schmidt, Phys. Rev. **C82**, 037901 (2010).
- [381] Y. L. Dokshitzer, V. A. Khoze, and S. Troian, J.Phys.G **G17**, 1481 (1991).
- [382] Y. L. Dokshitzer and D. Kharzeev, Phys.Lett. **B519**, 199 (2001).
- [383] B. Kopeliovich and F. Niedermayer, Sov.J.Nucl.Phys. **42**, 504 (1985).
- [384] C. Markert, R. Bellwied, and I. Vitev, Phys. Lett. **B669**, 92 (2008).
- [385] B. Kopeliovich *et al.*, Phys.Rev. **C78**, 055204 (2008).
- [386] B. Z. Kopeliovich and J. Nemchik, (2010), arXiv:1009.1162 [hep-ph].

- [387] E665, C. W. Salgado, FERMILAB-CONF-93-345-E, Presented at 23rd International Symposium on Ultra-High Energy Multiparticle Phenomena, Aspen, CO, 12-17 Sep 1993.
- [388] E665, H. L. Melanson, FERMILAB-CONF-93-165-E, Presented at 28th Rencontres de Moriond: QCD and High Energy Hadronic Interactions, Les Arcs, France, 20-27 Mar 1993.
- [389] G. Soyez, (2009), <https://eic.jlab.org/wiki/images/b/b0/Soyez.jet.note.pdf>.
- [390] A. Majumder, (2009), arXiv:0901.4516.
- [391] A. Majumder, (2009), arXiv:0912.2987.
- [392] S. Domdey, B. Z. Kopeliovich, and H. J. Pirner, (2010), 1010.0134.
- [393] S. Domdey *et al.*, Nucl. Phys. **A808**, 178 (2008).
- [394] S. Domdey, D. Grunewald, B. Z. Kopeliovich, and H. J. Pirner, Nucl. Phys. **A825**, 200 (2009).
- [395] [E665 Collaboration], M. Adams *et al.*, Phys.Rev.Lett. **74**, 5198 (1995).
- [396] M. Strikman, M. G. Tverskoi, and M. B. Zhalov, Phys. Lett. **B459**, 37 (1999).
- [397] C. Ciofi degli Atti and B. Z. Kopeliovich, Eur. Phys. J. **A17**, 133 (2003).
- [398] C. Ciofi degli Atti, L. P. Kaptari, and S. Scopetta, Eur. Phys. J. **A5**, 191 (1999).
- [399] C. Ciofi degli Atti, L. P. Kaptari, and B. Z. Kopeliovich, Eur. Phys. J. **A19**, 145 (2004).
- [400] V. Palli, C. Ciofi degli Atti, L. P. Kaptari, C. B. Mezzetti, and M. Alvioli, Phys. Rev. **C80**, 054610 (2009).
- [401] C. Ciofi degli Atti and L. P. Kaptari, (2010), arXiv:1011.5960 [nucl-th].
- [402] P. Norton, Rept.Prog.Phys. **66**, 1253 (2003).
- [403] See e.g. *Nuclear Exclusive and Semi-inclusive Physics with a New CLAS12 Low Energy Recoil Detector*, LOI to the PAC Jlab, K. Hafidi *et al.*
- [404] [CLAS Collaboration], A. V. Klimenko *et al.*, Phys. Rev. **C73**, 035212 (2006).
- [405] B. Kopeliovich, J. Nemchik, E. Predazzi, and A. Hayashigaki, Eur.Phys.J. **A19S1**, 111 (2004).
- [406] R. J. Glauber, *Lectures in Theoretical Physics* (Interscience Publishers, 1959).
- [407] A. Kievsky, S. Rosati, and M. Viviani, Phys. Rev. Lett. **82**, 3759 (1999).
- [408] R. B. Wiringa, V. G. J. Stoks, and R. Schiavilla, Phys. Rev. **C51**, 38 (1995).
- [409] C. Ciofi degli Atti, L. L. Frankfurt, L. P. Kaptari, and M. I. Strikman, Phys. Rev. **C76**, 055206 (2007).
- [410] J. Bondorf, A. Botvina, A. Ilinov, I. Mishustin, and K. Sneppen, Phys.Rept. **257**, 133 (1995).
- [411] [ZEUS Collaboration], S. Chekanov *et al.*, Phys. Lett. **B583**, 231 (2004).
- [412] G. Goldhaber, S. Goldhaber, W.-Y. Lee, and A. Pais, Phys.Rev. **120**, 300 (1960).
- [413] PHENIX, S. S. Adler *et al.*, Phys. Rev. Lett. **93**, 152302 (2004).
- [414] CMS, V. Khachatryan *et al.*, Phys. Rev. Lett. **105**, 032001 (2010).
- [415] T. Csorgo, R. Vertesi, and J. Sziklai, Phys. Rev. Lett. **105**, 182301 (2010).
- [416] CLAS, A. V. Stavinisky *et al.*, Phys. Rev. Lett. **93**, 192301 (2004).
- [417] P. Degtyarenko, Y. Efremenko, V. Gavrilov, G. Leksin, and N. Semenova, Z.Phys. **A335**, 231 (1990).
- [418] P. Degtyarenko *et al.*, Z.Phys. **A350**, 263 (1994).
- [419] P. Degtyarenko *et al.*, Z.Phys. **A357**, 419 (1997).

- [420] H. Hakobyan, 2010, private communication.
- [421] E. A. McCutchan *et al.*, Phys. Rev. Lett. **103**, 192501 (2009).
- [422] S. C. Pieper and R. B. Wiringa, Ann. Rev. Nucl. Part. Sci. **51**, 53 (2001).
- [423] K. Jansen, PoS **LATTICE2008**, 010 (2008).
- [424] [CLAS Collaboration], K. S. Egiyan *et al.*, Phys. Rev. Lett. **96**, 082501 (2006).
- [425] [CLAS Collaboration], H. Baghdasaryan *et al.*, Phys. Rev. Lett. **105**, 222501 (2010).
- [426] L. Frankfurt and M. Strikman, AIP Conf. Proc. **1056**, 241 (2008).
- [427] M. M. Sargsian *et al.*, J. Phys. **G29**, R1 (2003).
- [428] S. Albino *et al.*, (2008), arXiv:0804.2021 [hep-ph].
- [429] B. Andersson and W. Hofmann, Phys.Lett. **B169**, 364 (1986).
- [430] T. Sjostrand, S. Mrenna, and P. Z. Skands, JHEP **05**, 026 (2006).
- [431] L. Lonnblad and T. Sjostrand, Phys.Lett. **B351**, 293 (1995).
- [432] L. Lonnblad and T. Sjostrand, Eur. Phys. J. **C2**, 165 (1998).
- [433] T. Sjostrand *et al.*, Comput. Phys. Commun. **135**, 238 (2001).
- [434] M. Bahr *et al.*, Eur. Phys. J. **C58**, 639 (2008).
- [435] G. Ingelman, A. Edin, and J. Rathsmann, Comput. Phys. Commun. **101**, 108 (1997).
- [436] L. Mankiewicz, A. Schafer, and M. Veltri, Comput. Phys. Commun. **71**, 305 (1992).
- [437] H. Jung, Comput.Phys.Comm. **86**, 147 (1995).
- [438] L. Lonnblad, Comput.Phys.Comm. **71**, 15 (1992).
- [439] H. Jung, Comput. Phys. Commun. **143**, 100 (2002).
- [440] T. Gleisberg *et al.*, JHEP **02**, 007 (2009).
- [441] S. Roesler, R. Engel, and J. Ranft, (2000), hep-ph/0012252.
- [442] M. Good and W. Walker, Phys.Rev. **120**, 1857 (1960).
- [443] R. J. Charity, 2011, private communication.
- [444] A. Botvina, 2011, private communication.
- [445] W. Horowitz, 2011, these proceedings.
- [446] The EIC “Parton Propagation and Fragmentation” working group wiki:  
[https://eic.jlab.org/wiki/index.php/EA\\_ppf](https://eic.jlab.org/wiki/index.php/EA_ppf).
- [447] C. A. Salgado and U. A. Wiedemann, Phys. Rev. Lett. **89**, 092303 (2002).
- [448] H. De Vries, C. W. De Jager, and C. De Vries, Atom. Data Nucl. Data Tabl. **36**, 495 (1987).
- [449] C. A. Salgado and U. A. Wiedemann, Phys. Rev. **D68**, 014008 (2003).
- [450] A. Accardi, Phys. Rev. **C76**, 034902 (2007).
- [451] [PHENIX Collaboration], K. Adcox *et al.*, Nucl. Phys. **A757**, 184 (2005).
- [452] [STAR Collaboration], J. Adams *et al.*, Nucl. Phys. **A757**, 102 (2005).
- [453] [PHOBOS Collaboration], B. B. Back *et al.*, Nucl. Phys. **A757**, 28 (2005).
- [454] [BRAHMS Collaboration], I. Arsene *et al.*, Nucl. Phys. **A757**, 1 (2005).
- [455] M. Gyulassy and L. McLerran, Nucl. Phys. **A750**, 30 (2005).

- [456] T. Ludlam and L. McLerran, Phys. Today **56N10**, 48 (2003).
- [457] P. F. Kolb, P. Huovinen, U. W. Heinz, and H. Heiselberg, Phys. Lett. **B500**, 232 (2001).
- [458] [NA49 Collaboration], C. Alt *et al.*, Phys. Rev. **C68**, 034903 (2003).
- [459] M. Riordan and W. A. Zajc, Sci. Am. **294N5**, 24 (2006).
- [460] BNL press release, RHIC scientists serve up “perfect” liquid, 2005.
- [461] B. Jacak and P. Steinberg, Phys. Today **63N5**, 39 (2010).
- [462] J. I. Kapusta, (2008), arXiv:0809.3746 [nucl-th].
- [463] J. Takahashi *et al.*, Phys. Rev. Lett. **103**, 242301 (2009).
- [464] M. Gyulassy, D. H. Rischke, and B. Zhang, Nucl. Phys. **A613**, 397 (1997).
- [465] [PHENIX Collaboration], Y. Akiba, Nucl. Phys. **A774**, 403 (2006).
- [466] W. A. Horowitz and M. Gyulassy, Phys. Lett. **B666**, 320 (2008).
- [467] W. A. Horowitz and B. A. Cole, Phys. Rev. **C81**, 024909 (2010).
- [468] G. S. Blanford *et al.*, Phys. Rev. Lett. **39**, 1447 (1977).
- [469] R. Baier, A. H. Mueller, D. Schiff, and D. T. Son, Phys. Lett. **B539**, 46 (2002).
- [470] A. Dumitru, E. Molnar, and Y. Nara, Phys. Rev. **C76**, 024910 (2007).
- [471] D. Kharzeev and E. Levin, Phys. Lett. **B523**, 79 (2001).
- [472] Y. V. Kovchegov and K. Tuchin, Phys. Rev. **D65**, 074026 (2002).
- [473] [PHOBOS Collaboration], G. Roland *et al.*, Nucl. Phys. **A774**, 113 (2006).
- [474] H. J. Drescher, A. Dumitru, C. Gombeaud, and J. Y. Ollitrault, Phys. Rev. **C76**, 024905 (2007).
- [475] A. Dumitru, (2010), arXiv:1008.5162 [nucl-th].
- [476] P. Tribedy and R. Venugopalan, (2010), arXiv:1011.1895 [hep-ph].
- [477] J. Y. Ollitrault, Phys. Rev. **D46**, 229 (1992).
- [478] A. Adil, H. J. Drescher, A. Dumitru, A. Hayashigaki, and Y. Nara, Phys. Rev. **C74**, 044905 (2006).
- [479] U. W. Heinz, J. S. Morel, , and H. Song, Phys. Rev. **C80**, 061901 (2009).
- [480] B. Alver and G. Roland, Phys. Rev. **C81**, 054905 (2010).
- [481] B. H. Alver, C. Gombeaud, M. Luzum, and J. Y. Ollitrault, Phys. Rev. **C82**, 034913 (2010).
- [482] G. Y. Qin, H. Petersen, S. A. Bass, and B. Muller, (2010), arXiv:1009.1847 [nucl-th].
- [483] D. Teaney and L. Yan, (2010), arXiv:1010.1876 [nucl-th].
- [484] Y. V. Kovchegov, Phys. Rev. **D68**, 039901 (2001).
- [485] Y. Li and K. Tuchin, Phys. Rev. **C78**, 024905 (2008).
- [486] M. A. Braun, Phys. Lett. **B483**, 105 (2000).
- [487] J. P. Blaizot, F. Gelis, and R. Venugopalan, Nucl. Phys. **A743**, 13 (2004).
- [488] M. A. Braun, Eur. Phys. J. **C70**, 73 (2010).
- [489] D. Kharzeev, Y. V. Kovchegov, and K. Tuchin, Phys. Rev. **D68**, 094013 (2003).
- [490] R. Baier, A. Kovner, and U. A. Wiedemann, Phys. Rev. **D68**, 054009 (2003).

- [491] D. Kharzeev, Y. V. Kovchegov, and K. Tuchin, Phys. Lett. **B599**, 23 (2004).
- [492] A. Dumitru, A. Hayashigaki, and J. Jalilian-Marian, Nucl. Phys. **A770**, 57 (2006).
- [493] J. L. Albacete and C. Marquet, Phys. Lett. **B687**, 174 (2010).
- [494] A. Dumitru and J. Jalilian-Marian, Phys. Rev. Lett. **89**, 022301 (2002).
- [495] F. Gelis and A. Peshier, Nucl. Phys. **A697**, 879 (2002).
- [496] F. Gelis and J. Jalilian-Marian, Phys. Rev. **D67**, 074019 (2003).
- [497] D. Kharzeev, E. Levin, and M. Nard, Nucl. Phys. **A743**, 329 (2004).
- [498] K. Tuchin, Phys. Lett. **B593**, 66 (2004).
- [499] Y. V. Kovchegov and K. Tuchin, Phys. Rev. **D74**, 054014 (2006).
- [500] D. Kharzeev and K. Tuchin, Nucl. Phys. **A735**, 248 (2004).
- [501] F. G. H. Fujii and R. Venugopalan, Phys. Rev. Lett. **95**, 162002 (2005).
- [502] K. Tuchin, Nucl. Phys. **A798**, 61 (2008).
- [503] J. Hufner, B. Kopeliovich, and A. B. Zamolodchikov, Z. Phys. **A357**, 113 (1997).
- [504] D. Kharzeev and K. Tuchin, Nucl. Phys. **A770**, 40 (2006).
- [505] D. Kharzeev, E. Levin, M. Nardi, and K. Tuchin, Nucl. Phys. **A826**, 230 (2009).
- [506] J. Jalilian-Marian, Nucl. Phys. **A753**, 307 (2005).
- [507] F. Gelis and J. Jalilian-Marian, Phys. Rev. **D66**, 094014 (2002).
- [508] R. Baier, A. H. Mueller, and D. Schiff, Nucl. Phys. **A741**, 358 (2004).
- [509] J. Jalilian-Marian, Nucl. Phys. **A739**, 319 (2004).
- [510] D. Kharzeev, E. Levin, and L. McLerran, Nucl. Phys. **A748**, 627 (2005).
- [511] C. Marquet, Nucl. Phys. **A796**, 41 (2007).
- [512] J. L. Albacete and C. Marquet, Phys. Rev. Lett. **105**, 162301 (2010).
- [513] K. Tuchin, Nucl. Phys. **A846**, 83 (2010).
- [514] J. Jalilian-Marian and Y. V. Kovchegov, Phys. Rev. **D71**, 079901 (2005).
- [515] V. S. Fadin, M. I. Kotsky, and L. N. Lipatov, (1997), hep-ph/9704267.
- [516] A. Leonidov and D. Ostrovsky, Phys. Rev. **D62**, 094009 (2000).
- [517] A. Kovner and U. A. Wiedemann, Phys. Rev. **D64**, 114002 (2001).
- [518] Y. Li and K. Tuchin, Phys. Rev. **D77**, 114012 (2008).
- [519] K. Tuchin, Phys. Rev. **C79**, 055206 (2009).
- [520] K. J. Golec-Biernat and C. Marquet, Phys. Rev. **D71**, 114005 (2005).
- [521] K. Tuchin and D. Wu, (2011), arXiv:1101.2179 [hep-ph].
- [522] M. Strikman, R. Vogt, and S. N. White, Phys. Rev. Lett. **96**, 082001 (2006).
- [523] L. Frankfurt and M. Strikman, Phys. Lett. **B645**, 412 (2007).